

BURNING BEHAVIORS OF SOLID PROPELLANTS USING  
GRAPHENE-BASED MICRO-STRUCTURES: EXPERIMENTS AND  
SIMULATIONS

A Dissertation

Submitted to the Faculty

of

Purdue University

by

Shourya Jain

In Partial Fulfillment of the  
Requirements for the Degree

of

Doctor of Philosophy

December 2018

Purdue University

West Lafayette, Indiana

**THE PURDUE UNIVERSITY GRADUATE SCHOOL  
STATEMENT OF DISSERTATION APPROVAL**

Dr. Li Qiao, Chair

School of Aeronautics and Astronautics

Dr. Alina A. Alexeenko

School of Aeronautics and Astronautics

Dr. Stephen D. Heister

School of Aeronautics and Astronautics

Dr. Liang Pan

School of Mechanical Engineering

**Approved by:**

Dr. Weinong Wayne Chen

Head of the School Graduate Program

Dedicated to my parents

## ACKNOWLEDGMENTS

I would like to thank my advisor, Prof. Li Qiao, for her constant guidance and support and for her exceptional attitude. Her dedication towards my research has helped me remain motivated and has been instrumental in my development as a researcher. I would also like to thank Prof. Stephen D. Heister, Prof. Alina Alexeenko, Prof. Timothy S. Fisher and Prof. Liang Pan for serving on my PhD committee and for their valuable suggestions and discussions.

Secondly, I would like to thank Dr. Aamer Mahmood for his help and advice with the fabrication techniques involved in the design of the micro-thermal sensor needed for the experimental work involving combustion of nanobubbles. I would also like to thank Prof. Yong P. Chen and his graduate student Dr. Wonjun Park for their help in the fabrication of the graphene foam micro-structures.

Finally, I would like to thank my research group for their wonderful support and many valuable discussions about research and life. I would also like to thank the technical staff at the School of Aeronautics and Astronautics: David Reagan, John Phillips and Scott Meyer for their technical support in designing my experiments.

## TABLE OF CONTENTS

	Page
LIST OF TABLES . . . . .	vii
LIST OF FIGURES . . . . .	viii
ABSTRACT . . . . .	xiv
1 INTRODUCTION . . . . .	1
1.1 Research Objectives . . . . .	13
2 BURN RATE ENHANCEMENT: PURE GRAPHENE-STRUCTURES . . . . .	14
2.1 Sample Preparation and Characterization . . . . .	15
2.1.1 Graphite Sheet (GS) . . . . .	15
2.1.2 Graphene Nanopellets (GNPs) . . . . .	17
2.1.3 Graphene Foam (GF) . . . . .	21
2.2 Experimental Setup . . . . .	27
2.3 Experimental Results . . . . .	30
2.3.1 Graphite Sheet (GS) . . . . .	30
2.3.2 Graphene Nanopellets (GNPs) . . . . .	33
2.3.3 Graphene Foam (GF) . . . . .	37
2.4 1-D Modeling of Reaction Wave Propagation in the NC-GS System . . . . .	44
2.4.1 Model Setup . . . . .	44
2.4.2 1-D Results . . . . .	48
2.5 MD Simulation of the Coupled PETN-MWCNT System . . . . .	56
2.5.1 Computational Method . . . . .	56
2.5.2 Reaction Wave Propagation in Pure PETN . . . . .	62
2.5.3 Reaction Wave Propagation in PETN-MWCNT . . . . .	66
2.5.4 Ignition of Pure PETN and PETN-MWCNT . . . . .	72
2.5.5 Interfacial Thermal Transport . . . . .	73
3 BURN RATE ENHANCEMENT: MnO <sub>2</sub> COATED GF STRUCTURES . . . . .	78
3.1 Experimental Method . . . . .	78
3.1.1 Preparation of MnO <sub>2</sub> Coated GF Structures . . . . .	78
3.1.2 TG and DSC: Experimental Setup . . . . .	82
3.1.3 Burn Rate: Experimental Setup . . . . .	87
3.2 Results and Discussion . . . . .	87
3.2.1 Burn Rates and Thermal Decomposition Parameters . . . . .	87
3.2.2 Surface Temperature Measurements . . . . .	93
4 COMBUSTION ON A MICRO-CHIP . . . . .	94

	Page
4.1 Introduction . . . . .	94
4.2 Experimental Study: MEMS Thermal Sensor . . . . .	100
4.2.1 Fabrication . . . . .	100
4.2.2 Experimental Setup . . . . .	104
4.2.3 Results and Discussion . . . . .	109
4.3 Nanobubble Pressure and Surface Tension . . . . .	116
4.3.1 Interaction Potential . . . . .	117
4.3.2 Validation of the SPC/E Force Field . . . . .	119
4.3.3 Surface Tension under Supersaturated Conditions . . . . .	121
4.4 H <sub>2</sub> /O <sub>2</sub> Combustion at Low Temperatures and High Pressures . . . . .	124
4.4.1 Computational Method . . . . .	124
4.4.2 Results and Discussion . . . . .	128
4.5 Conclusions . . . . .	144
5 CONCLUSIONS . . . . .	147
6 FUTURE WORK . . . . .	152
REFERENCES . . . . .	154
VITA . . . . .	170

## LIST OF TABLES

Table	Page
2.1 Thermal conductivity measurements for the GNP-NC sample with 0% wt. GNPs . . . . .	19
2.2 Thermal conductivity measurements for the GNP-NC sample with 2% wt. GNPs . . . . .	20
2.3 Thermal conductivity measurements for the GNP-NC sample with 5% wt. GNPs . . . . .	20
2.4 Thermal conductivity measurements for the GF density - 22 mg/cm <sup>3</sup> . . . . .	23
2.5 Thermal conductivity measurements for the GF density - 11.3 mg/cm <sup>3</sup> . . . . .	23
2.6 Fuel and graphite sheet properties at 450 K [19, 130–133] . . . . .	46
2.7 Minimum bond order values (PETN-MWCNT system) . . . . .	57
2.8 MD simulation matrix (PETN-MWCNT system) . . . . .	62
4.1 L-J parameters [197, 202] . . . . .	118
4.2 Minimum bond order values (H <sub>2</sub> /O <sub>2</sub> system) [138] . . . . .	125
4.3 MD simulation matrix (H <sub>2</sub> /O <sub>2</sub> system) . . . . .	125

## LIST OF FIGURES

Figure	Page
2.1 a) Top view and b) side view of the NC-GS sample. The particular case shown corresponds to 4 layers of NC deposition. . . . .	15
2.2 Fuel thickness as a function of the number of NC layers drop-casted onto the graphihte sheet. . . . .	16
2.3 SEM image of a single GNP. . . . .	17
2.4 SEM images of GNP-doped NC films; a) 0% wt. (pure NC), b) 3% wt. and c) 5% wt. GNPs. . . . .	18
2.5 Experimental setup for measuring GNP-NC film thermal conductivity. . . . .	19
2.6 SEM images of the GF structure before NC deposition. . . . .	21
2.7 The pure GF sheet cut in the required dimension of 2.5 cm x 0.6 cm. . . . .	22
2.8 TG analysis of GF (up to 100 °C) with and without NC addition. . . . .	25
2.9 SEM images of the GF surface after NC deposition; a) 95%, b) 75%, c) 55% and d) 35% NC-GF loading. . . . .	26
2.10 Experimental Setup (not to scale) for burn rate measurements. . . . .	27
2.11 Intensity profiles during the reaction wave propagation as a function of time and space. . . . .	27
2.12 Reaction wave propagation in the NC-GF sample (55% NC-GF loading, 3.82 cm/s) and pure NC (0.7 cm/s). The distance of propagation in both the samples was 1.3 cm. . . . .	28
2.13 Instantaneous burn rates as a function of the distance traveled along the length of a NC-GS sample. The particular case shown corresponds to the fuel thickness of 70 $\mu\text{m}$ . . . . .	31
2.14 Average burn rates as a function of the fuel thickness for the NC-GS system.	32
2.15 Effective thermal conductivity of the GNP-NC sample as a function of the % wt. of GNPs. . . . .	33
2.16 Average burn rates as a function of the % wt. of GNPs. . . . .	33
2.17 a) SEM image of the top view of a GNP-NC sample after combustion; b) TG analysis of GNPs in air. . . . .	37

Figure	Page
2.18 Average burn rates as a function of the NC-GF loading (%). GF density fixed at 18 mg/cm <sup>3</sup> . . . . .	38
2.19 Average burn rates as a function of the GF density. NC-GF loading fixed at 55%. . . . .	38
2.20 SEM images of the GF strut walls with different densities; a) 11.3 mg/cm <sup>3</sup> and b) 22 mg/cm <sup>3</sup> . . . . .	40
2.21 SEM images of GF; a) before combustion and b) after combustion. The particular case shown corresponds to GF of density 18 mg/cm <sup>3</sup> and NC-GF loading of 75%. . . . .	41
2.22 TG analysis of GF in air. . . . .	42
2.23 SEM images of the Ni foam structure. . . . .	43
2.24 The measured and predicted average burn rates as a function of the fuel thickness. $\beta = 10.7$ , $\alpha_0 = 5900$ . . . . .	48
2.25 Effect of R (fuel to graphite thickness) on the amplitude and period of the combustion waves. $\beta = 10.7$ , $\alpha_0 = 5900$ . . . . .	50
2.26 Effect of $\beta$ on the amplitude and period of the combustion waves. R = 3.5, $\alpha_0 = 5900$ . . . . .	51
2.27 Effect of $\alpha_0$ on the amplitude and period of the combustion waves. R = 3.5, $\beta = 10.7$ . . . . .	52
2.28 Structure of the combustion front: non-dimensional reaction temperature (black), reaction rate (blue) and extent of the reaction (red line). The particular NC-GS system shown corresponds to the fuel thickness of 70 $\mu\text{m}$ (R = 3.5). . . . .	54
2.29 Predicted burn rate profile for R = 3.5, $\beta = 10.7$ and $\alpha = 5900$ . . . . .	54
2.30 Unit cell of a PETN crystal. . . . .	58
2.31 Pure PETN simulation domain. . . . .	59
2.32 PETN-MWCNT simulation domain. The particular case shown corresponds to the PETN-MWCNT loading of 65%. . . . .	60
2.33 Reaction wave propagation in a pure PETN sample. The reaction fronts are marked with red lines. . . . .	63
2.34 Spatial temperature profiles along the x-direction at different times during the PETN combustion. . . . .	64

Figure	Page
2.35 Pure PETN. Location of a) different temperatures and b) peak NO <sub>2</sub> concentration as a function of time. . . . .	64
2.36 Pure PETN burn rate comparison check. . . . .	65
2.37 Pure PETN. Species distribution as a function of time during the pure PETN decomposition for a slab located at X = 4 nm. . . . .	66
2.38 Reaction wave propagation in a PETN-MWCNT system (case 3: 65% PETN-MWCNT loading). The reaction fronts are marked with black lines. . . . .	67
2.39 Comparing spatial temperature profiles of PETN-MWCNT (case 4: 50% PETN-MWCNT loading) and pure PETN. . . . .	68
2.40 Coupled PETN-MWCNT system (case 4: 50% PETN-MWCNT loading). Location of a) different temperatures and b) peak NO <sub>2</sub> concentration as a function of time. . . . .	69
2.41 Coupled PETN-MWCNT system (case 4: 50% PETN-MWCNT loading). Species distribution as a function of time during the pure PETN decomposition for a slab located at X = 4 nm. . . . .	70
2.42 Average burn rates as a function of the PETN-MWCNT loading (%). . . . .	71
2.43 The Effect of ignition temperature on the average burn rates for a) pure PETN and b) PETN-MWCNT (case 4: 50% PETN-MWCNT loading). . . . .	72
2.44 a) The slabs in the y and z directions; b) Temperature profile in the y-direction (case 3: 65% PETN-MWCNT loading). . . . .	75
2.45 Normalized density profile of the PETN molecules around the MWCNTs surface (case 3: 65% PETN-MWCNT loading). . . . .	77
3.1 The MnO <sub>2</sub> coated GF sheet cut in the required dimension of 2.5 cm x 0.6 cm.	79
3.2 SEM images of the GF surface after MnO <sub>2</sub> coating; a) 0%, b) 13%, c) 23%, d) 34% and e) 43% MnO <sub>2</sub> in the GF-MnO <sub>2</sub> system. . . . .	80
3.3 Amount of MnO <sub>2</sub> added as a function of the KMnO <sub>4</sub> solution concentration.	81
3.4 SEM - zoomed out (a and b) and zoomed in (c and d) images of the GF-MnO <sub>2</sub> surface after NC deposition for 75% and 55% NC-GF loadings. . . . .	83
3.5 Effect of heating rate (H) on the extent of reaction ( $\alpha_m$ ) at the point of maximum heat flow. The particular case shown corresponds to 10% MnO <sub>2</sub> -NC and 75% NC-GF loading. . . . .	85
3.6 Plot of $\ln(H/T_m^2)$ vs. $-1/(RT_m)$ . The particular case shown corresponds to 10% MnO <sub>2</sub> -NC and 75% NC-GF loading. . . . .	86

Figure	Page
3.7 DSC curves of pure NC for various heating rates. . . . .	86
3.8 Average burn rates as a function of the MnO <sub>2</sub> -NC and NC-GF loadings. . . . .	88
3.9 Activation energy and PTD temperature as a function of the MnO <sub>2</sub> -NC and NC-GF loadings (%). . . . .	90
3.10 SEM images of the GF-MnO <sub>2</sub> surface after combustion for 75% NC-GF loading. . . . .	92
4.1 Gas production as a function of the polarity and frequency of the voltage pulses. Left: alternating sign, middle: negative sign and right: positive sign voltage pulses [177]. . . . .	95
4.2 (Step 1) Si <sub>x</sub> N <sub>y</sub> deposition using the LPCVD technique. . . . .	101
4.3 (Step 2) Pt/Ti layer deposition using the Lift-off technique. . . . .	102
4.4 Top view of the serpentine shaped Pt thermal sensor. Length and width of one rectangular unit: 100 μm × 6 μm. . . . .	102
4.5 (Step 3) Si <sub>x</sub> N <sub>y</sub> deposition using the PECVD technique. . . . .	103
4.6 (Step 4) Au/Ti layer deposition using the Lift-off technique. . . . .	104
4.7 (Step 5) Si <sub>x</sub> N <sub>y</sub> deposition using the PECVD technique. . . . .	104
4.8 The side and top view of a single pair of gold micro-electrodes. . . . .	105
4.9 Zoomed out, top view of a single pair of gold micro-electrodes. . . . .	106
4.10 Side view of the device at a location across the probing pads for the Pt thermal sensors. . . . .	106
4.11 Gold micro-heater for calibration purposes. . . . .	107
4.12 Packaging of the micro-chip. . . . .	107
4.13 Schematic of the experimental setup. . . . .	109
4.14 Current response curves for 1 kHz, 10 kHz and 100 kHz. The particular case shown corresponds to using 20 × 20 μm <sup>2</sup> electrodes. The voltage and duty cycle were kept fixed at 7 V and 0.5, respectively. . . . .	110
4.15 Current response curves for two different electrode surface areas. Left: 20 × 20 μm <sup>2</sup> and right: 80 × 80 μm <sup>2</sup> . The voltage, duty cycle and frequency of the applied alternating pulses were kept fixed at 7 V, 0.5 and 50 kHz, respectively. . . . .	112

Figure	Page
4.16 Effect of frequency on the temperature of the Pt thermal sensor. The particular case shown corresponds to using $20 \times 20 \mu\text{m}^2$ electrodes. The voltage and duty cycle of applied alternating pulses were kept fixed at 7 V and 0.5, respectively. . . . .	113
4.17 Effect of frequency on the average surface heat produced. The particular case shown corresponds to using $20 \times 20 \mu\text{m}^2$ electrodes. The voltage and duty cycle of the applied alternating pulses were kept fixed at 7 V and 0.5, respectively. . . . .	113
4.18 Effect of duty cycle on the temperature of the Pt thermal sensor layer. The particular case shown corresponds to using $20 \times 20 \mu\text{m}^2$ electrodes. The voltage, duty cycle and frequency of the applied alternating pulses were kept fixed at 7 V, 0.5 and 500 kHz, respectively. . . . .	115
4.19 SPC/E water model. . . . .	117
4.20 Initial setup of the simulation domain for pure water surface tension calculations. . . . .	120
4.21 Saturated vapor-liquid density profile. . . . .	120
4.22 Bubble growth and stability after the creation of the cavity: a) $t = 200$ ps, b) $t = 1$ ns and c) $t = 2$ ns. The particular case shown corresponds to $S = 200$ and the blue molecules represent $\text{O}_2$ . . . . .	121
4.23 Relative surface tension of water, $\gamma(S)/\gamma(S = 1, \text{ saturated water})$ , as a function of the supersaturation ratio. . . . .	123
4.24 Bubble pressure as a function of the bubble diameter for different supersaturation ratios. . . . .	123
4.25 Snapshot of the simulation box. H/O radicals were added only in the green shaded area. . . . .	127
4.26 Species mole fraction as a function of time for 3% initial H radical concentration. The initial system pressure was set to 30 atm with the box size fixed at 50 nm. Mole fraction is defined as the number of moles of a species per total number of initial moles of $\text{H}_2$ and $\text{O}_2$ . . . . .	129
4.27 Relative concentration of $\text{H}_2\text{O}_2$ to $\text{H}_2\text{O}$ as a function of time for 3% initial H radical concentration. The initial system pressure was set to 30 atm with the box size fixed at 50 nm. . . . .	132
4.28 Effect of initial H radical concentration on the reactivity of the $\text{H}_2/\text{O}_2$ system. The initial system pressure was set to 30 atm with the box size fixed at 50 nm. . . . .	133

Figure	Page
4.29 Relative concentration of $\text{H}_2\text{O}_2$ to $\text{H}_2\text{O}$ as a function of time for various H radical concentrations. The initial system pressure was set to 30 atm with the box size fixed at 50 nm. . . . .	134
4.30 Effect of initial system pressure on the reactivity of the $\text{H}_2/\text{O}_2$ system. The initial H radical concentration was kept fixed at 3%. . . . .	135
4.31 Relative concentration of $\text{H}_2\text{O}_2$ to $\text{H}_2\text{O}$ as a function of time for various initial system pressure. The initial H radical concentration was kept fixed at 3%. . . . .	136
4.32 Species reactivity for H radical addition vs. O radical addition. The initial system pressure was set to 30 atm with the box size fixed at 50 nm. . . . .	137
4.33 Relative concentration of $\text{H}_2\text{O}_2$ to $\text{H}_2\text{O}$ produced for H radical addition vs. O radical addition. The initial system pressure was set to 30 atm with the box size fixed at 50 nm. . . . .	138
4.34 Core system temperature as a function of time for various H radical concentrations and box sizes. . . . .	139
4.35 Mole fraction of $\text{H}_2$ , $\text{O}_2$ , $\text{H}_2\text{O}_2$ and $\text{H}_2\text{O}$ as a function of time. The initial system pressure was set to 30 atm with the box size fixed at 50 nm. . . . .	141
4.36 Core system temperature as a function of time. The initial system pressure was set to 30 atm with the box size fixed at 50 nm. . . . .	142
4.37 Mole fraction of $\text{HO}_2$ , H, O and OH as a function of time. The initial system pressure was set to 30 atm with the box size fixed at 50 nm. . . . .	143

## ABSTRACT

Jain, Shourya PhD, Purdue University, December 2018. Burning Behaviors of Solid Propellants using Graphene-based Micro-structures: Experiments and Simulations. Major Professor: Dr. Li Qiao.

Enhancing the burn rates of solid propellants and energetics is a crucial step towards improving the performance of several solid propellant based micro-propulsion systems. In addition to increasing thrust, high burn rates also help simplify the propellant grain geometry and increase the volumetric loading of the rocket motor, which in turn reduces the overall size and weight. ***Thus, in this work, burn rate enhancement of solid propellants when coupled to highly conductive graphene-based micro-structures was studied using both experiments and molecular dynamic (MD) simulations.***

The experiments were performed using three different types of graphene-structures i.e. graphite sheet (GS), graphene nano-pellets (GNPs) and graphene foam (GF), with nitrocellulose (NC) as the solid propellant.

For the NC-GS samples, propellant layers ranging from 25  $\mu\text{m}$  to 170  $\mu\text{m}$  were deposited on the top of a 20  $\mu\text{m}$  thick graphite sheet. Self-propagating combustion waves were observed, with burn rate enhancements up to 3.3 times the bulk NC burn rate (0.7 cm/s). The burn rates were measured as a function of the ratio of fuel to graphite layer thickness and an optimum thickness ratio was found corresponding to the maximum enhancement. Moreover, the ratio of fuel to graphite layer thickness was also found to affect the period and amplitude of the combustion wave oscillations. Thus, to identify the important non-dimensional parameters that govern the burn rate enhancement and the oscillatory nature of the combustion waves, a numerical model using 1-D energy conservation equations along with simple first-order Arrhenius kinetics was also developed.

For the GNP-doped NC films, propellant layers,  $500 \pm 30 \mu\text{m}$  thick, were deposited on the top of a thermally insulating glass slide with the doping concentrations of GNPs being varied from 1-5% by mass. An optimum doping concentration of 3% was obtained for which the burn rate enhancement was 2.7 times. In addition, the effective thermal conductivities of GNP-doped NC films were also measured experimentally using a steady state, controlled, heat flux method and a linear increase in the thermal conductivity value as a function of the doping concentration was obtained.

The third type of graphene structure used was the GF - synthesized using a chemical vapor deposition (CVD) technique. The effects of both the fuel loading ratio and GF density were studied. Similar to the GNPs, there existed an optimum fuel loading ratio that maximized the burn rates. However, as a function of the GF density, a monotonic decreasing trend in the burn rate was obtained. Overall, burn rate enhancement up to 7.6 times was observed, which was attributed to the GF's unique thermal properties resulting from its 3D interconnected network, high thermal conductivity, low thermal boundary resistance and low thermal mass. Moreover, the thermal conductivity of GF strut walls as a function of the GF density was also measured experimentally.

Then as a next step, the GF structures were functionalized with a transition metal oxide ( $\text{MnO}_2$ ). The use of GF-supported catalyst combined the physical effect of enhanced thermal transport due to the GF structure with the chemical effect of increased chemical reactivity (decomposition) due to the  $\text{MnO}_2$  catalyst, and thus, resulted in even further burn rate enhancements (up to 9 times). The burn rates as a function of both the NC-GF and  $\text{MnO}_2$ -NC loadings were studied. An optimum  $\text{MnO}_2$ -NC loading corresponding to the maximum burn rate was obtained for each NC-GF loading. In addition, thermogravimetric (TG) and differential scanning calorimetry (DSC) analysis were also conducted to determine the effect of NC-GF and  $\text{MnO}_2$ -NC loadings on the activation energy (E) and peak thermal decomposition (PTD) temperatures of the propellant NC.

In addition to the experimental work, molecular dynamics simulations were also conducted to investigate the thermal transport and the reactivity of these coupled solid-propellant/graphene-structures. A solid monopropellant, Pentaerythritol Tetranitrate (PETN), when coupled to highly conductive multi-walled carbon nanotubes (MWCNTs) was considered. The thickness of the PETN layer and the diameter of the MWCNTs were varied to determine the effect of PETN-MWCNT loading on the burn rates obtained. Burn rate enhancement up to 3 times was observed and an optimal PETN-MWCNT loading of 45% was obtained. The enhancement was attributed to the faster heat conduction in CNTs and to the layering of PETN molecules around the MWCNTs surface. Moreover, the CNTs remained unburned after the combustion process, confirming that these graphene-structures do not take part in the chemical reactions but act only as thermal conduits, transferring heat from the burned to the unburned portions of the fuel.

A long-pursued goal, which is also a grand challenge, in nanoscience and nanotechnology is to create nanoscale devices, machines and motors that can do useful work. However, loyal to the scaling law, combustion would be impossible at nanoscale because the heat loss would profoundly dominate the chemical reactions. *Thus, in addition to the solid propellant work, a preliminary study was also conducted to understand as how does the heat transfer and combustion couple together at nano-scales.*

First, an experimental study was performed to understand the feasibility of combustion at nano-scales for which a nano-scale combustion device called “nanobubbles” was designed. These nanobubbles were produced from short-time ( $< 2000 \mu\text{s}$ ) water electrolysis by applying high-frequency alternating sign square voltage pulses (1-500 kHz), which resulted in  $\text{H}_2$  and  $\text{O}_2$  gas production above the same electrode. Moreover, a 10 nm thick Pt thermal sensor (based on resistance thermometry) was also fabricated underneath the combustion electrodes to measure the temperature changes obtained. A significant amount of bubble production was seen up to 30 kHz but after

that the bubble production decreased drastically, although the amount of faradaic current measured remained unchanged, signifying combustion. The temperature changes measured were also found to increase above this threshold frequency of 30 kHz.

Next, non-reactive molecular dynamic simulations were performed to determine how does the surface tension of water surrounding the electrodes is affected by the presence of dissolved external gases, which would in turn help to predict the pressures inside nanobubbles. Knowing the bubble pressure is a prerequisite towards understanding the combustion process. The surface tension of water was found to decrease with an increase in the supersaturation ratio (or an increase in the external gas concentration), thus, the internal pressure inside a nanobubble is much smaller than what would have been predicted using the planar-interface surface tension value of water. Once the pressure behavior as a function of external gas supersaturation was understood, then as a next step, reactive molecular dynamic simulations were performed to study the effects of surface-assisted dissociation of  $\text{H}_2$  and  $\text{O}_2$  gases and initial system pressure on the ignition and reaction kinetics of the  $\text{H}_2/\text{O}_2$  system at nano-scales. A significant amount of hydrogen peroxide ( $\text{H}_2\text{O}_2$ ), 6-140 times water ( $\text{H}_2\text{O}$ ), was observed in the combustion products. This was attributed to the low temperature ( $\sim 300$  K) and high pressure (2-80 atm) conditions at which the chemical reactions were taking place. Moreover, the rate at which heat was being lost from the combustion chamber (nanobubble) was also compared to the rate at which heat was being released from the chemical reactions and only a slight rise in the reaction temperature was observed ( $\sim 68$  K), signifying that, at such small-scales, heat losses dominate.

## 1. INTRODUCTION

The control and enhancement of combustion wave propagation velocities is very important for the development of low cost and efficient solid propellant based micro-propulsion systems. Micro-propulsion systems are designed to provide small amounts of thrust ranging from micro-newtons to a few milli-newtons that are then used for precise attitude and orbit corrections, drag compensations, and small impulse maneuvers [1]. A variety of micro-propulsion systems have been proposed: solid propellant thrusters [1–4], cold gas thrusters [5, 6], bi/mono-propellant thrusters [7, 8], colloid thrusters [9], plasma thrusters [10–13], laser plasma thrusters [14] and field-emission electric propulsion thrusters [15–17]. Of all the micro-thrusters proposed, the solid propellant based thruster provides the most advantages with the least complications i.e. less possibility of fuel leakage, better system miniaturization due to absence of valves, fuel lines or pumps, no moving parts, and high total impulse. The traditional solid propellant micro-thruster concept is based on burning a propellant stored in the micro-combustion chamber. The combustion products are then accelerated in the nozzle giving the required thrust. Thus, enhancing the burn rate of a solid propellant is a crucial step towards improving the performances of these systems. In addition to increasing thrust, high burn rates also help simplify the propellant grain geometry and increase the volumetric loading of the rocket motor, which in turn reduces the overall size and weight.

In addition, solid propellants have also been used, very effectively, in thermal-to-electrical energy conversion devices [18–22]. The propellant is used to produce a propagating exothermic combustion wave that results in a spatially and temporally varying thermal gradient, which then results in the voltage generation across the thermo-electric material. The thermo-electric (TE) systems exploit the unique elec-

trical, semiconducting, and thermal properties of the TE materials in order to both achieve and facilitate the processes of converting thermal to electrical energy. In general, whenever a propellant (solid or liquid) is ignited, the energy released is isotropic in nature. Confinement or contact with a thermally conductive surface is required to make the resulting combustion wave anisotropic. In most of the traditional solid propellant micro-thrusters, confinement is used for the anisotropic combustion release. Choi et al. [18] proposed anisotropic burn rate enhancements in a TNA (Trinitramine) solid monopropellant by coupling the exothermic reactions to a thermally conductive base such as MWCNTs (multi-walled carbon nanotubes). Burn rate enhancements up to 500 times (at ambient conditions) were obtained. Moreover, the amount of enhancement obtained was found to be dependent on the direction in which the reaction waves were propagated. For example, the burn rate enhancement obtained for the reaction waves propagated in the direction parallel to MWCNTs, was found to be 10 times more than the burn rate enhancement obtained for the reaction waves propagated in the direction perpendicular to MWCNTs. In addition, Choi et al. also explored the TE properties of MWCNTs by connecting the two ends of the nanotubes to an oscilloscope and observed thermopower waves of single polarities being generated. Very high specific powers, up to 7 kW/Kg, were obtained, much higher than that of the conventional Li-ion batteries (1 KW/Kg). In general, a propagating combustion wave (thermal gradient) across the TE material can produce voltage pulses of varying polarities (positive, negative or both). For a single polarity voltage pulse to be generated, the reaction wave should propagate faster than the cooling time of the regions behind the reaction zone. Thus, high burn rates are necessary for the TE systems to be effective. The thrust produced from these devices were also measured and specific impulses up to  $5.5 \text{ s } \mu\text{kg}^{-1}$  were obtained, 10 times more than that of typical solid propellant micro-thrusters. Other studies on the guided thermopower wave systems have also been performed in which, instead of MWCNTs, a combination of a thermally conductive oxide (alumina) and TE materials ( $\text{Bi}_2\text{-Te}_3$ ,  $\text{Sb}_2\text{-Te}_3$  and  $\text{ZnO}$ ) was used as the substrate with the nitrocellulose as the solid propellant [19–22].

Thus, the main objective of this study was to enhance the burn rates of traditional solid propellants. Next, various studies that have been performed towards enhancing the burn rates of solid propellants have been summarized:

- ***Burn rate enhancement using metal/metal-oxide:*** The most common method for enhancing burn rates of solid propellants is the addition of oxides of transition metals such as Ag, Cu, Fe, Cd, Mn, Cr, Zn, and Li (TMO), which enhances the burn rate by assisting in the thermal decomposition of the propellant [23–29]. For example, with the addition of  $\text{Mn}_2\text{O}_3$ , CuO,  $\text{Fe}_2\text{O}_3$  and  $\text{Cr}_2\text{O}$  nanocrystalline catalysts (1% wt.), the peak thermal decomposition temperature of AP (ammonium perchlorate) was observed to be lowered by 150 °C, 125 °C, 100 °C and 75 °C, respectively [27]. In another study performed by Fong and Smith [28], 2% (by wt.) of a metallic oxide was used to enhance the burn rates of PETN (Pentaerythritol Tetranitrate) and RDX (Cyclotrimethylenetrinitramine). For both the propellants, enhancements up to 2 times were observed. Chakravarthy et al. [29] studied the effect of the addition of  $\text{Fe}_2\text{O}_3$  (1% wt.) on the burn rate enhancement of AP/HTPB (Hydroxyl-terminated polybutadiene) composite propellant and found enhancements up to 1.75 times.

The micro-structure of a solid propellant can also play a significant role towards the burn rate enhancement. For example, the burn rate of 87.4% AP/HTPB system at 68 atm was found to be increased from 0.7 cm/s to 5 cm/s as the AP particle size was decreased from 1000  $\mu\text{m}$  to 10  $\mu\text{m}$  [30]. Shalom et al. [31] also studied the particle size effect and found the burn rate of the composite propellant (Al/AP/HTPB) system containing 18% wt. of Al to be enhanced by 84% as 9% of the coarse aluminum powder was replaced by the nano-aluminum powder.

- ***Burn rate enhancement using graphene-based micro-structures:*** Choi et al. [18] was the first to study the burn rate enhancement of a solid monopropellant (TNA) when coupled to a graphene-based micro-structure (MWCNTs) and enhancements up to 500 times were obtained. Zhang et al. [32] studied the effect of the addition of graphene oxides (GO) on the burn rates of nitrocellulose (NC) and enhancements up to 7 times were observed. The huge amount of burn rate enhancement observed in these studies was attributed to the unique thermo-physical properties of these graphene-structures.

Graphene-based materials, such as graphene nano-pellets (GNPs) [33], carbon nanotubes (CNTs) [34], and graphene foam (GF) [35] because of their high thermal (100-4600 W/mK) [36–41] and electrical conductivity [35, 42, 43], mechanical strength, optical properties, and large surface-to-volume ratio, have been used as nano-fillers to enhance the thermal conductivity of various composites [44–65], as thermal interface materials [66–75] and as heat exchangers in nano-electronic devices [76, 77]. They also have applications in polymer fabrication, biomedicine, organic synthesis, catalysis and sensors [78–85]. In the following, the various thermal conductivity and thermal boundary resistance studies that have been performed will be discussed:

***Thermal conductivity enhancement using GNPs:*** Yu et al. [44] showed that the thermal conductivity of pure epoxy could be increased by 3000% by using GNPs at 25% volumetric loading. They also conducted experiments with SWCNTs but found the amount of enhancement obtained to be 2.5 times less as compared to that obtained using the GNPs (at 10% volumetric loading). Goyal [45] showed that the thermal conductivity of pure epoxy could be increased by 500% using hybrid graphene-metal particles at 5% volumetric loading. Similar amount of enhancements were also reported by Shahil [46], where they found the thermal conductivity of epoxy to be increased by 2300% using mixed monolayer and multilayer graphene at 10% volumetric loading.

***Thermal conductivity enhancement using CNTs:*** Biercuk [47] found the thermal conductivity of epoxy to be increased by 125% using SWCNTs at 1% volumetric loading. However, Huang et al. [48] conducted experiments with vertically aligned multi-walled carbon nanotubes (MWCNTs) and found the thermal conductivity of the polymer/MWCNT complex to be increased by 280% at 0.3% weight fraction. Thus, the amount of enhancement that is obtained depends on whether the carbon nanotubes (CNTs) are vertically aligned (280%) or randomly orientated (125%). Kwon et al. [49] studied the thermal conductivity of MWCNT/polymer composites as a function of the MWCNT volume fraction and found enhancements up to 390% for a MWCNT volume fraction of 1.4%. MWCNTs with very high aspect ratios were used ( $> 2500$ ). Bonnet et al. [50] studied the thermal conductivity enhancement of polymethylmetacrylate using SWCNTs but found enhancements only up to 55% for a 7% SWCNT volume fraction. This was because of the randomly orientated CNTs used in their study, which decreased the net thermal conductivity enhancement of the sample and also due to the low aspect ratio of the CNTs used. Liao et al. [51] and Lee et al. [52] performed molecular dynamic simulations to predict the thermal conductivity enhancements using CNTs. Liao et al. [51] investigated the thermal conductivity of aligned carbon nanotube-polyethylene composites (ACPCs) and found enhancements up to 3 times. They attributed such a considerable enhancement to the alignment of CNTs and polymer, and to the high thermal conductivity of CNTs. Lee et al. [52] investigated the effect of SWCNTs on the thermal conductivity of water, and found enhancements up to 370% for a 7% volume fraction. However, an opposite trend was observed by Moisala et al. [53], in which the thermal conductivity of the epoxy/CNT composite was found to decrease by 5% with the addition of SWCNTs at 0.5% weight fraction.

***Thermal conductivity enhancement using GF:*** Of all the graphene-structures, GF was found to provide the maximum thermal conductivity enhancements. Zhao et

al. [54] showed that the thermal conductivity of PDMS (polydimethylsiloxane) could be increased 3-fold by using GF (at 0.7% wt.). Liu et al. [55] and Chen et al. [56] showed that the thermal diffusivity of epoxy could be increased 10 and 46 times by using GF at 5% and 9% by weight, respectively. Moreover, a comprehensive study was conducted by Ji et al. [57], in which the thermal conductivity enhancement of wax obtained using GF, GNPs and CNTs was compared. The thermal conductivity of the composite was found to be increased by 18 (1% vol.), 11 (4% vol.) and 6 (10% vol.) times using GF, GNPs and CNTs, respectively.

***Thermal boundary resistance of graphene-structures:*** A major limitation of using carbon nanotubes is the high thermal boundary resistance (TBR) issue observed at their interface [86–91]. The TBR values for the CNTs have been reported to be between 0.07-0.8 cm<sup>2</sup>K/W [66, 69–71, 91]. However, for the GF, a TBR value of only 0.04 cm<sup>2</sup>K/W was reported by Zhang et al. [72]. The thermal boundary resistance is greatly reduced in GF because of its three-dimensional highly ordered network of covalently bonded ultra-thin graphite structures [63, 72, 92]. Park et al. [73] reported a TBR value of 0.043 cm<sup>2</sup>K/W for the GNPs, whereas Raza et al. [74] and Shen et al. [75] reported TBR values of around 0.1 cm<sup>2</sup>K/W and 0.3 cm<sup>2</sup>K/W, respectively. Thus, the TBR values for the GNPs could be expected to lie somewhere between that of CNTs and GF. The high thermal boundary resistance observed in CNTs could be attributed either to the mismatch between the phonon density of states (DOS) between the 1-D CNTs and the 3D bulk material [92–94] or to the lack of thermal percolation in the CNT composites [87, 91]. In CNTs, the heat is conducted either ballistically or quasi-ballistically (depending on the mean free path of the phonons, boundary defects and length of the CNTs), whereas in a polymer (or any 3D bulk material) the heat is always conducted diffusively [95, 96]. Thus, it is the mismatch of the two thermal transport modes between the two materials that leads to a high thermal boundary resistance [95, 97]. Nevertheless, the addition of CNTs to a bulk material can still lead to significant thermal conductivity enhancements. Zahedi et

al. [98] studied the structural properties of a polymer matrix around the CNTs and observed enhanced polymer ordering in the interfacial region. This organized layering of the polymer molecules around the CNTs was found to increase the thermal transport among the polymer molecules in the direction along the CNTs, resulting in a net thermal conductivity enhancement of the composite.

• ***Burn rate enhancement using functionalized graphene-structures:*** A

few studies have also been conducted to explore the combined effect of metal/metal oxides and graphene-structures on the burn rates and thermal decomposition characteristics of propellants. Sabourin et al. [99] used functionalized graphene sheets to enhance the flame speed of a liquid monopropellant, nitromethane. These graphene sheets were functionalized with epoxides and hydroxides on the surfaces and hydroxides and carboxylates on the edges. Flame speed enhancement up to 3 times the bulk value was achieved by adding only 0.5% wt. of functionalized graphene. Motivated by the experimental findings of Sabourin et al. [99], Liu et al. [100] performed molecular dynamic simulations to better understand the thermal decomposition mechanism of nitromethane in the presence of functionalized graphene sheets. The graphene sheets, in addition to enhancing the thermal transport, were also found to promote the decomposition of nitromethane and its derivatives through a modified reaction pathway because of the presence of oxygen-containing functional groups. Li et al. [101, 102] studied the catalytic performance of Ni-graphene and  $\text{Mn}_3\text{O}_4$ -graphene nanocomposites and found the peak thermal decomposition (PTD) temperature of AP to be lowered by 97.3 °C (1% wt.) and 142 °C (5% wt.), respectively. Zhang et al. [103] prepared Ni doped CNTs (13.82% wt. Ni) and found the PTD temperature of AP/HTPB to be lowered by 100 °C (1% wt.). Furthermore, burn rate enhancements up to 1.5 times were obtained for pressures ranging from 5-11 MPa with using only 1% Ni-CNTs. In a similar study performed by Liu et al. [104], the effect of Cu-CNTs was studied. Burn rate enhancements up to 1.2 times were obtained with the PTD temperature of AP/HTPB being lowered by almost 50 °C. Rengpeng et al. [105] studied

the effect of the catalyst  $\text{Fe}_2\text{O}_3$ -CNTs (25.8%  $\text{Fe}_2\text{O}_3$ ) on the activation energy of AP and found it to be reduced from 310.3 to 81.4 kJ/mol with using only 10% wt. of the catalyst. Similar research has also been carried out with other type of propellants. Hong et al. [106,107] and Tan et al. [108] showed that the burn rate of a DBP - double base propellant (nitrocellulose + nitroglycerin) could be enhanced up to 2, 1.5, 4 and 2.5 times by using CuO-CNTs,  $\text{Bi}_2\text{O}_3$ -CNTs (2.5% wt.), PbO-GO and  $\text{Bi}_2\text{O}_3$ -GO (2.5% wt.) additives, respectively. Another study using the DBP (nitrocellulose + nitroglycerin) was performed by Zhao et al. [109], in which the activation energy was found to be lowered by 7.3% and 30.4% using CuO-CNTs (CuO 53.3% wt.) and  $\text{Bi}_2\text{O}_3$ -CNTs, respectively, at 16.67% wt. Ren et al. [110] studied the catalytic effect of PbO-CuO/CNTs (5% wt.) on the RDX thermal decomposition and found the PTD temperature and activation energy to be lowered by 14 °C and 29.5%, respectively. However, in a study conducted by An et al. [111], the PTD temperature of RDX was lowered by only 9 °C when using 33% wt. of Ag-CNTs (92% wt. Ag). Thus, the amount of catalytic effect obtained is a strong function of the type of propellant and catalyst used, and of the distribution of the catalyst in the propellant system.

As can be inferred from the above studies, burn rates of solid propellants can be enhanced in two ways:

- 1) **Chemically**, using metal/metal-oxide catalyst that increases the chemical reactivity of a propellant by lowering its activation energy and thermal decomposition temperatures.
- 2) **Physically**, using highly conductive graphene-structures that increases the thermal transport in a propellant. Since, the burn rate of a solid propellant depends on the rate at which the heat is being transferred from the burned to the unburned portions of the fuel, it can be enhanced by using highly conductive graphene-structures. Most of the solid propellants have a thermal conductivity

in the range of 0.1-1 W/m-K [112], which is much lower than that of these graphene-based materials (100-4600 W/m-K).

In this study, the ability of these graphene-based structures (GS, GNPs, GF and MWCNTs) towards enhancing the burn rates of solid propellants was investigated in detail because of the huge potential that they show, as was demonstrated by the various studies performed in the literature. The goal was to understand the coupling between the chemical reactions and the thermal transport (both within the propellant and between the propellant and the graphene-structure), and how that affects the burn rates and the combustion wave propagation behavior.

First, the burn rate enhancement of a solid monopropellant, nitrocellulose (NC), when coupled to a highly conductive graphite sheet was studied. The graphite sheet was chosen as the thermally conductive base for the propellant because of its high thermal conductivity and good thermal properties at high temperatures [113]. Another reason for using the graphite sheets was that they are readily available and have much lower manufacturing costs as compared to the other types of graphene materials (GNPs, GF and CNTs). In order to facilitate the coupling of the propellant with the graphene-structures, the propellant was required to be easily dissolvable in an organic solvent such as acetone and then later be recovered by evaporating the solvent at ambient conditions. Moreover, a solid propellant with a high enthalpy of combustion was needed to ensure the sustenance of a reaction front at room temperature and pressure. Hence, nitrocellulose ( $C_6H_8(NO_2)_2O_5$ ), with a nitration level of 10.9-11.2%, was selected as the solid propellant because of its ease of combustion at atmospheric conditions and wide use as an energetic polymeric binder in solid rocket motors. In addition, the nitration level of nitrocellulose is such that it exhibits deflagration and not detonation during combustion. For the experimental work, propellant layers ranging from 25  $\mu\text{m}$  to 170  $\mu\text{m}$  were deposited on the top of a 20  $\mu\text{m}$  thick graphite sheet. The burn rates were measured as a function of the ratio of fuel to graphite layer thickness and an optimum thickness ratio was found corresponding to

the maximum enhancement. Additionally, a numerical model, using one-dimensional (1-D) energy conservation equations along with simple one-step chemistry, was also developed to identify the important non-dimensional parameters that govern the burn rate enhancement and the oscillatory nature of the combustion waves. The burn rates and the period and amplitude of the combustion waves were found to be dependent on three non-dimensional parameters: ratio of graphite to fuel thermal diffusivity ( $\alpha_o$ ), ratio of fuel to graphite thickness (R) and inverse adiabatic temperature rise ( $\beta$ ). Moreover, the predicted burn rates and characteristics of the oscillations agreed well with the experimental data.

Next, another experimental study was conducted but with GNPs and GF as the conductive graphene-structures. GNPs and GF were selected because of their high thermal conductivity and low thermal boundary resistance, as was shown in the studies mentioned earlier. And again, similar to the graphite sheet, nitrocellulose (NC) was used as the solid propellant. For GNP-doped NC films, the amount of GNPs added to the fuel was varied from 1-5% by mass and an optimum doping concentration corresponding to the maximum enhancement was obtained. In contrast to the graphite sheet, the thickness of the GNPs-doped NC films was kept constant at  $500 \pm 30 \mu\text{m}$ . In addition, the effective thermal conductivity of the GNP-doped NC films was also measured experimentally using a steady state, controlled, heat flux method using the Fourier's law of heat conduction. A linear increase in the thermal conductivity value as a function of the doping concentration was obtained. For GF, the effects of both the fuel loading ratio and GF density on the burn rates obtained were studied. For a given GF density, an optimum fuel loading ratio was obtained that maximized the burn rates. However, as a function of the GF density, a monotonic decreasing trend was observed. The thermal conductivity of GF strut walls was also measured, using the method similar to that of the GNPs. In addition, the reusability of GF structures was also tested and similar burn rate enhancements were obtained using the fresh and reused GF structures.

To further enhance the burn rates, then as a next step, the GF structures were coated with a transition metal oxide (TMO), manganese dioxide ( $\text{MnO}_2$ ), layer. This would couple the chemical effect of the TMO (enhanced thermal decomposition) with the physical effect of the graphene-structure (enhanced thermal transport). For this part of the study, GF was selected as the conductive graphene-structure because of its unique thermal properties resulting from the 3-D interconnected network, high thermal conductivity, low thermal boundary resistance and low thermal mass and thus, was expected to provide the maximum burn rate enhancement among all the graphene-structures. Moreover, the use of GF as a functionalized substrate has not been explored yet. For the solid propellant, again NC was used. During the NC decomposition, the main exothermic reaction is the redox reaction between  $\text{NO}_2$  and aldehydes. In literature, various studies have been performed that shows that  $\text{NO}_2$  dissociates to  $\text{NO}$ ,  $\text{N}_2$  and  $\text{O}_2$  in the presence of a metal oxide surface at high temperatures [114–116]. The amount of decomposition obtained was found to be dependent on the type of metal oxide used, temperature of the metal oxide surface and composition of the surrounding gas. Thus, for the catalyst,  $\text{MnO}_2$  was selected as it exhibits high activity (87% conversion) for the decomposition of  $\text{NO}_2$  to  $\text{NO}$  [114]. The burn rates of NC as a function of the  $\text{MnO}_2$ -NC and NC-GF loadings were studied and the micro-structures of GF, GF- $\text{MnO}_2$ , and NC-GF- $\text{MnO}_2$  were characterized. An optimum  $\text{MnO}_2$ -NC loading corresponding to the maximum burn rate was obtained for each NC-GF loading, which shifted to the right as the NC-GF loading was decreased. In addition, TG (Thermogravimetric) and DSC (Differential scanning calorimetry) analysis were also conducted to determine the activation energy (E) and peak thermal decomposition (PTD) temperatures of NC for various values of NC-GF and  $\text{MnO}_2$ -NC loadings. Similar to the burn rate results, for each NC-GF loading tested, an initial decrease in both E and PTD temperatures was obtained as a function of the  $\text{MnO}_2$ -NC loading but above a certain  $\text{MnO}_2$  concentration, a slight rise was observed.

Although, a number of experiments were performed to study the burn rate enhancement process, a complete atomic-level understanding of the mechanism was still missing. Thus, molecular dynamic simulations were conducted next. The main objectives were to understand the thermal transport at the interface and the reactivity of the graphene-structures. For the solid propellant, PETN, ( $C_5H_8N_4O_{12}$ ), was selected because of its high enthalpy of combustion and wide use as a powerful secondary explosive material. Moreover, a number of experiments and simulations studying the burn rates of pure PETN have been performed [117–119], thus providing a base case check for the MD simulations. MWCNTs were chosen as the conductive substrate because of their high axial thermal conductivity and 1-D nature in the reaction wave propagation, which would reduce the computational cost considerably. First, reactive MD simulations were performed to determine the effect of PETN-MWCNT loading on the burn rates obtained. The thickness of the PETN layer and the diameter of the MWCNTs were varied to get the desired PETN-MWCNT loading. In addition to the reactive MD simulations, two additional non-reactive MD simulations were also conducted to better understand the mechanisms contributing to the thermal enhancement of the composite and in turn, the burn rate enhancement.

## 1.1 Research Objectives

- 1) To explore the possibility of enhancing the burn rates of solid propellants using different types of graphene-based micro-structures: *GS, GNPs, GF and MWCNTs*.
- 2) To determine *experimentally*, the *effect of structure* and *loading ratio* of these graphene materials on the burn rate enhancement.
- 3) To perform *reactive and non-reactive MD simulations* to understand the thermal transport at the interface and the reactivity of the graphene-structures.
- 4) To understand the effect of *transition metal oxide doping* of the graphene-structures on the burn rate enhancement, especially the coupled thermal and chemical effects.

## 2. BURN RATE ENHANCEMENT: PURE GRAPHENE-STRUCTURES

This chapter focuses on the experimental and numerical studies that were conducted to investigate the burn rate enhancement of solid propellants when coupled to highly conductive pure graphene-structures.

The first three sections talk about the experimental work performed, in which three different types of graphene materials were considered: graphite sheet (GS), graphene nano-pellets (GNPs) and graphene foam (GF). In the first section, the methods used for preparing these tailored solid propellants are presented along with the techniques used for the characterization of the graphene-structures (with and without the fuel addition). Two different techniques were used: Scanning Electron Microscopy (SEM) imaging and thermal conductivity measurements. In the second section, the experimental setup used is described in detail. A sample screenshot of the reaction wave propagation, with and without the addition of a graphene-structure, is also given to aid in visualization. Finally, in the third section, the results on the burn rate enhancement as a function of the structure and loading ratio of these graphene materials are presented.

Once the usefulness of these graphene-structures towards enhancing the burn rates was demonstrated, as a next step, simple 1-D modeling using energy conservation equations and one-step chemistry was performed to identify the important parameters that govern the burn rate enhancement behavior. Section 2.4 describes the 1-D modeling in detail. The particular system analyzed was the coupled nitrocellulose-graphite sheet system (NC-GS), as it allowed the effect of each parameter to be visualized

separately with the least computational complexity. Although a number of important parameters contributing towards the burn rate enhancement were identified, a complete atomic-level understanding of the mechanism was still missing. Thus, molecular dynamic simulations were conducted next, as described in Section 2.5, to better understand the thermal transport at the interface and the reactivity of the graphene-structures. The particular system analyzed was the coupled PETN-MWCNT system.

*Most of the text and figures presented in this section are reproduced from {S. Jain, O. Yehia, and L. Qiao, Journal of Applied Physics 119, 094904 (2016), S. Jain, W. Park, Y. P. Chen, and L. Qiao, Journal of Applied Physics 120, 174902 (2016), and S. Jain, G. Mo, and L. Qiao, Journal of Applied Physics 121, 054902 (2017)} with permission of AIP Publishing.*

## 2.1 Sample Preparation and Characterization

For all the experiments conducted, Nitrocellulose (NC),  $C_6H_8(NO_2)_2O_5$ , with a nitration level of 10.9–11.2% was used as the solid fuel. The nitrocellulose solution (6% in ethanol/diethyl ether), as purchased from Sigma-Aldrich, was further diluted to a 4% solution using acetone, which was then used for the fuel depositions.

### 2.1.1 Graphite Sheet (GS)

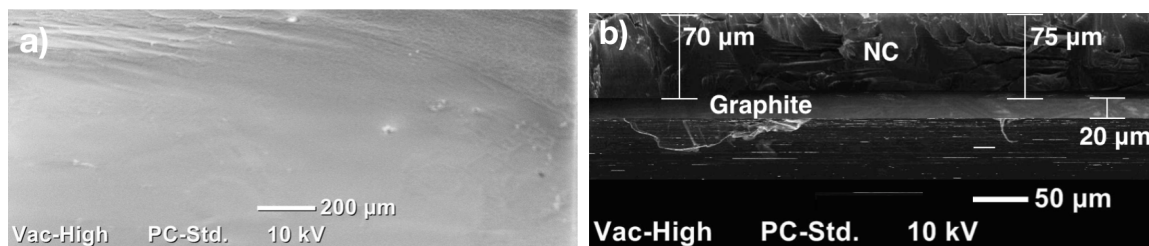


Figure 2.1.: a) Top view and b) side view of the NC-GS sample. The particular case shown corresponds to 4 layers of NC deposition.

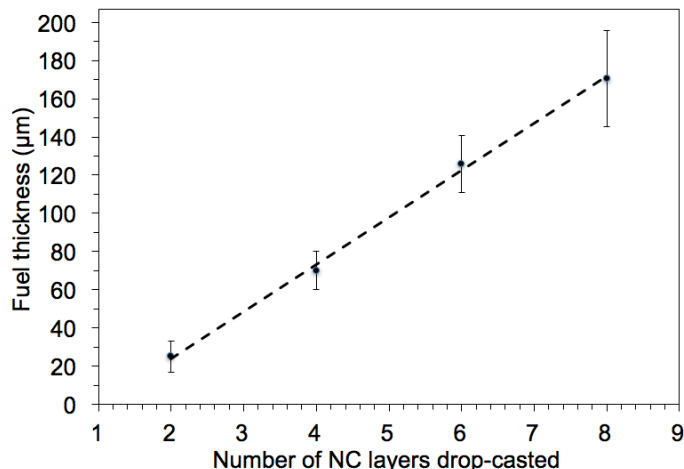


Figure 2.2.: Fuel thickness as a function of the number of NC layers drop-casted onto the graphihte sheet.

A strip of graphite,  $20\ \mu\text{m}$  thick, with a length of 2.5 cm and a width of 0.6 cm was used as the substrate. The thickness of the sheet was decided considering the fuel to graphite layer thickness ratio ( $R$ ), which needed to be varied from 1.25 to 8.5, whereas the length and width of the sheet were chosen as such to make sure that the reaction wave propagation obtained would be 1-D. To prepare the fuel samples, the NC solution was drop-casted onto the graphite sheet in multiple layers (2-8) to get the desired fuel thickness, ranging from  $25\ \mu\text{m}$  to  $170\ \mu\text{m}$ . After the deposition, the fuel samples were left to dry in ambient conditions for 24 hours, which gave enough time for all the solvent to completely evaporate.

SEM imaging was conducted next to examine the deposition thickness variation, uniformity, surface features and the adhesion of the fuel layer to the graphite sheet. Such information is vital to understand the observed combustion behavior of the NC-GS system. Fig. 2.1a shows the top view of the deposited fuel and as can be seen, the fuel surface was quite smooth and continuous, which was consistent with the adhesive nature of the NC coating. However, the thickness and the adhesion of the deposited fuel was found to vary slightly along the length of the sample, as shown in Fig. 2.1b.

Around 15% variation in the deposited fuel thickness was observed. Moreover, for some thicker fuel depositions ( $> 125 \mu\text{m}$ ), tiny air gaps were also detected between the deposited fuel and the graphite sheet, which could increase the thermal contact resistance and as a result, lower the high thermal conductivity effect of the graphite sheet. Fig. 2.2 shows how the average fuel thickness varies as a function of the number of NC layers drop-casted.

### 2.1.2 Graphene Nanopellets (GNPs)

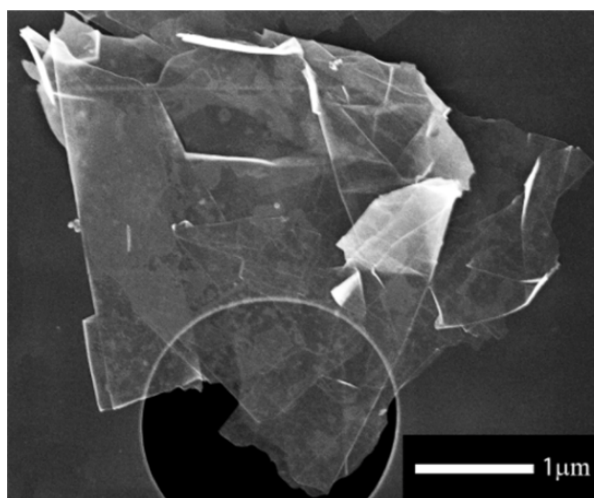


Figure 2.3.: SEM image of a single GNP.

Fig. 2.3 shows the SEM image of a single GNP (obtained from Graphene Laboratories Inc.). The GNPs used were less than 3 nm thick (3–8 graphene monolayers) with their lateral dimensions ranging from 2  $\mu\text{m}$  and 8  $\mu\text{m}$ . First, the GNPs were added to the pure NC solution at various concentrations ranging from 1% to 5% of the NC weight. An ultrasonic disruptor was used to evenly disperse the GNPs in the NC solution and to minimize agglomeration. A series of four-second-long and four-second apart pulses was used for 8 min. The GNP-NC solution was then drop-casted onto a thermally insulating glass slide (2.5 cm long and 0.6 cm wide) and evaporated at ambient conditions (for 24 hrs.), leaving an adhesive coating of the GNP-doped NC film behind. Moreover, for all the cases tested, the thickness of the GNP-doped NC film

was kept constant at  $500 \pm 30 \mu\text{m}$ . This was done to make sure that the deposited fuel layer was thick enough so that the burn rates obtained were not dependent on the thickness of the fuel layer deposited, as was observed in the NC-GS case.

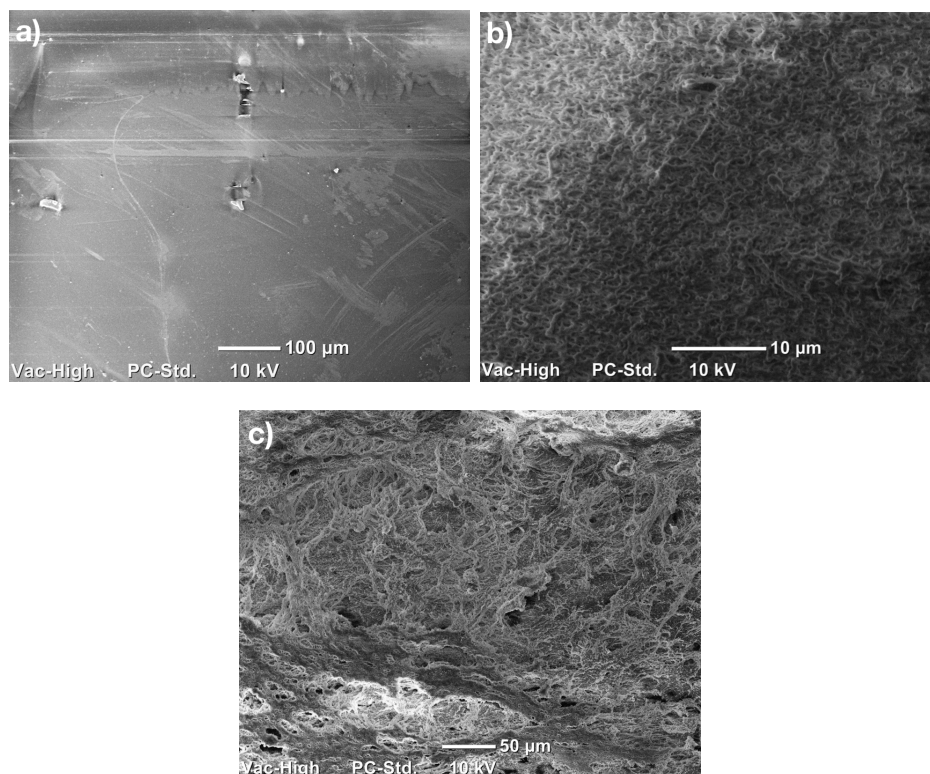


Figure 2.4.: SEM images of GNP-doped NC films; a) 0% wt. (pure NC), b) 3% wt. and c) 5% wt. GNPs.

Fig. 2.4 shows the SEM images of pure and GNP-doped NC films. As can be seen, the surface of the pure NC film was quite smooth and continuous, as expected. However, after adding GNPs, the surface roughness of the fuel samples was found to increase. The amount of surface roughness obtained increased with an increase in the % wt. of the GNPs added. This was consistent with the work performed by Zhang et al. [32], in which a similar trend of increasing surface roughness with increasing graphene oxide (GO) wt. concentration was observed.

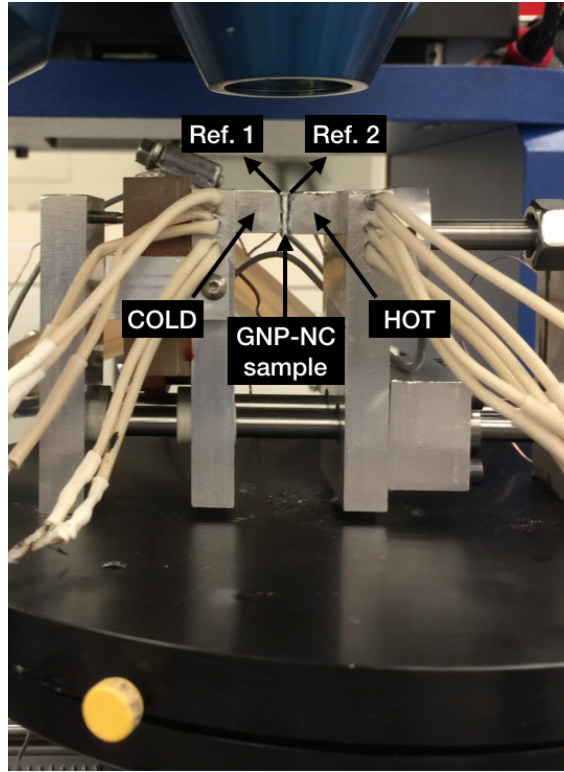


Figure 2.5.: Experimental setup for measuring GNP-NC film thermal conductivity.

Table 2.1.: Thermal conductivity measurements for the GNP-NC sample with 0% wt. GNPs

Case No.	Temp range ( $^{\circ}\text{C}$ )	Voltage (V)	$\Delta T_{ref1}$ ( $^{\circ}\text{C}$ )	$\Delta T_{sample}$ ( $^{\circ}\text{C}$ )	$\Delta T_{ref2}$ ( $^{\circ}\text{C}$ )	$q''$ ( $\text{W}/\text{m}^2$ )	$k_{eff}$ ( $\text{W}/\text{m}\cdot\text{K}$ )
1	20-55	32	7.29	19.42	5.73	$1.95 \times 10^3$	0.10
2	20-47	27	5.38	13.89	3.53	$1.34 \times 10^3$	0.096
3	20-40	22	3.80	11.94	2.56	$0.95 \times 10^3$	0.080

Given the importance of thermal conductivity in the burn rate enhancement concept proposed, the effective thermal conductivity of the GNP-NC samples was characterized next using a steady state, controlled, heat flux method using the Fourier's law of heat conduction. Fig. 2.5 shows the experimental setup used, which is based on the one dimensional heat flow between two parallel reference materials being separated

Table 2.2.: Thermal conductivity measurements for the GNP-NC sample with 2% wt. GNPs

Case No.	Temp range ( $^{\circ}\text{C}$ )	Voltage (V)	$\Delta T_{ref1}$ ( $^{\circ}\text{C}$ )	$\Delta T_{sample}$ ( $^{\circ}\text{C}$ )	$\Delta T_{ref2}$ ( $^{\circ}\text{C}$ )	$q''$ ( $\text{W}/\text{m}^2$ )	$k_{eff}$ ( $\text{W}/\text{m-K}$ )
1	20-55	32	10.71	21.49	8.39	$2.87 \times 10^3$	0.13
2	20-47	27	4.78	10.68	3.61	$2.26 \times 10^3$	0.12
3	20-38	22	4.43	10.52	3.66	$2.21 \times 10^3$	0.12

Table 2.3.: Thermal conductivity measurements for the GNP-NC sample with 5% wt. GNPs

Case No.	Temp range ( $^{\circ}\text{C}$ )	Voltage (V)	$\Delta T_{ref1}$ ( $^{\circ}\text{C}$ )	$\Delta T_{sample}$ ( $^{\circ}\text{C}$ )	$\Delta T_{ref2}$ ( $^{\circ}\text{C}$ )	$q''$ ( $\text{W}/\text{m}^2$ )	$k_{eff}$ ( $\text{W}/\text{m-K}$ )
1	20-57	32	7.80	13.61	7.50	$2.30 \times 10^3$	0.17
2	20-47	27	5.86	11.68	5.43	$1.69 \times 10^3$	0.15
3	20-38	22	3.82	6.48	3.45	$0.09 \times 10^3$	0.17

by a sample of uniform thickness. The reference material used was polytetrafluoroethylene (PTFE) with a thermal conductivity of 0.3 W/m-K. A thermal gradient was imposed across the GNP-NC sample using a hot and a cold surface (aluminum) in contact with the reference materials. The temperature of the hot surface was controlled using an electric type heater with a constant voltage supply, while the temperature of the cold surface was maintained at a fixed temperature using a circulated cold liquid (duratherm liquids around 20-22  $^{\circ}\text{C}$ ). Three different GNP-NC samples with 0%, 2% and 5% wt. of GNPs were tested. Moreover, for all the cases, the thickness of the fuel samples and the reference materials were kept fixed at 1 mm. For each type of sample, three different measurements were made using three different heat fluxes (temperature ranges). The different heat fluxes were obtained by

changing the temperature of the hot surface, using the voltage supply, while keeping the temperature of the cold surface fixed. The temperature measurements were made using an IR camera (MWIR-1024), but before, a calibration using the IR camera was performed to get the emissivity values of the reference materials and the GNP-NC samples. Tables 2.1, 2.2, and 2.3 show the different cases that were run. In the above tables,  $q''$  is the average steady state heat flux imposed across the reference materials and the GNP-NC sample,  $\Delta T_{ref1}$  is the temperature difference across the reference material in contact with the cold surface,  $\Delta T_{ref2}$  is the temperature difference across the reference material in contact with the hot surface and  $\Delta T_{sample}$  is the temperature difference across the GNP-NC sample. An effective thermal conductivity ( $k_{eff}$ ) of  $0.092 \pm 0.01$  (W/m-K),  $0.123 \pm 0.01$  (W/m-K) and  $0.163 \pm 0.012$  (W/m-K) was obtained for the GNP-NC sample having 0%, 2% and 5% wt. of GNPs, respectively. Thus, for the 5% wt. GNP-NC sample, a 70% enhancement in the thermal conductivity value was obtained.

### 2.1.3 Graphene Foam (GF)

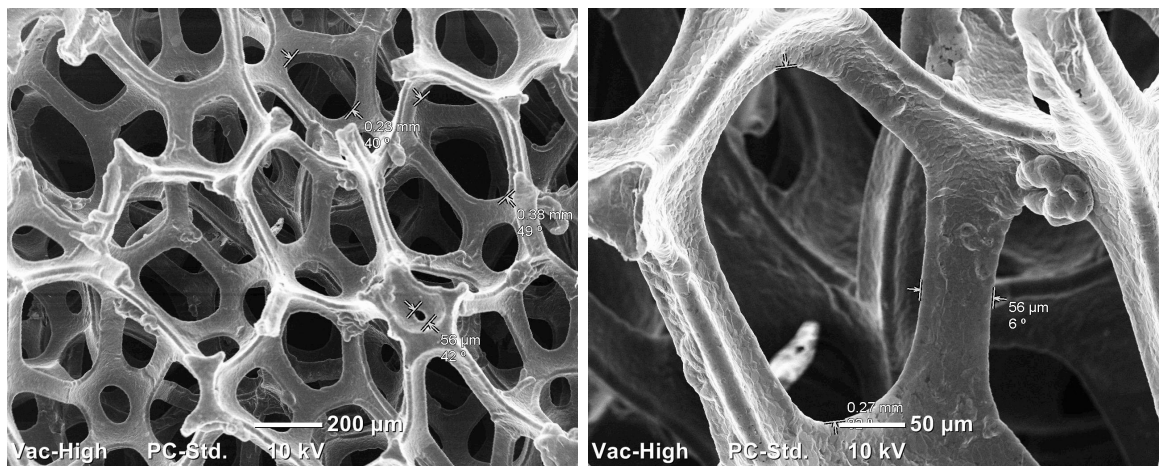


Figure 2.6.: SEM images of the GF structure before NC deposition.

The GF exhibited a three-dimensional, interconnected, highly porous structure (98.2%–99.64% porous), as shown in Fig. 2.6. The pore diameters ranged from 50–600  $\mu\text{m}$ ,

whereas the width of the strut walls was around 50-80  $\mu\text{m}$ . Moreover, the GF strut walls were not solid but hollow in nature, with the exact wall thickness depending on the density of the GF structure. Pettes et al. [63] conducted TEM (transmission electron microscopy) imaging of these GF structures and found the strut wall thickness to vary from 14 nm to 45 nm for the GF densities ranging from 10  $\text{mg}/\text{cm}^3$  to 32  $\text{mg}/\text{cm}^3$ .

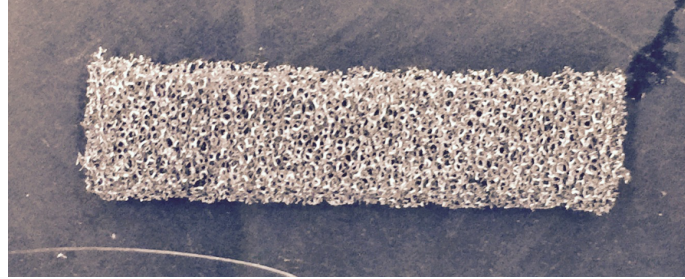


Figure 2.7.: The pure GF sheet cut in the required dimension of 2.5 cm x 0.6 cm.

The pure GF structure, following the method outlined by Chen et al. [35], was grown on a Ni template (3 mm-thick open-cell foam with 75 pores per inch) using a chemical vapor deposition (CVD) technique. For the growth process, a mixture of 3 gases i.e.  $\text{CH}_4$  (20 sccm), Ar (210 sccm) and  $\text{H}_2$  (20 sccm) was used at 1050  $^\circ\text{C}$ . The exact growth time controlled the GF density, which in this study was varied from 8  $\text{mg}/\text{cm}^3$  to 40  $\text{mg}/\text{cm}^3$ . After the growth of graphene layers on the Ni template, the GF-Ni surface was drop-casted with a PMMA (polymethyl methacrylate) solution to protect the surface from the vigorous etching process. The Ni template was then etched out in two steps: (1) first using the  $\text{Fe}(\text{NO}_3)_3 \cdot 9\text{H}_2\text{O}$  solution (1 M) at 90  $^\circ\text{C}$  for 2 days and then (2) using the HCl solution (1 M) at 90  $^\circ\text{C}$  for the next 2 days. After the Ni has been completely etched out, the GF surface was rinsed with DI water and then hot acetone to completely dissolve the PMMA solution away. The final GF sheet cut in the required dimension of 2.5 cm by 0.6 cm is shown in Fig. 2.7. A total of 8 GF sheets were obtained from each growth process. The average GF density and porosity, for each growth, was then calculated by averaging the densities and porosities of these 8 individual GF sheets. The porosity of each GF sheet was determined using

the equation:  $1 - M_s/(\rho_g * V_s)$ , where  $M_s$  and  $V_s$  is the mass and volume of the GF sheet, respectively, and  $\rho_g$  is the graphite bulk density ( $2260 \text{ kg/m}^3$ ). The uncertainty associated in calculating average GF densities was  $\pm 2 \text{ mg/cm}^3$ .

Table 2.4.: Thermal conductivity measurements for the GF density -  $22 \text{ mg/cm}^3$

Case No.	Temp range ( $^{\circ}\text{C}$ )	Voltage (V)	$k_{GF}$ (W/m-K)
1	21.98-58	39	0.352
2	21.85-50	34	0.303
3	21.6-42.3	29	0.341

Table 2.5.: Thermal conductivity measurements for the GF density -  $11.3 \text{ mg/cm}^3$

Case No.	Temp range ( $^{\circ}\text{C}$ )	Voltage (V)	$k_{GF}$ (W/m-K)
1	21.95-57.6	38	0.465
2	21.8-47.7	33	0.47
3	21.6-41.6	28	0.422

Next, thermal conductivity measurements were performed to determine the effect of GF density on the thermal conductivity of GF strut walls. First, the effective thermal conductivity of the GF sheet was measured experimentally and then using the correlation proposed by Pettes et al. [63], the thermal conductivity of GF strut walls was estimated. The measurements were performed using the same experimental method as that used for the GNP-NC samples (Fig. 2.5) i.e. using a steady state, controlled, heat flux method. However, in this case, a different reference material, NIST standard gum rubber material, with a thermal conductivity value of  $0.15 \text{ W/m-K}$  was used. Two GF sheets of densities:  $22 \text{ mg/cm}^3$  and  $11.3 \text{ mg/cm}^3$  were tested and again, for each case, three different measurements were made using three different

heat fluxes (temperature ranges). Tables 2.4 and 2.5 show the two different cases that were run. An effective thermal conductivity of  $0.332 \pm 0.03$  (W/m-K) and  $0.452 \pm 0.05$  (W/m-K) was obtained for the GF sheet of density  $22 \text{ mg/cm}^3$  and  $11.3 \text{ mg/cm}^3$ , respectively. Then, to determine the thermal conductivity of GF strut walls, the following correlation as proposed by Pettes et al. [63] was used:

$$k_w = \frac{3}{\phi} k_{GF} = \frac{3\rho_g}{\rho_{GF}} k_{GF} \quad (2.1)$$

where,  $k_w$  is the thermal conductivity of GF strut walls,  $k_{GF}$  is the effective thermal conductivity of the GF sheet,  $\rho_g$  is the graphite bulk density,  $\rho_{GF}$  is the GF density and  $\phi$  is the volume fraction of graphene in the GF structure (1-porosity).

Using the above Eqn. 2.1, the  $k_w$  values came out to be  $102 \pm 9$  W/m-K and  $271 \pm 30$  W/m-k for the high and the low density cases, respectively. However, these  $k_w$  values were much lower as compared to the  $k_w$  values obtained by Pettes et al. [63]. In their experiments,  $k_w$  values of  $454 \pm 38$  W/m-K and  $995 \pm 162$  W/m-K were obtained for the GF densities of  $31.7 \pm 2.7 \text{ mg/cm}^3$  and  $11.6 \pm 1.9 \text{ mg/cm}^3$ , respectively. This could be attributed to the different experimental conditions used. Pettes et al. performed the thermal conductivity measurements in vacuum in contrast to this study where the measurements were performed in open air, which could lead to additional convective heat losses and thus, reduce the  $k_w$  values obtained. Moreover, the type of Ni etchant and the quality of the Ni foam used can also have a significant effect on the quality of the GF structure grown. In the GF preparation of Pettes et al., a much gentler Ni etchant,  $(\text{NH}_4)_2\text{S}_2\text{O}_8$ , was used in contrast to the aggressive HCl etchant used in this study. Moreover, before the growth of the GF structure, Pettes et al. annealed the Ni foam at  $1100 \text{ }^\circ\text{C}$  to increase the grain size, which would in turn increase the mean free path of the phonons in the GF. However, despite the discrepancy obtained in the absolute  $k_w$  values, a trend similar to that of Pettes et al. was observed, in which the  $k_w$  value obtained for the lower GF density was found

to be much higher (3 times more) as compared to that obtained for the higher GF density. The explanation for this trend in the  $k_w$  values as a function of the GF density is given later in the results section 2.3.3 of this chapter.

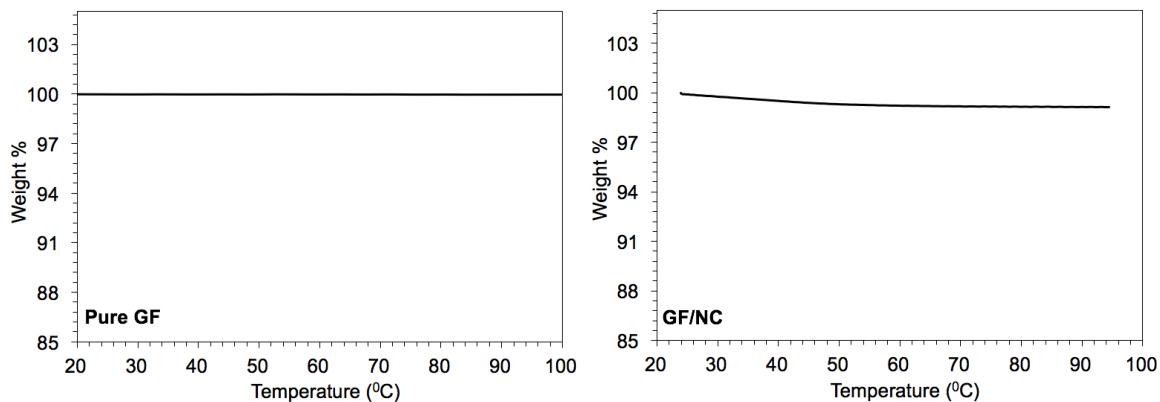


Figure 2.8.: TG analysis of GF (up to 100 °C) with and without NC addition.

After the preparation of the GF structures, the NC solution was drop-casted onto the GF surface at various amount to get the desired NC-GF (fuel) loading, which is defined as the mass of NC per total mass of NC + GF. These fuel doped GF samples were then left to dry in ambient conditions for 24 hours. Moreover, special attention was paid to the fluctuations observed while measuring the weight of the samples (before ignition). If the fluctuations observed were significant, then the samples were left to dry for a longer time. The samples were considered dried only when there were no fluctuations in the weight measurement and a constant weight was achieved. Fig. 2.8 shows the TG analysis of GF in air before and after the fuel addition. Since the boiling point of ethanol/acetone/diethyl ether is 79/56/35 °C, respectively, the TG analysis was conducted only up to 100 °C (at a rate of 10 °C/min) and thus, allowing any weight loss due to the presence of the residual solvent to be detected. The NC-GF sample, as shown in Fig. 2.8, was evaporated at ambient conditions for 24 hours before conducting the TG analysis. As can be seen, for the NC-GF sample, only a tiny loss (< 1%) in the sample weight was obtained, thus confirming that there was negligible residual solvent left after the evaporation process.

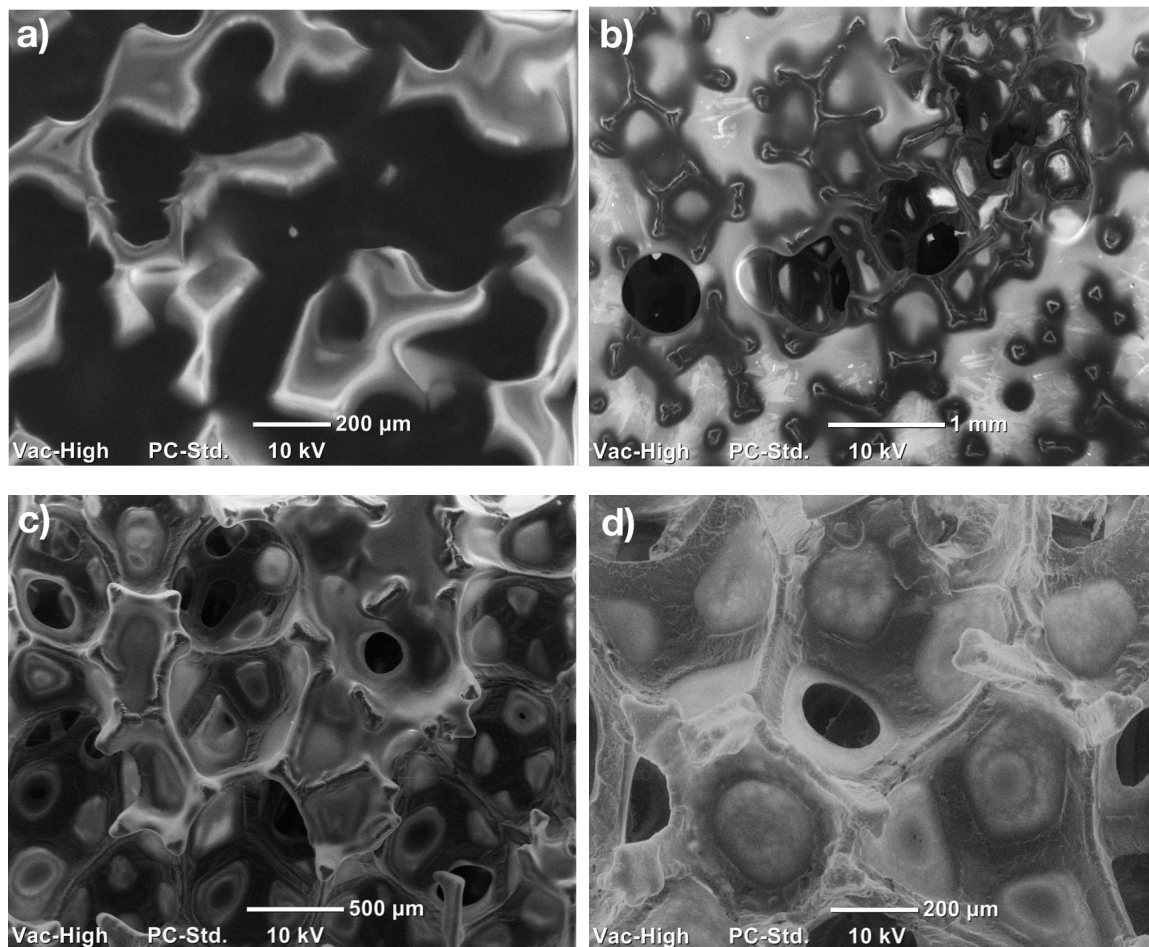


Figure 2.9.: SEM images of the GF surface after NC deposition; a) 95%, b) 75%, c) 55% and d) 35% NC-GF loading.

Fig. 2.9 shows the SEM images of the GF surface after the fuel deposition, at various NC-GF loadings. As can be seen, with a decrease in the NC-GF loading, the morphology of the GF structure was more clearly visible, which was because of the decreased deposited fuel thickness on the GF strut walls. Moreover, the number of GF pores that remained partially unfilled after the fuel deposition were also found to increase with a decrease in the NC-GF loading. Thus, special precautions were made for the lower NC-GF loadings (<60%) to make sure that during the deposition process, the NC solution wets most of the GF strut walls. This was done by further diluting the NC solution to 2% wt., so that it could more easily enter the pores. Thus, after the

evaporation process, a thin layer of fuel was left coating the inner and outer areas of the GF strut walls and as a result, providing an interconnected NC-GF network for the thermal conduction during the combustion process.

## 2.2 Experimental Setup

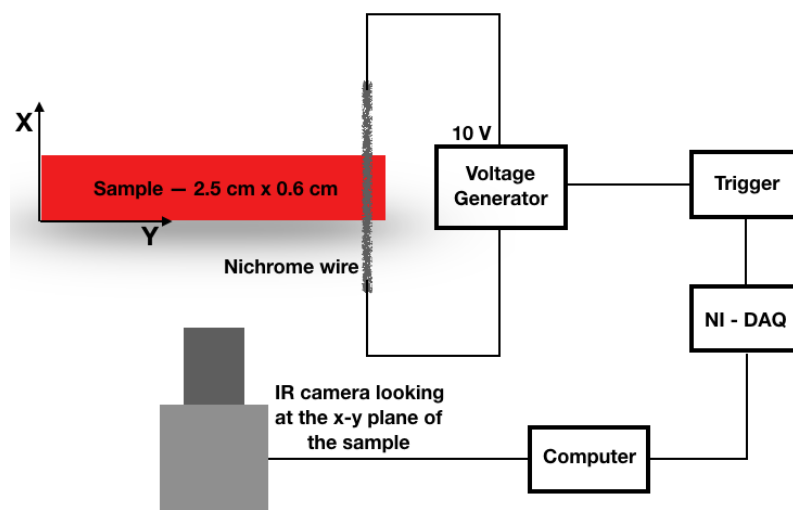


Figure 2.10.: Experimental Setup (not to scale) for burn rate measurements.

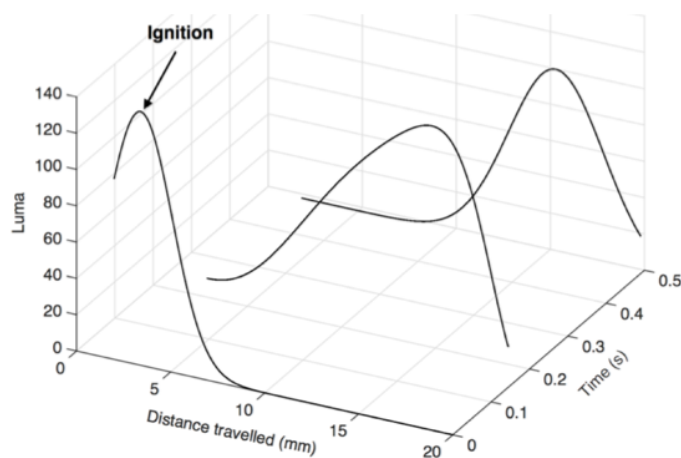


Figure 2.11.: Intensity profiles during the reaction wave propagation as a function of time and space.

Fig. 2.10 shows the experimental setup used, in which the ignition of the prepared samples was achieved by using a resistive heating nichrome wire placed in a transverse manner at one end of the sample. A constant voltage of 10 V was applied across the wire, which was sufficient to ignite the samples. Moreover, an IR camera (FLIR- SC6100) was used to capture the ignition and reaction wave propagation process. Fig. 2.11 gives an example of the typical intensity profiles obtained during the reaction wave propagation at different times along the length of a sample. The burn rate, which is defined as the rate at which the reaction zone travels across the fuel layer, was then calculated by tracking the brightest peak of these intensity profiles.

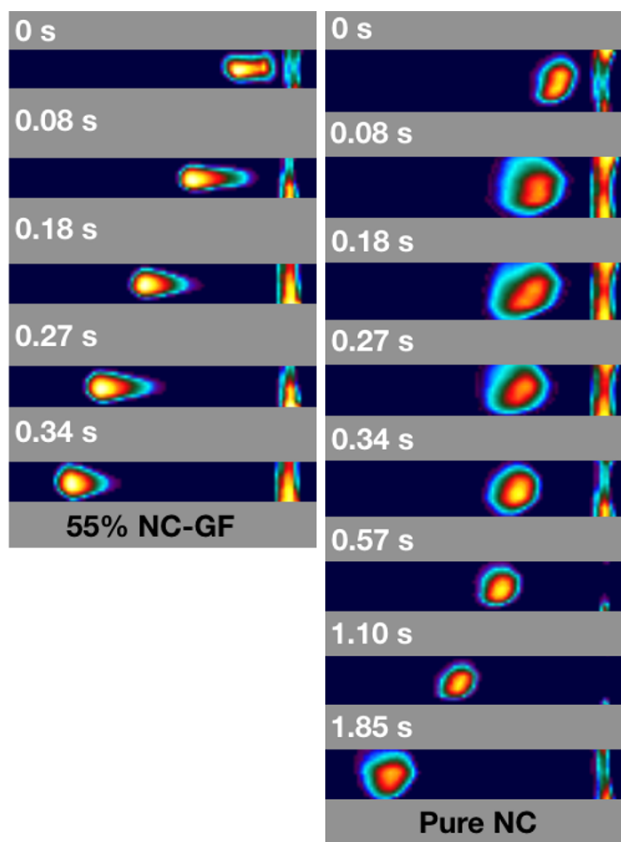


Figure 2.12.: Reaction wave propagation in the NC-GF sample (55% NC-GF loading, 3.82 cm/s) and pure NC (0.7 cm/s). The distance of propagation in both the samples was 1.3 cm.

Fig. 2.12 shows snapshots of the reaction propagation wave at different times for two different cases: (1) NC-GF (55% NC-GF loading) and (2) pure NC (no graphene-structure added). As can be seen, the burn rate for the NC-GF sample was much faster (5.5 times for this particular case) as compared to the pure NC burn rate. In addition, the errors associated with the determination of burn rates were also estimated. The burn rate ( $b$ ) between any two points ( $r_1, r_2$ ) can be expressed as:

$$b = \frac{r_2 - r_1}{t_2 - t_1} \quad (2.2)$$

where,  $t_2 - t_1$  is the total time it takes for the reaction zone to travel from  $r_1$  to  $r_2$ . Then, using the procedure given by Moffat [120], the uncertainties associated with the burn rate ( $\Delta b$ ) measurements can be calculated as follows:

$$\frac{\Delta b}{b} = \sqrt{\left(\frac{\Delta(r_2 - r_1)}{r_2 - r_1}\right)^2 + \left(\frac{\Delta(t_2 - t_1)}{t_2 - t_1}\right)^2} \quad (2.3)$$

where,  $\Delta(r_1 - r_2)$  and  $\Delta(t_1 - t_2)$  are the uncertainties associated with the spatial and temporal measurements and were estimated to be less than 2% and 6%, respectively. The temporal uncertainty was taken to be as the temporal width of the intensity profiles within 90% of their peak value, whereas the spatial uncertainty was calculated using the pixel resolution. Using Eqn. 2.3, the uncertainties in the burn rate measurements came out to be less than 6.5%. Moreover, a K-type thermocouple, embedded in the fuel surface, was also used to measure the peak surface temperature of the pure NC sample. An average peak surface temperature of 613 K was obtained with a standard deviation of  $\pm 30$  K.

## 2.3 Experimental Results

### 2.3.1 Graphite Sheet (GS)

For solid propellants, the reaction wave does not propagate at a steady speed but has an oscillatory profile associated with it. Mercer et al. [121, 122], based on numerical modeling, proposed that during the reaction wave propagation there are three types of combustion regimes (type I, type II, and type III) possible depending on the particular value of  $\beta$  and the amount of interfacial heat flow between the deposited fuel and the substrate. The parameter  $\beta$  is defined as the non-dimensional inverse adiabatic temperature rise and can be expressed as follows:

$$\beta = \frac{Cp_f E}{QR_u} \quad (2.4)$$

where,  $Cp_f$  is the specific heat of the fuel,  $E$  is the fuel activation energy,  $Q$  is the heat of combustion and  $R_u$  is the universal gas constant. Thus, a high  $\beta$  value corresponds to either a high  $E$  or a low  $Q$  value i.e. greater the  $\beta$  value, lower would be the average burn rates obtained.

A type I combustion wave is obtained when  $\beta < 5$  (irrespective of the heat flow value) or when  $5 < \beta < 6.5$  (with low values of heat flow) and is characterized by the appearance of a steady combustion wave (constant speeds) with no or very little oscillations. For intermediate values of heat flow and for  $5 < \beta < 6.5$ , a type II combustion wave is obtained, whereas a type III combustion wave is obtained for high values of heat flow. A type II wave is characterized by the appearance of peaks of similar magnitudes, whereas a type III combustion wave is characterized by the appearance of peaks of varying magnitudes. For  $\beta > 6.5$ , a type II is obtained if the heat flow is low, and a type III wave is obtained for intermediate to high values of heat flow.

Fig. 2.13 shows the measured instantaneous burn rates as a function of the distance traveled along the length of a NC-GS sample for the fuel thickness of  $70 \mu\text{m}$ . A type III combustion wave was obtained with an average oscillation period of  $0.068 \text{ s}$ . This was expected, since for the NC-GS system, both  $\beta$  ( $10.7$ ) and the interfacial heat flow (because of the graphite sheet) values were high. Moreover, the amplitude and period of the oscillations observed were found to be dependent on the thickness of the fuel layer deposited. For example, for the fuel thickness of  $25 \mu\text{m}$ , oscillation periods as high as  $0.1 \text{ s}$  were obtained. However, as the fuel thickness was increased to  $70 \mu\text{m}$  and  $125 \mu\text{m}$ , oscillation periods on the order of  $0.05 \text{ s}$  and  $0.03 \text{ s}$  were obtained, respectively. Oscillatory velocity profiles with similar time periods were also reported by Walia et al. [19]. To better understand the experimental trends obtained, a simple 1-D modeling using energy conservation equations and one-step chemistry was also performed. Refer to section 2.4 for more details.

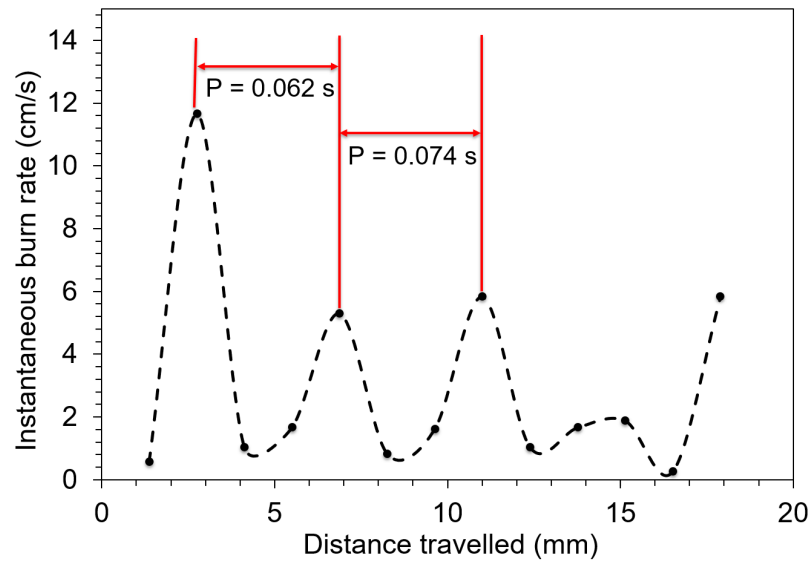


Figure 2.13.: Instantaneous burn rates as a function of the distance traveled along the length of a NC-GS sample. The particular case shown corresponds to the fuel thickness of  $70 \mu\text{m}$ .

Fig. 2.14 shows the average burn rates obtained for the NC-GS sample as a function of the fuel thickness deposited. These average burn rates were calculated by averag-

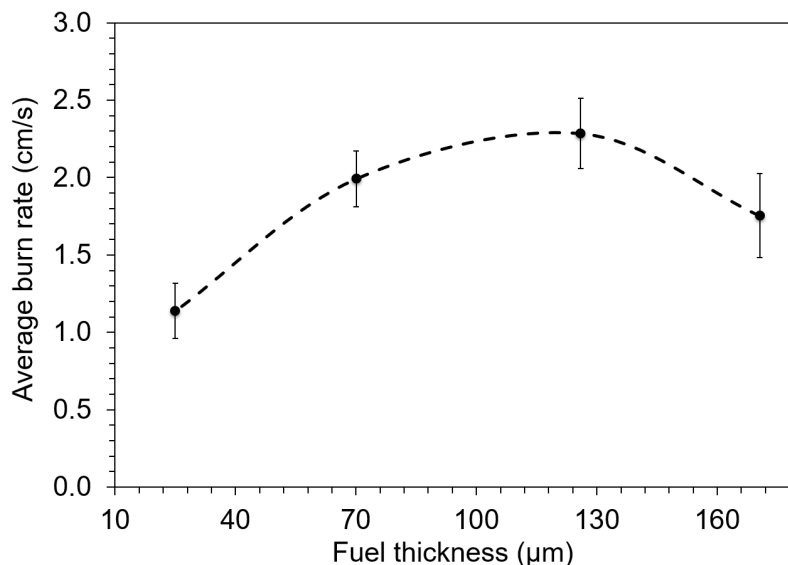


Figure 2.14.: Average burn rates as a function of the fuel thickness for the NC-GS system.

ing the instantaneous burn rates, as shown in Fig. 2.13. As can be seen, an optimal fuel thickness of around  $125 \mu\text{m}$  was obtained with average burn rates up to  $2.3 \text{ cm/s}$  (3.3 times the bulk NC burn rate of  $0.7 \text{ cm/s}$ ). The optimum fuel thickness behavior observed could be attributed to the competition between the amount of energy released from the exothermic reactions and the amount of heat lost to the graphite sheet. For low fuel thicknesses, the amount of energy released from the exothermic reactions was not high enough to result in an efficient reaction propagation, as most of the energy released was being lost in heating the graphite sheet, which remained unburned during the combustion process due to the low NC peak surface temperature ( $\sim 600 \text{ K}$ ). Thus, a drop in the burn rate from the optimum value was obtained. However, for very thick depositions, although the amount of energy released from the exothermic reactions was sufficient to aid in an efficient reaction propagation, only a small amount of fuel was in contact with the graphite sheet, as a result of which the net thermal transport within the fuel in the direction along the reaction propagation was reduced and again a drop in the burn rate from the optimum value was obtained. Thus, a unique fuel to graphite thickness ratio existed that maximized the burn rates.

### 2.3.2 Graphene Nanopellets (GNPs)

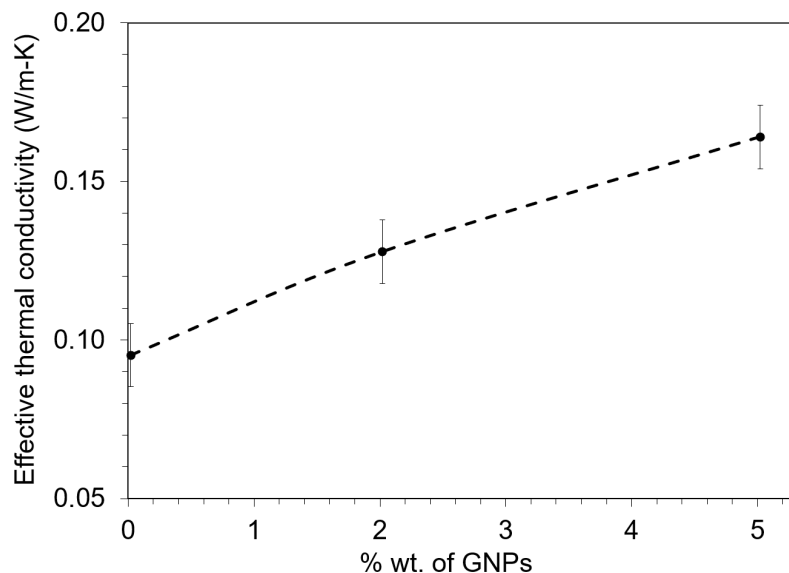


Figure 2.15.: Effective thermal conductivity of the GNP-NC sample as a function of the % wt. of GNPs.

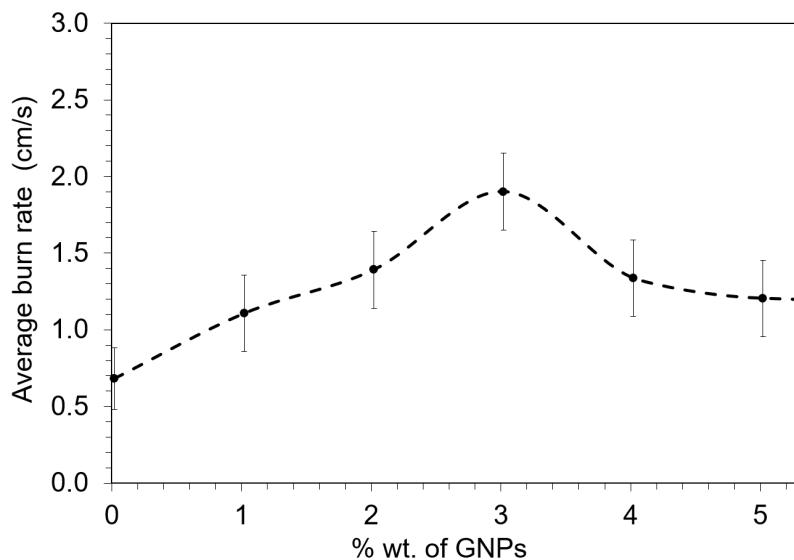


Figure 2.16.: Average burn rates as a function of the % wt. of GNPs.

Fig. 2.15 plots the effective thermal conductivity of the GNP-doped NC sample as a function of the % wt. of GNPs added. As can be seen, a linear increase in the

thermal conductivity value was obtained with a 70% enhancement for the GNP-NC sample having 5% wt. of GNPs. Thus, for low % wt. of GNPs, the net thermal conductivity of the sample was not high enough to conduct heat efficiently from the exothermic reactions to aid in reaction propagation. On the contrary, for high % wt. of GNPs, although the net thermal conductivity of the GNP-doped NC sample was a lot higher, the amount of heat conducted to the unburned portions of the fuel was substantially reduced because some of the energy that was released during the exothermic reactions was being used in heating the GNPs, which acted as heat sinks and as a result, reduced the net amount of burn rate enhancement that could be obtained. Consequently, an optimum % wt. of GNPs of around 3% was obtained for which the burn rate enhancement was 2.7 (1.9 cm/s) times the bulk NC burn rate (Fig. 2.16).

The main parameters affecting the burn rates can be identified by looking at a simple 1-D energy equation, modified for the present case of GNP-NC films, as given below:

$$\rho_{eff}Cp_{eff}\left(\frac{\partial T}{\partial t}\right) = k_{eff}\left(\frac{\partial^2 T}{\partial x^2}\right) - \frac{h * S}{V}\left(T - T_a\right) - \frac{\epsilon\sigma * S}{V}\left(T^4 - T_a^4\right) + \rho_{eff}QA w_f \exp\left(\frac{-E}{R_u T}\right) \quad (2.5)$$

which can be re-written as:

$$\left(\frac{\partial T}{\partial t}\right) = \alpha_{eff}\left(\frac{\partial^2 T}{\partial x^2}\right) - \left(\frac{h * S}{\rho_{eff}Cp_{eff}V}\right)\left(T - T_a\right) - \frac{\epsilon\sigma * S}{\rho_{eff}Cp_{eff}V}\left(T^4 - T_a^4\right) + \left(\frac{QA}{Cp_{eff}}\right)w_f \exp\left(\frac{-E}{R_u T}\right) \quad (2.6)$$

In the above equations,  $\rho_{eff}$  is the effective density,  $Cp_{eff}$  is the effective specific heat capacity,  $k_{eff}$  is the effective thermal conductivity and  $\alpha_{eff}$  is the effective thermal diffusivity of the GNP-NC film;  $w_f$  is the mass fraction of the unburned fuel,  $T_a$  is the ambient temperature,  $Q$  is the heat of combustion,  $R_u$  is the universal gas constant,  $A$  is the Arrhenius constant,  $E$  is the fuel activation energy,  $h$  is the convective heat loss coefficient,  $\epsilon$  is the emissivity of the fuel/GNPs, and  $\sigma$  is the Stefan-Boltzmann constant. As can be seen from Eqn. 2.6, the rate at which the temperature of a point along the length of a sample changes depends only on three parameters: effective thermal diffusivity, amount of heat lost to the environment and amount of energy released from the chemical reactions. Moreover, for the present case of GNP-NC films, the increase observed in the thermal diffusivity was mostly from the enhanced effective thermal conductivity of the samples as the changes observed in the density and specific heat values were marginal. For example, only a 2% change in the  $(\rho Cp)_{eff}$  value was obtained for the case of 5% wt. GNPs, as was calculated using the classical Effective Medium Theory (EMT). However, a 70% enhancement in the  $k_{eff}$  value was obtained.

The above 1-D energy equation was based on the assumption that the temperature rise observed in the unburned portions of the fuel was only from the conductive heat transfer. Thus, an order of magnitude analysis was performed next to determine the relative importance of conductive, convective and radiative heat transfers. The convective heat flux ( $q''_{conv}$ ) from the hot gaseous combustion products to the cold unreacted solid fuel in front of the reaction zone can be approximated as [123]:

$$q''_{conv} = \rho_g C p_g v_g (T_f - T_u) \quad (2.7)$$

The conductive heat flux can be written as: [123]

$$q''_{cond} = k_{eff} (T_s - T_u) / l_f \quad (2.8)$$

The radiative heat flux can be written as:

$$q''_{rad} = \epsilon \sigma \left( T_s^4 - T_u^4 \right) \quad (2.9)$$

In the above equations,  $\rho_g$  is the density,  $Cp_g$  is the specific heat capacity and  $v_g$  is the velocity of the hot gases,  $T_f$  is the flame temperature,  $T_s$  is the surface temperature,  $l_f$  is the thickness of the reaction zone, and  $T_u$  is the temperature of the unburned fuel. The density and specific heat of the hot gases were estimated using the NASA CEA code. Performing an order of magnitude analysis of the above equations:

$$v_g \sim 1 \frac{cm}{s} = 0.01 \frac{m}{s}$$

$$\rho_g \sim 0.1 \frac{kg}{m^3}$$

$$Cp_g \sim 10 \frac{J}{KgK}$$

$$k_{eff} \sim 0.1 \frac{W}{mK}$$

$$l_f \sim 10^{-3} m$$

$$T_f \sim 1700 K$$

$$T_s \sim 600 K$$

$$\epsilon \sim 0.8$$

$$\frac{q''_{cond}}{q''_{conv}} \sim 10^3 \quad \text{and} \quad \frac{q''_{cond}}{q''_{rad}} \sim 6 \quad (2.10)$$

As can be seen, the conductive heat flux comes out to be  $10^3$  and 6 times as that of the convective and radiative heat fluxes, respectively, and thus, the convective and radiative contributions could be ignored. This was similar to the observations made by Choi et al. [18].

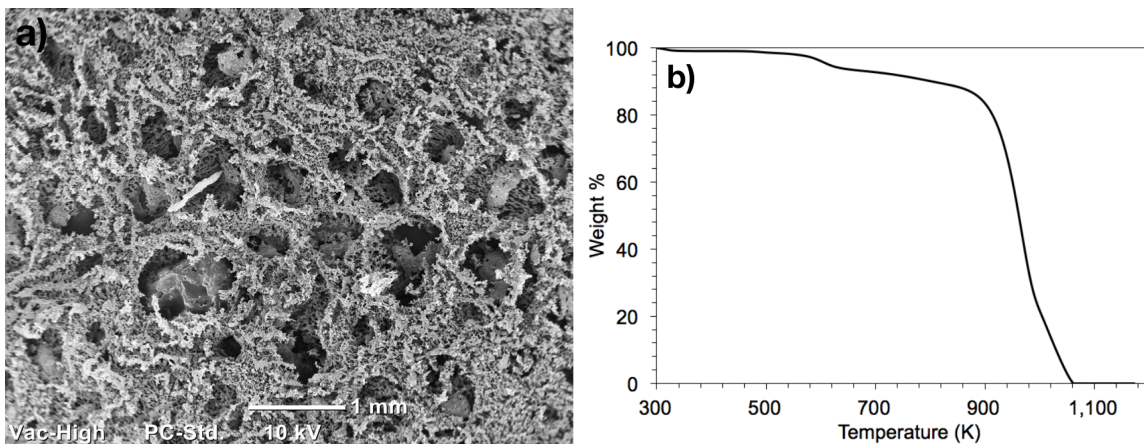


Figure 2.17.: a) SEM image of the top view of a GNP-NC sample after combustion; b) TG analysis of GNPs in air.

Fig. 2.17a shows the SEM image of the top view of a GNP-NC sample after combustion. As can be seen, the GNPs remained unburned and a porous-like structure was obtained. To confirm the non-reactivity of GNPs, a TG analysis of GNPs was conducted in air up to 1200 K (using a heating rate of 10 °C/min) and as shown in Fig. 2.17b, negligible weight loss was obtained up to 870 K. Since, the maximum NC surface temperature measured during the combustion process was only 613 K, the thermal stability of the GNPs obtained was expected.

### 2.3.3 Graphene Foam (GF)

Fig. 2.18 shows the effect of NC-GF loading on the burn rates obtained. The GF density was kept fixed at 18 mg/cm<sup>3</sup>. As can be seen, an optimum NC-GF loading of 55% was obtained with burn rates up to 4 cm/s (5.7 times the bulk NC burn rate). Compared to the GNP-doped NC films, almost 2 times more enhancement was observed. This could be attributed to two factors. First of all, the GF strut walls have been shown in previous studies to have the high in-plane thermal conductivity values while avoiding the thermal boundary resistance issue found in GNPs and CNTs [63, 69–75, 91]. The TBR value can have a significant effect on the net effective thermal conductivity of the sample. For example, Ji et al. [57] conducted a compre-

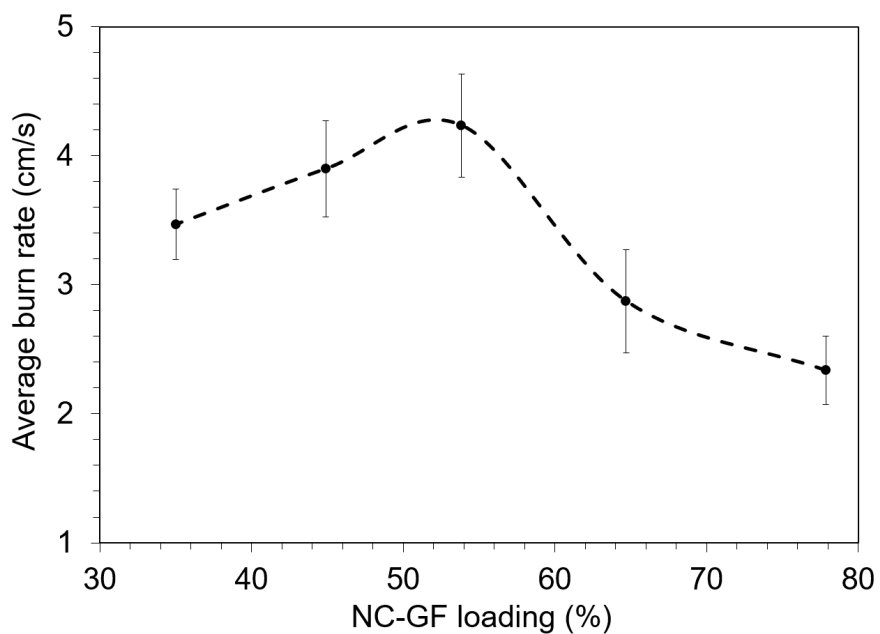


Figure 2.18.: Average burn rates as a function of the NC-GF loading (%). GF density fixed at  $18 \text{ mg/cm}^3$ .

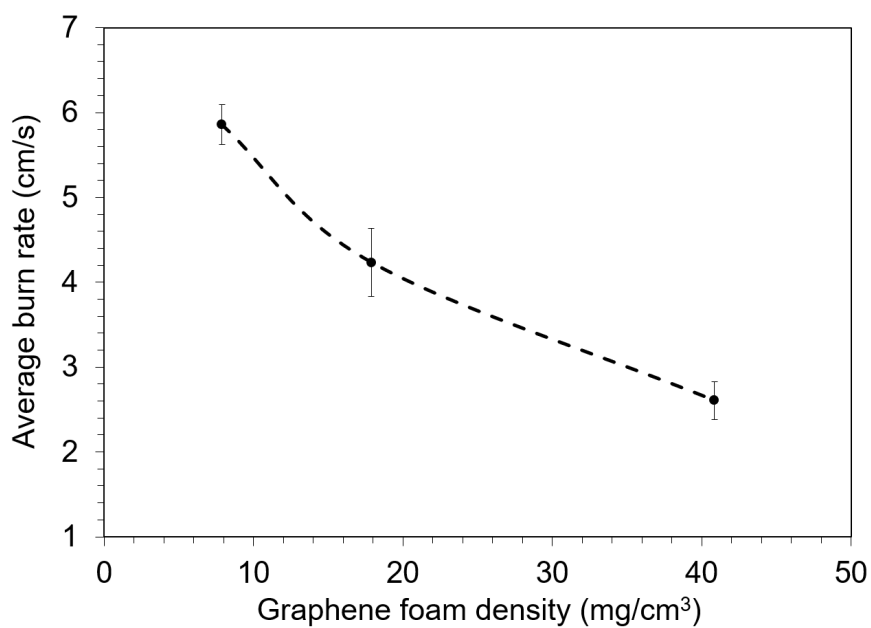


Figure 2.19.: Average burn rates as a function of the GF density. NC-GF loading fixed at 55%.

hensive study, in which the thermal conductivity enhancement of wax using GF and GNPs was compared. GF was found to increase the thermal conductivity of the composite 18 times (1% vol.), which was much higher than the amount of enhancement observed using the GNPs (only 1.5 times for the same volumetric loading). Second, GF, because of its interconnected 3D structure, provided a continuous thermal conduction path, which did not exist in the case of GNP-doped NC films because of the random orientation of the added GNPs. Since GNPs are 2D graphene materials, their in-plane and transverse thermal conductivity values are significantly different. For example, the GNP's in-plane and transverse thermal conductivities have been measured to be around 3000 W/m-K and 6 W/m-K, respectively [124, 125]. Thus, the thermal conduction in GNPs is anisotropic and their orientation can have a significant effect on the rate of thermal transport obtained. In addition, along the reaction wave propagation direction, the GNPs were not in direct contact with each other but had fuel in between, which even further increased the thermal resistance. This was in contrast to GF, in which the graphene structures were connected from end to end with the fuel depositions around the GF strut walls (Fig. 2.9).

Fig. 2.19 shows the effect of GF density on the burn rates obtained at the optimum NC-GF loading of 55%. A monotonically decreasing trend as a function of the GF density was observed, which could be attributed to the crystallographic defects present in the higher density GF structures. For the GF density of 8 mg/cm<sup>3</sup>, burn rates up to 5.5 cm/s (7.6 times the bulk NC burn rate) were obtained, which were 2.62 and 2.9 times greater than the burn rates obtained using the GF density of 40 mg/cm<sup>3</sup> and the GNPs, respectively.

Fig. 2.20 shows the SEM images of a low density (11.3 mg/cm<sup>3</sup>) and a high density (22 mg/cm<sup>3</sup>) GF structure. The higher density GF structure was found to be more defective as can be seen from the increased surface roughness. This was consistent with the observations made by Pettes et al. [63], in which the surface morphology

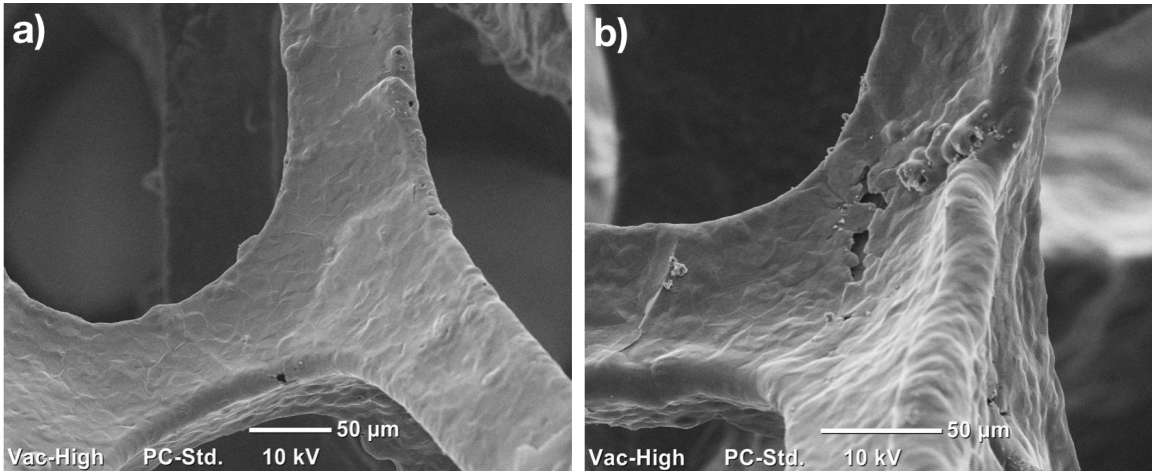


Figure 2.20.: SEM images of the GF strut walls with different densities; a) 11.3  $\text{mg}/\text{cm}^3$  and b) 22  $\text{mg}/\text{cm}^3$ .

of the GF structure obtained using different growth times (densities) were studied. The defects in the GF structures can be characterized by looking at the ratio of the intensities of the disorder-induced D-band to the symmetry-allowed G-band [126]. In graphene, the Stokes phonon energy shift caused by the laser excitation gives rise to three peaks in the Raman spectrum: G peak - a primary in-plane vibrational mode, 2D peak - a second-order overtone of a different in-plane vibration mode, and a D peak - a defect activated Raman mode [127]. Pettes et al. [63] performed the Raman spectroscopy of the GF strut walls and found that for the lower density cases (11.6  $\text{mg}/\text{cm}^3$ ), no observable D peak was observed, which matched well with those of high quality ordered-graphite, signifying no defects. This was in contrast to the higher density cases (31.7  $\text{mg}/\text{cm}^3$ ), where a D peak to G peak intensity ratio of 2% was observed. The surface defects can significantly affect the phonon scattering mean free path, which in turn can affect the thermal conductivity of the GF strut walls [63,128]. In the previous section 2.1.3, thermal conductivity measurements were performed to determine the effect of GF density on the thermal conductivity of GF strut walls ( $k_w$ ) and for the lower GF density structure (11.3  $\text{mg}/\text{cm}^3$ ) much higher  $k_w$  values were obtained (3 times more) as compared to the higher GF density structure (22  $\text{mg}/\text{cm}^3$ ).

Thus, the trend observed in the  $k_w$  values is consistent with the surface defects explanation given above, confirming that the lower density GF structures grown were indeed of much better quality. Moreover, since, the NC-GF samples were prepared by drop-casting the fuel solution on to the GF surfaces, the surface roughness can have an additional effect of increasing the TBR value between the deposited fuel and the GF strut walls, which could even further decrease the effective thermal conductivities of the NC-GF samples.

Another reason for obtaining high burn rates in the lower density samples could be attributed to the fact that the GF strut walls were not solid but hollow in nature. The higher the GF density, the thicker would be the GF strut walls. Thus, for the higher density sample, the deposited fuel was in contact with much thicker walls, which in turn lead to a greater amount of heat being lost from the fuel to the GF structures. Moreover, to keep the NC-GF loading fixed at 55%, more amount of fuel was required to be added in the higher density sample. As a result of which, less amount of fuel was in contact with the GF strut walls and thus, reducing the net thermal transport that could be obtained within the fuel.

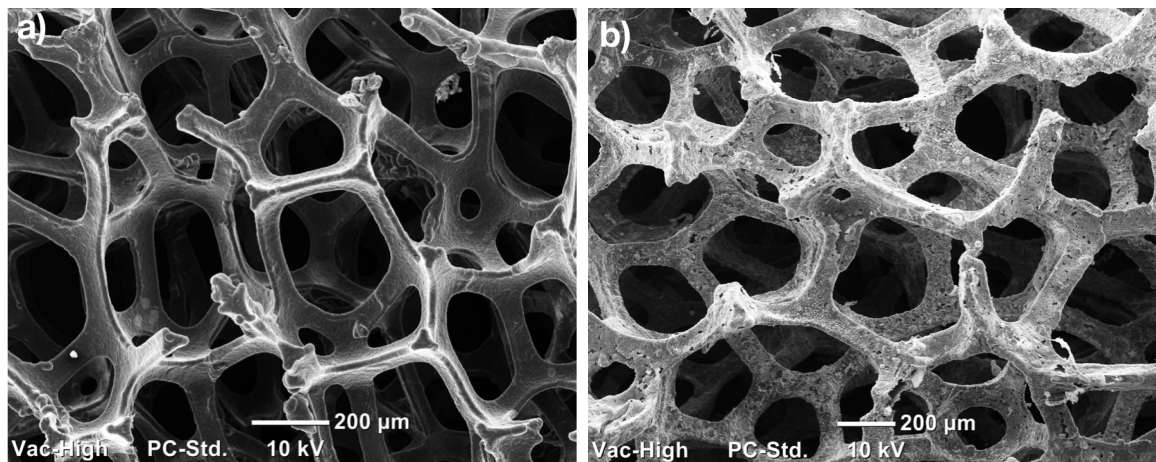


Figure 2.21.: SEM images of GF; a) before combustion and b) after combustion. The particular case shown corresponds to GF of density  $18 \text{ mg/cm}^3$  and NC-GF loading of 75%.

Fig. 2.21 shows the SEM images of the GF structure before and after combustion. As can be seen, not only the GF structure remained unburned but also the 3D interconnected network was preserved. Moreover, a TG analysis of the GF structure was also conducted in air up to 1200 K (using a heating rate of 10 °C/min) and as shown in Fig. 2.22, negligible weight loss was obtained up to 900 K. Since, the maximum NC surface temperature observed was only 613 K, the thermal stability of the GF structure obtained was expected. In addition, the reusability of the GF structure was also tested by re-depositing fuel on the GF surface after combustion. The particular case tested was with the GF of density 18 mg/cm<sup>3</sup> and NC-GF loading of 75%. Similar burn rates were obtained using the fresh (2.1 cm/s) and re-used (1.7 cm/s) GF structures, implying that the thermal properties of the GF structure are only slightly changed after the combustion process.

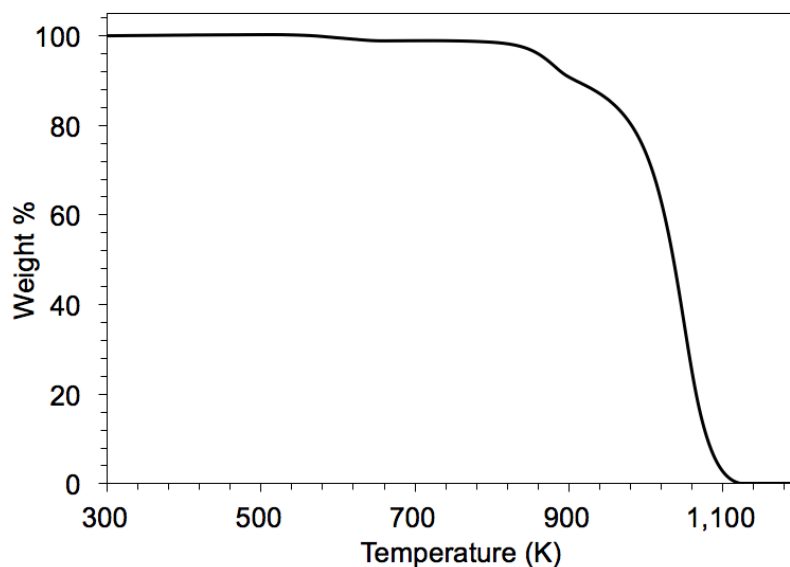


Figure 2.22.: TG analysis of GF in air.

Next, to further emphasize on the importance of the use of GF structures, a Ni foam was used to test the burn rate enhancement. The particular Ni foam investigated was the 3 mm thick template on which the GF structures were grown (section 2.1.3). Fig. 2.23 shows the SEM images of the Ni foam and similar to the GF, it exhibits a

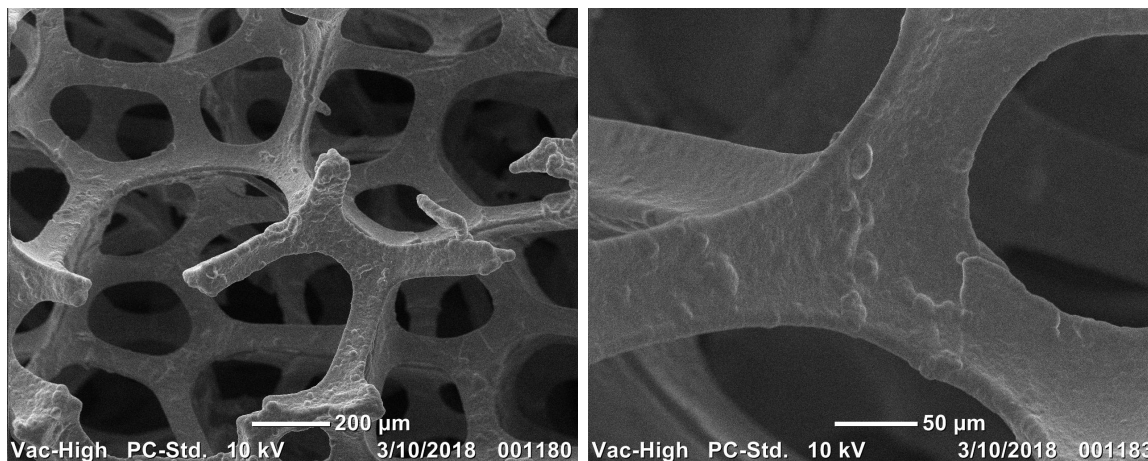


Figure 2.23.: SEM images of the Ni foam structure.

3D, interconnected, highly porous structure with the pore diameters and the width of the strut walls ranging from 50-600  $\mu\text{m}$  and 50-80  $\mu\text{m}$ , respectively. Moreover, the average porosity and density of the Ni foam was calculated to be 98% and 155  $\text{mg}/\text{cm}^3$ , respectively. To prepare the fuel samples, the NC solution was drop-casted on to the Ni surface at various amounts to get the desired NC-Ni loading. And again, after the fuel deposition, the samples were left to dry in ambient conditions for 24 hours. No burn rate enhancement was obtained up to the NC-Ni loading of 35% and at 15% NC-Ni loading, only a 14% enhancement was observed. This could be attributed to two factors. First, in contrast to the GF, the Ni foam strut walls were solid, as a result of which, much more amount of heat was being lost from the exothermic reactions to the Ni foam structures. Second, although the thermal conductivity of Ni was high ( $\sim 70 \text{ W}/\text{m}\cdot\text{K}$ ) and in fact comparable to that of the GF strut walls (102 and 271  $\text{W}/\text{m}\cdot\text{K}$  for the GF of densities 11.3  $\text{mg}/\text{cm}^3$  and 22  $\text{mg}/\text{cm}^3$ ), the bulk density of Ni was much higher (around 8900  $\text{kg}/\text{m}^3$  [129]), more than 4 times that of the graphite bulk density (2260  $\text{kg}/\text{m}^3$ ). Thus, for Ni, the thermal diffusivity value came out to be only  $1.8 \times 10^{-5} \text{ m}^2/\text{s}$ , an order of magnitude lower than that of the GF strut walls ( $1.5 \times 10^{-4} \text{ m}^2/\text{s}$ ). Since, it is the thermal diffusivity and not the thermal conductivity that controls the rate of heat transfer, as was shown using simple 1-D analysis in section 2.3.2, very low burn rate enhancements were obtained

using the Ni foam. The above reasoning can be applied to most of the metals and thus, their use as highly conductive substrates is not very effective. In conclusion, it is the unique combination of thermal and physical properties of these graphene-based micro-structures that makes them so efficient towards enhancing the burn rates of solid propellants.

## 2.4 1-D Modeling of Reaction Wave Propagation in the NC-GS System

Next, the coupled NC-GS system was analyzed in detail using 1-D energy conservation equations along with simple one-step chemistry. Three important non-dimensional parameters were identified that governed the burn rate enhancement and the oscillatory nature of the combustion waves:  $R$  - ratio of fuel to graphite thickness,  $\alpha_0$  - ratio of graphite to fuel thermal diffusivity and  $\beta$  - inverse adiabatic temperature rise.

### 2.4.1 Model Setup

Assuming that the fuel undergoes complete combustion and that the reaction rate is governed by first-order Arrhenius kinetics, the mass balance equation can be written as:

$$\rho_f \left( \frac{\partial w_f}{\partial t} \right) = -\rho_f A w_f \exp\left( \frac{-E}{R_u T_f} \right) \quad (2.11)$$

In the above equation,  $R_u$  is the universal gas constant ( $8.314 \text{ J K}^{-1} \text{ mol}^{-1}$ ),  $\rho_f$  is the fuel density,  $A$  is the Arrhenius constant,  $E$  is the fuel activation energy and  $w_f$  is the mass fraction of the unburned fuel. The fuel and the graphite energy conservation equations, assuming constant properties ( $k$ ,  $C_p$  and  $\rho$ ) and only conductive heat transfers, can be written as: [121, 122]

$$\rho_f C_p \left( \frac{\partial T_f}{\partial t} \right) = k_f \left( \frac{\partial^2 T_f}{\partial x^2} \right) - \frac{G_0}{d_f} \left( T_f - T_g \right) + \rho_f Q A w_f \exp\left( \frac{-E}{R_u T_f} \right) \quad (2.12)$$

$$\rho_g C_{p_g} \left( \frac{\partial T_g}{\partial t} \right) = k_g \left( \frac{\partial^2 T_g}{\partial x^2} \right) + \frac{G_0}{d_g} (T_f - T_g) \quad (2.13)$$

In the above equations,  $\rho_g$  is the graphite density,  $C_{p_f}$  is the fuel specific heat capacity,  $C_{p_g}$  is the graphite specific heat capacity,  $d_f$  is the fuel thickness,  $d_g$  is the graphite sheet thickness,  $k_f$  is the fuel thermal conductivity,  $k_g$  is the graphite thermal conductivity,  $Q$  is the heat of combustion and  $G_0$  is the thermal boundary conductance term that controls the amount of heat flow between the fuel and the graphite sheet and as a result, couples the two energy equations together. Table 2.6 lists the values of the parameters used in Eqns. 2.11, 2.12 and 2.13. Since, the maximum NC surface temperature was measured to be around 600 K, average values over the temperature range of 300-600 K were used. The parameters  $A$  and  $G_0$  were, however, unknown and their values were determined by fitting the 1-D results to the pure NC average burn rate and to the average burn rate obtained for the fuel thickness of 125  $\mu\text{m}$ , respectively. A  $G_0$  value of around  $10^4$  W/(m<sup>2</sup>-K) was obtained, which is on the same order of magnitude of the thermal conductance values that have been reported in literature for various graphene-based micro-structures [66, 69–75, 91]. Following Choi et al. [18], Eqns. 2.11, 2.12 and 2.13 were then non-dimensionalized to identify the important parameters that govern the nature of the solutions. The fuel temperature, graphite temperature, time and distance were non-dimensionalized as follows:

$$u_f = \left( \frac{R_u}{E} \right) T_f, \quad u_g = \left( \frac{R_u}{E} \right) T_g, \quad \tau = \left( \frac{AQR_u}{C_{p_f}E} \right) t, \quad \epsilon = x \sqrt{\frac{A\rho_f QR_u}{Ek_f}} \quad (2.14)$$

Substituting these non-dimensional variables into Eqns. 2.11, 2.12 and 2.13 results in:

$$\left( \frac{\partial w}{\partial \tau} \right) = -\beta w_f \exp\left( -1/u_f \right) \quad (2.15)$$

Table 2.6.: Fuel and graphite sheet properties at 450 K [19, 130–133]

Property	Symbol	Value
Arrhenius constant	A	$1.5 \times 10^7$ 1/s
NC specific heat capacity	$C_{p_f}$	1787 J/(kg-K)
NC density	$\rho_f$	1600 kg/m <sup>3</sup>
NC thermal conductivity	$k_f$	0.315 W/(m-K)
NC activation energy	E	158.8 kJ/mol
NC heat of combustion	Q	$3.18 \times 10^6$ J/Kg
NC layer thickness	$d_f$	25 - 170 $\mu$ m
Graphite specific heat capacity	$C_{p_g}$	975 J/(kg-K)
Graphite density	$\rho_g$	2260 kg/m <sup>3</sup>
Graphite thermal conductivity	$k_g$	1434 W/(m-K)
Graphite sheet thickness	$d_g$	20 $\mu$ m
Interface thermal conductance	$G_0$	$10^4$ W/(m <sup>2</sup> -K)

$$\left(\frac{\partial u_f}{\partial \tau}\right) = \left(\frac{\partial^2 u_f}{\partial \epsilon^2}\right) - \gamma_f (u_f - u_g) + w_f \exp\left(-1/u_f\right) \quad (2.16)$$

$$\left(\frac{\partial u_g}{\partial \tau}\right) = \alpha_0 \left(\frac{\partial^2 u_g}{\partial \epsilon^2}\right) + \gamma_g (u_f - u_g) \quad (2.17)$$

From the above equations, the four important non-dimensional parameters can be identified as:

**Inverse adiabatic temperature rise:**  $\beta = \frac{C_{p_f} E}{Q R_u}$

**Ratio of thermal diffusivity of graphite to fuel:**  $\alpha_0 = \frac{\alpha_g}{\alpha_f}$

**Interfacial heat flow lost from fuel to graphite:**  $\gamma_f = \frac{G_0 \beta}{A d_f \rho_f C_{p_f}}$

**Interfacial heat flow gained by graphite from fuel:**  $\gamma_g = \frac{G_0\beta}{Ad_g\rho_g C p_g}$

For a given value of  $G_0$  and constant properties (as was assumed in these simulations), the relative value of  $\gamma_f/\gamma_g$  only depends on the ratio of fuel to graphite sheet thickness ( $R$ ). Thus, a parametric study was performed to determine the effects of  $\beta$ ,  $\alpha_0$ , and  $R$  on the average burn rates and the oscillatory nature of the combustion waves.

The non-dimensionalized equations 2.15, 2.16 and 2.17 were then solved using the COMSOL Multiphysics Mathematics module. A finite element method was used for the spatial derivatives along with an adaptive time-stepping technique (BDF - backward differentiation formula) for the time derivatives. First, a grid and time step sensitivity study was performed to get the most efficient mesh sizes and time steps. The time step size was limited by the period of the combustion wave oscillations, which in turn was dependent on the particular value of  $\beta$ . Abrahamson [134] did a parametric study in which the time periods as a function of the  $\beta$  values were studied. For a  $\beta$  value of 5, time periods as low as 50  $\mu$ s were observed. Thus, for the present simulations, adaptive time steps ranging from 35  $\mu$ s to 100  $\mu$ s were used, which correspond to 50-140 in the non-dimensional time ( $\Delta\tau$ ). The smaller the mesh size, the better would be the accuracy of the burn rate predictions, however, the computational time would also increase. Thus, the maximum possible mesh size that would give accurate results was used. A number of simulations of varying mesh sizes ( $\Delta\epsilon$ ) were run for the pure NC case (using only Eqns. 2.15 and 2.16 with  $G_0 = 0$ ) and above a mesh size of  $\Delta\epsilon = 7$  (corresponding to  $1.95 \times 10^{-4}$  cm), the burn rate predictions started to deviate. Since, for the simulations with graphite sheets, much higher burn rates were expected (3 times as that of the pure NC burn rate), a mesh size of 5 instead of 7 was used. The absolute convergence for the non-dimensional temperatures and the mass fraction was set to  $10^{-4}$  and  $10^{-6}$ , respectively. Moreover, the total non-dimensional simulation time was set to 2,150,000 (1.5 s), whereas, the

total non-dimensional domain length was set to 54,000 (1.5 cm).

The initial and boundary conditions used were as follows:

At  $\tau = 0$ :

$$u_g = 0.0157 \text{ (300 K) for all } \epsilon$$

$$u_f = 0.0157 + 0.3 \cdot \exp(-10^{-5} \epsilon^2)$$

$$w_f = 1 - \exp(-10^{-5} \epsilon^2)$$

At  $\tau > 0$ :

Adiabatic boundaries (no heat losses)

### 2.4.2 1-D Results

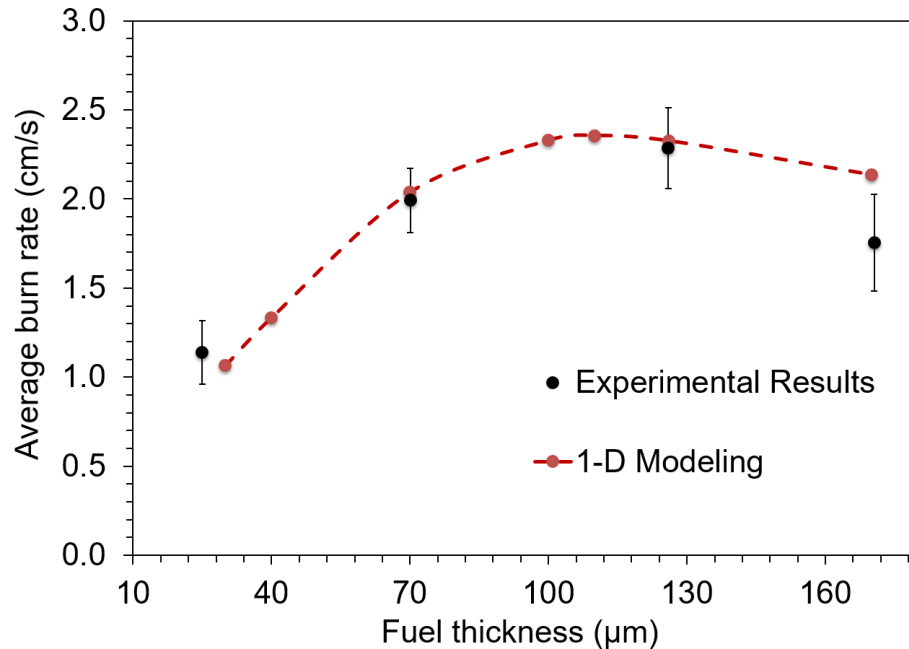


Figure 2.24.: The measured and predicted average burn rates as a function of the fuel thickness.  $\beta = 10.7$ ,  $\alpha_0 = 5900$ .

Fig. 2.24 shows the measured and predicted average burn rates as a function of the fuel thickness. For the 1-D modeling, the burn rates were calculated by tracking the point along the length of a sample at which the mass fraction of the unburned fuel ( $w_f$ ) was 0.5. The agreement between the 1-D calculations and the experimental data

was good for thin-layered depositions ( $< 125 \mu\text{m}$ ). The calculated optimum thickness was around  $110 \mu\text{m}$ , which agreed well with the experimentally obtained optimum thickness of  $125 \mu\text{m}$ . However, for the fuel thickness of  $170 \mu\text{m}$ , significant deviation from the experimental result was observed. Such a deviation could be attributed to the deposition method used, as is explained next. The graphite sheets have a unique arrangement of carbon atoms, very different from the crystalline arrangement found in metals. They are composed of a periodical stack of 2-D graphene layers where each of these layers are weakly bonded to the neighboring layers via the inter-molecular van der Waals forces. Thus, these graphene layers can easily slide against each other and can even be peeled off. In contrast, NC is a strong adhesive and as a result, strongly bonds to the graphene layers on the top of the graphite sheet. The strength of this bond was found to be dependent on thickness of the NC layer deposited. For thin depositions ( $< 125 \mu\text{m}$ ), the strength of this bond was not strong enough to peel the top graphene layers off, during the evaporation process. However, for the thicker deposition ( $170 \mu\text{m}$ ), in some cases after the evaporation process, tiny air gaps were detected between the top graphene layers and the rest of the graphite sheet. In fact, in a few cases, the top graphene layers were completely peeled off (these samples were then discarded). Thus, this weak contact of the deposited NC layer with the bulk of the graphite sheet resulted in an increase in the thermal boundary resistance value, which in turn decreased the net thermal transport in the reaction propagation direction. Since, in the 1-D modeling a constant thermal boundary resistance value was assumed, much higher burn rates were predicted for the thicker fuel deposition ( $170 \mu\text{m}$ ) as compared to that obtained during the experiments.

Fig. 2.25 shows the predicted burn rate profiles as a function of the distance traveled along the length of a sample for various values of  $R$  (fuel to graphite thickness). The values of  $\beta$  and  $\alpha_0$  were kept fixed at 10.7 and 5900, respectively, corresponding to NC and graphite sheet. As can be seen, similar to the experimental results, the peak and period of the oscillations were found to be dependent on the particular value

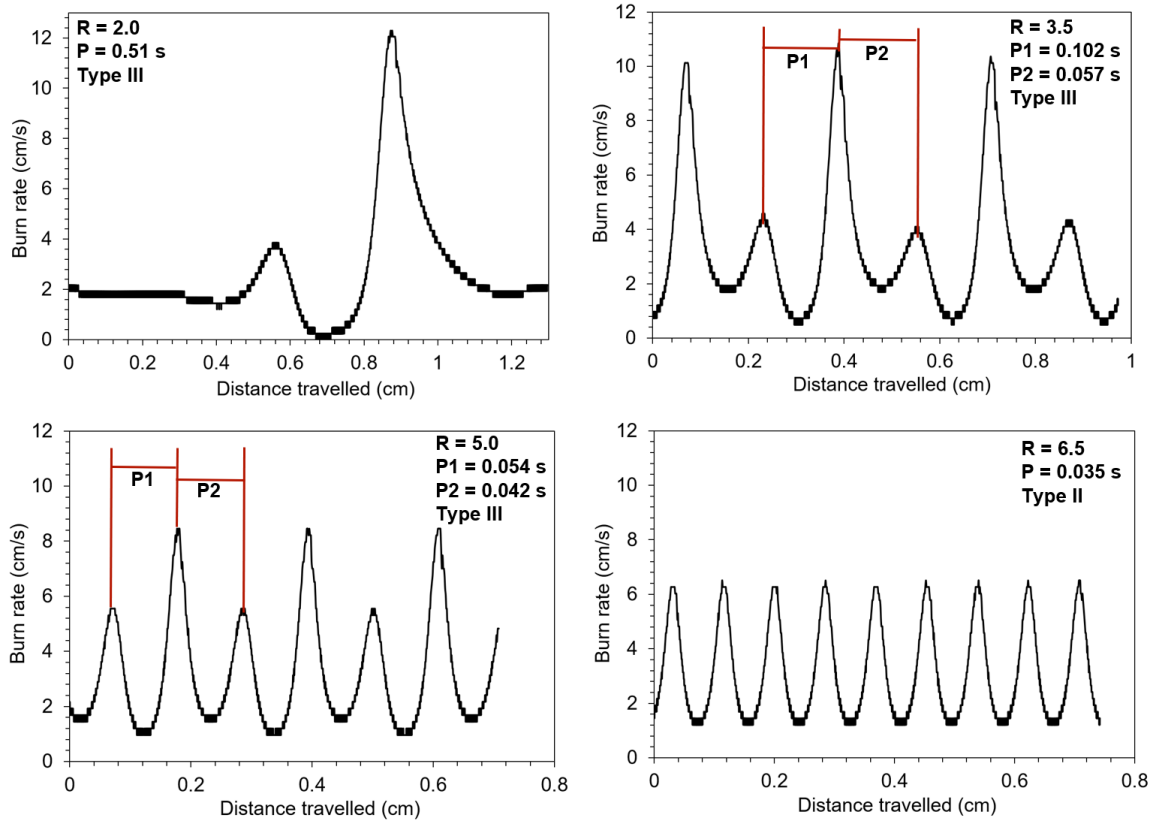


Figure 2.25.: Effect of  $R$  (fuel to graphite thickness) on the amplitude and period of the combustion waves.  $\beta = 10.7$ ,  $\alpha_0 = 5900$ .

of  $R$ . For  $R = 2.0$ , a type III combustion wave was obtained with peaks of varying amplitude and an average oscillation period of 0.51 s. As the value of  $R$  was increased to 3.5, and 5.0, again type III combustion waves were obtained but with much lower oscillation periods: 0.057 s, 0.102 s and 0.042 s, 0.054 s, respectively. However, above  $R = 5.0$ , the two peak magnitudes and the oscillation period values approached each other and at  $R = 6.5$ , a type II combustion wave was obtained with an oscillation period of 0.035 s. The oscillation periods obtained from the 1-D calculations agreed well with the experimental oscillation periods in terms of the order of magnitude and the decreasing trend observed. For example, for  $R = 1.25$ , 3.5 and 6.5, experimental oscillation periods on the order of 0.1 s, 0.05 s and 0.03 s were obtained, respectively.

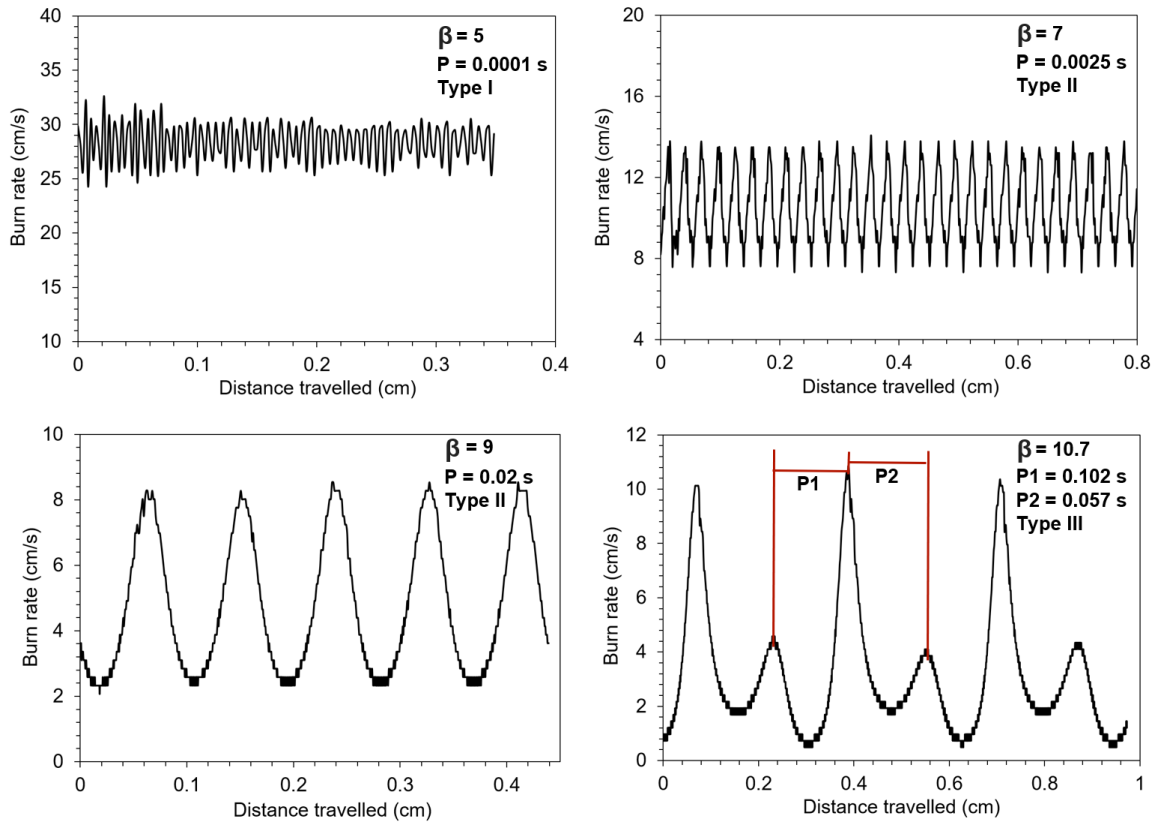


Figure 2.26.: Effect of  $\beta$  on the amplitude and period of the combustion waves.  $R = 3.5$ ,  $\alpha_0 = 5900$ .

Fig. 2.26 shows the effect of  $\beta$  on the period and amplitude of the combustion waves obtained. The value of  $\alpha_0$  was kept fixed at 5900 and the  $R$  value was set to 3.5 (corresponding to the fuel thickness of  $70 \mu\text{m}$ ). With an increase in the value of  $\beta$ , an increase was observed both in the amplitude and period of the oscillations but the average burn rate values were found to decrease. Since,  $\beta$  is proportional to  $E/Q$ , an increase in  $\beta$  value implies either a decrease in the heat of combustion or an increase in the fuel's activation energy, both of which decrease the adiabatic flame temperature and thus, reduce the average burn rates obtained. For  $\beta = 5$ , negligible oscillations were observed and a type I combustion wave was obtained. As the  $\beta$  value was increased, a transition from type I to type II combustion wave was found to occur and at  $\beta = 9$ , sinusoidal oscillations were observed. Further increase in  $\beta$  resulted in a type III combustion wave.

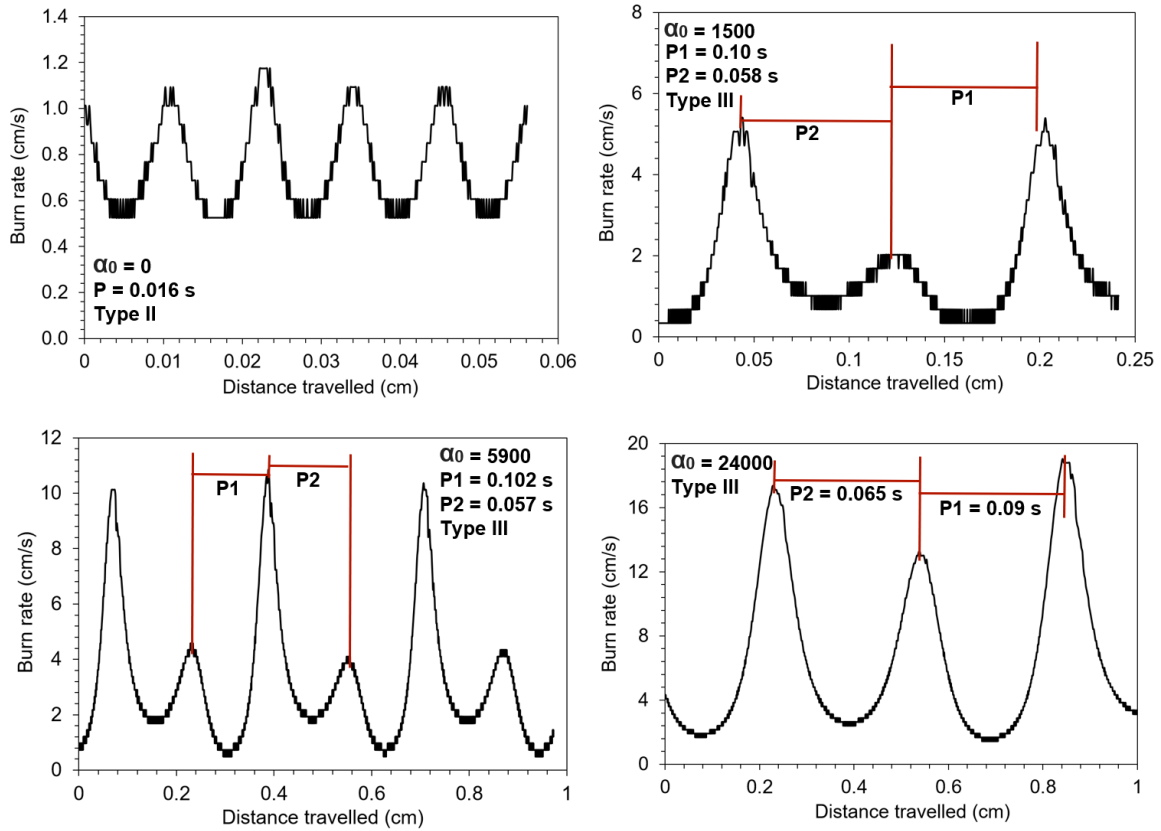


Figure 2.27.: Effect of  $\alpha_0$  on the amplitude and period of the combustion waves.  $R = 3.5$ ,  $\beta = 10.7$ .

The effect of  $\alpha_0$  on the period and amplitude of the combustion waves is shown in Fig. 2.27. The values of  $\beta$  and  $R$  were kept fixed at 10.7 and 3.5, respectively. An increase in the value of  $\alpha_0$  implies an increase in the thermal conduction along the reaction propagation direction, which in turn enhances the burn rates. For  $\alpha_0 = 0$ , corresponding to pure NC, a type II combustion wave was observed with an average burn rate of 0.7 cm/s and an oscillation period of 0.016 s, as expected. As the  $\alpha_0$  value was increased, a type III combustion was obtained. Although, the amplitude of the oscillations were found to vary significantly with  $\alpha_0$ , only a slight change was observed in the period of the oscillations. For example, for  $\alpha_0 = 0$  and 24,000, oscillation periods on the same order of magnitude: 0.016 s and 0.0775 s (averaged),

respectively, were obtained. This is in contrast to the effect of  $\beta$ , where the oscillation period was found to increase by  $10^3$  times, as the  $\beta$  value was increased from 5 to 10.7. Thus, the period of the oscillation can be regarded as a property of the fuel, depending mostly on  $\beta$  and only slightly on  $\alpha_0$ .

The oscillation behavior observed in the experiments and the 1-D modeling can be explained using the excess enthalpy concept, which was first proposed by Shkadinskii et al. [135] for solid propellant combustion. Here the effect of adding a thermally conductive base on the excess enthalpy was considered. The total amount of excess enthalpy available per unit area at a given time can be calculated as follows [135]:

$$\begin{aligned}
 E_H &= \int_0^L \rho_f \left( h_1(T)w_f + h_2(T)(1 - w_f) - h_1(T_a) \right) dx \\
 &= \int_0^L \rho_f \left( Cp_f(T - T_a) - Q(1 - w_f) \right) dx \quad (2.18)
 \end{aligned}$$

In the above equation,  $h_1$  and  $h_2$  are the specific enthalpies of the unreacted fuel and combustion products, respectively,  $T_a$  is the ambient temperature (300 K), and  $L$  is the total length of the sample. As can be seen from Fig. 2.28, for both the cases, the curves corresponding to  $\frac{\partial w_f}{\partial t}$  and  $(1 - w_f)$  were much narrower as compared to the heated layer  $\left(\frac{Cp_f(T_f - T_a)}{Q}\right)$  and as a result, a significant amount of excess enthalpy was available. Moreover, the total amount of excess enthalpy available for the NC-GS system was observed to be much greater as compared to that available for pure NC. This could be attributed to the thermal coupling between the fuel and the graphite sheet, because of which, the net thermal conductivity (thermal transport) in the reaction propagation direction was enhanced and as a result, a much wider heated layer was obtained. In addition, the reaction zone, as represented by  $\frac{\partial w_f}{\partial t}$ , was also observed to be much wider for the NC-GS system as compared to pure NC.

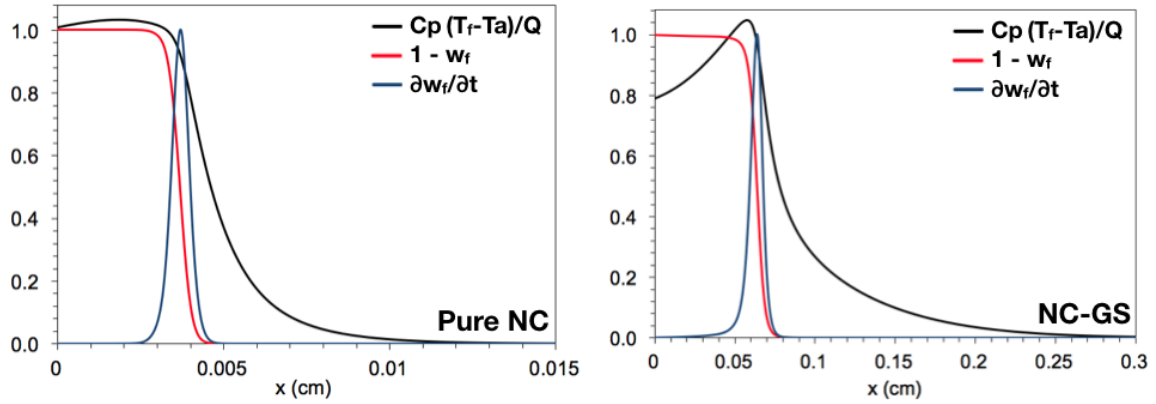


Figure 2.28.: Structure of the combustion front: non-dimensional reaction temperature (black), reaction rate (blue) and extent of the reaction (red line). The particular NC-GS system shown corresponds to the fuel thickness of  $70 \mu\text{m}$  ( $R = 3.5$ ).

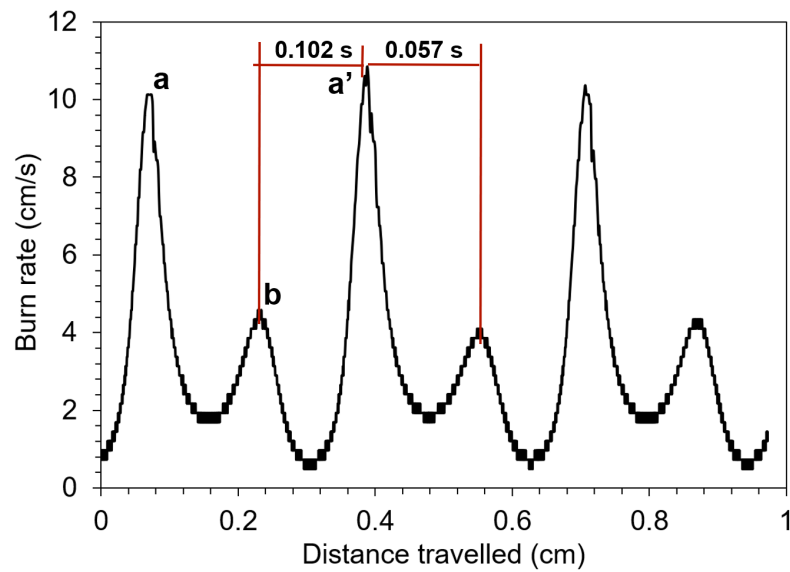


Figure 2.29.: Predicted burn rate profile for  $R = 3.5$ ,  $\beta = 10.7$  and  $\alpha = 5900$ .

In a solid (premixed) combustion, the thickness of the heated layer is proportional to  $k_{eff}/(Cp_f b)$  [135], where  $b$  is the instantaneous burn rate,  $Cp_f$  is the specific heat capacity of the fuel and  $k_{eff}$  is the effective thermal conductivity of the coupled system. Thus, for a given system, during the reaction propagation, when the burn rates are low (corresponding to the lowest burn rates in Fig. 2.29), a significant

amount of excess enthalpy is available, which then heats the unburned portions of the fuel. Due to the heat flow from the reaction zone to the unburned fuel, a decrease in the reaction temperature is observed, which in turn further lowers the burn rates. This loss in heat is somewhat compensated by the heat flow from the hot combustion products and as a result, a plateaued behavior in the burn rate is obtained. The heating continues until the temperature of the unburned fuel reaches a point at which a rapid ignition of the fuel occurs and a significant enhancement in the burn rate is observed and thus, the reason for the appearance of the first ignition peak in the burn rate profiles. The reaction temperature is also increased and even exceeds the average adiabatic flame temperature. This rise in temperature, however, is halted due to the heat flow from the reaction zone to both the combustion products and the unburned fuel, because of which, a decreasing trend in the burn rate is observed thereafter. And again, the burn rates remain low until the temperature of the unburned fuel reaches a point at which another rapid ignition occurs, thus giving rise to the second ignition peak. As can be seen from Fig. 2.29, the oscillation period (0.057 s) between the first ignition peak (marked by a) and the second ignition peak (marked by b) is less than the oscillation period (0.102 s) between the second ignition peak (marked by b) and the first ignition peak of the next cycle (marked by a'). Thus, after the onset of the first ignition, the fuel is heated for a lesser amount of time as compared to that after the second ignition, which then results in the magnitude of the second ignition peak to be less than that of the first peak. The second ignition marks the end of one cycle after which the pattern is repeated giving rise to multiple peaks. The strength and number of peaks obtained in one cycle depends on the total heat reserve available when the first ignition occurred and greater the heat reserve or the local excess enthalpy available initially, greater will be the magnitude and number of peaks observed, which is consistent with the conclusions of Shkadinskii et al. [135].

## 2.5 MD Simulation of the Coupled PETN-MWCNT System

This section describes the molecular dynamics simulations that were performed to analyze the coupled PETN-MWCNT system. Both reactive and non-reactive simulations were conducted to understand the coupling between the chemical and physical processes occurring during the reaction wave propagation. Moreover, the simulations were performed using LAMMPS (Large-scale Atomic/Molecular Massively Parallel Simulator) [136], an open source MD simulation code developed by Sandia National Labs.

### 2.5.1 Computational Method

For the solid propellant, PETN ( $C_5H_8N_4O_{12}$ ) was selected because of its high enthalpy of combustion and wide use as a powerful secondary explosive material. Moreover, a number of experiments and simulations on pure PETN have been performed [117–119], thus providing a base case check for the MD simulations. In addition, for all the simulations, a high initial pressure of 3 GPa was used. This was done to increase the average burn rate values so that the simulation run times could be reduced. For the conductive substrate, MWCNTs were selected because of their high axial thermal conductivity and 1-D nature in the reaction wave propagation, thus, further reducing the computational cost.

### Interaction Potential

The interactions between the atoms were calculated using the first-principles derived reactive force field, ReaxFF, which includes both the physical changes such as thermal transport and the chemical changes such as bond breaking and forming [137]. The particular ReaxFF force field used in this study was developed by Budzien et al. [138] for PETN using DFT (density function theory) calculations and was implemented within LAMMPS using the USER-REAXC module [139]. To identify the species

produced during the combustion process, minimum bond order values as listed by Budzien et al. [138] were used. A Pair of atoms that had the bond order value greater than the threshold bond order value, as given in Table 2.7, was considered to be bonded.

Table 2.7.: Minimum bond order values (PETN-MWCNT system)

Atom type	Atom type	Bond order
C	C	0.55
C	H	0.40
C	N	0.30
C	O	0.65
H	H	0.55
H	N	0.55
H	O	0.45
N	N	0.55
N	O	0.40
O	O	0.65

The temperature of the system or a group of molecules was calculated using the average kinetic energy of the atoms, as given by the following equation:

$$T = \sum_{i=1}^N \frac{m_i v_i^2}{3NK_B} \quad (2.19)$$

In the above equation, N is the total number of atoms in a group,  $m_i$  and  $v_i$  are the mass and velocity of the  $i^{th}$  atom, respectively, and  $K_B$  is the Boltzmann constant.

The pressure of the system was calculated using the following equation:

$$P = \frac{NK_B T}{V} + \left( \sum_{i=1}^N \vec{r}_i \cdot \vec{F}_i \right) / dV \quad (2.20)$$

The first term on the right hand side is the kinetic energy term while the second term is the virial tensor,  $\vec{r}_i$  is the radius-vector of the  $i^{th}$  atom,  $\vec{F}_i$  is the force acting on the  $i^{th}$  atom,  $V$  is the volume of the simulation domain, and  $d$  is the dimension of the system. This pressure formulation has been shown to be valid for any arbitrary interaction potential with periodic boundary conditions [140]. Moreover, since the simulations were performed at very high pressures of 3 GPa, the second virial term dominates and has a much bigger contribution as compared to the kinetic energy term.

### Simulation Domain

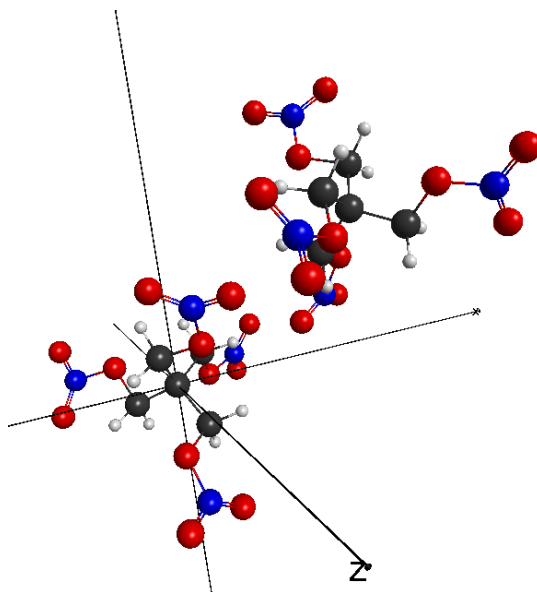


Figure 2.30.: Unit cell of a PETN crystal.

The unit cell of a PETN crystal (space group:  $P\bar{4}2_1c(D_{2d}^4)$ ) has a tetragonal lattice ( $9.2759 \text{ \AA} \times 9.2759 \text{ \AA} \times 6.6127 \text{ \AA}$ ) and contains 2 PETN molecules [141], as shown in Fig. 2.30. The center of one of the molecules is at the center of the unit cell, whereas the center of the other molecules are at the vertices. The PETN unit cell was then repeated in the x, y and z directions giving the final simulation domain, as shown in Fig. 2.31. The pure PETN case consisted of 1075 unit cells ( $43 \times 5 \times 5$ ),

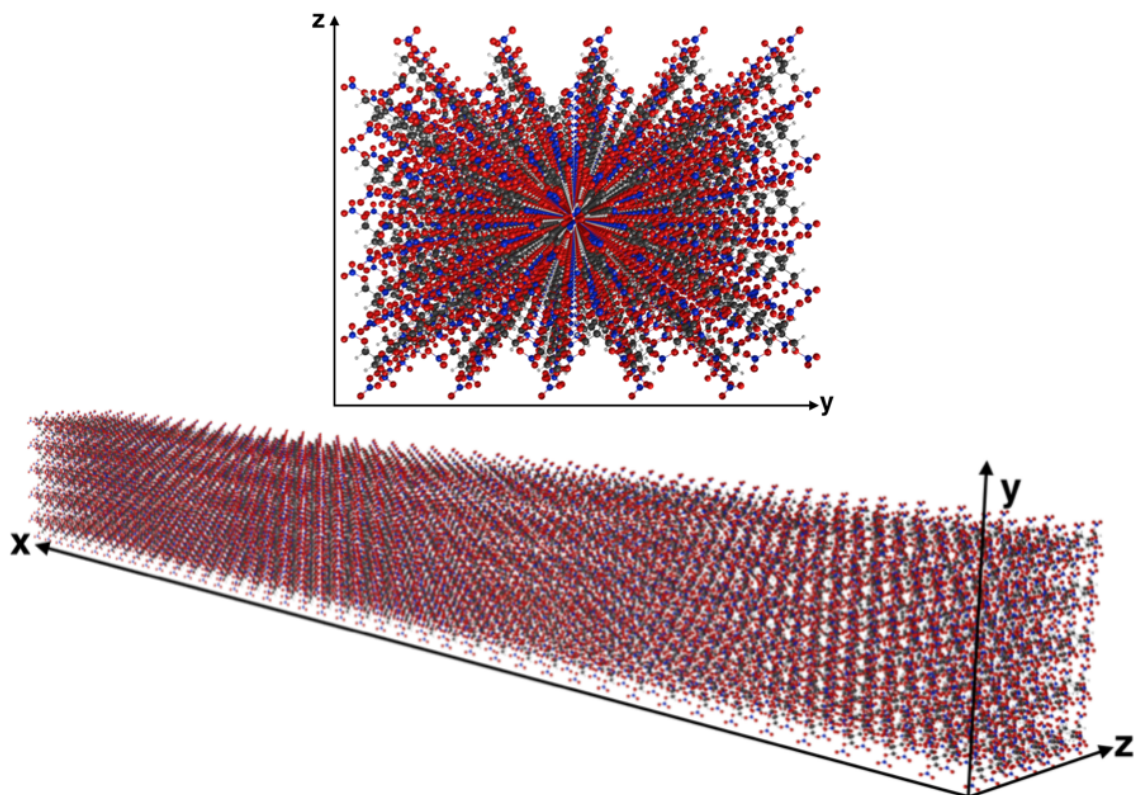


Figure 2.31.: Pure PETN simulation domain.

corresponding to 2,150 PETN molecules and a simulation domain length of 40 nm. The PETN crystal orientation can also have a major effect on the combustion and detonation properties observed [142, 143]. Sergeev et al. [117] studied the reaction wave propagation in a PETN crystal as function of its orientation and for the  $[1\ 0\ 0]$  orientation, burn rates 2 times faster were observed as compared to that observed for the  $[0\ 0\ 1]$  orientation. Thus, in this work, the reaction wave propagation was carried out along the  $[1,0,0]$  direction.

Kim et al. [144] investigated the propagation of heat pulses in zigzag and armchair double wall carbon nanotubes (DWCNTs) using molecular dynamics simulations and found the heat energy carried by the leading heat wave packets in zigzag DWCNTs

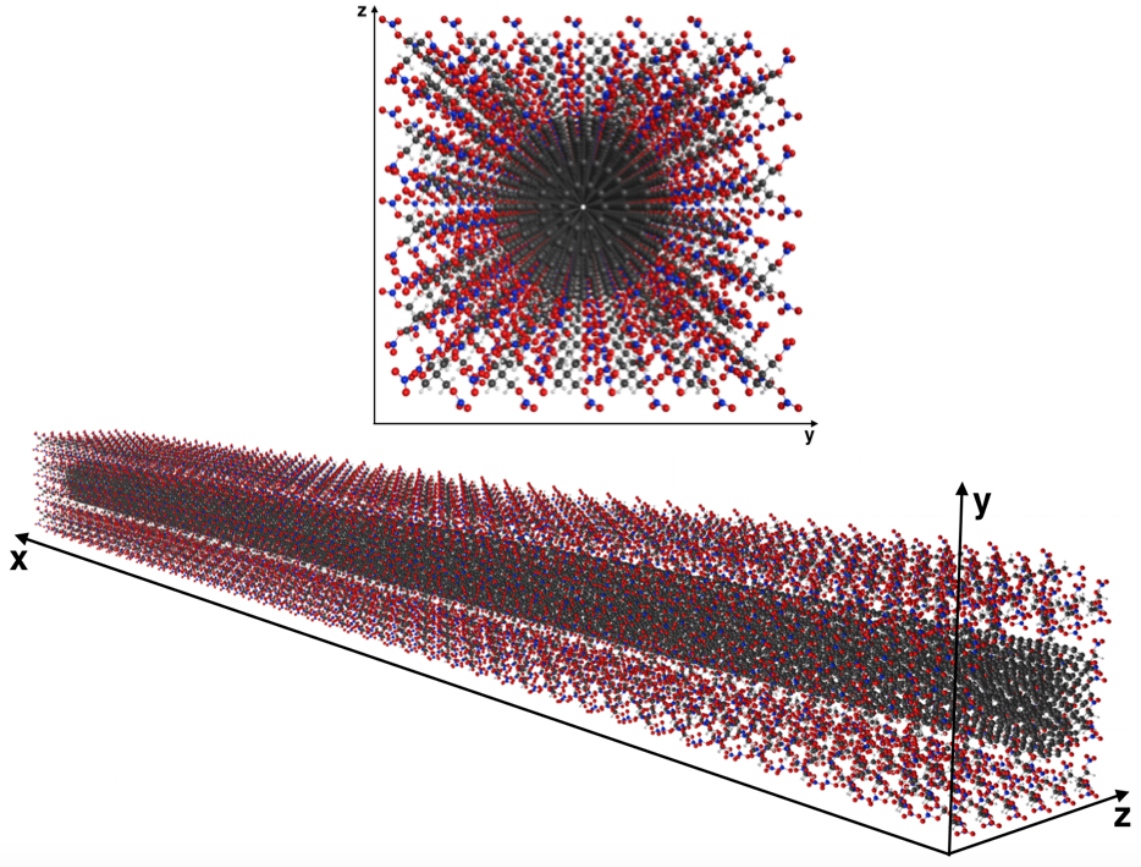


Figure 2.32.: PETN-MWCNT simulation domain. The particular case shown corresponds to the PETN-MWCNT loading of 65%.

to be four times larger as compared to that obtained in armchair DWCNTs. Thus, in this study, achiral zigzag type of MWCNTs were used as they are expected to have the highest axial thermal conductivities. For the PETN-MWCNT system, a cylinder was cut out from the center of the pure PETN simulation domain along the  $[1,0,0]$  direction and MWCNTs were then inserted into the hollow space. To get the desired PETN-MWCNT loading ratio (defined as the mass of PETN per total mass of PETN + MWCNT), both the thickness of the PETN layer and the MWCNTs outer diameter were varied. The thickness of the PETN layer was varied from 6.6 Å to 13.5 Å, whereas the MWCNTs outer diameter was varied from 16 Å (20,0) to 27 Å (35,0) with the MWCNTs inner diameter and the inter tube-to-tube distances

being kept fixed at  $3.914 \text{ \AA}$  (5,0) and  $1.957 \text{ \AA}$ , respectively. The values of PETN layer thickness, MWCNTs diameters and tube-to-tube distances, however, changed slightly after performing the pressure and temperature equilibration. For all the simulations conducted, the length of the PETN-MWCNT system was kept fixed at 40 nm to be consistent with the pure PETN case. Fig. 2.32 shows the simulation domain of a typical PETN-MWCNT system. The particular case shown corresponds to the PETN-MWCNT loading of 65%.

### Simulation Parameters

After the initial set-up of the simulation domain, as shown in Figs. 2.31 and 2.32, temperature equilibration under the NVT (constant number of particles (N), temperature (T), and volume (V)) conditions to 300 K using the Nose-Hoover thermostat [145,146] was performed. The NVT equilibration was run for 70 ps with the time step and the relaxation time being 0.1 fs and 100 fs, respectively. After the NVT equilibration, the system was equilibrated to the desired pressure of 3 GPa under the NPT (constant number of particles (N), temperature (T), and pressure (P)) conditions. The relaxation time for the Nose-Hoover thermostat and barostat [147] was set to 100 fs with the time step again being 0.1 fs. Only the y and z dimensions of the simulation box were altered under the NPT equilibration, while the x dimension was held constant. The NPT equilibration was run for 50 ps. The final MWCNTs diameters and PETN layer thicknesses for the 6 different cases that were run, corresponding to different PETN-MWCNT loadings, are listed in Table 2.8. After the NPT equilibration, the NVE ensemble was used to simulate the combustion process. Periodic boundary conditions were employed in all the three directions and a time step of 0.1 fs was used. This time step of 0.1 fs provided sufficient energy conservation under the NVE conditions involving chemical reactions. To simulate an ignition source, the temperature of the PETN molecules in the middle of the simulation domain being 5-unit cells thick in the x-direction was set to 4000 K, for both PETN-MWCNT sys-

tems and pure PETN, while the temperature of the rest of the molecules remained at 300 K. The ignition temperature was based on the minimum energy value needed for the reaction wave propagation to occur. Since the minimum ignition temperature was found to increase for the PETN molecules when coupled to CNTs, the minimum ignition temperature corresponding to that of the PETN-MWCNT system was used for all the cases simulated, in order to have the same ignition energy input.

Table 2.8.: MD simulation matrix (PETN-MWCNT system)

Case No.	System type	PETN-MWCNT loading (%)	No. of CNTs	Final PETN thickness	Final MWCNTs outer diameter
1	Pure PETN	0	-	-	-
2	PETN-MWCNT	76	4	11.35 Å	18 Å
3	PETN-MWCNT	65	4	8.8 Å	18 Å
4	PETN-MWCNT	50	4	5 Å	18 Å
5	PETN-MWCNT	43	6	5.55 Å	26 Å
6	PETN-MWCNT	36	7	5 Å	31 Å

### 2.5.2 Reaction Wave Propagation in Pure PETN

Fig. 2.33 shows the propagation of a combustion wave in a pure PETN sample. The reaction fronts in the figure can be identified by the increased disturbance of the atoms and are marked with red lines. Fig. 2.34 shows the spatial temperature profiles along the x-direction at different times during the PETN combustion. The reaction wave propagates from the ignition zone in the middle towards the two ends. The ignition zone, as defined above, was set to 5-unit cell thick in the x-direction, which corresponds to approximately 4.7 nm. Two different criteria were used to calculate the burn rates. The first criterion was based on the location of the peak  $\text{NO}_2$  concentration. During the PETN decomposition,  $\text{NO}_2$  is the first intermediate product formed due to the dissociation of the O- $\text{NO}_2$  bond [148] and thus, the location of the

reaction zone could be easily identified from the  $\text{NO}_2$  formation. For this criterion, the simulation domain was divided into 15 slabs in the x-direction with each slab being 2.7 nm or 3-unit cell thick. For the second criterion, the burn rates were calculated by tracking the temperature changes along the PETN sample. Locations of three different temperatures (1000, 1500 and 2000 K, respectively) along the x-direction as a function of time were used. However, for this criterion, the simulation domain was divided into slabs being 1-unit cell thick (1 nm) in the x-direction.

Fig. 2.35a plots the location of different temperatures as a function of time. As can be seen, the three temperature curves obtained were nearly parallel to each other, indicating that the shape of the reaction front was preserved during the reaction wave propagation. Moreover, using the slopes of the temperature curves, an average burn

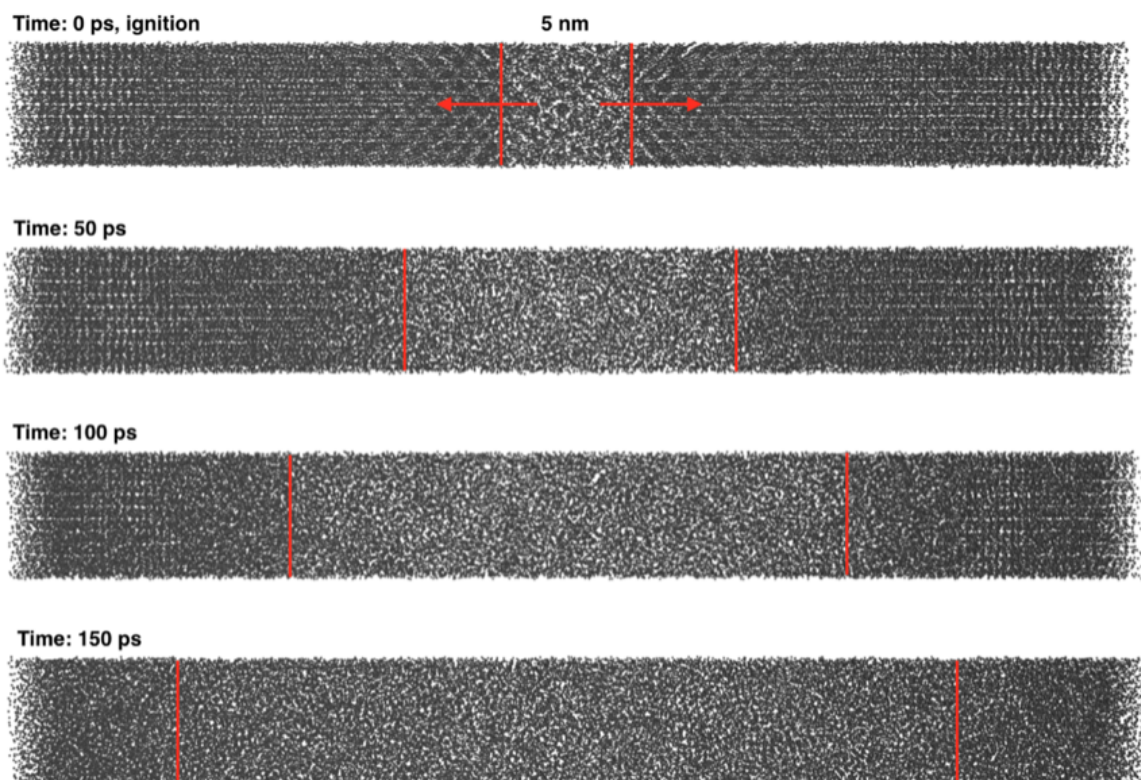


Figure 2.33.: Reaction wave propagation in a pure PETN sample. The reaction fronts are marked with red lines.

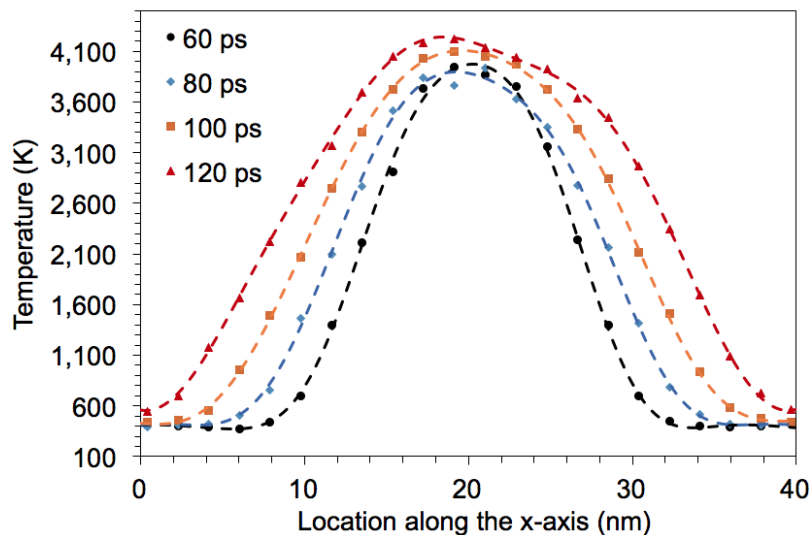


Figure 2.34.: Spatial temperature profiles along the x-direction at different times during the PETN combustion.

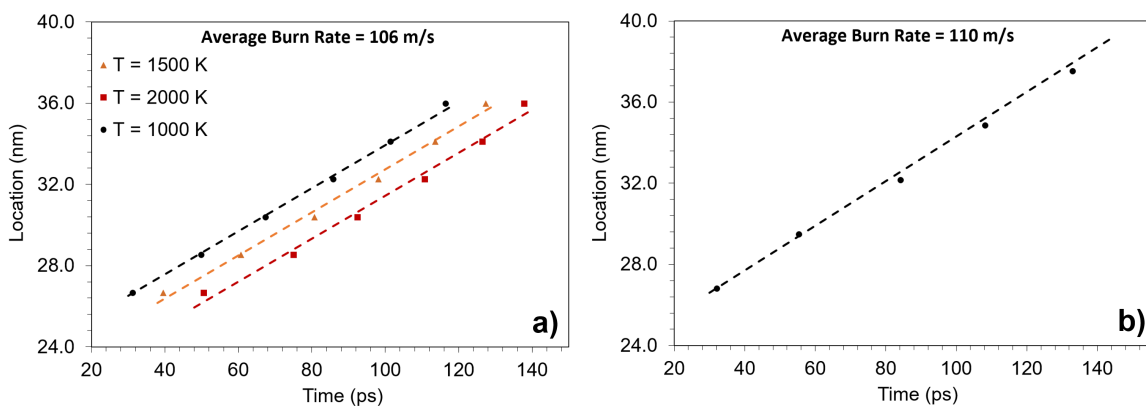


Figure 2.35.: Pure PETN. Location of a) different temperatures and b) peak  $\text{NO}_2$  concentration as a function of time.

rate of  $106 \pm 10$  m/s was obtained. Fig. 2.35b shows the location of the peak  $\text{NO}_2$  concentration as a function of time. Linear fitting of the data gave an average burn rate of  $110 \pm 5$  m/s, similar to the burn rates obtained using the temperature criterion, thus, confirming that  $\text{NO}_2$  was indeed one of the key intermediates produced in the reaction zone. The computed burn rate of pure PETN (using the  $\text{NO}_2$  criterion) was also compared to the experimental data of Andreev [118] and Foltz [119] along

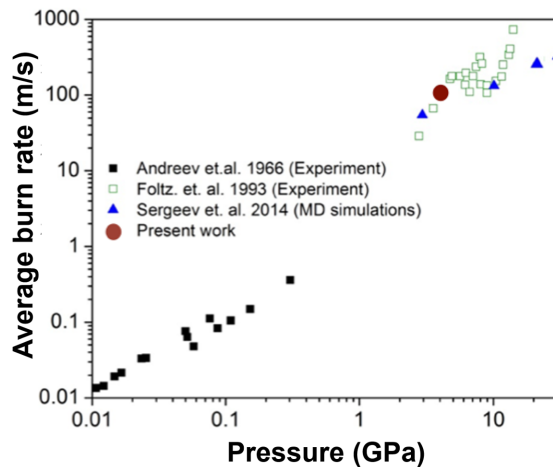


Figure 2.36.: Pure PETN burn rate comparison check.

with the simulated values of Sergeev et al. [117] and as can be seen from Fig. 2.36, good agreement was obtained.

Fig. 2.37 shows the species distribution as a function of time during the PETN decomposition. In the figure,  $X_M$  represents the number of molecules of a species per initial PETN molecules (150) in a given slab (3-unit cell thick) located at  $X = 4$  nm. As can be seen,  $\text{NO}_2$  was the dominant initial product formed i.e. the O- $\text{NO}_2$  bond was the weakest and thus, was broken first during the PETN decomposition. After  $\text{NO}_2$ , HONO, NO and OH were the other major intermediate products formed.  $\text{H}_2\text{O}$  formation began only after the appearance of OH and NO and then later in the post-reaction zone, CO and  $\text{CO}_2$  were formed. The reaction pathway revealed from the present MD simulation was consistent with that given by Sergeev et al. [117], except for two observations: (1) the peak NO concentration was much greater than the peak  $\text{NO}_2$  concentration and that (2) the  $\text{CO}_2$  and CO concentrations were a lot closer to each other. These observations could be attributed to the different minimum bond order values used, which could redistribute the identification of molecules between  $\text{NO}_2$  and NO, and  $\text{CO}_2$  and CO. For example, Sergeev et al. [117] used a minimum bond order value of 0.5 between a pair of O and O atoms, comparing this to the present study where a minimum bond order value of 0.65 was used. Thus, a molecule

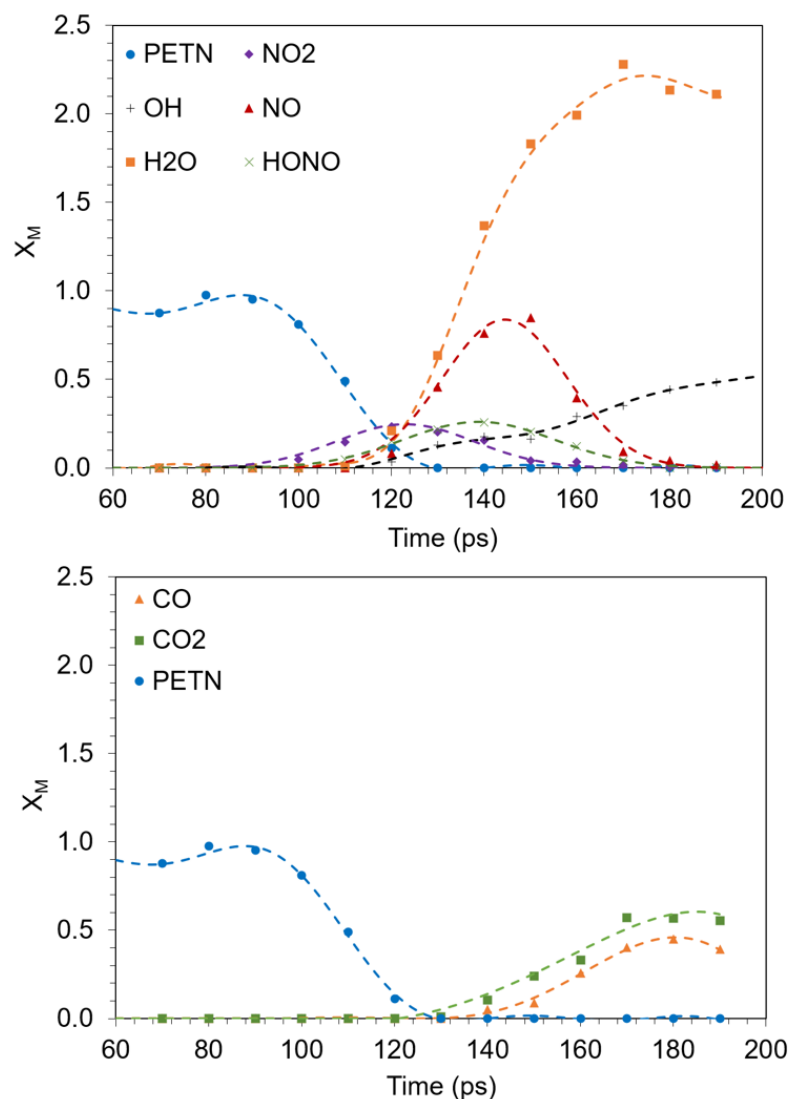


Figure 2.37.: Pure PETN. Species distribution as a function of time during the pure PETN decomposition for a slab located at  $X = 4$  nm.

identified as NO or CO in the present study could have been identified as NO<sub>2</sub> or CO<sub>2</sub> in work performed by Sergeev et al. [117].

### 2.5.3 Reaction Wave Propagation in PETN-MWCNT

Fig. 2.38 shows the propagation of a combustion wave in a PETN-MWCNT system (case 3: 65% PETN-MWCNT loading). As can be seen, the CNTs remained intact

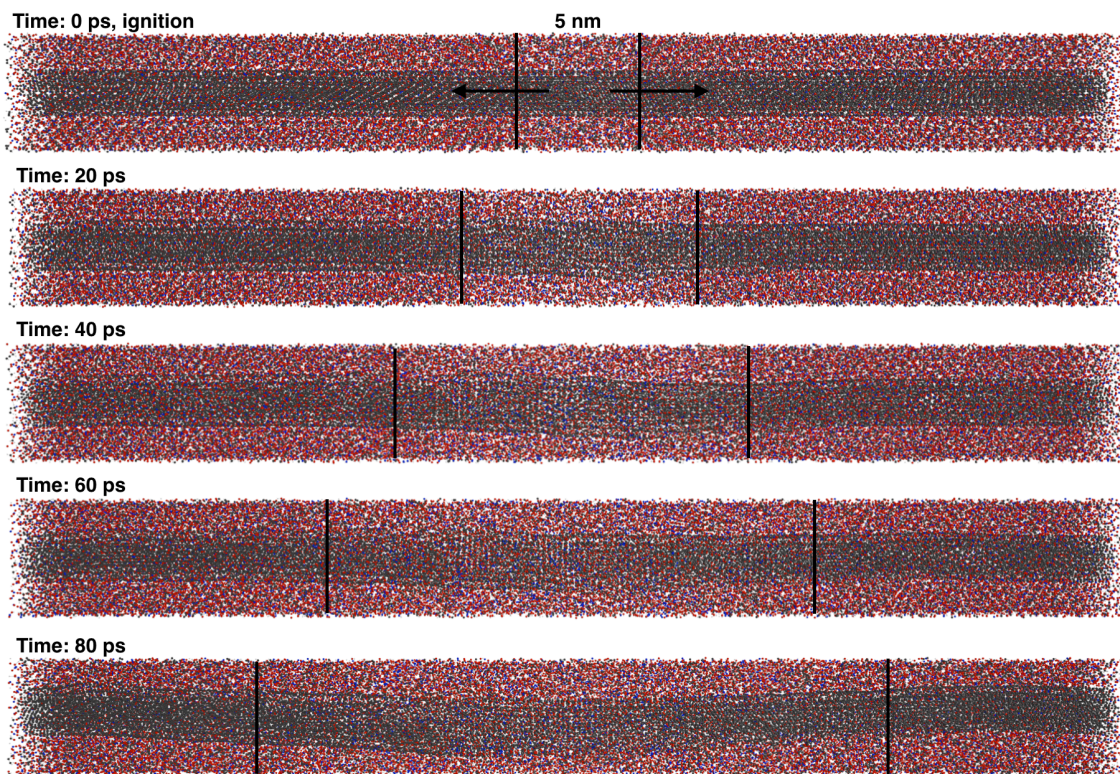


Figure 2.38.: Reaction wave propagation in a PETN-MWCNT system (case 3: 65% PETN-MWCNT loading). The reaction fronts are marked with black lines.

during the combustion process, although their structure in the burned zone was modified from the twisting and bending.

Fig. 2.39 compares the spatial temperature profile of a coupled PETN-MWCNT system (case 4: 50% PETN-MWCNT loading) with that of the pure PETN, at a certain time after ignition. In both the cases, only the temperatures of the PETN molecules are shown. As can be seen, the maximum temperature observed in the PETN-MWCNT system was much lower as compared to that observed in the pure PETN case. This could be attributed to the fact that some of the energy released during the exothermic reactions was used in heating the MWCNTs, which acted as heat sinks and thus, reduced the maximum temperature that could be obtained. Moreover, as can be seen from Fig. 2.39, the PETN-MWCNT system has a much wider reaction

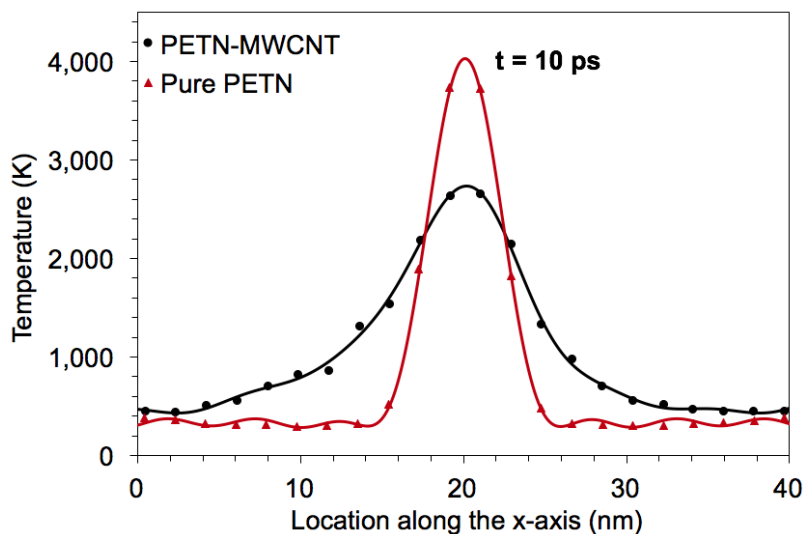


Figure 2.39.: Comparing spatial temperature profiles of PETN-MWCNT (case 4: 50% PETN-MWCNT loading) and pure PETN.

and a pre-heat zone. At  $t = 10$  ps, for the PETN-MWCNT system, the temperature of the PETN molecules near the reaction zone has increased to 700 K, which is in contrast to the pure PETN case, where the temperature near the reaction zone remained at 300 K. This could be attributed to the thermal coupling of the PETN molecules with that of the MWCNTs due to which, the thermal transport along the reaction propagation direction was enhanced and as a result, a greater portion of the PETN molecules in front of the reaction zone was heated. A similar observation was also made during the 1-D modeling of the coupled NC-GS system (section 2.4.2), where the coupled NC-GS system was observed to have a much wider reaction and a pre-heat zone as compared to pure NC.

Similar to the pure PETN case, the burn rates were calculated using two different criteria i.e. the peak  $\text{NO}_2$  concentration and different temperatures in the reaction zone. The thickness of the slabs that were used to determine the peak  $\text{NO}_2$  concentration and different temperatures were also kept same i.e. 3-unit cell and 1-unit cell thick, respectively. Fig. 2.40a plots the location of the reaction zone at two different temperatures as a function of time. As can be seen, the two curves were again parallel

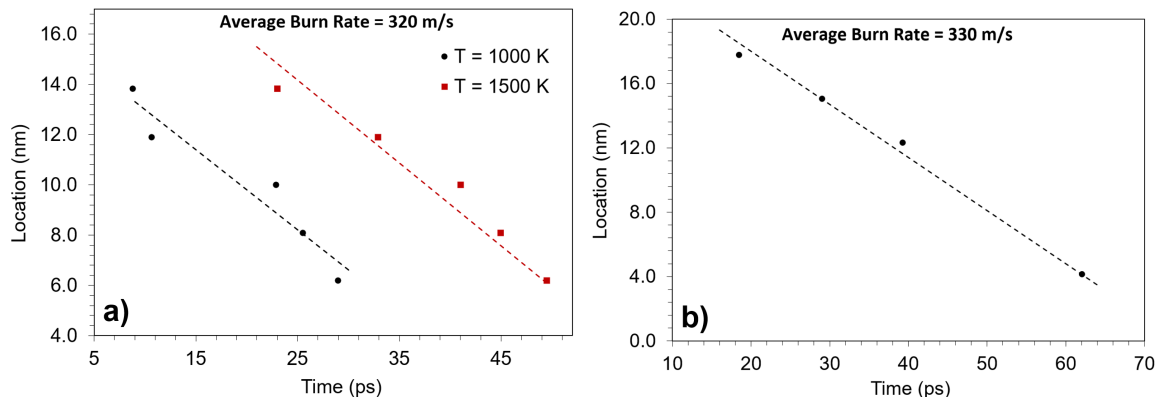


Figure 2.40.: Coupled PETN-MWCNT system (case 4: 50% PETN-MWCNT loading). Location of a) different temperatures and b) peak  $\text{NO}_2$  concentration as a function of time.

to each other and an average burn rate of  $320 \pm 10\text{ m/s}$  was obtained. Fig. 2.40b shows the location of the peak  $\text{NO}_2$  concentration as a function of time, using which, an average burn rate of  $330 \pm 10\text{ m/s}$  was obtained. Thus, nearly identical burn rates were measured using either criteria. The particular simulation shown in Fig. 2.40 corresponds to the PETN-MWCNT loading of 50%.

Fig. 2.41 shows the species profiles for a coupled PETN-MWCNT system (case 4: 50% PETN-MWCNT loading) as a function of time. The location of the slab was kept same as that in the pure PETN case i.e. at  $X = 4\text{ nm}$ , in order to facilitate one-to-one comparison. Comparing Figs. 2.37 and 2.41, the species distribution curve for the PETN-MWCNT system was shifted to the left but a similar reaction path was obtained. Again,  $\text{NO}_2$  was the dominant initial product formed during the PETN decomposition. HONO, NO and OH were other major intermediate products formed after  $\text{NO}_2$ , with  $\text{H}_2\text{O}$  being formed after the appearance of OH and NO. Thus, the species distribution during the PETN decomposition remained unchanged after the addition of MWCNTs. However, the rate of production of  $\text{CO}_2$  and CO were slightly less in the PETN-MWCNT system as compared to that observed in pure PETN, which could be attributed to the lower surface temperature, as shown in Fig. 2.39.

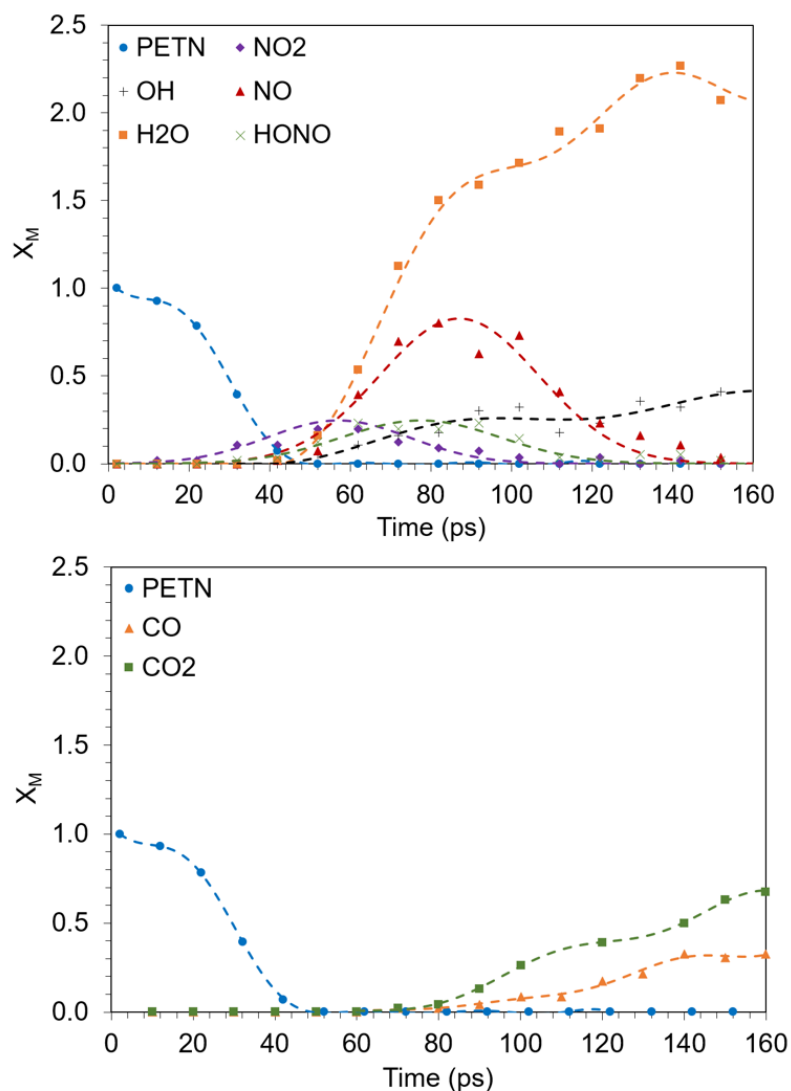


Figure 2.41.: Coupled PETN-MWCNT system (case 4: 50% PETN-MWCNT loading). Species distribution as a function of time during the pure PETN decomposition for a slab located at  $X = 4$  nm.

The fact that the MWCNTs remained unburned during the combustion process could be confirmed by looking at the mole fractions of  $\text{CO}_2$  and  $\text{CO}$  (Fig. 2.41). Since  $\text{CO}_2$  and  $\text{CO}$  did not appear until after  $\text{H}_2\text{O}$  formation, the temporal evolution of these oxides were consistent with that of pure PETN. Moreover, their peak mole fractions were also on the same order of magnitude as that observed in pure PETN. Thus, the CNTs were not consumed during the combustion process but only act to increase

the thermal transport among the PETN molecules, causing the species distribution curves to shift to the left. The deformation of the CNTs, as shown in Fig. 2.38, was from the increased temperature resulting from the PETN decomposition.

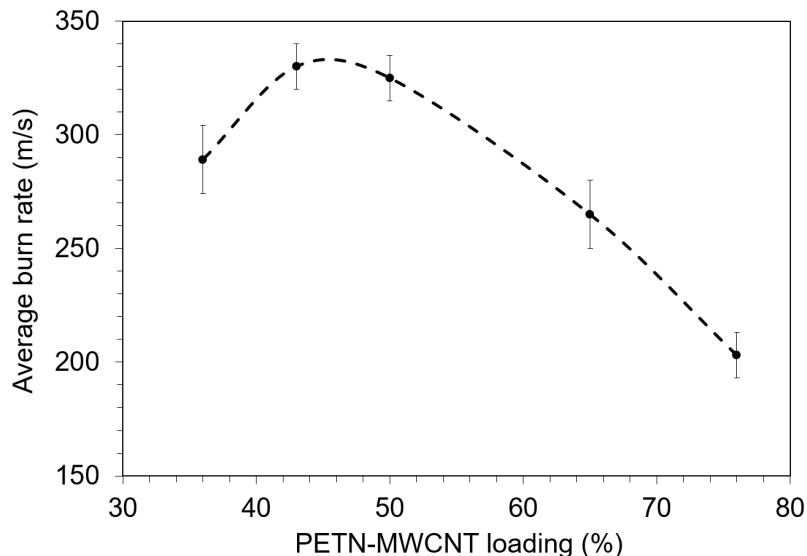


Figure 2.42.: Average burn rates as a function of the PETN-MWCNT loading (%).

Five different PETN-MWCNT combinations were simulated (cases 2 to 6), as shown in Table 2.8, in order to determine the effect of PETN-MWCNT loading on the average burn rates obtained. The results are shown in Fig. 2.42. Since slightly different (up to 10%) burn rates were obtained using the two criteria (different temperatures vs. peak  $\text{NO}_2$  concentration), the burn rate values provided in Fig. 2.42 were determined using the peak  $\text{NO}_2$  concentration criterion. For very thick PETN layers, a large amount of energy was released but the heat transfer among the PETN molecules near the MWCNTs surface was not high enough to conduct heat efficiently from the exothermic reactions to aid in reaction propagation. On the contrary, for very thin PETN layers, although the thermal transport among the PETN molecules was enhanced, the amount of heat reaching the unburned portions of the fuel was substantially reduced because some of the energy released during the exothermic reaction was used in heating the MWCNTs, which acted as heat sinks and thus, lowered the reaction propagation speeds. Consequently, an optimum PETN-MWCNT loading of

around 45% was obtained for which the burn rate enhancement was 3 times the bulk PETN burn rate of 110 cm/s (at a pressure of 3 GPa).

#### 2.5.4 Ignition of Pure PETN and PETN-MWCNT

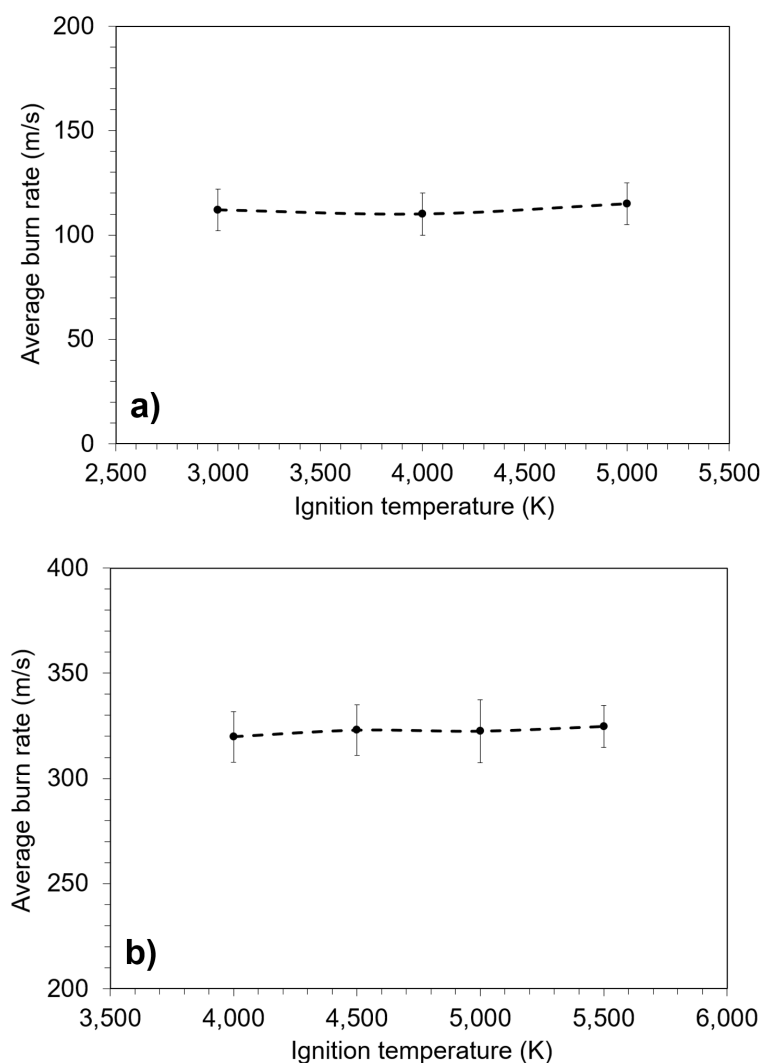


Figure 2.43.: The Effect of ignition temperature on the average burn rates for a) pure PETN and b) PETN-MWCNT (case 4: 50% PETN-MWCNT loading).

In this section, the effect of adding CNTs to PETN on the minimum ignition energy required to initiate successful reaction wave propagation was examined. To achieve

this goal, the temperature of the ignition zone was varied with its length unchanged (5-unit cell thick) for both pure PETN and PETN-MWCNT. Fig. 2.43 plots the average burn rate as a function of various ignition temperatures in the range of 3000–5000 K. The minimum ignition temperature is defined as the temperature below which the reaction wave propagation could not be sustained and that the system would eventually cool down. The minimum ignition temperature for the PETN molecules was found to increase from 3000 K to 4000 K when coupled to CNTs. This was again attributed to the high thermal transport observed among the PETN molecules near the MWCNTs surface, which resulted in a faster heat dissipation (or heat loss) and thus, a higher minimum ignition temperature was required. Nevertheless, above the minimum ignition temperature, the burn rate values remained unchanged. This was because of the method used in calculating the burn rates, where the slabs close to the ignition source were ignored so that the elevated enthalpy that was provided through the ignition could be damped out.

### 2.5.5 Interfacial Thermal Transport

In addition to reactive simulations, two additional non-reactive simulations were also conducted to better understand the mechanisms contributing towards the thermal enhancement in the coupled PETN-MWCNT system and in turn the burn rate enhancement. The particular PETN-MWCNT system considered was the case 3 (Table 2.8) corresponding to the PETN-MWCNT loading of 65%.

First, a non-reactive reverse non-equilibrium MD (RNEMD) simulation was conducted using LAMMPS to investigate the interfacial heat transfer in the PETN-MWCNT system. The MD study performed was based on the procedure outlined in the studies conducted by Zahedi et al. [98] and Alaghemandi et al. [97] In the RNEMD approach (also known as the Muller-Plathe algorithm [149]), a constant heat flux is imposed on the simulation box by performing velocity exchanges between the coldest

particle from the hot layer and the hottest particle from the cold layer in a given direction. If the masses of the particles being exchanged are different, then an exchange of velocities relative to the center of mass of the two atoms is performed to conserve the total kinetic energy of the system. The RNEMD simulation was performed under the NVE conditions at a chosen temperature of 330 K. The system was first equilibrated to the desired temperature and pressure of 330 K and 3 GPa, respectively, using the NVT and NPT equilibrations. The relaxation time for the Nose-Hoover thermostat and barostat was set to 100 fs with the time step being 0.2 fs. After the equilibration, a constant heat flux was applied across the system in the y-direction under the NVE conditions. Sufficient energy and temperature conservation were obtained using a timestep of 0.2 fs. At higher time steps, deviations in the total energy were observed. The y-direction (heat flux direction) of the simulation box was divided into 16 slabs (0.271 nm thick), whereas the z-direction was divided into 13 slabs (0.33 nm thick). The velocity exchanges were then performed every 20 fs between 2 atoms, with one atom located in the slabs at  $y = 0$  (hot layer) and other atom located in the slabs at  $y = y_{max}$  (cold layer). The heat flux imposed was computed using the LAMMPS fix thermal conductivity command as given below:

$$j_y = \left( \frac{1}{2tA} \right) \frac{\sum \left( m_{hot} v_{hot}^2 - m_{cold} v_{cold}^2 \right)}{2} \quad (2.21)$$

In the above equation,  $m_{hot}$  and  $m_{cold}$  are the masses of the hot and the cold particles, respectively, whose velocities are being exchanged,  $A$  is the cross-sectional area perpendicular to the heat flux direction (z-x),  $v_{hot}$  and  $v_{cold}$  are the velocities of the hot and the cold particle, respectively, and  $t$  is the total simulation time. A factor of 2 was added to Eqn. 2.21 because of the periodic boundary conditions employed in the direction of the heat flux [149]. Using the imposed heat flux, the thermal conductivity value was calculated using the following equation:

$$k_y = \frac{-j_y}{(dT/dy)} \quad (2.22)$$

In the above equation,  $k_y$  is the thermal conductivity value along the y-direction and  $dT/dy$  is the temperature gradient due to the imposed heat flux. The  $k_y$  value was obtained using the temperature gradient ( $dT/dy$ ) for the z-slab located at  $(y,0)$ .

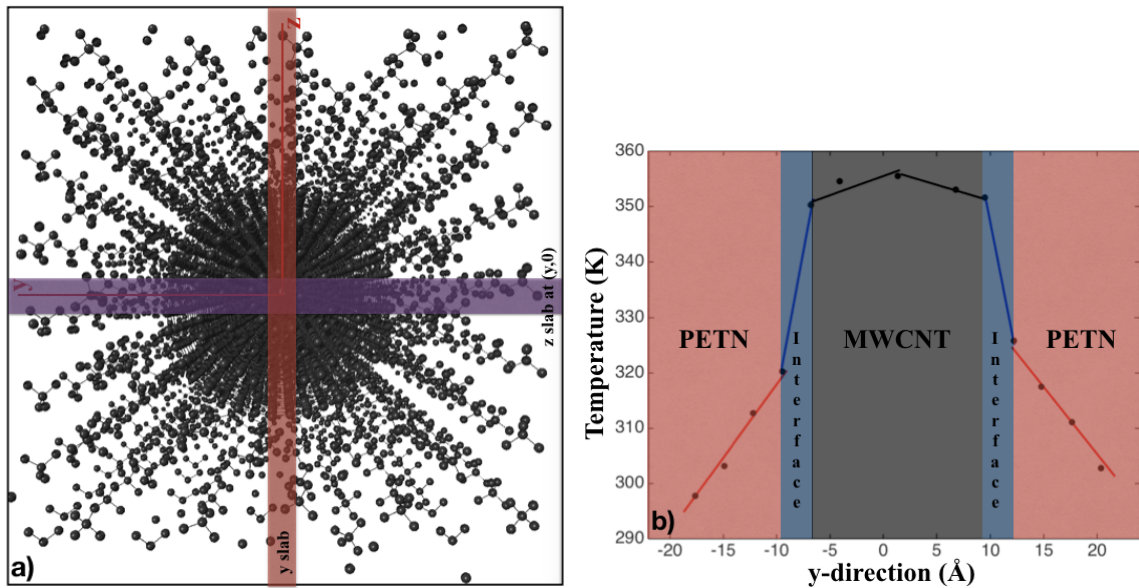


Figure 2.44.: a) The slabs in the y and z directions; b) Temperature profile in the y-direction (case 3: 65% PETN-MWCNT loading).

Fig. 2.44 shows the temperature profile for the z-slab located at  $(y,0)$ . As can be seen, linear temperature profiles were obtained in the individual regions belonging to PETN, interface, and MWCNTs, thus, validating the application of Eqn. 2.22 towards calculating the thermal conductivity values. Thermal conductivity values of  $0.173 \pm 7\%$  (W/m-K),  $0.0457 \pm 5\%$  (W/m-K), and  $0.7610 \pm 10\%$  (W/m-K) were obtained for PETN, interface, and MWCNTs, respectively. The interface thermal conductivity value obtained was 4 times lower than that of the PETN thermal conductivity value, which could be attributed to the mismatch of the thermal transport

regimes in PETN and CNTs [95,96]. The mean free path of CNTs is a strong function of the size of the tubes, boundary defects present and the system temperature, and can be expected to lie anywhere between 50 nm to 1.5  $\mu\text{m}$ . Since, the CNTs used were only 40 nm in length, it can be assumed that the heat was conducted ballistically or at least quasi-ballistically [150,151]. This was in contrast to the PETN molecules where the heat was conducted diffusively (through collisions). Thus, it is the sudden transition from the ballistic to the diffusive regime that limits the interfacial thermal transport.

A similar study was conducted by Alaghemandi et al. [97], in which the thermal conductivity of a composite of single-walled carbon nanotubes and polyamide-6,6 (PA) was investigated using the RNEMD simulations. An interface thermal conductivity of 0.003 W/m-K was obtained, which was 2 orders of magnitude lower than the thermal conductivity of pure PA (0.24 W/m K). Moreover, this interface thermal conductivity value of 0.003 W/m-K was even an order of magnitude less than the interface thermal conductivity value of 0.0457 W/m-K obtained in this work, which could be attributed to different materials and simulation conditions used. The present simulations were conducted at an extremely high pressure of 3 GPa as opposed to the simulations performed by Alaghemandi et al. [97], which were conducted at atmospheric pressures. In conclusion, because of such a high thermal interface resistance, there must be another mechanism, in addition to the high axial thermal conductivity of the CNTs, which is responsible for the increased thermal transport among the PETN molecules.

Zahedi et al. [98] studied the structural properties of a polymer matrix around the CNTs and observed enhanced polymer ordering in the interfacial region. They concluded that because of this wrapping of the polymer molecules around the CNTs, the molecules are predominantly tangential to the CNT surface, which in turn increases the heat transport along the CNTs but decreases the heat transport in the direction perpendicular to the CNTs. Motivated by this, the layering of the PETN

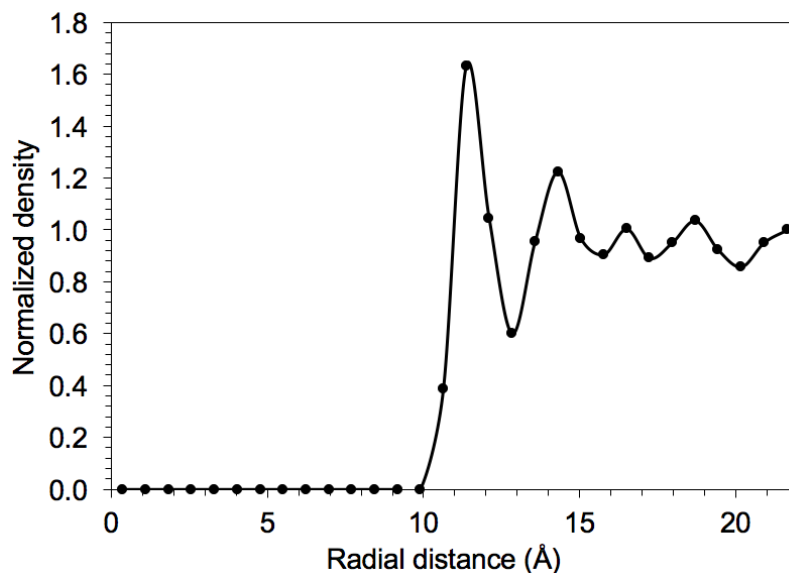


Figure 2.45.: Normalized density profile of the PETN molecules around the MWCNTs surface (case 3: 65% PETN-MWCNT loading).

molecules as a result of their interactions with CNTs was also examined. An equilibrium non-reactive MD simulation was conducted under the NVE conditions. And again, the system was first equilibrated to the temperature and pressure of 300 K and 3 GPa, respectively. After the system equilibration, the density profile calculations were performed. The simulation box was divided into cylindrical bins having a length of 4 nm and a radial thickness of 0.07 nm. Fig. 2.45 shows the normalized density profile of the PETN molecules around the MWCNTs surface (case 3: 65% PETN-MWCNT loading). As can be seen, the PETN molecules were indeed ordered around the MWCNTs, and as a result, enhancing the thermal transport among the PETN molecules in the direction parallel to the CNTs. Thus, the increased thermal transport observed among the PETN molecules was from the combined effect of high axial thermal conductivity of the MWCNTs and enhanced ordering of the PETN molecules.

### 3. BURN RATE ENHANCEMENT: MnO<sub>2</sub> COATED GF STRUCTURES

This chapter describes the experimental study that was conducted to investigate the burn rate enhancement of nitrocellulose (NC) using the MnO<sub>2</sub> coated GF structures. This would couple the chemical effect of the MnO<sub>2</sub> catalyst (increased chemical reactivity) with the physical effect of the GF structure (enhanced thermal transport) and thus, has the potential to further enhance the burn rates. The effects of both the MnO<sub>2</sub>-NC and NC-GF loadings on the burn rates obtained were studied. In addition, the TG (Thermogravimetric) and DSC (Differential scanning calorimetry) analysis were also conducted, in order to determine the effects of the addition of MnO<sub>2</sub> and GF on the NC's activation energy (E) and peak thermal decomposition (PTD) temperatures.

*Most of the text and figures presented in this section are reproduced from {S. Jain and L. Qiao, Proceedings of the Combustion Institute (2018)} with permission of Elsevier Publishing.*

#### 3.1 Experimental Method

##### 3.1.1 Preparation of MnO<sub>2</sub> Coated GF Structures

The pure GF structure was grown on a 3 mm thick Ni template (75 pores per inch) using a chemical vapor deposition (CVD) technique with flowing a mixture of three gases, CH<sub>4</sub> (20 sccm), H<sub>2</sub> (20 sccm), and Ar (210 sccm), at 1050 °C for about 2 hrs. [35]. The details of the GF preparation method are given in section 2.1.3. In this study, the GF density was kept fixed at 14 mg/cm<sup>3</sup> ± 2 mg/cm<sup>3</sup>.



Figure 3.1.: The MnO<sub>2</sub> coated GF sheet cut in the required dimension of 2.5 cm x 0.6 cm.

After the growth of the GF structure, it was coated with the MnO<sub>2</sub> oxide layer using a simple hydrothermal approach [152]. The KMnO<sub>4</sub> powder (223468 Sigma-Aldrich) was first dissolved in DI water (200 ml) at various concentrations (1.5 mM to 45 mM) through vigorous stirring for 30 mins at room temperature. The resulting KMnO<sub>4</sub> solution was then poured into a 150 ml PTFE (polytetrafluoroethylene) lined, Cr-Ni-Ti stainless steel autoclave chamber (CIT-HTC230-V150, Columbia International). The pure GF structure was immersed into this KMnO<sub>4</sub> solution and autoclaved in an oven at 150 °C for 6 hrs. The MnO<sub>2</sub> coated GF structures were then dried for 12 hrs. at 80 °C, which gave enough time for the metal oxide layer to completely crystallize. The final MnO<sub>2</sub> coated GF sheet cut in the required dimension of 2.5 cm by 0.6 cm is shown in Fig. 3.1.

Fig. 3.2 shows the GF surface after the MnO<sub>2</sub> coating. As can be seen, the GF surface coverage by the deposited oxide was found to increase with an increase in the % amount of MnO<sub>2</sub> added to the GF structure. At low MnO<sub>2</sub> concentrations, parts of the GF strut walls were still visible and the deposited MnO<sub>2</sub> were in the form of fiber-like particle agglomerates with their mean sizes ranging from a few hundred nm to tens of  $\mu\text{m}$ . However, at high MnO<sub>2</sub> concentrations, the GF strut walls were completely covered by these dense fiber-like MnO<sub>2</sub> particles. The GF supported MnO<sub>2</sub> particles provided a more efficient contact between the propellant NC and MnO<sub>2</sub> in terms of the uniformity and surface area of the catalyst exposed. This is in contrast to

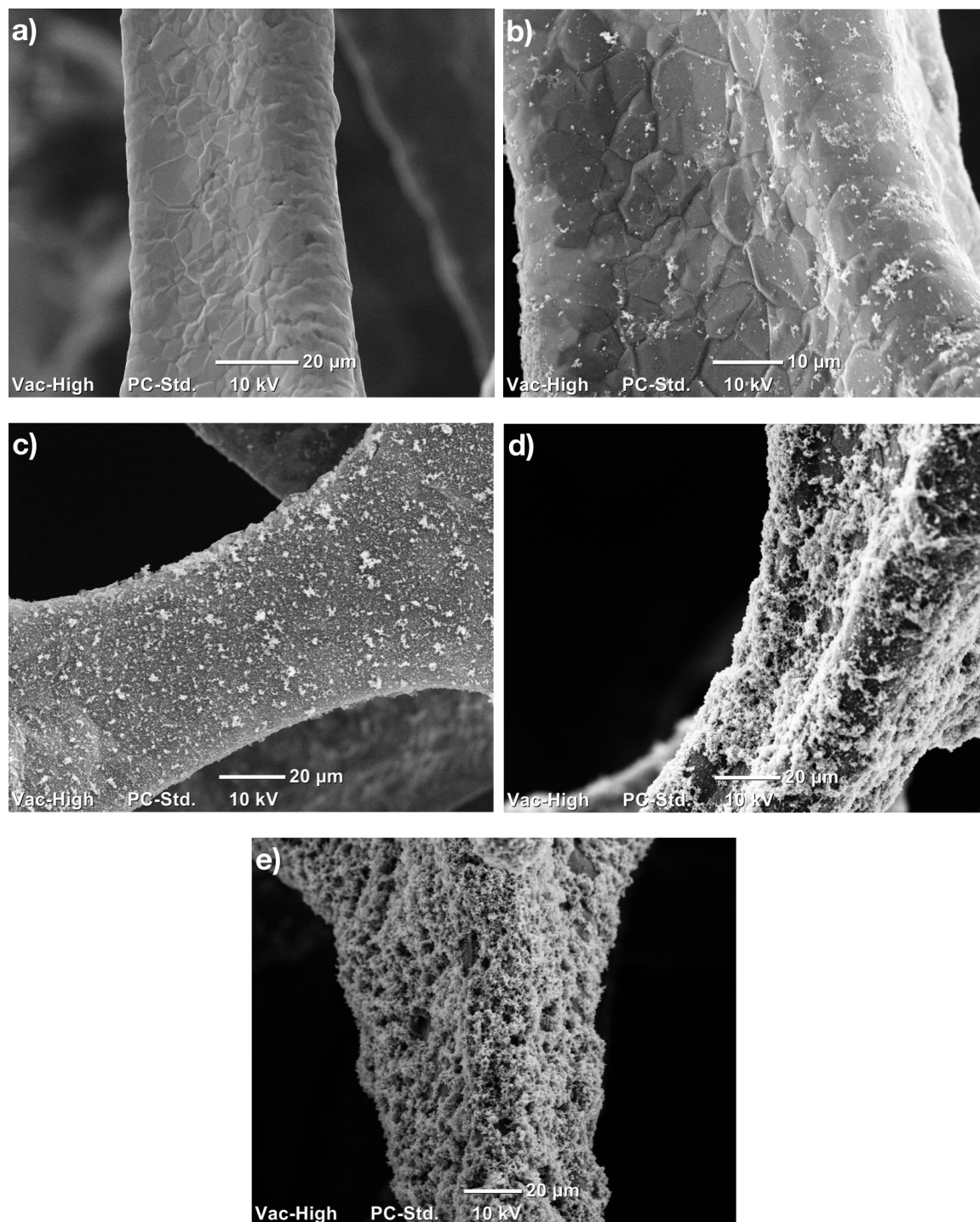


Figure 3.2.: SEM images of the GF surface after MnO<sub>2</sub> coating; a) 0%, b) 13%, c) 23%, d) 34% and e) 43% MnO<sub>2</sub> in the GF-MnO<sub>2</sub> system.

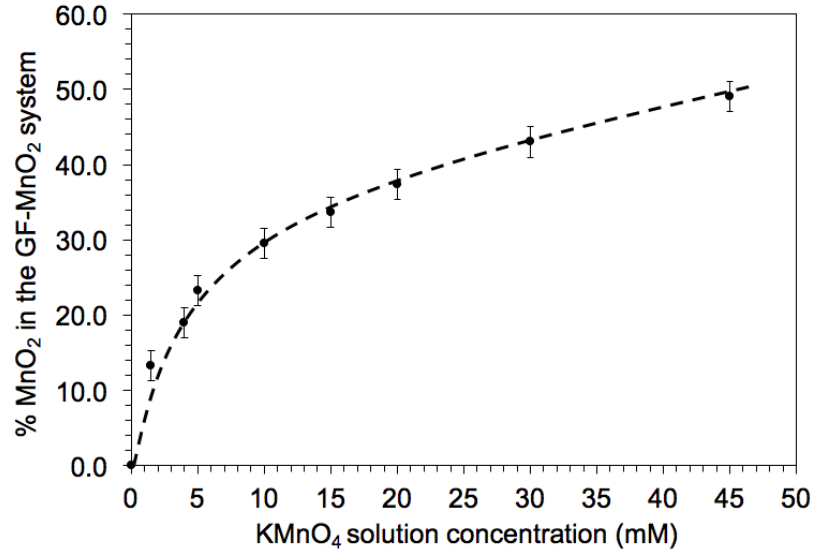
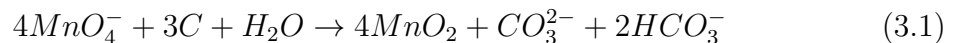


Figure 3.3.: Amount of MnO<sub>2</sub> added as a function of the KMnO<sub>4</sub> solution concentration.

the traditional composite propellant mixtures in which a continuous contact between the propellant and the catalyst is not achieved because of the random addition of catalyst particles into the propellant solution.

As can see from Fig. 3.3, initially, a rapid rate of addition of MnO<sub>2</sub> to the GF surface was observed but above 10 mM KMnO<sub>4</sub> solution concentration, the rate of addition slowed down. For concentrations below 10 mM, the dominate chemical reaction producing MnO<sub>2</sub> on the GF surface was [152]:



The C atoms of GF convert Mn<sup>7+</sup> to Mn<sup>4+</sup> leading to the initial formation of MnO<sub>2</sub> on the GF surface. But above concentrations of 10 mM, due to the surface coverage by the MnO<sub>2</sub> particles, the amount of carbon atoms available for the KMnO<sub>4</sub> solution to react with was limited. Thus, a second chemical reaction as given below between H<sub>2</sub>O and KMnO<sub>4</sub> started to dominate [153]:



Thus, initially, MnO<sub>2</sub> was produced through the redox reaction between C and KMnO<sub>4</sub> (Eqn. 3.1) but after the initial surface coverage of the GF surface by the MnO<sub>2</sub> particles, the decomposition reaction of KMnO<sub>4</sub> (Eqn. 3.2) dominated.

After the preparation of the MnO<sub>2</sub> coated GF structures, the NC solution (4% wt.) was drop-casted onto the GF-MnO<sub>2</sub> surface at various amount to get the desired NC-GF loading, which is defined as the mass of NC per total mass of NC and GF. The mass of MnO<sub>2</sub> was not included in the NC-GF loading definition to facilitate the burn rate enhancement comparison with and without the addition of MnO<sub>2</sub>. Moreover, the amount of catalysts present in the NC-GF-MnO<sub>2</sub> system was given in terms of the MnO<sub>2</sub>-NC loading, which is defined as the mass of MnO<sub>2</sub> per total mass of MnO<sub>2</sub> and NC. These fuel doped GF-MnO<sub>2</sub> surfaces were then dried at ambient conditions for 24 hrs., which gave enough time for all the solvent to completely evaporate.

Fig. 3.4 shows the SEM images of the GF-MnO<sub>2</sub> surface after NC deposition for two different NC-GF loadings: 75% and 55%. As can be seen, for the 55% NC-GF loading, a thin layer of NC was formed over the MnO<sub>2</sub>-coated GF strut walls. However, for the 75% NC-GF loading, due to the thicker NC layer deposited, no structure of the MnO<sub>2</sub> particles was visible underneath the fuel layer.

### 3.1.2 TG and DSC: Experimental Setup

The TG and DSC analysis were conducted using a thermal analyzer (SDT Q600) to determine how the activation energy (E) and peak thermal decomposition (PTD) temperatures of NC were affected by changing the MnO<sub>2</sub>-NC loading for three different NC-GF loadings (100%, 75% and 55%). The PTD temperature was taken as the point at which the heat flow was maximum. For all the tests conducted, the specimen mass was kept fixed at 3 mg, the temperature range was set to 25-400 °C

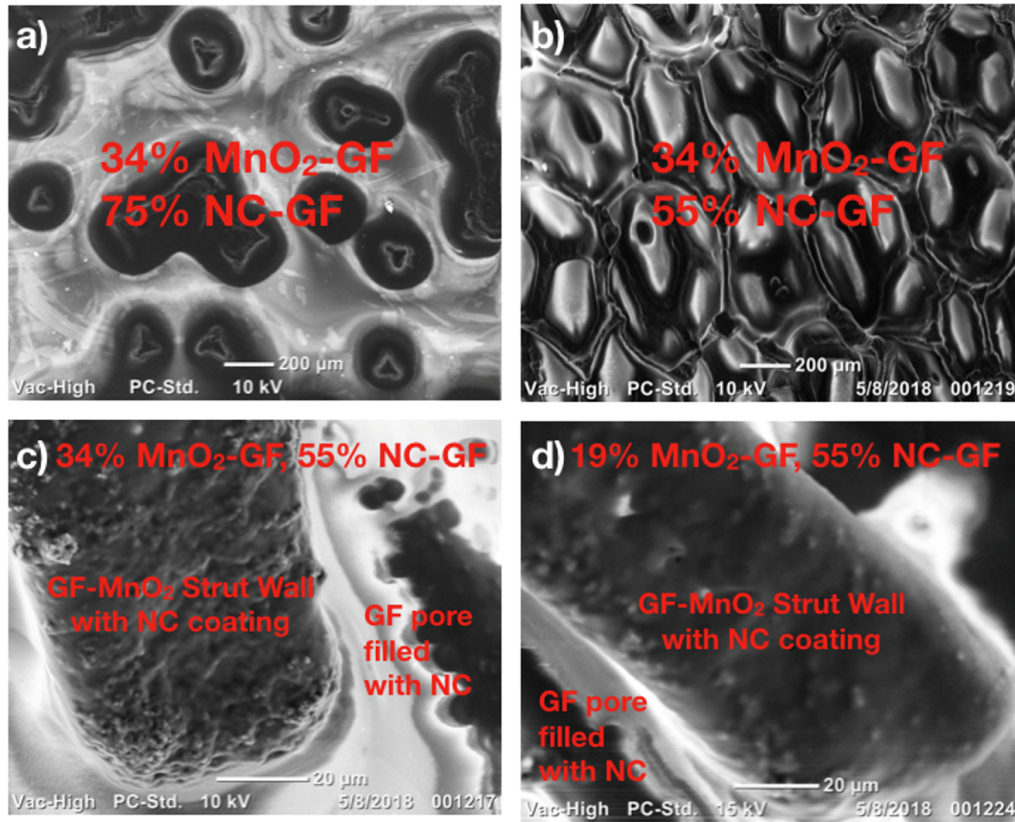


Figure 3.4.: SEM - zoomed out (a and b) and zoomed in (c and d) images of the GF-MnO<sub>2</sub> surface after NC deposition for 75% and 55% NC-GF loadings.

and alumina crucibles were used. Moreover, the thermal analyzer was operated in an inert He environment at 1 atm using a flow rate of 100 ml/min. In addition, the Kissinger Method [154] was used to calculate the activation energies. Five different heating rates i.e. 2 °C/min, 5 °C/min, 10 °C/min, 15 °C/min and 20 °C/min were used and for each heating rate, two different runs were made.

Next, a typical activation energy calculation will be shown, validating the use of the Kissinger Method. A general reaction rate equation valid for an arbitrary kinetic model, for a single-step process, can be written as:

$$\frac{\partial \alpha}{\partial t} = k(T)f(\alpha) \quad (3.3)$$

In the above equation,  $\alpha$  is the extent of reaction obtained from the TG graph as the mass fraction of the burned fuel,  $k(T)$  is the rate constant and  $f(\alpha)$  is an arbitrary function depending on the particular kinetic model used. For example, for a first order kinetic model,  $f(\alpha)$  would be  $1-\alpha$ . Next, parameterizing  $k(T)$  using the Arrhenius assumption, the Eqn. 3.3 can be re-written as:

$$\frac{\partial\alpha}{\partial t} = A \exp\left(-\frac{E}{R_u T}\right) f(\alpha) \quad (3.4)$$

where  $A$  is the Arrhenius constant,  $E$  is the activation energy and  $R_u$  is the universal gas constant. The Kissinger equation is then derived from Eqn. 3.4 under the condition of maximum reaction rate (or maximum heat flow in terms of the DSC analysis) at which  $\partial^2\alpha/\partial t^2$  is zero [155]:

$$\frac{\partial^2\alpha}{\partial t^2} = \left(\frac{EH}{RT_m^2} + Af'(\alpha_m)\exp\left(\frac{-E}{RT_m}\right)\right)\left(\frac{\partial\alpha}{\partial t}\right)_m = 0 \quad (3.5)$$

$$\Rightarrow \frac{EH}{RT_m^2} = -Af'(\alpha_m)\exp\left(\frac{-E}{RT_m}\right) \quad (3.6)$$

Taking natural log of both the sides gives the Kissinger equation:

$$\ln\left(H/T_m^2\right) = \ln(-ARf'(\alpha_m)/E) - \frac{E}{RT_m} \quad (3.7)$$

In the above Eqns. 3.5, 3.6 and 3.7,  $H$  is the heating rate and the subscript  $m$  represents the point at which the reaction rate (or the heat flow) was maximum. Moreover, the temperature  $T_m$  corresponds to the PTD temperature. The activation energy was then determined from the slope of  $\ln(H/T_m^2)$  vs.  $-1/(RT_m)$  graph. However, for the graph to be a straight line,  $\alpha_m$  should be independent of the heating rate ( $H$ ). This is only strictly true for first order kinetic models in which  $f'(\alpha) = -1$ . However, for  $n$ th-order and Avrami–Erofeev kinetic models [156], the variation of  $\alpha_m$  with

H is also negligible but for other types of kinetic models, the variation can be significant [157–159]. Thus, the application of the Kissinger method needs to be verified.

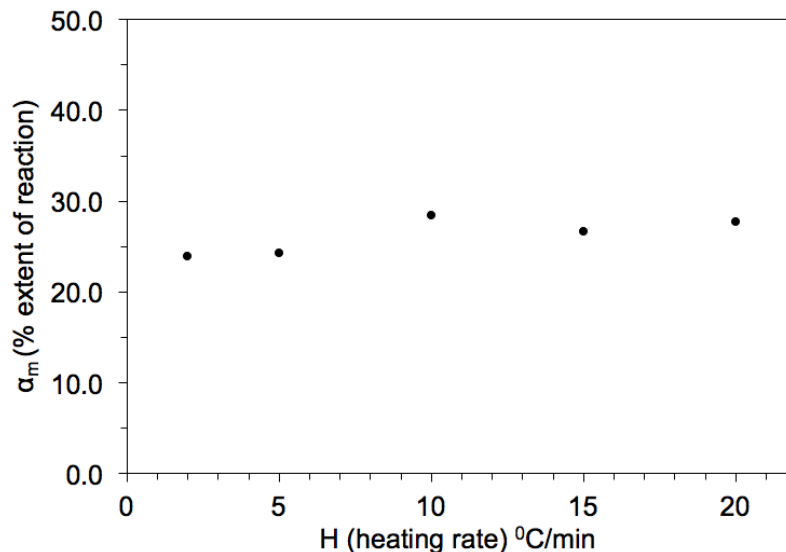


Figure 3.5.: Effect of heating rate (H) on the extent of reaction ( $\alpha_m$ ) at the point of maximum heat flow. The particular case shown corresponds to 10% MnO<sub>2</sub>-NC and 75% NC-GF loading.

Fig. 3.5 plots  $\alpha_m$  as a function of the heating rate. The particular case shown corresponds to 10% MnO<sub>2</sub>-NC and 75% NC-GF loading. As can be seen, negligible variation of  $\alpha_m$  with the heating rate was observed, thus, validating the use of the Kissinger method. Fig. 3.6 shows the corresponding graph of  $\ln(H/T_m^2)$  vs.  $-1/(RT_m)$  and as expected, a straight line was observed with a R<sup>2</sup> value of 0.9989.

Fig. 3.7 shows the typical DSC curves obtained, which are representative of all the various combinations of the MnO<sub>2</sub>-NC and NC-GF loadings examined. For all the samples tested, a single exothermic peak was observed. For pure NC, an exothermic peak at 207.76 °C (for a heating rate of 10 °C/min) was obtained, similar to the exothermic peaks obtained by Pourmortazavi et al. [160], Sovizi et al. [161] and Makashir et al. [162] at 206 °C, 208.1 °C and 206.88 °C, respectively, using the same

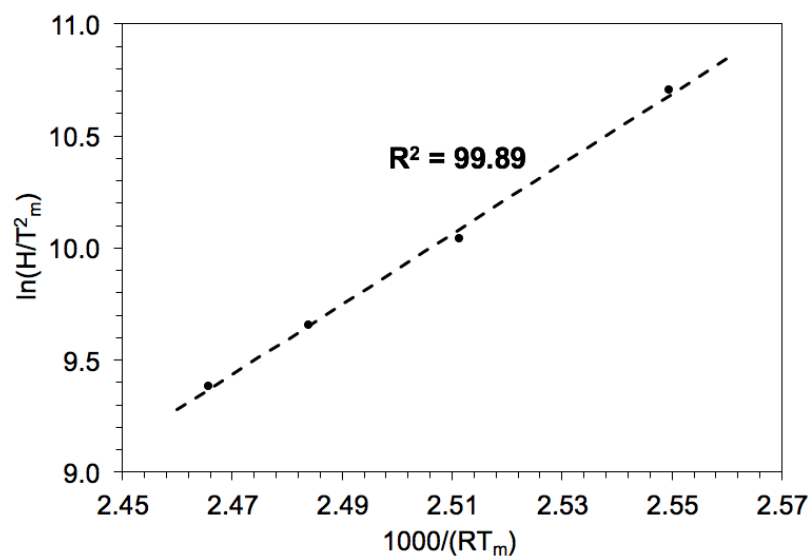


Figure 3.6.: Plot of  $\ln(H/T_m^2)$  vs.  $-1/(RT_m)$ . The particular case shown corresponds to 10%  $\text{MnO}_2$ -NC and 75% NC-GF loading.

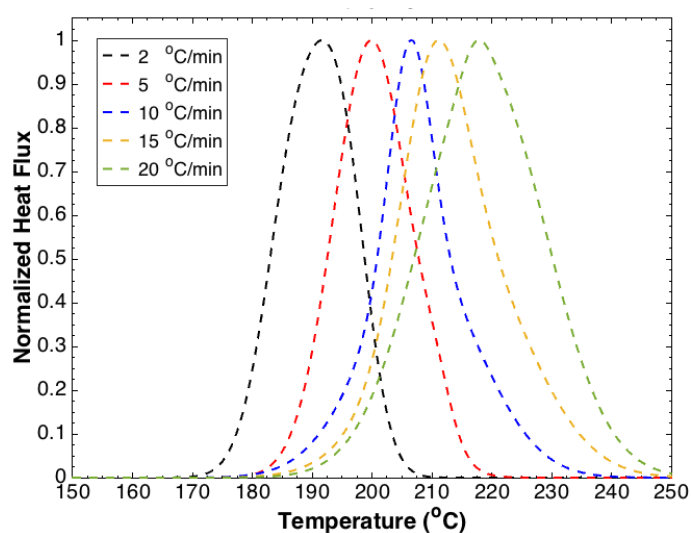


Figure 3.7.: DSC curves of pure NC for various heating rates.

heating rate of 10 °C/min. In addition, using the Kissinger method for pure NC, an activation energy of 158.79 KJ/mol was measured, consistent with the activation energy values of 156.8 KJ/mol, 157.2 KJ/mol and 165 KJ/mol reported by Pourmortazavi et al. [160], Sovizi et al. [161] and Zhang et al. [32], respectively. The

NC decomposition can be divided into two steps that occur simultaneously: (1) the endothermic step, in which the CO-NO<sub>2</sub> bond in NC is ruptured forming NO<sub>2</sub> and aldehydes and (2) the exothermic step, in which NO<sub>2</sub> and aldehydes react to form NO, CO, CO<sub>2</sub>, H<sub>2</sub>O and H<sub>2</sub>. These two steps then combine to give a net energy balance for the decomposition that is exothermic, which is consistent with the DSC observations of this study and with the other DSC studies performed in the literature [160–167].

### 3.1.3 Burn Rate: Experimental Setup

The details of the experimental setup is given in section 2.2 and is briefly described below. The ignition of the NC-GF-MnO<sub>2</sub> samples (2.5 cm x 0.6 cm x 0.3 cm) was achieved by using a resistive heating nichrome wire. A constant voltage of 10 V was applied across the wire, which was sufficient to ignite the samples. An IR camera (FLIR- SC6100) was used to capture the reaction wave propagation process. The burn rate, which is defined as the rate at which the reaction zone travels across the fuel layer, was then calculated by tracking the brightest peak within the flame.

## 3.2 Results and Discussion

### 3.2.1 Burn Rates and Thermal Decomposition Parameters

Fig. 3.8 shows the burn rates obtained as a function of the MnO<sub>2</sub>-NC loading for three different NC-GF loadings (100%, 75% and 55%). For pure NC (100% NC-GF loading), no burn rate enhancement was obtained until the MnO<sub>2</sub>-NC loading of 10% was reached, after which an increase was observed in the burn rates. Above 16.5% MnO<sub>2</sub>-NC loading, a plateaued behavior was obtained with burn rate enhancements up to 2 times (1.5 cm/s) the bulk NC burn rate of 0.7 cm/s. The GF structure, which was used to support the MnO<sub>2</sub> catalyst, clearly significantly increases the burn rates. As can be seen, the maximum burn rate enhancement, corresponding to 20% MnO<sub>2</sub>-NC and 55% NC-GF loading, was about 9 times (6.2 cm/s) the bulk NC burn rate.

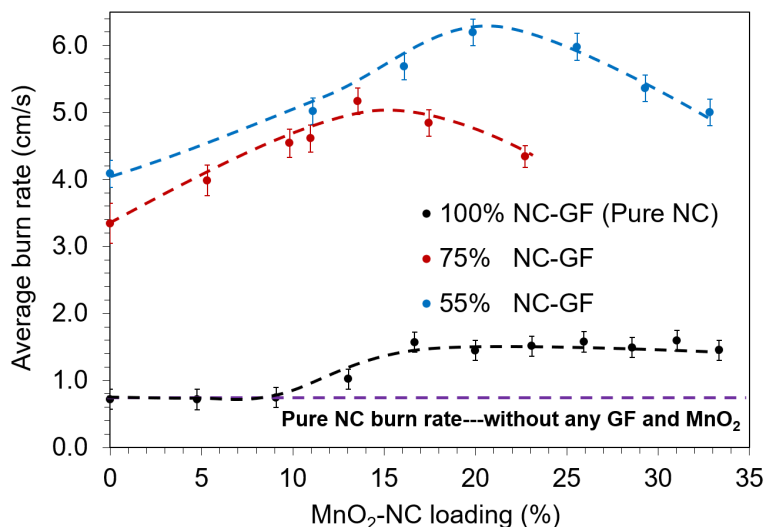


Figure 3.8.: Average burn rates as a function of the MnO<sub>2</sub>-NC and NC-GF loadings.

This was attributed to the combined physical and chemical effects of the GF-MnO<sub>2</sub> structures, as will be explained in the following paragraphs. Lastly, for both 75% and 55% NC-GF loadings, initially, an increase in the burn rates was observed as a function of the MnO<sub>2</sub>-NC loading but above a certain MnO<sub>2</sub> concentration, a slight decrease was obtained.

(1) **The physical effect** comes from the use of the GF structure, which has been shown to retain the high in-plane thermal conductivity of thin graphite while avoiding the high thermal interface resistance issue found in GNPs and CNTs [63, 69–75, 91], as was discussed in detail in section 2.3.3. Another advantage with the use of the GF structure comes from its 3D interconnected hollow network of GF strut walls, which provides a continuous thermal conduction path for the heat transport during the combustion process. Thus, even with the use of pure GF structure, without any MnO<sub>2</sub>, a significant amount of burn rate enhancement was observed (up to 6 times as shown in Fig. 3.8).

(2) **The Chemical effect:** Fig. 3.9 plots the thermal decomposition parameters (activation energy and PTD temperature) as a function of the MnO<sub>2</sub>-NC and NC-GF

loadings. The PTD temperatures shown in the figure were obtained using a heating rate of 10 °C/min. The addition of MnO<sub>2</sub> increases the chemical reactivity of the fuel by catalyzing the exothermic step of NC decomposition between NO<sub>2</sub> and aldehydes. As can be seen, for all the three NC-GF loadings (100%, 75% and 55%) tested, the activation energy initially decreases with an increase in the MnO<sub>2</sub>-NC loading but above a certain MnO<sub>2</sub> concentration, a slight rise was observed. This was because, the addition of the MnO<sub>2</sub> catalyst has a dual counteracting affect. The positive effect comes from the fact that it catalysis the exothermic reaction, whereas the negative effect comes from the fact that some of the energy that is released during the exothermic decomposition is used in heating these MnO<sub>2</sub> particles and as a result, decreasing the net catalytic effect that could be obtained. This dual counteracting effect could be further confirmed by looking at the behavior of the PTD temperature as a function of the MnO<sub>2</sub> concentration, and similar to the activation energy, initially a decreasing trend was observed but after that a plateaued behavior was obtained.

Another interesting observation that could be made from Fig. 3.9 is that before the plateaued behavior was obtained, the PTD temperatures were found to increase as the NC-GF loading was decreased i.e. for MnO<sub>2</sub>-NC < 13%: PTD<sub>55%</sub> > PTD<sub>75%</sub> > PTD<sub>100%</sub>. This could be attributed to the addition of the GF structure. Since GF does not take part in the decomposition process, some of the energy that is released during the exothermic decomposition is used in heating these non-reactive GF structures, which basically acts as heat sinks and in turn, increases the PTD temperatures. However, for 13% < MnO<sub>2</sub>-NC < 28%, 75% NC-GF has the lowest PTD temperatures, whereas for MnO<sub>2</sub>-NC > 28%, 55% NC-GF has the lowest PTD temperatures. This was because of the delayed plateaued behavior that was observed for the PTD temperatures as the NC-GF loading was decreased, as will be explained next. For a given MnO<sub>2</sub>-NC loading, the lower NC-GF loading corresponds to a greater % wt. of the GF structure in the GF-MnO<sub>2</sub>-NC system and thus, more GF was available to support the MnO<sub>2</sub> catalyst, which in turn affected the growth and distribution of

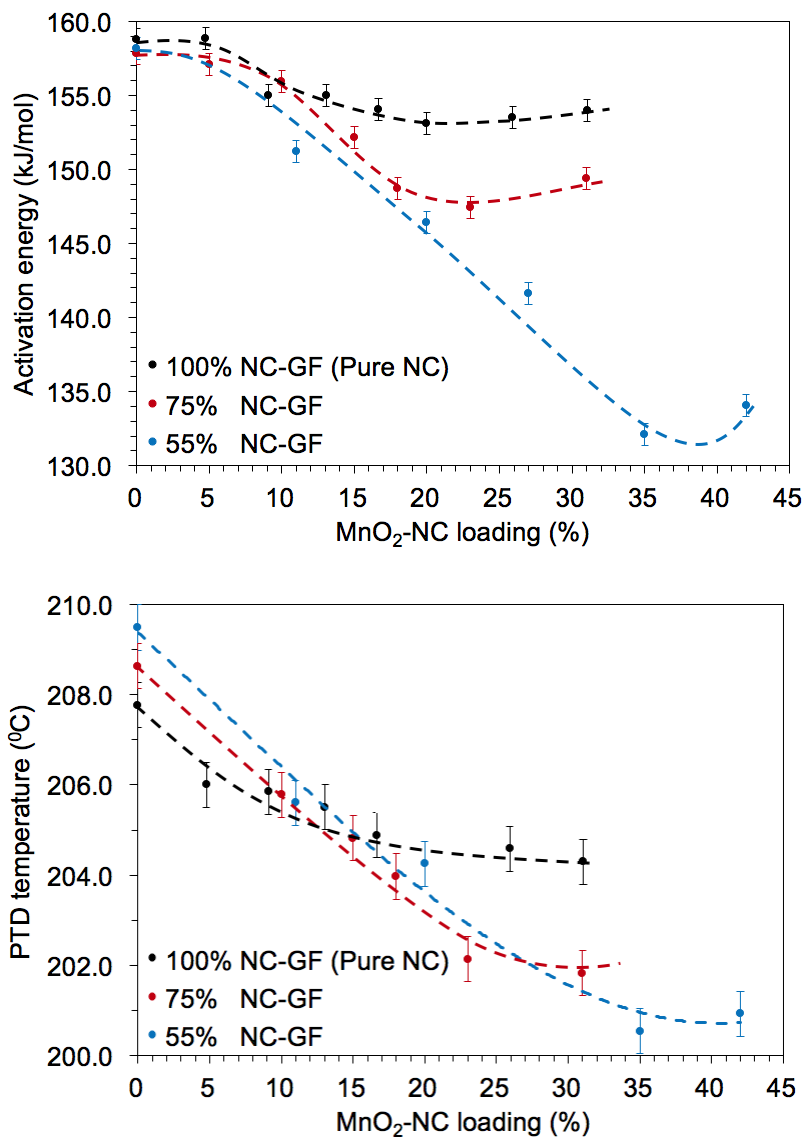


Figure 3.9.: Activation energy and PTD temperature as a function of the MnO<sub>2</sub>-NC and NC-GF loadings (%).

the MnO<sub>2</sub> particles. The distribution of a catalyst in the solid phase is very important and can strongly affect the decomposition characteristics [168]. Distribution, in general, can be used to describe factors such as thickness, shape and randomness of the catalyst particles grown. The lower NC-GF loading, for a given MnO<sub>2</sub>-NC loading, leads to thinner MnO<sub>2</sub> films, assuming the randomness and shape of the MnO<sub>2</sub> particles grown remained unchanged, which in turn increases the surface area of the catalyst exposed and as a result, enhances the catalytic effect.

A similar behavior was observed in the activation energy, where the optimum  $\text{MnO}_2$  concentration was increased as the NC-GF loading was decreased. However, in contrast to the PTD temperatures, the activation energy remained unchanged with the addition of GF structures without any  $\text{MnO}_2$ . This was expected as the GF structure being a physical catalyst was only enhancing the thermal transport rates between the burned and unburned portions of the fuel, without having any affect on the thermal decomposition rates. A similar observation was made during the MD simulations of the coupled PETN-MWCNT system, where only the species distribution curves were shifted to the left but the reaction pathway remained unchanged (section 2.5.3). For 100% NC-GF loading (without any GF), the PTD temperature, obtained using a heating rate of  $10\text{ }^\circ\text{C}/\text{min}$ , was lowered by only  $3.5\text{ }^\circ\text{C}$  but with the use of the GF structure, the PTD temperatures were lowered by  $6\text{ }^\circ\text{C}$  and  $7.5\text{ }^\circ\text{C}$  for 75% NC-GF and 55% NC-GF loadings, respectively. As far the activation energy was considered, for 100% NC-GF loading, it was lowered by only 3.6% but for 75% NC-GF and 55% NC-GF loadings, the activation energies were lowered by 7.5% and 17.0%, respectively.

In literature, a number of studies have been performed confirming the optimum catalytic behavior [169–173]. Kishore et al. [169] studied the catalytic effect of various oxides such as  $\text{MnO}_2$ ,  $\text{Fe}_2\text{O}_3$ ,  $\text{Co}_2\text{O}_3$ , and  $\text{Ni}_2\text{O}_3$  on the burn rate enhancement and thermal decomposition characteristics of the AP/polystyrene propellant system. For all the oxides, an optimum catalytic concentration was obtained after which a fall in the burn and thermal decomposition rates was observed. Joshi et al. [170] also observed an optimum catalytic behavior in the activation energy of AP as a function of the  $\text{Fe}_2\text{O}_3$  concentration. However, for the PTD temperature, a plateaued behavior was obtained, similar to the trends observed in the present study. Bakhman et al. [171] studied the effect of the addition of  $\text{Fe}_2\text{O}_3$  on the burn rate enhancement for a number of oxidizer/fuel combinations (AP/Sulphur, AP/Soot, AP/Polymethylmethacrylate,

and AP/guanidine nitrate) and for all the cases tested, an optimum  $\text{Fe}_2\text{O}_3$  concentration was obtained that maximized the burn rates. Naya et al. [172] also observed an optimum  $\text{MnO}_2$  concentration that maximized the burn rate of an ammonium-nitrate based propellant. Oyumi et al. [173], however, observed a plateaued burning and thermal decomposition behavior using the  $\text{Fe}_2\text{O}_3$  catalyst for an AP propellant system.

Another interesting observation that could be made from Fig. 3.8 is that the optimum  $\text{MnO}_2$  concentration corresponding to the burn rate enhancement was also found to shift to the right as the NC-GF loading was decreased. This could be attributed again to the presence of the GF structure. The addition of  $\text{MnO}_2$  increases the heat flux back to the surface by catalyzing the exothermic reaction, which was even further enhanced by the use of these highly conductive GF structures. For example, as the NC-GF loading was decreased from 75% to 55%, the % wt. of the GF in the GF- $\text{MnO}_2$ -NC system was increased and as a result, more GF was available for each  $\text{MnO}_2$ -NC loading, which in turn increased the amount of  $\text{MnO}_2$  required to counteract this positive effect of increased thermal transport.

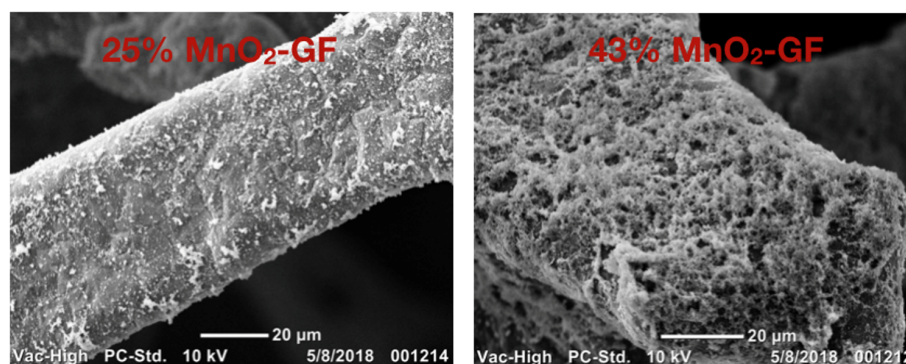


Figure 3.10.: SEM images of the GF- $\text{MnO}_2$  surface after combustion for 75% NC-GF loading.

Fig. 3.10 shows the SEM images of the GF- $\text{MnO}_2$  surface after combustion, for two different  $\text{MnO}_2$ -GF loadings: 25% and 43%. In both the cases, the NC-GF loading

was kept fixed at 75%. As can be seen, both the  $\text{MnO}_2$  particles and GF strut walls remained unburned after the combustion process, thus, confirming that  $\text{MnO}_2$  and GF act only as chemical and physical catalysts, respectively, without being consumed in the combustion process.

### 3.2.2 Surface Temperature Measurements

Thermocouple measurements were performed next to determine the effect of the addition of  $\text{MnO}_2$  and GF on the NC's peak surface burning temperature. A K-type thermocouple was used for the measurements. For Pure NC, a peak surface temperature of  $613 \pm 30$  K was obtained. With the addition of  $\text{MnO}_2$ , a slight decrease in the peak surface temperature was observed but with the GF, the decrease observed was significant. For example, with 75% and 55% NC-GF loadings, peak surface temperatures of  $555 \pm 20$  K and  $504 \pm 20$  K were obtained. However, after the  $\text{MnO}_2$ -coating, only a slight decrease to  $543 \pm 17$  K (75% NC-GF) and  $496 \pm 20$  K (55% NC-GF) was observed, for 14% and 29%  $\text{MnO}_2$ -NC loadings, respectively. Moreover, CEA calculations were also conducted to estimate the effect of the addition of GF and  $\text{MnO}_2$  on the adiabatic flame temperature. Similar to the trends observed in the peak surface measurements, a slight decrease in the adiabatic flame temperature was obtained with the addition of  $\text{MnO}_2$  particles but with the addition of GF, a significant decrease was observed. For example, for pure NC, an adiabatic flame temperature of 2481 K was obtained. For 10%  $\text{MnO}_2$ -NC loading (without any GF), the adiabatic flame temperature was decreased only slightly to 2374 K but with the addition of GF, the adiabatic flame temperatures were decreased to 1650 K and 1140 K, respectively, for 75% NC-GF and 55% NC-GF loadings ( $\text{MnO}_2$ -NC loading was kept fixed at 10%).

## 4. COMBUSTION ON A MICRO-CHIP

### 4.1 Introduction

During the past decade, research on combustion at micro- and nano-scales has received great interest. A number of applications have been proposed for small-scale combustion devices: micro-thrusters, micro-heaters, actuators, sensors, portable power devices and unmanned micro-vehicles [174]. At smaller scales, the surface-to-volume ratio increases and the combustion becomes difficult to be initiated and sustained because of the increased heat loss from the combustion chamber walls and strong wall-flame kinetic interactions [175, 176]. Thus, the successful development of small-scale combustion-based power devices continues to face significant challenges. Loyal to the scaling law, combustion should be impossible at nanoscales because the heat loss would profoundly dominate the chemical reactions. However, Svetovoy et al. [177, 178] showed that hydrogen and oxygen gases could be ignited spontaneously inside nanobubbles with diameters less than 150 nm. These nanobubbles were produced from short-time ( $< 100 \mu\text{s}$ ) water electrolysis by applying high-frequency square alternating sign voltage pulses, which resulted in  $\text{H}_2$  and  $\text{O}_2$  gas production above the same electrode.

Fig. 4.1 shows how the bubble production is affected by changing the polarity and frequency of the applied voltage pulses. The left images correspond to alternating sign voltage pulses where both  $\text{H}_2$  and  $\text{O}_2$  gases were produced, the middle images correspond to negative sign voltage pulses where only  $\text{H}_2$  gases were produced and the right images correspond to positive sign voltage pulses where only  $\text{O}_2$  gases were produced. As can be seen, for frequencies  $> 20 \text{ kHz}$  and only for alternating polarity pulses, the bubble production has reduced drastically and has completely disappeared

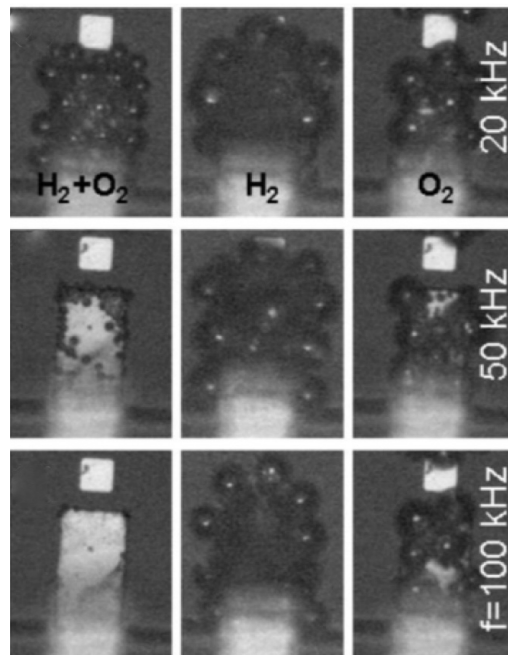


Figure 4.1.: Gas production as a function of the polarity and frequency of the voltage pulses. Left: alternating sign, middle: negative sign and right: positive sign voltage pulses [177].

at a frequency of 100 kHz, although the amount of faradaic current measured remained unchanged, signifying that combustion might have taken place. In addition, the electrode surface was also found to be considerably modified after the application of alternating sign voltage pulses for frequencies  $> 20$  kHz. The surface modification was attributed to have a mechanical origin due to the combustion of  $H_2$  and  $O_2$  gases. The chemical origin for the wear was disregarded as the wear was observed for a range of electrode materials tested. Moreover, since the wear was not observed for single polarity pulses or for alternating sign pulses with frequencies  $< 20$  kHz, the electrochemical origin for the wear was also not possible. The authors also measured the increase in the temperature of the electrode surface by determining the temperature of the liquid surrounding the electrodes using a thin gold probe and a slight rise in the resistance of the probe was observed, thus, further confirming combustion.

In another study, to demonstrate the practicality of nanobubble combustion, Svetovoy et al. [179] fabricated a microfluidic device, in which the nanobubbles were produced inside a closed microchamber with dimensions  $100 \times 100 \times 5 \mu\text{m}^3$ . The top of the chamber was covered by a glass but the bottom consisted of a transparent flexible SiN (silicon nitride) membrane (500 nm thick). And again, the combustion process was initiated by applying alternating sign voltage pulses with frequencies  $> 20$  kHz. In contrast to their previous study described above, much larger temperature changes were observed, which were attributed to the small thermal mass of the device being used. Moreover, the amount of temperature change observed was found to increase with an increase in the frequency of applied voltage signals. This was due to the fact that with an increase in frequency, the residence time for the bubble growth at the end of one cycle decreases and thus, the  $\text{H}_2$  and  $\text{O}_2$  gases were contained inside bubbles with much smaller sizes. These smaller sizes then translate into higher bubble pressures, as given by the Laplace-Young equation and in turn, increases the probability of combustion. The effect of Joule heating on the temperature changes observed was also considered and was obtained to be negligible as compared to the amount of heat released from the  $\text{H}_2/\text{O}_2$  combustion. Moreover, since joule heating does not depend on the frequency of the applied voltages, the nature of the temperature changes observed further confirms combustion inside the nanobubbles. Postnikov et al. [180] conducted a similar study using a closed microchamber but instead extended the electrolysis process to much longer times up to 1 ms. After a delay of 300-600  $\mu\text{s}$ , micro-bubbles of 5-20  $\mu\text{m}$  in diameter were observed to be formed in-between the electrodes. The amount of delay observed was found to increase with either an increase in the frequency or with a decrease in the voltage of the applied signal. Moreover, the micro-bubbles were only detected for frequencies greater than 100 kHz and existed for about 3  $\mu\text{s}$  after which, a significant pressure jump, as determined from the membrane deflection, was observed. The authors attributed this pressure jump to the combustion of  $\text{H}_2/\text{O}_2$  gases inside the micro-bubbles. For a typical combustion event:  $\Delta P \sim 0.2$  bar and  $\Delta t \sim 3 \mu\text{s}$ , which using the chamber vol-

ume roughly comes out to be around 1 nJ of energy being released. However, the mechanism responsible for this combustion event was not known.

Apart from the experimental evidences, a complete theoretical understanding of the combustion process inside the nanobubble is still missing. The only numerical study that have been performed was conducted by Prokaznikov et al. [181], in which the continuum-scale kinetic models were used to study the combustion process. The key mechanism identified was the dissociation of  $\text{H}_2$  molecules at the bubble surface producing H radicals, which in turn initiated and sustained the combustion process at room temperature. It was argued that a bubble surface is not neutral but negatively charged [182–185] and it is these charged centers at the liquid-vapor interface that leads to the dissociation of  $\text{H}_2$  and  $\text{O}_2$  gases into H and O radicals, respectively. These negative charges are related to the  $\zeta$ -potential of the bubbles and could either be attributed to the adsorption of  $\text{OH}^-$  ions or to the anisotropy of water hydrogen-bonding at the bubble interface [186, 187].

If Svetovoy's [177–179] conclusion of spontaneous  $\text{H}_2/\text{O}_2$  combustion inside the nanobubbles is indeed true, then these nanobubbles would be the first nanoscale devices in which the combustion has taken place. As stated above, loyal to the scaling law, combustion should be impossible at nanoscale because the heat loss would profoundly dominate the chemical reactions. Thus, before we could truly understand the mechanism behind the nanobubble combustion, we must first make sure that combustion has indeed taken place.

Hence, as a first step, a micro-chip was fabricated to conduct small-scale electrolysis of water along with an in-built 10 nm thick platinum thermal sensor underneath the combustion electrodes to measure the temperature changes occurring during the combustion process. The bubble production as a function of the voltage, polarity, frequency and duty cycle of the applied square pulses was investigated. Significant

amount of bubbles were observed to be formed up to 30 KHz but after that the bubble production decreased drastically. Moreover, the amount of heat released and the temperature changes measured were also found to increase above this threshold frequency of 30 kHz and for each frequency, the temperature rise obtained was maximized at a duty cycle of 0.5 (stoichiometric H<sub>2</sub>/O<sub>2</sub> production).

The findings of our experimental work mentioned above were consistent with that of Svetovoy et al. [177, 178], thus, further confirming the occurrence of combustion inside the nanobubbles. However, the mechanisms that contributed to this spontaneous combustion were still not clear. Thus, as a next step, non-reactive molecular dynamic simulations were conducted to understand how the pressure inside a nanobubble is affected by the presence of these dissolved external gases (H<sub>2</sub> and O<sub>2</sub>). Knowing the bubble pressure is a prerequisite towards understanding the combustion process.

For a nanobubble to be completely stable in a liquid, it needs to be in both mechanical and chemical equilibrium simultaneously. The application of the Laplace-Young equation assumes only mechanical equilibrium. However, for the bubble to be in chemical equilibrium, the chemical potential of the gases inside and outside the bubble must also be equal, which requires the liquid to be supersaturated with bubble gases [188]. This is because of the curved interface of the nanobubble and surface tension forces, which increases the pressures inside nanobubbles, and higher the pressure, higher would be the chemical potential of the bubble gasses. The supersaturation ( $S$ ) is defined as the ratio of concentration of a gas ( $C$ ) in the liquid to the saturated concentration of the gas at 1 atm ( $C^*$ ) i.e.  $S = C/C^*$ . Moody et al. [189] and He et al. [190] conducted monte-carlo simulations to calculate the surface tension of supersaturated Lennard-Jones planar liquid-vapor interfaces. They found the surface tension value to decrease with increasing supersaturation and to vanish at the vapor spinodal. Thus, the surface tension of water needs to be modified according to the local supersaturation value in order to get the correct pressure difference across the

nanobubble surface. All of the previous studies [189,190] relating to supersaturation have been performed for pure systems. However, in this work, the curved interface of a nanobubble was used to determine the surface tension of water as a function of the concentration of dissolved  $O_2$  gaseous molecules. Here only  $O_2$  molecules were considered but the qualitative behavior of the surface tension value with other types of gases like  $H_2$  would be similar. The surface tension of water was found to decrease with an increase in the amount of supersaturation, thus, the internal pressure inside a nanobubble is much smaller than what would have been predicted using the planar-interface surface tension value of water. Nevertheless, the pressures were still very high, which could provide a suitable environment for the spontaneous ignition and combustion to occur.

Chemical reactions, in general, cannot be initiated at room temperature without a stimulation such as an ignition source. In practical macroscale combustion devices, once the ignition takes place, the combustion drives up the temperatures (generally over 1000 K). However, at nanoscales, the surface to volume ratio increases, which in turn increases the heat loss and as a result, the temperature of the gases will not increase significantly due to the fast heat diffusion. The ignition and combustion process inside a nanobubble is believed to be distinctively different from the macroscopic high temperature combustion that has been studied widely. In the present study, reactive molecular dynamic simulations were used to explore the mechanism for the spontaneous combustion of  $H_2/O_2$  gases inside nanobubbles for several reasons. First, due to the constraints of dimensions (since the nanobubbles were restricted to a few hundred nanometers), conventional modeling, numerical simulations, or kinetic studies were not suitable. Second, many of the physical and chemical processes taking place inside the nanobubbles were unknown and, hence, could not be modeled. For example, the heat diffusion rates, bi- and tri-molecular reaction rate constants, and bubble pressures were all unknown. Third, the surface-assisted dissociation process at the gas/liquid interface was unclear; although it was believed to be due to the

dissociation of  $H_2$  molecules at the bubble surface [181], the exact mechanism causing this dissociation was not well understood. Thus, using MD simulations, the various different ways through which the H radicals could be produced were examined and compared. Motivated by the above, the effects of surface-assisted dissociation of  $H_2$  and  $O_2$  gases and the initial system pressure on the ignition and reaction kinetics of the  $H_2/O_2$  system were studied. Moreover, in contrast to the work of Prokaznikov et al. [181], which explored the spontaneous combustion of  $H_2/O_2$  gases from the chemical kinetics perspective, no assumptions regarding bi- and tri-molecular reaction rate constants were made as the combustion process was simulated using the first principles derived reactive force field, ReaxFF, which includes both the physical changes such as thermal/mass transport and the chemical changes such as bond breaking and forming. In addition, the temperature of the  $H_2/O_2$  system was not held constant at 300 K but was allowed to be varied in order to compare the rates at which the heat was being lost vs the rate at which the heat was being produced from the exothermic reactions.

## 4.2 Experimental Study: MEMS Thermal Sensor

A 10 nm thick Pt thermal sensor was fabricated directly underneath the combustion electrodes to facilitate the temperature measurements. In addition, the electrolysis process was also viewed optically using a microscope to determine how the bubble production was affected by changing the frequency, voltage, polarity and duty cycle of the applied square pulses.

### 4.2.1 Fabrication

For fabrication, a double sided, polished, 500  $\mu\text{m}$  thick, 4 inch in diameter, P-type silicon wafer was used. A 2 metal layer design was employed, where the bottom metal layer acted as the thermal sensor and the top metal layer as the combustion electrodes. For the thermal sensor, platinum (Pt) was selected as the metal type because of its

high electrical resistivity and thermal coefficient of resistance values, whereas for the combustion electrodes, gold (Au) was used because of its weak yield strength so that a significant wear of the electrodes could be detected during the combustion process. In the following, a step by step description of the fabrication process is given:



Figure 4.2.: (Step 1)  $\text{Si}_x\text{N}_y$  deposition using the LPCVD technique.

**Step 1:** First, on the top of the Si wafer, a 150 nm thick  $\text{Si}_x\text{N}_y$  (silicon nitride) layer was deposited using the LPCVD (low pressure chemical vapor deposition) technique. The deposition was performed at a process temperature and pressure of 770 °C and 200 mTorr, respectively, and a combination of two gases was used i.e.  $\text{NH}_3$  (ammonia) at 200 sccm and  $\text{SiH}_2\text{Cl}_2$  (dichlorosilane) at 80 sccm. At these conditions, a growth rate of 37 Å/min was obtained. There were several advantages for depositing  $\text{Si}_x\text{N}_y$  on the top of the Si wafer such as better adhesion of the metal layers, electrical insulation, prevention against oxidation and good barrier against moisture penetration [191].

**Step 2:** A 10 nm thick Pt layer was then deposited and patterned on the top of the  $\text{Si}_x\text{N}_y$  layer using the lift-off technique, as will be explained next. First, a 2 μm thick positive photo-resist (AZ 1518) was spin-coated onto the nitride layer and patterned using the contact photolithography method. For the lithography, a UV light of wavelength 405 nm was used and the exposure time was set to 30 s. Moreover, a dark field mask was used and the photo-resist was developed using a solvent called MF-26A for 30 s. After patterning the photo-resist, a 10 nm/3 nm thick Pt/Ti layer was deposited on the top using an E-beam evaporator. The Ti (titanium) layer was deposited below the Pt layer for adhesion purposes. After the metal deposition, the wafer was soaked in PRS-2000 at 90 °C overnight, which gave enough time for all

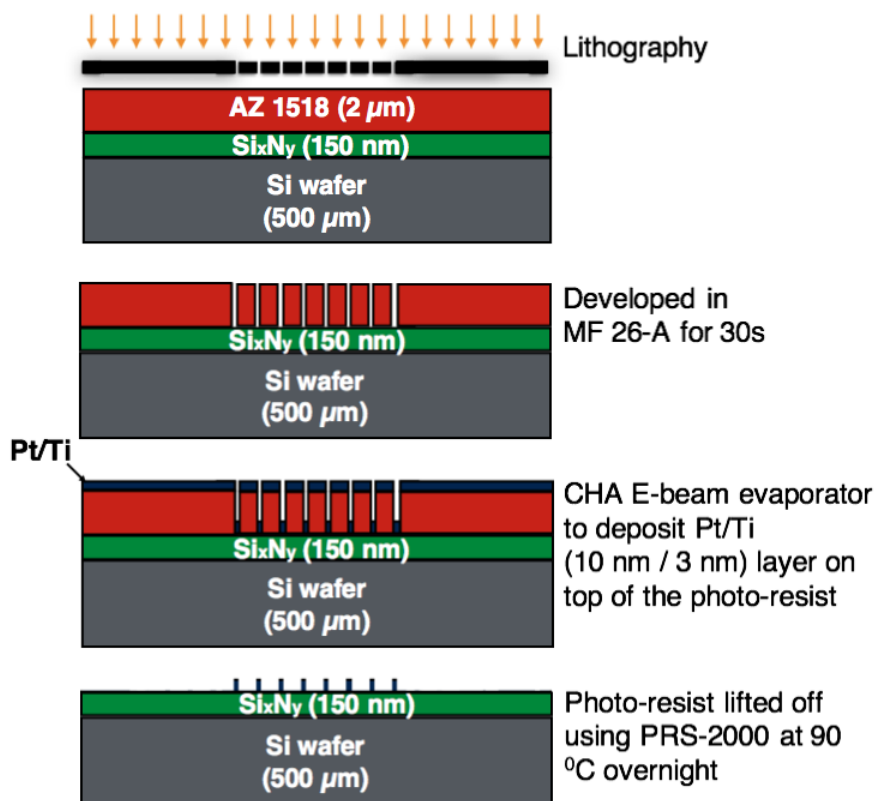


Figure 4.3.: (Step 2) Pt/Ti layer deposition using the Lift-off technique.

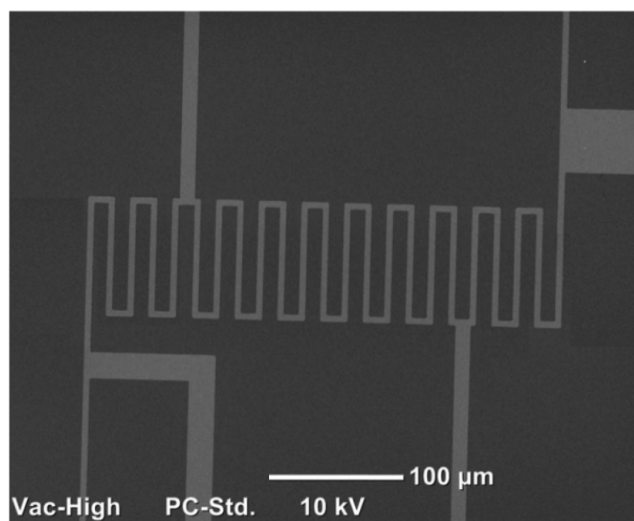


Figure 4.4.: Top view of the serpentine shaped Pt thermal sensor. Length and width of one rectangular unit: 100  $\mu\text{m}$   $\times$  6  $\mu\text{m}$ .

the photo-resist to completely lift-off, leaving the desired Pt thermal sensor pattern behind, as shown in Fig. 4.4. As can be seen, the Pt thermal sensor layer was designed in the shape of a serpentine, which was to increase its zero-current value of resistance (8.6 k $\Omega$ ) so that during the combustion process even small amount of changes in the resistance values could easily be detected.

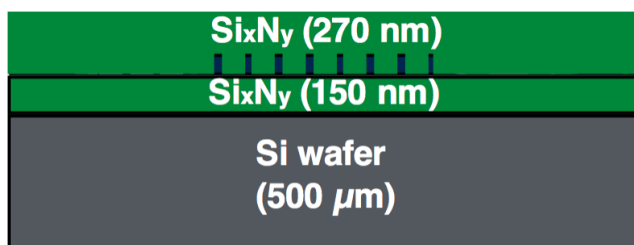


Figure 4.5.: (Step 3) Si<sub>x</sub>N<sub>y</sub> deposition using the PECVD technique.

**Step 3:** After the Pt/Ti metal deposition, another Si<sub>x</sub>N<sub>y</sub> layer (270 nm thick) was deposited to electrically insulate the Pt thermal sensors from the gold combustion electrodes (to be deposited). However, in contrast to the previously deposited Si<sub>x</sub>N<sub>y</sub> layer, a PECVD (plasma enhanced chemical vapor deposition) technique was used instead of the LPCVD. This was done to facilitate the Si<sub>x</sub>N<sub>y</sub> deposition at low temperatures (300 °C) instead of high temperatures (770 °C), which was required because of the presence of the metal layers. For the PECVD method, the deposition was performed at a temperature and pressure of 300 °C and 600 mTorr, respectively, and a combination of two gases was used i.e. NH<sub>3</sub> at 100 sccm and SiH<sub>4</sub> (silane, 10% in N<sub>2</sub>) at 120 sccm. Moreover, the RF power applied was set to 100 W and an on/off technique was used for the depositions. At these conditions, a deposition rate of 20 nm/min was obtained.

**Step 4:** Next, the gold combustion electrode layer was deposited and patterned using the similar lift-off technique, as was used in the case of the Pt thermal sensor layer. And again, a 3 nm thick Ti layer was deposited below the gold layer for adhesion purposes. The thickness of the gold layer was set to 100 nm to ensure that enough metal was available for wire-bonding and conducting electrolysis.

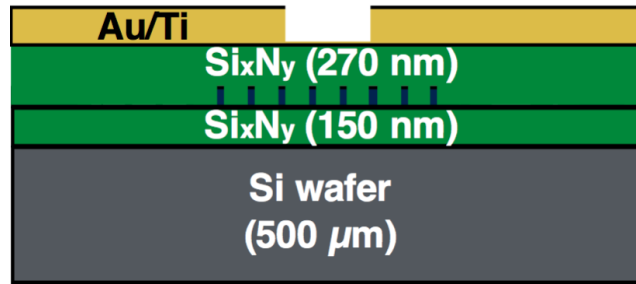


Figure 4.6.: (Step 4) Au/Ti layer deposition using the Lift-off technique.

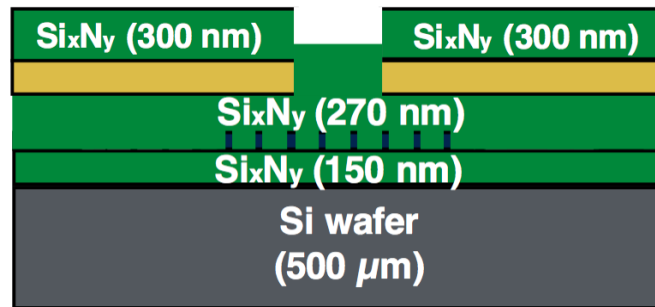


Figure 4.7.: (Step 5)  $\text{Si}_x\text{N}_y$  deposition using the PECVD technique.

**Step 5:** Finally, on the top of the gold layer, a 300 nm thick  $\text{Si}_x\text{N}_y$  layer was deposited, using again the PECVD technique. After which, openings were made in this nitride layer for the combustion electrodes and probing pads using the RIE (reactive-ion etching) tool. The etching was performed using a combination of  $\text{O}_2$  and  $\text{SF}_6$  gases (50 sccm each and at a total pressure of 50 mTorr) with the RF power being set to 100 W. At these conditions, an etching rate of 10 nm/min was obtained. For the combustion electrodes, square-shaped openings ranging from  $20 \times 20 \mu\text{m}^2$  to  $80 \times 80 \mu\text{m}^2$  were made and for all the cases fabricated, a separation distance of  $150 \mu\text{m}$  was used. Moreover, the thicknesses of the  $\text{Si}_x\text{N}_y$  and metal layers, as given in steps 1-5, were measured using Filmetrics and KLA-Tencor P-7 Profilometer, respectively.

#### 4.2.2 Experimental Setup

The side and top view of a single pair of gold micro-electrodes is shown in Fig. 4.8. After the fabrication process, the experimental setup was quite straight forward.

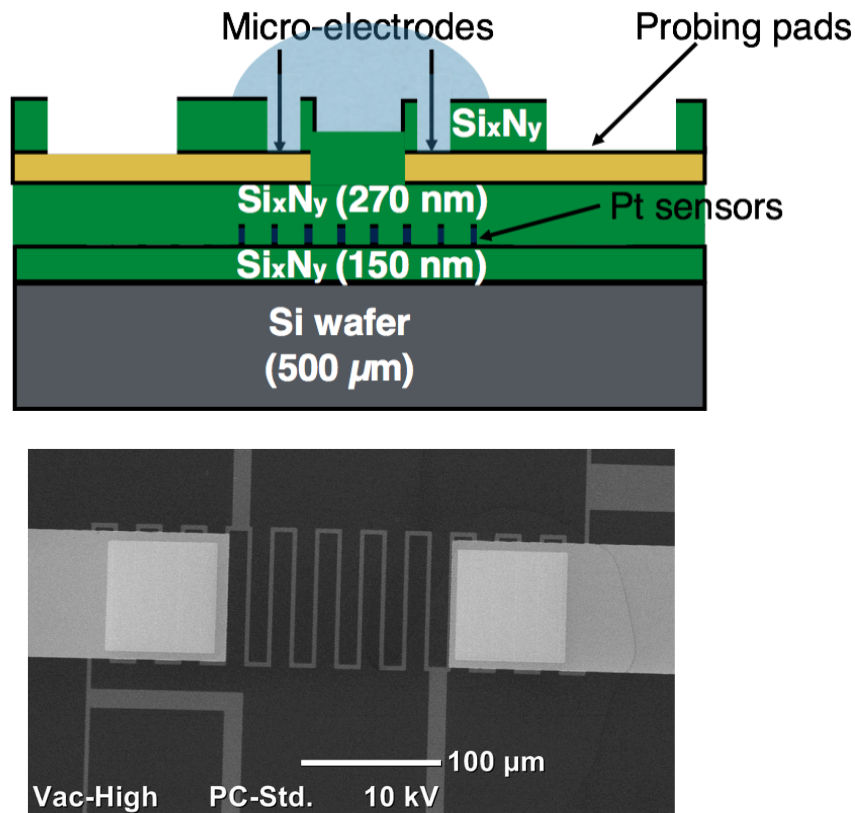


Figure 4.8.: The side and top view of a single pair of gold micro-electrodes.

A drop of water (1 M solution of  $\text{Na}_2\text{SO}_4$ ) was placed on the top of gold micro-electrodes across which the electrolysis took place, the square voltage pulses were applied through the probing pads and the temperature changes were measured using the Pt thermal sensors underneath. The voltage, frequency, duty cycle and polarity of the applied pulses were varied from 1-7 V, 1-500 kHz, 0.4-0.6 and single-to-alternate, respectively. Moreover, for the electrolysis, threshold voltages ranging from 3.5 V to 5 V were obtained, which were much higher than the water's equilibrium potential of 2.06 V at standard conditions [192]. The reason for this discrepancy could be attributed to the small size and planar arrangement of the electrodes used [177, 178]. In addition, the electrolysis was conducted only for short times:  $< 2000 \mu\text{s}$ . Fig. 4.9 shows the zoomed out top view of a single pair of gold micro-electrodes and Fig. 4.10 shows the side view of the device at a location across the probing pads for the Pt thermal sensors.

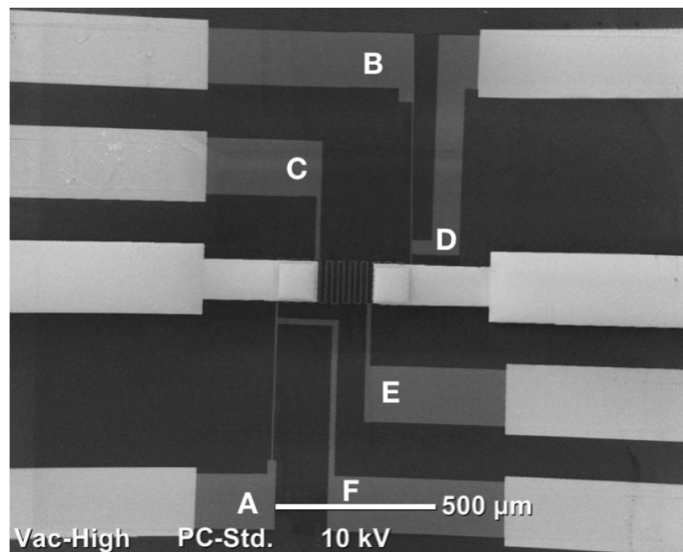


Figure 4.9.: Zoomed out, top view of a single pair of gold micro-electrodes.

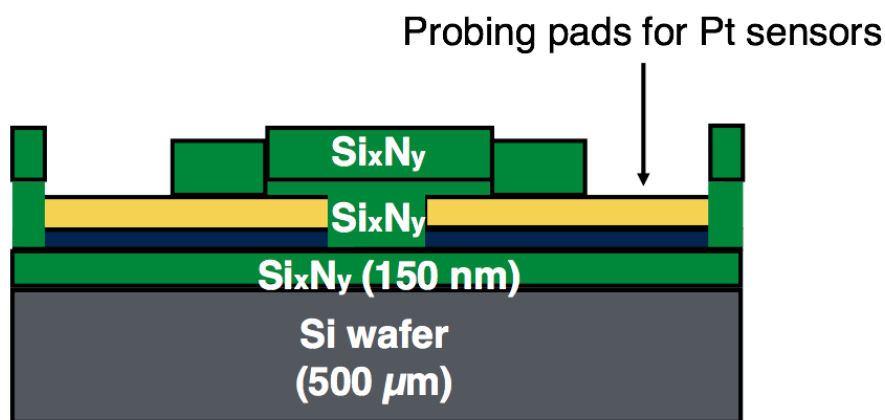


Figure 4.10.: Side view of the device at a location across the probing pads for the Pt thermal sensors.

For packaging, the silicon wafer was mechanically diced into  $7 \times 17 \text{ mm}^2$  chips, with each chip consisting of 6 pairs of gold micro-electrodes and a single pair of gold micro-heater. This gold micro-heater, as shown in Fig. 4.11, was used for the calibration purposes as will be explained later in this section. Each chip was then wire-bonded to a custom PCB board, as shown in Fig. 4.12.

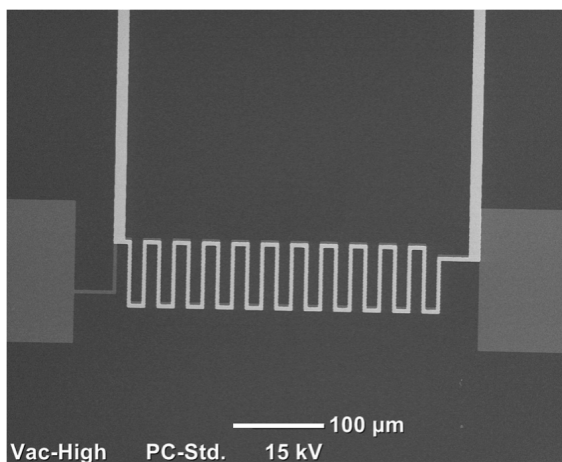


Figure 4.11.: Gold micro-heater for calibration purposes.

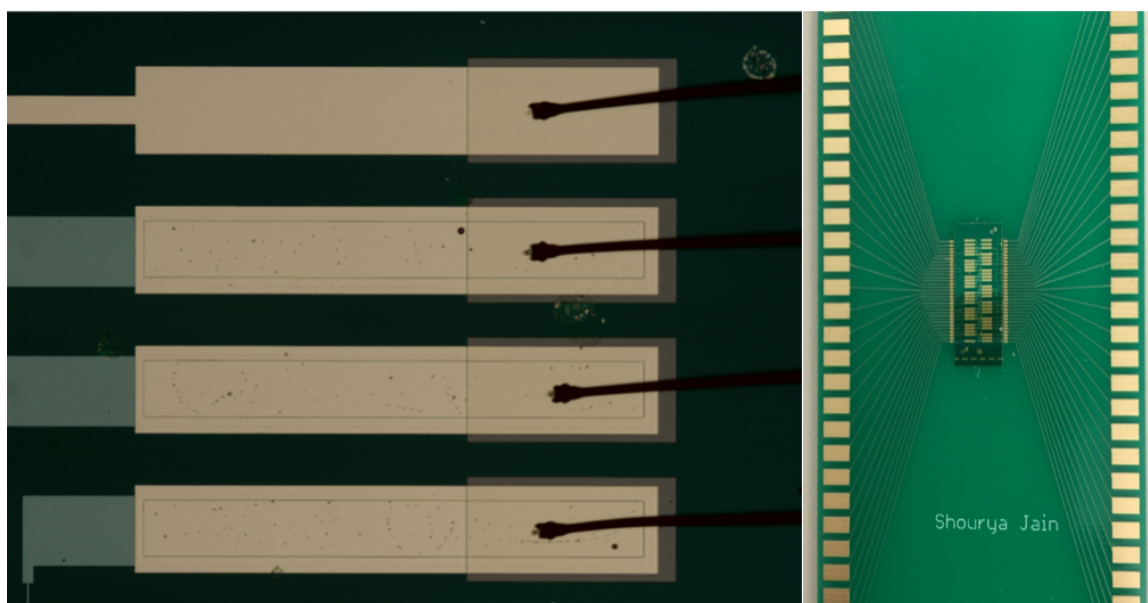


Figure 4.12.: Packaging of the micro-chip.

Before conducting electrolysis, two types of calibrations were performed:

(1) Resistance of the Pt thermal sensor vs. temperature: Each chip (before wire-bonding to the PCB board) was heated on a calibrated thermal stage in vacuum up to 400 K in increments of 10 K. At each incremental temperature step, the four-point probe technique (Fig. 4.9) was used to calculate the resistance of the Pt layer. A small amount of DC current of  $100 \mu\text{A}$  was applied across the Pt layer through the

points A and B, and the corresponding change in the resistance was then determined by measuring the voltage drop across the points D and F. A TCR (thermal coefficient of resistance) value of  $1 \pm 0.1 \text{ m}\Omega/\text{K}$  was obtained for the Pt layer.

(2) Resistance of the Pt thermal sensor vs. input power: Next, using the in-built micro-heater, as shown in Fig. 4.11, the resistance of the Pt layer was calibrated to the heater input power. In order to replicate the heat conduction in the micro-heater, the thickness of the gold and Pt layers were kept same as that in the actual device. The joule heating of the gold serpentine layer was used as the power source. Powers ranging from  $4 \times 10^4$  to  $10^6 \text{ W/m}^2$  (DC currents from 2 mA to 10 mA) were applied across the gold layer, and the corresponding changes in the resistance of the Pt layer were measured using the four-point probe technique. This change in resistance was then converted to the change in temperature using the previous resistance vs. temperature calibration.

Fig. 4.13 shows the schematic of the experimental setup used and as can be seen, it consists of two main circuits:

(1) The combustion circuit, across which the square voltage pulses were applied. The amount of current flowing through this circuit, as a result of the electrolysis, was calculated by measuring the voltage drop across a dummy resistance  $R_0$  ( $820 \Omega$ ) using an oscilloscope. In Fig. 4.13,  $R_1$  is the effective resistance across the planar gold micro-electrodes during the electrolysis process and  $C$  is the capacitance due to the charging and discharging of the electrical double layer near the electrode surface. Moreover, the value of  $R_0$  ( $820 \Omega$ ) was kept much smaller as compared to the  $R_1$  value (6-11 k $\Omega$  for  $20 \times 20 \mu\text{m}^2$  electrodes) to avoid loading the circuit.

(2) The second circuit consist of the Pt layer across which a small amount of DC current of  $100 \mu\text{A}$  was applied and the amount of change in the resistance of the Pt

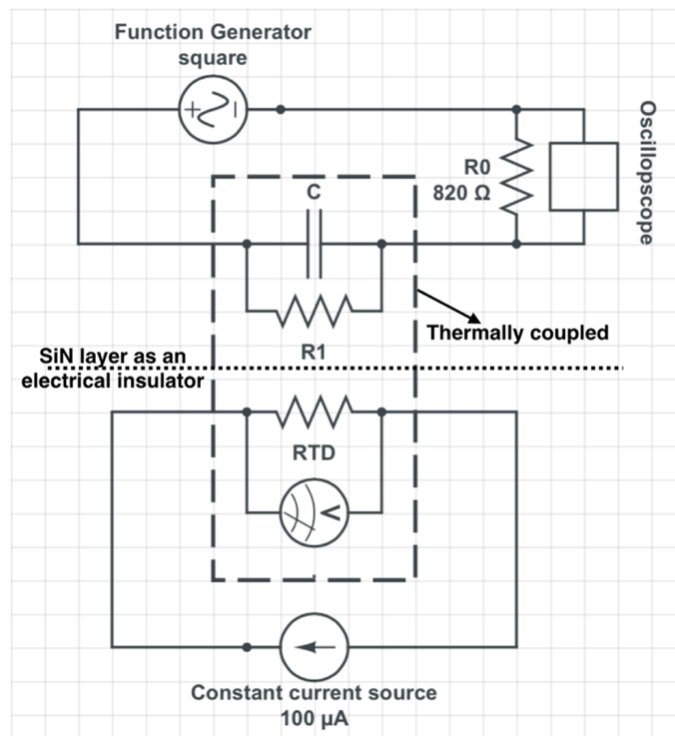


Figure 4.13.: Schematic of the experimental setup.

layer was then determined by measuring the voltage drop across this layer. The DC current was applied using the Keithley 2400 source meter, whereas the voltage drop was measured using the Keithley (2000) 6 1/2 digit multimeter. Moreover, special precautions were made to ensure that the DC current source was floating so that the two circuits would be electrically independent. In addition, the two circuits were electrically insulated from one another using a 270 nm thick  $\text{Si}_x\text{N}_y$  layer.

### 4.2.3 Results and Discussion

Fig. 4.14 shows the effect of frequency on the current response curves obtained, for alternating polarity pulses. The voltage and duty cycle were kept fixed at 7 V and 0.5, respectively, and for the particular case shown,  $20 \times 20 \mu\text{m}^2$  electrodes were used. As can be seen, the measured currents were made up of two components: faradaic and non-faradaic. The faradaic current was due to the electrochemical reactions occurring

at the electrode surface and as a result, remained constant, whereas the non-faradaic current was due to the charging and discharging of the electrical double layer formed near the electrode surface and thus, had an exponential decaying character associated with it [178]. The total current response can be written as:

$$I_T = I_F + I_{NF} \exp\left(\frac{-t}{\tau}\right) \quad (4.1)$$

In the above equation,  $I_T$  is the total current,  $I_F$  is the faradaic current,  $I_{NF}$  is the non-faradaic current constant and  $\tau$  is the time constant. Fitting Eqn. 4.1 to the

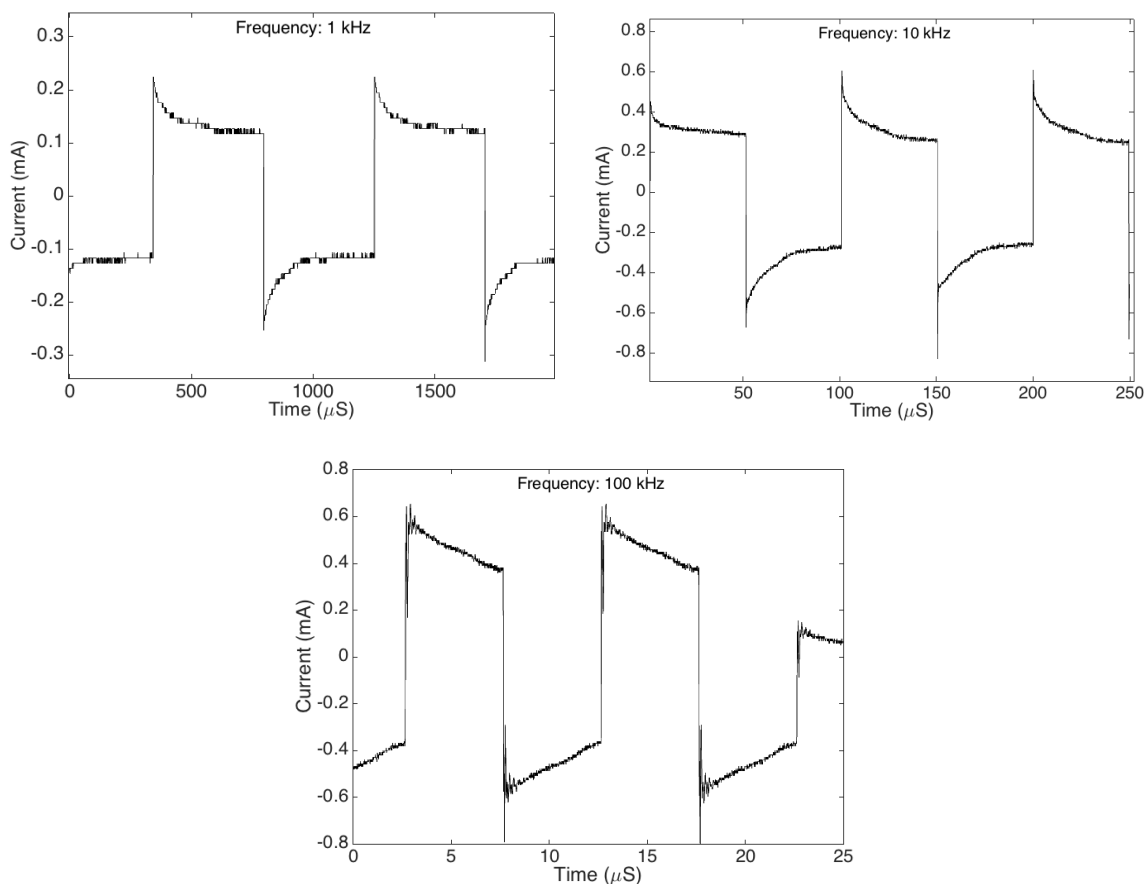


Figure 4.14.: Current response curves for 1 kHz, 10 kHz and 100 kHz. The particular case shown corresponds to using  $20 \times 20 \mu\text{m}^2$  electrodes. The voltage and duty cycle were kept fixed at 7 V and 0.5, respectively.

measured currents shown in Fig. 4.14, steady state faradaic currents ( $I_F$ ) and time constants ( $\tau$ ) of 0.12 mA, 0.25 mA and 0.28 mA, and 72  $\mu\text{s}$ , 12  $\mu\text{s}$  and 4.6  $\mu\text{s}$  were obtained for the frequencies 1 kHz, 10 kHz and 100 kHz, respectively. For the 1 kHz frequency, much lower steady state faradaic currents were observed as compared to that observed for the 10 kHz and 100 kHz frequencies. This could be attributed to the fact that with a decrease in frequency, the residence time for the bubble growth at the end of one cycle increases, thus, the  $\text{H}_2$  and  $\text{O}_2$  gases were contained inside bubbles with much larger sizes, which in turn increased the electrode's surface bubble coverage and as a result, limited the amount of electrochemical reactions that could place. Another reason could be attributed to the absence of combustion at lower frequencies, which even further increased the bubble coverage. Moreover, a decreasing trend was observed in the time constant values ( $\tau$ ) as a function of the frequency, which indicated that not all adsorption sites were filled in such a short time [178]. In addition, the measured current curves, as shown in Fig. 4.14, were symmetric i.e. similar time constants and faradaic currents were obtained from the positive and negative parts of the current curves. However, for single polarity pulses, the positive and negative parts of the current curves were not symmetric, reflecting the dependence of the capacitance of the electrical double layer on the applied potential. These findings were consistent with that observed by Svetovoy et al. [177–179] in which, for an alternating polarity pulse of 40 kHz and 6 V, symmetrical current responses with a time constant of 4  $\mu\text{s}$  were obtained.

Fig. 4.15 shows how the current response curves are affected by changing the electrode surface area. The voltage, duty cycle and frequency of the applied alternating pulses were kept fixed at 7 V, 0.5 and 50 kHz, respectively. The steady state faradaic current was found to increase from 0.28 mA to 0.5 mA as the electrode surface area was increased from  $20 \times 20 \mu\text{m}^2$  to  $80 \times 80 \mu\text{m}^2$ . However, in terms of the current density, a decrease was observed from 70 A/cm<sup>2</sup> to 8 A/cm<sup>2</sup>. The increase in the absolute value of the faradaic current with the electrode surface area was expected

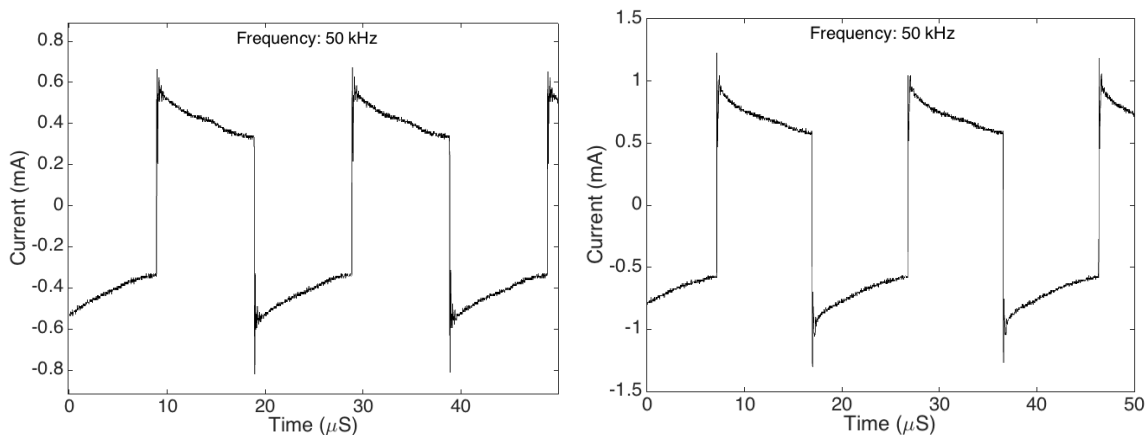


Figure 4.15.: Current response curves for two different electrode surface areas. Left:  $20 \times 20 \mu\text{m}^2$  and right:  $80 \times 80 \mu\text{m}^2$ . The voltage, duty cycle and frequency of the applied alternating pulses were kept fixed at 7 V, 0.5 and 50 kHz, respectively.

because of the increased gold surface area available for the electrochemical reactions to occur. However, the increase observed wasn't proportional to the increase in the surface area, which could be attributed to the fact that the resistance  $R_1$  between the planar electrodes was initially very high (6-11 k $\Omega$  for  $20 \times 20 \mu\text{m}^2$  electrodes) and thus, any improvements in this resistance value due to an increase in the electrode surface area produced only minor changes in the faradaic currents. Moreover, for both the electrodes, similar time constant values of 6.5  $\mu\text{s}$  ( $20 \times 20 \mu\text{m}^2$ ) and 5.5  $\mu\text{s}$  ( $80 \times 80 \mu\text{m}^2$ ) were obtained. This was expected, since the charging/discharging rates of the electrical double layer controls the time constant values and as a result, for a given applied potential, the time constant values were mostly dependent on the frequency of the applied pulses.

Fig. 4.16 shows the effect of frequency on the temperature of the Pt thermal sensor layer. The voltage and duty cycle of the applied signals were kept constant at 7 V and 0.5, respectively, and the particular case shown corresponds to using  $20 \times 20 \mu\text{m}^2$  electrodes. As can be seen, the temperature starts rising only above a threshold frequency of 30 kHz. Initially, the temperature increases linearly but then

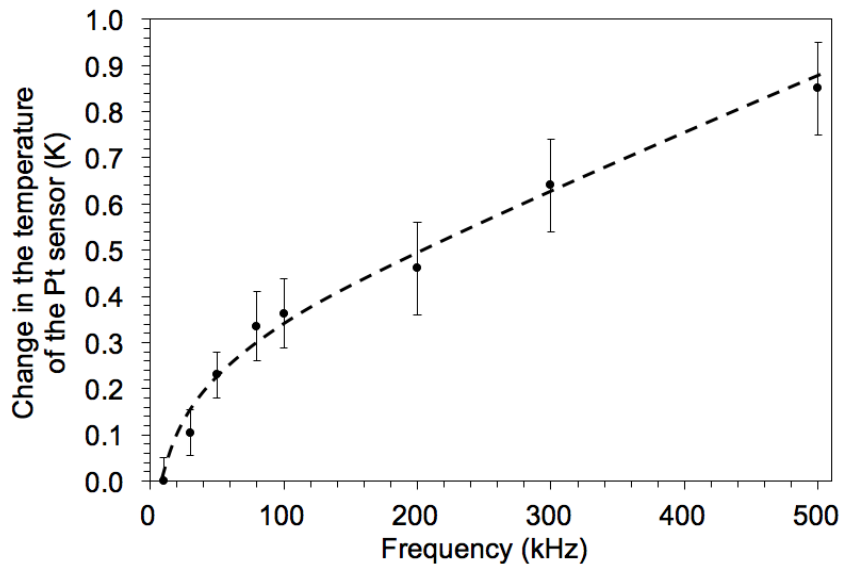


Figure 4.16.: Effect of frequency on the temperature of the Pt thermal sensor. The particular case shown corresponds to using  $20 \times 20 \mu\text{m}^2$  electrodes. The voltage and duty cycle of applied alternating pulses were kept fixed at 7 V and 0.5, respectively.

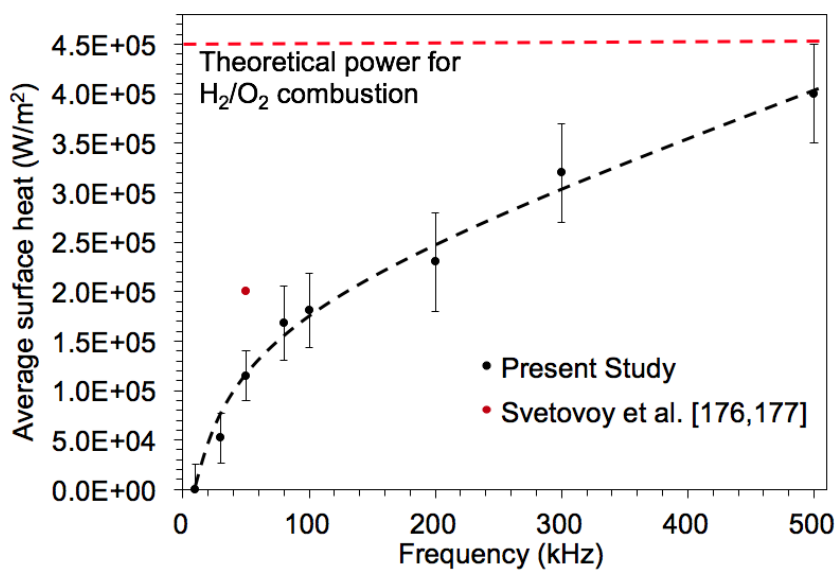


Figure 4.17.: Effect of frequency on the average surface heat produced. The particular case shown corresponds to using  $20 \times 20 \mu\text{m}^2$  electrodes. The voltage and duty cycle of the applied alternating pulses were kept fixed at 7 V and 0.5, respectively.

a plateaued behavior was obtained, with temperature changes up to 0.85 K. Three sets of run were made for each data point and an accuracy of at least  $\pm 0.1$  K was obtained. A similar observation was made while viewing the electrolysis process under a microscope, where significant amount of bubbles were produced up to 30 kHz but after that the bubble production decreased drastically, although the faradaic current, as shown in Fig. 4.14, remained unchanged. Thus, confirming that the rise in temperature observed was indeed from the combustion of  $H_2/O_2$  gases contained inside the nanobubbles. To further confirm, the average surface heat values produced were also plotted, as shown in Fig. 4.17, and similar to the temperature changes observed, initially a linear increase was obtained followed by a plateaued behavior. This plateaued behavior could be explained from the pressure effect. With an increase in frequency, the residence time for the bubble growth at the end of one cycle decreases, and thus, the  $H_2$  and  $O_2$  gases were contained inside bubbles with much higher pressures which in turn increased the combustion probability. However, above a certain point, further increase in the pressure does not significantly increase the combustion probability [193] and hence, a plateaued behavior in the temperature/surface heat values was observed. Surface heat values up to  $4.0 \times 10^5$  W/m<sup>2</sup> were obtained (500 kHz), which was in close agreement with the theoretical power of  $4.5 \times 10^5$  W/m<sup>2</sup> calculated for the  $H_2/O_2$  combustion using a steady state current value of 0.28 mA and for the  $20 \times 20$   $\mu\text{m}^2$  electrodes. However, as can be seen from Fig. 4.17, the surface heat value obtained by Svetovoy et al. [177, 178], for a frequency of 50 kHz, was much higher as compared to the surface heat value obtained in this work, which could be attributed to a number of factors such as the electrode shape, separation distance, electrode surface area, deposition quality, thickness of the metal layers and the measurement technique used. The accuracy of the surface heat measurements, as deduced from the temperature measurements, came out to be at least  $\pm 5.0 \times 10^4$  W/m<sup>2</sup>. The effect of Joule heating on the temperature changes observed was also considered and was obtained to be negligible as compared to the amount of heat released from the  $H_2/O_2$  combustion. Only  $6 \times 10^3$  W/m<sup>2</sup> of surface heat was generated

from the passage of  $100 \mu\text{A}$  through the Pt layer, which was much less as compared to the surface heat values shown in Fig. 4.17. Moreover, since joule heating does not depend on the frequency of the applied voltages, the nature of the temperature changes observed confirms the occurrence of combustion inside the nanobubbles.

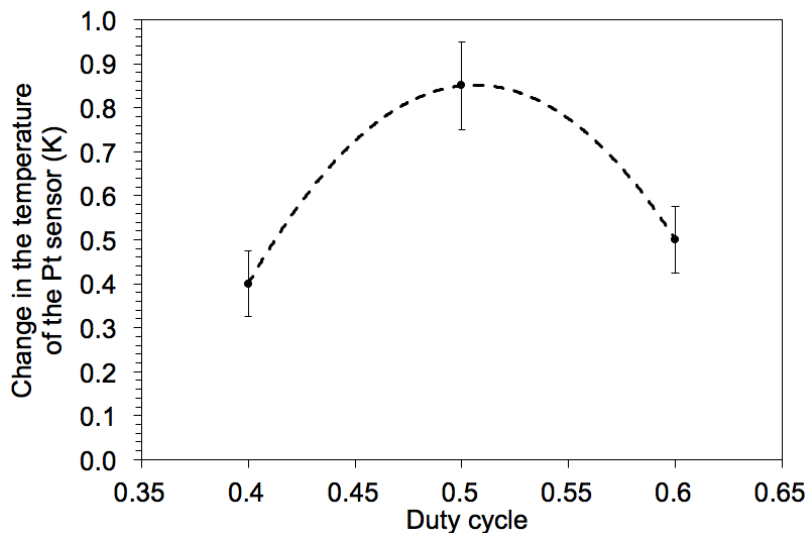


Figure 4.18.: Effect of duty cycle on the temperature of the Pt thermal sensor layer. The particular case shown corresponds to using  $20 \times 20 \mu\text{m}^2$  electrodes. The voltage, duty cycle and frequency of the applied alternating pulses were kept fixed at 7 V, 0.5 and 500 kHz, respectively.

Next, as shown in Fig. 4.18, the effect of duty cycle on the temperature of the Pt thermal sensor layer was studied. For the particular case shown,  $20 \times 20 \mu\text{m}^2$  electrodes were used and the voltage and frequency were kept fixed at 7 V and 500 kHz, respectively. As can be seen, an optimum duty cycle of 0.5 was obtained which maximized the temperature changes. This was expected, since, at duty cycles other than 0.5, the  $\text{H}_2/\text{O}_2$  gas production was not stoichiometric and as a result, the amount of heat that could be produced was reduced. Thus, the duty cycle dependency further confirms that the rise in temperature obtained was not because of some adverse side effects of high frequencies but was from the combustion of  $\text{H}_2/\text{O}_2$  gases.

### 4.3 Nanobubble Pressure and Surface Tension

*Some of the text and figures presented in this section are reproduced from {S. Jain and L. Qiao, AIP Advances 7, 045001 (2017)} with permission of AIP Publishing.*

During the nanobubble experimental study, faradaic currents up to 0.28 mA were obtained for  $20 \times 20 \mu\text{m}^2$  electrodes. Then using the diffusion length and faradaic current equation, the amount of supersaturation of gases in the water surrounding the electrodes can be estimated. For example, for  $\text{O}_2$  gases, the diffusion length can be approximated using the following equation:

$$l_{\text{O}_2} = \sqrt{D_{\text{O}_2}t} \quad (4.2)$$

In the above equation, D is the diffusion coefficient of oxygen in water ( $2.2 \times 10^{-9} \text{ m}^2/\text{s}$  at 300 K [194]) and t is the time period of a complete cycle. For a frequency of 30 kHz (the threshold frequency to observe combustion), the diffusion length comes out to be 270 nm. Then using the faradaic current equation, the concentration of  $\text{O}_2$  gases ( $C_{\text{O}_2}$ ) in water can be estimated as follows [195]:

$$C_{\text{O}_2} = \frac{I_F t}{4eA l_{\text{O}_2}} \quad (4.3)$$

In the above equation,  $I_F$  is the faradaic current, e is the electron charge value and A is the cross-sectional area of the electrode surface. For a frequency of 30 kHz, faradaic current of 0.28 mA and  $20 \times 20 \mu\text{m}^2$  electrodes, a  $C_{\text{O}_2}$  value of  $1.35 \times 10^{20} \text{ cm}^{-3}$  is obtained. The supersaturation ratio (S) is then determined by dividing the  $C_{\text{O}_2}$  value with the saturated concentration of  $\text{O}_2$  in water at 1 atm and 300 K ( $7.7 \times 10^{17} \text{ cm}^{-3}$  [196]), and it comes out to be around 175. A similar supersaturation ratio can also be estimated for  $\text{H}_2$  gases and for the conditions considered above, a value of 400 is obtained. Thus, in the present non-reactive MD simulations, the water was supersaturated with gases with the S values ranging from 1-850, which covered most of

the saturation levels achieved during the experiments. Moreover, the supersaturation effect of only one type of gas ( $O_2$ ) was considered, since, the qualitative behavior with other types of gases would be similar.

### 4.3.1 Interaction Potential

The simulations were performed using LAMMPS [136] and three types of interactions were considered:

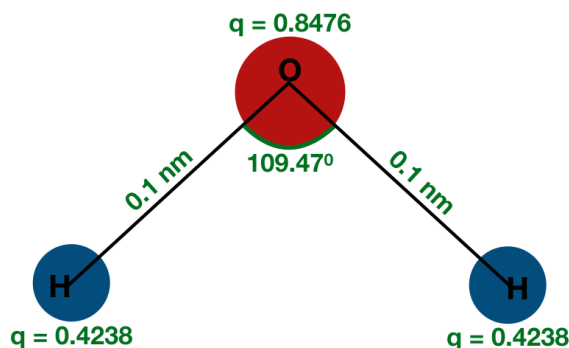


Figure 4.19.: SPC/E water model.

(1)  $H_2O$ - $H_2O$  Interactions: The water molecules were modeled using the extended simple point charge (SPC/E) force field [197], an improved version of the original SPC water model [198]. In the SPC/E force field, the water is modeled as a rigid molecule with three point charges, with one point charge located at the oxygen atom ( $-0.8476|e|$ ) and the other two point charges at the hydrogen atoms ( $0.4238|e|$ ). In addition to columbic interactions, in the SPC/E force field, dispersive Lennard-Jones (L-J) interactions between the oxygen atoms are also considered. The geometry of the SPC/E water model is illustrated schematically in Fig. 4.19. The rigid tetrahedral angle (H-O-H) was set to  $109.47^\circ$  and a bond length (O-H) of  $0.1 \text{ nm}$  was used. Moreover, the SHAKE algorithm [199] was used to rigidify the water molecules and was implemented within LAMMPS using the fix shake command.

(2) O<sub>2</sub>-O<sub>2</sub> interactions: The oxygen molecules were modeled as linear with the partial charges on the oxygen atoms being zero. The equilibrium bond length was set to 0.121 nm [200] and again, the SHAKE algorithm was used to rigidify the oxygen molecules.

(3) H<sub>2</sub>O-O<sub>2</sub> Interactions: The Lorentz-Berthelot mixing rules [201] were used to calculate the L-J parameters, required for the interactions between water and oxygen molecules, as given below:

$$\sigma_{H_2O-O_2} = \frac{1}{2}(\sigma_{H_2O-H_2O} + \sigma_{O_2-O_2}) \quad (4.4)$$

$$\varepsilon_{H_2O-O_2} = \sqrt{\varepsilon_{H_2O-H_2O}\varepsilon_{O_2-O_2}} \quad (4.5)$$

In the above equations,  $\sigma$  and  $\varepsilon$  are the L-J size and energy parameters, respectively, and their values are given in Table 4.1.

Table 4.1.: L-J parameters [197, 202]

Parameter	H <sub>2</sub> O (O atom)	H <sub>2</sub> O (H atom)	O <sub>2</sub> (O atom)
$\sigma$ (Å)	3.166	0	3.094
$\varepsilon$ (kcal/mol)	0.1553	0	0.09538

The net interaction between any two atoms (i, j), belonging to different molecules, can be written as [203, 204]:

$$E_{net} = E_{L-J} + E_{coul} \quad (4.6)$$

where,

$$E_{L-J} = 4\varepsilon_{ij} \left( \left( \frac{\sigma_{ij}}{r_{ij}} \right)^{12} - \left( \frac{\sigma_{ij}}{r_{ij}} \right)^6 \right) \quad \text{for } r_{ij} < r_{cut} \quad (4.7)$$

$$E_{coul} = \frac{q_i q_j}{4\pi\epsilon_o r_{ij}} \quad (4.8)$$

In above equations,  $q$  is the partial charge on an atom,  $r$  is the distance between the centers of two atoms,  $\epsilon_o$  is the electric constant and  $r_{cut}$  is the L-J cut-off distance. A high L-J cut-off value of 2.5 nm was used to ensure that the L-J tail-contributions were minimum.

### 4.3.2 Validation of the SPC/E Force Field

In order to validate the SPC/E force field and the simulation parameters used, the surface tension of pure water was first determined. A planar interface perpendicular to the  $z$ -direction was used to calculate the surface tension of water, according to the Kirkwood and Buff formula [205]:

$$\gamma = 0.5 \int_{-\infty}^{\infty} \left( P_n(z) - P_t(z) \right) dz \quad (4.9)$$

In the above equation,  $P_n(z) = P_{zz}(z)$  is the normal pressure-tensor in the  $z$ -direction and  $P_t(z) = 0.5*(P_{xx}(z) + P_{yy}(z))$  is the tangential pressure-tensor. At locations far from the interface,  $P_t = P_n = P$ , thus, regions only near the interface contribute to the integral value. A factor of 0.5 was included in Eqn. 4.9 because of the double counting of the two interfaces of the liquid film. Next, the simulation box was binned in the  $z$ -direction using 3d bins of sizes 7 nm x 7 nm x 5 Å. The pressure tensors ( $P_{xx}$ ,  $P_{yy}$  and  $P_{zz}$ ) were calculated for each 3d bin by summing over the per-atom stress quantities. Other thermodynamic properties such as density/number and temperature were calculated, similarly, for each bin by summing over their corresponding per-atom quantities. These thermodynamic properties were then averaged over time using the LAMMPS fix ave/spatial command.

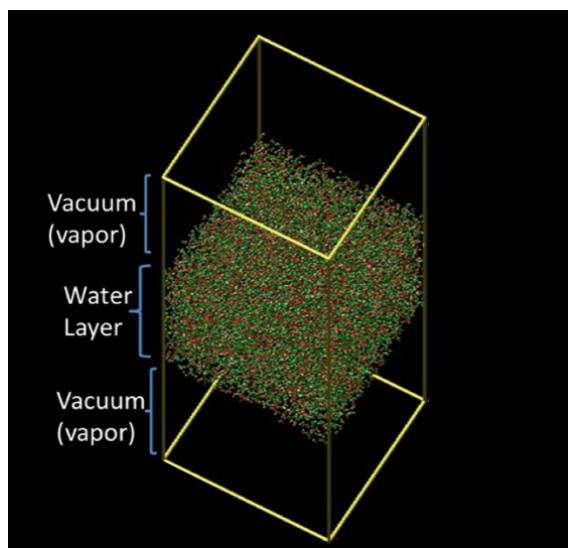


Figure 4.20.: Initial setup of the simulation domain for pure water surface tension calculations.

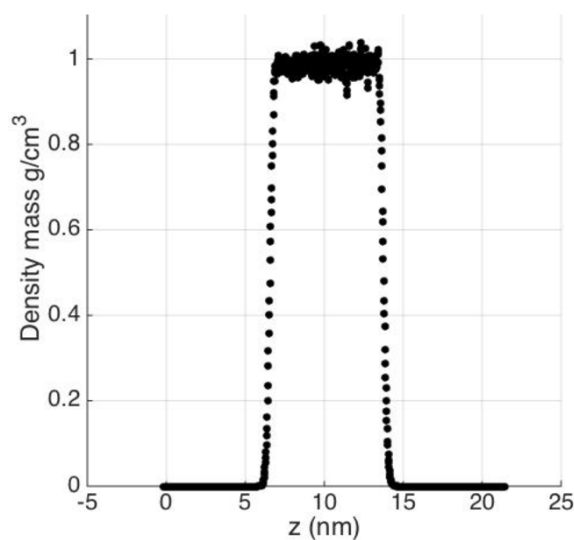


Figure 4.21.: Saturated vapor-liquid density profile.

Fig. 4.20 shows the initial setup of the simulation domain, which as can be seen, was divided into three slabs of sizes  $7 \times 7 \times 7 \text{ nm}^3$ , with the middle slab consisting of  $N = 12,000$  water molecules based on the water density at  $P = 1 \text{ atm}$  and  $T = 300 \text{ K}$ . Periodic boundary conditions were employed in all the three directions and a time step of  $2 \text{ fs}$  was used. After the initial setup of the simulation domain, the system

equilibration to 300 K using the Nose-Hoover thermostat [145,146] with a relaxation time of 100 fs was conducted for 2 ns. Fig. 4.21 shows the saturated vapor-liquid density profile obtained along the z-direction after the equilibration and as can be seen, a symmetrical profile was obtained, thus, confirming that the system has been properly equilibrated (saturated liquid density - 0.996 g/ml and saturated vapor density -  $3 \times 10^{-5}$  g/ml)

After the system equilibration, the NVT ensemble was used to calculate the average thermodynamic properties such as density/number, pressure tensors and temperature. For pure water, a surface tension value of  $59.83 \pm 2$  mN/m was obtained, similar to the value of  $63.6 \pm 1.5$  mN/m calculated by Vega et al. [206] using the SPC/E rigid water model. In the same study performed by Vega et al., much better agreements with the experimental surface tension value of 71.3 mN/m were obtained by using the SPC/E, TIP4P/Ew, and TIP4P/2005 water models rather than the SPC, TIP3P, and TIP4P models. Thus, because of the wide use and simplicity, all of the following surface tension values were calculated using the SPC/E force field.

### 4.3.3 Surface Tension under Supersaturated Conditions

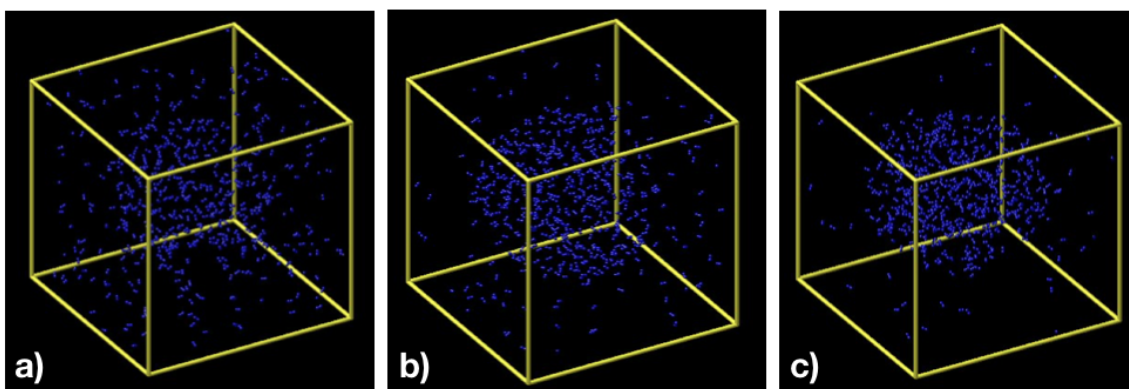


Figure 4.22.: Bubble growth and stability after the creation of the cavity: a)  $t = 200$  ps, b)  $t = 1$  ns and c)  $t = 2$  ns. The particular case shown corresponds to  $S = 200$  and the blue molecules represent  $O_2$ .

To determine the surface tension of water under supersaturated conditions, the curved interface of a nanobubble was used instead of the planar interface. Initially, the  $O_2$  and  $H_2O$  molecules (12,000) were randomly added to the simulation box of size: 7 nm x 7 nm x 7 nm. The number of initial  $O_2$  molecules added was based on the supersaturation value desired (1 to 850). First, the system equilibration to 300 K and 1 atm was performed for 2 ns. The relaxation time for the Nose-Hoover thermostat and barostat was set to 100 fs and a time step of 2 fs was used. The L-J cut-off value was again set to 2.5 nm and periodic boundary conditions were used in all the three directions. After the equilibration, a cavity of diameter 4.0 nm was created at the center of the simulation box (by deleting some of the water molecules). The simulation was then run under the NVT conditions (300 K) until the bubble radius attains a steady state value, after which the pressure inside and outside of the bubble was calculated. 3d bins of sizes  $5 \text{ \AA} \times 5 \text{ \AA} \times 5 \text{ \AA}$  were used to calculate the pressure tensors and other thermodynamic properties. Next, assuming the validity of the Laplace-Young equation and using the  $\Delta P$  across the bubble surface along with the equilibrated bubble radius value, the surface tension of water was determined. Fig. 4.22 shows the bubble growth and stability after the creation of the cavity. In the figure, only  $O_2$  molecules are shown for visualization purposes.

Four cases corresponding to the supersaturation values of 1, 200, 400 and 850 were considered. As can be seen from Fig. 4.23, the relative surface tension value of water was found to decrease with an increase in the supersaturation ratio. Fig. 4.24 shows how the pressure inside a bubble changes with the bubble diameter, for different supersaturation values. A big drop in the bubble pressure was obtained as the value of  $S$  was changed from 1 to 200 but after that the change in bubble pressure with the  $S$  value was not significant. During the nanobubble combustion experiments, a threshold frequency of 30 kHz was observed, which using Eqns. 4.2 and 4.3 corresponds to a diffusion length of 270 nm and a supersaturation ratio of 175, implying that in one cycle, bubbles with diameters as large as 270 nm could be formed. Then using

Fig. 4.24, a corresponding pressure of 10 atm was obtained. Thus, approximately, the pressure inside the bubble must be greater than 10 atm in order to have a possibility to observe combustion. This hypothesis will be further confirmed using reactive molecular dynamic simulations, as discussed in the next section.

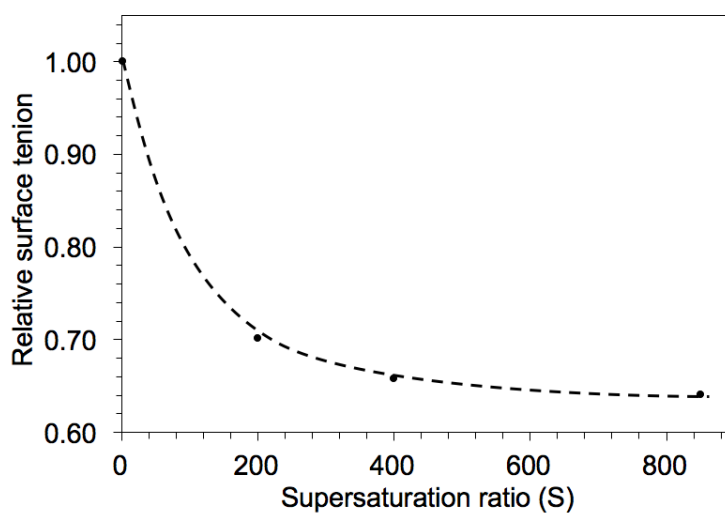


Figure 4.23.: Relative surface tension of water,  $\gamma(S)/\gamma(S = 1, \text{ saturated water})$ , as a function of the supersaturation ratio.

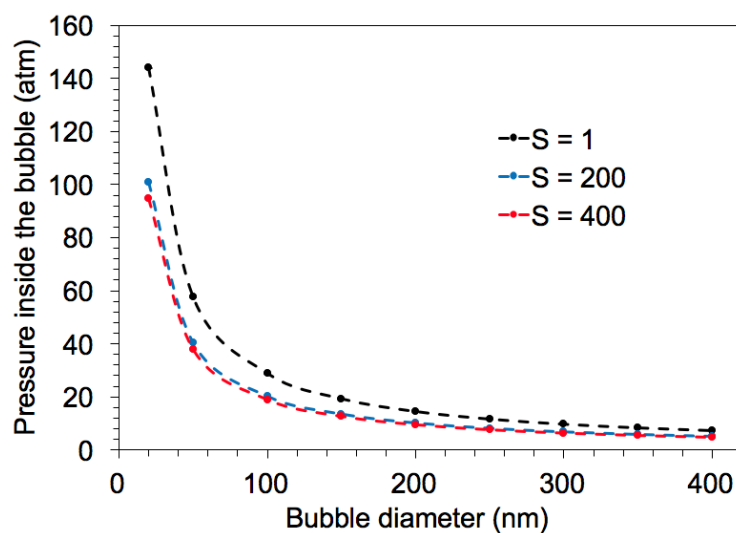


Figure 4.24.: Bubble pressure as a function of the bubble diameter for different supersaturation ratios.

## 4.4 H<sub>2</sub>/O<sub>2</sub> Combustion at Low Temperatures and High Pressures

*Most of the text and figures presented in this section are reproduced from {S. Jain and L. Qiao, The Journal of Physical Chemistry A 122, 5261 (2018)} with permission of American Chemical Society Publishing.*

In this section, the ignition of H<sub>2</sub>/O<sub>2</sub> gases and species evolution as a function of the initial system pressure (or bubble size) and the amount of H and O radicals added were studied. In addition, the temperature of the H<sub>2</sub>/O<sub>2</sub> system was not held constant at 300 K but was allowed to be varied in order to compare the rate at which the heat was being lost vs. the rate at which the heat was being produced from the exothermic reactions. The resulting chemistry was quite different from macroscopic combustion, which usually takes place at much higher temperatures of above 1000 K. For the simulations, cubic boxes were used to represent the nanobubbles. Since, the main goal of this work was to understand the mechanism behind the spontaneous combustion of H<sub>2</sub>/O<sub>2</sub> gases at room temperature, a good qualitative understanding of the initial and boundary conditions (pressure, temperature and H/O radical concentrations) could be obtained with the cubic boxes. Moreover, the cubic boxes reduce the computational cost and complexity considerably.

### 4.4.1 Computational Method

The simulations were again performed using LAMMPS [136] and the interactions between the atoms were calculated using the ReaxFF force field [137, 139], in which the bond order between a pair of atoms is determined from their interatomic distance. Table 4.2 lists the minimum bond order values used to identify the species produced during the combustion process. Pair of atoms that had the bond order value greater than the listed threshold bond order value were considered to be bonded. The particular ReaxFF force field used in this study was developed by Agrawalla [207], which was designed to investigate the reaction kinetics of the H<sub>2</sub>/O<sub>2</sub> system at high pressures

and low temperatures and thus, contains information on different pathways leading to the formation and consumption of HO<sub>2</sub> and H<sub>2</sub>O<sub>2</sub> molecules, which will play a key role in understanding the reaction kinetics of nanobubbles. Moreover, this force field has also been validated with the predictions of existing continuum-scale kinetic models for H<sub>2</sub>/O<sub>2</sub> combustion at high temperatures and low pressures [207].

Table 4.2.: Minimum bond order values (H<sub>2</sub>/O<sub>2</sub> system) [138]

Atom type	Atom type	Bond order
H	H	0.55
H	O	0.40
O	O	0.65

Table 4.3.: MD simulation matrix (H<sub>2</sub>/O<sub>2</sub> system)

Case No.	Initial % of H radicals added	Initial % of O radicals added	System size (nm <sup>3</sup> )	Method type
1	3	0	30×30×30	I
2	1	0	50×50×50	I
3	3	0	50×50×50	I
4	6	0	50×50×50	I
5	0	3	50×50×50	I
6	-	0	50×50×50	II
4	3	0	70×70×70	I
5	3	0	100×100×100	I
6	3	0	120×120×120	I

Initially,  $\text{H}_2$  (124,200) and  $\text{O}_2$  (62,100) molecules were randomly added to the simulation box in a stoichiometric proportion, which was because during the nanobubble experimental work, the electrolysis was conducted at a duty cycle of 0.5 that generated  $\text{H}_2$  and  $\text{O}_2$  gases in stoichiometric proportions of 2:1. The simulation box size was based on the desired initial pressure and was varied from 30 nm to 120 nm, corresponding to the initial pressure ranging from 2 atm to 80 atm. After the initial setup of the simulation domain, temperature equilibration under the NVT conditions to 300 K was performed using the Noose-Hoover thermostat. The NVT equilibration was performed for 0.5 ns with the time step and the relaxation time being 0.1 fs and 100 fs, respectively. After the NVT equilibration, the desired amount of H and O radicals were added to the simulation box. Since, the details of the process through which the radicals are produced at the bubble surface is not well understood, two different methods were used to add the radicals. In the first method, the radicals were added only initially, during the start of the combustion process, whereas in the second method, the radicals were added continuously at regular intervals of 0.01 ns. Moreover, for both the methods, the radicals were added only near the surface of the simulation box (at distance  $< 3\%$  of the box length). For the first method, the initial H and O radical concentrations were varied from 1% to 6% (of the total number of initial  $\text{H}_2$  and  $\text{O}_2$  moles present in the system), whereas for the second method, the amount of H radicals added at each interval of 0.01 ns was based on the estimated reaction rate constant, as given by Prokaznikov et al. [181]. Table 4.3 lists the different cases that were simulated.

To simulate the combustion process, a non-thermostatted dynamics was used. Since, during the experiments, nanobubbles were produced inside the water droplet, which was at 300 K, an isothermal boundary of 300 K was assumed for the cubic boxes. Thus, for atoms near the surface of the box (at distance  $< 3\%$  of the box length), the NVT ensemble at 300 K was used. This enforced the isothermal boundary condition required. However, for atoms in the interior of the box, the NVE ensemble was used,

allowing the temperature of the atoms to rise from the heat produced during the combustion process. A time step of 0.1 fs was used with the relaxation time (for the NVT ensemble) being 100 fs. Moreover, special precautions were made to make sure that the NVT boundary was set on a group of atoms defined as dynamic. The atoms were allowed to move in and out of the boundary but the NVT condition was applied only to the atoms near the boundary. The dynamic group was updated at every time step of 0.1 fs, and the atoms were assigned to or removed from the group depending on their respective locations. Thus, the NVT boundary never collapsed and remained valid throughout the simulation. Fig. 4.25 shows a snapshot of the simulation box.

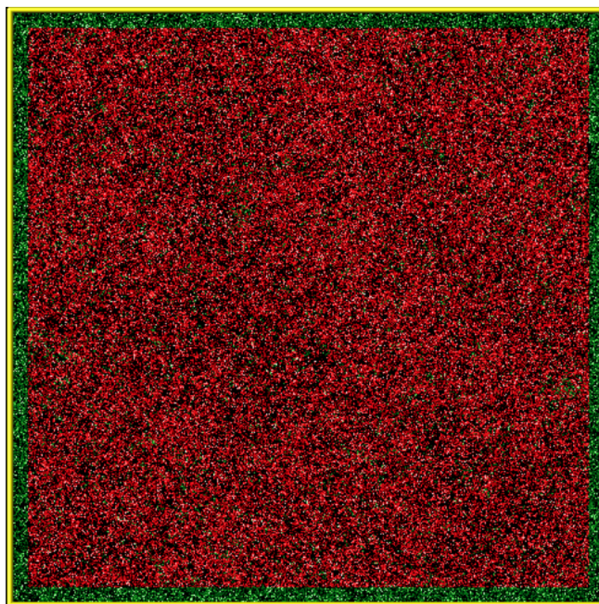


Figure 4.25.: Snapshot of the simulation box. H/O radicals were added only in the green shaded area.

#### 4.4.2 Results and Discussion

##### $\text{H}_2/\text{O}_2$ reaction characteristics at high pressures and low temperatures

Fig. 4.26 shows the species distribution as a function of time during the combustion of  $\text{H}_2/\text{O}_2$  gases. The initial H radical concentration and system pressure were set to 3% and 30 atm, respectively. No O radicals were added initially but during the combustion process, the formation of O radicals was observed. In a combustion process at high temperature conditions ( $> 1000$  K),  $\text{H}_2\text{O}$  is the dominant stable species formed. However, for the present low temperature conditions ( $\sim 300$  K), instead of  $\text{H}_2\text{O}$ ,  $\text{H}_2\text{O}_2$  was the dominant stable species formed, as can be seen from Fig. 4.26. Moreover, for combustion at macroscales, whenever an ignition is provided, chain branching reactions are initiated and a significant rise in the temperature is observed. However, in the present case, due to the large surface to volume ratio, most of the energy released from the exothermic reactions was lost from the walls of the combustion chamber and as a result, only a slight rise in the temperature of the reaction products was obtained, around 50 K (for this particular case). Thus, to initiate the combustion process at low temperatures, high pressure and a certain amount of H/O radicals are required initially, as will be discussed later. Next, the reaction mechanism observed for H radical addition at high pressures and low temperatures is explained in detail [181, 207]:

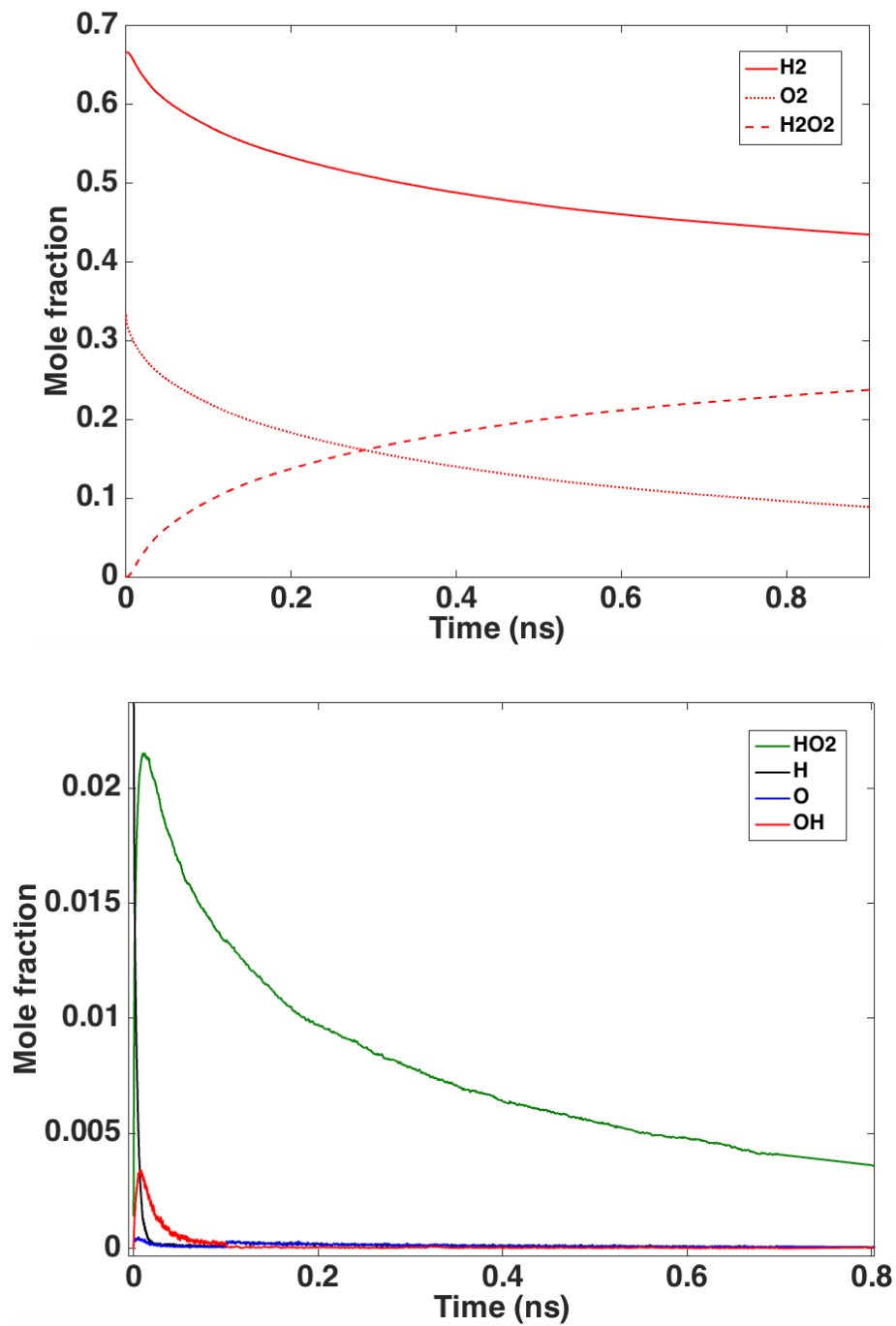
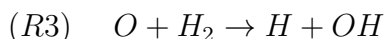
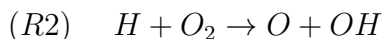


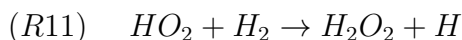
Figure 4.26.: Species mole fraction as a function of time for 3% initial H radical concentration. The initial system pressure was set to 30 atm with the box size fixed at 50 nm. Mole fraction is defined as the number of moles of a species per total number of initial moles of H<sub>2</sub> and O<sub>2</sub>.

(1) Chain initiating step: The added H radicals reacted with the H<sub>2</sub> and O<sub>2</sub> molecules through the following 3 reactions:



In reaction R1, M is the concentration of the third body and represents the overall system concentration, which in turn can be expressed in terms of the pressure and temperature of the system using the ideal gas law. Thus, the reaction rate for R1 is pressure dependent and increases with an increase in the system pressure. Moreover, reaction R1 has a much lower activation energy as compared to reaction R2 [207]. Thus, at high temperatures and low pressures, reaction R2 dominates but at low temperatures and high pressures, reaction R1 dominates.

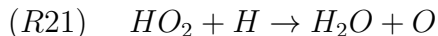
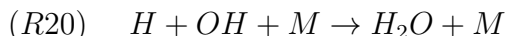
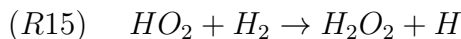
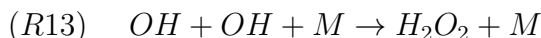
(2) Chain propagating step: Reactions in which at least one radical was produced:



As can be seen from Fig. 4.26, HO<sub>2</sub> was the dominant intermediate product obtained, as expected. H (except during the initial part), OH and O radicals, however, were

present in much smaller amounts with their concentrations quickly reaching steady state values i.e. these radicals were being consumed as soon as they were produced. The OH radicals were produced through reactions R4, R6, R7 and R9, whereas the H and O radicals were produced through reactions R5, R8, R10, R11 and R12.

(3) Chain terminating step: Reactions with either H<sub>2</sub>O or H<sub>2</sub>O<sub>2</sub> in the products:



Next, the intermediate radicals, according to reactions R13-21, combined to form the stable species: H<sub>2</sub>O and H<sub>2</sub>O<sub>2</sub>. Fig. 4.27 plots the relative amount of H<sub>2</sub>O<sub>2</sub> to H<sub>2</sub>O as a function of time. As can be seen, significant amount of H<sub>2</sub>O<sub>2</sub>, up to 32 times that of H<sub>2</sub>O, was produced. Reactions R14-15 uses the reactants HO<sub>2</sub> and H<sub>2</sub>, which were available in abundance, to produce H<sub>2</sub>O<sub>2</sub>. On the other hand, for the H<sub>2</sub>O production, the main intermediate product required was OH, which was present in much smaller quantities as compared to HO<sub>2</sub> and H<sub>2</sub>. Thus, although the rate constants for reactions R18 and R20 (required for H<sub>2</sub>O production) were much larger as compared to the rate constants for reactions R13-15 (required for H<sub>2</sub>O<sub>2</sub> production) [181], the concentration of reactants available limited the rate of reactions, resulting in much greater H<sub>2</sub>O<sub>2</sub> production. Other chain terminating reactions requiring H and O rad-

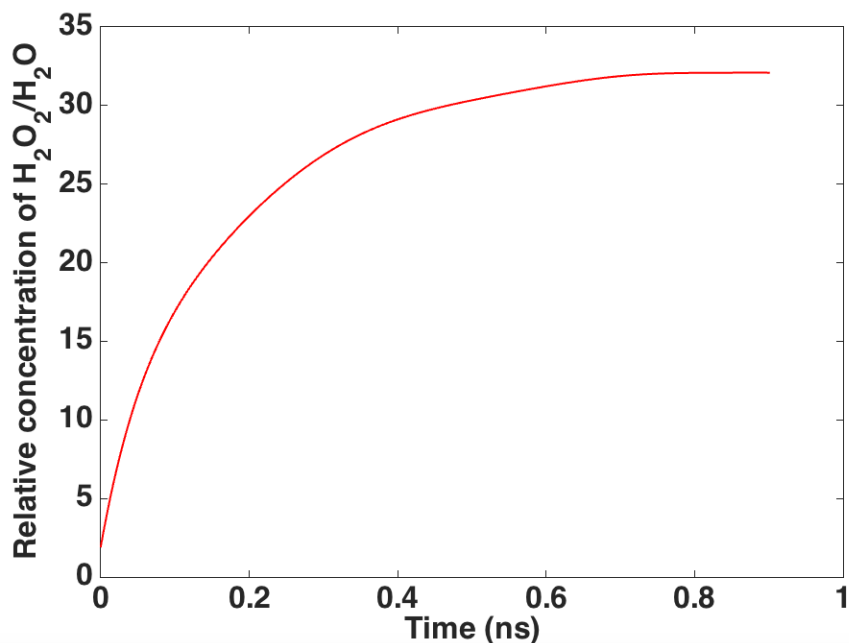


Figure 4.27.: Relative concentration of H<sub>2</sub>O<sub>2</sub> to H<sub>2</sub>O as a function of time for 3% initial H radical concentration. The initial system pressure was set to 30 atm with the box size fixed at 50 nm.

icals as reactants are not listed as they have very small rate constant values at room temperature.

### Effect of initial H radical concentration

Fig. 4.28 shows the effect of H radical concentration on the reactivity of the H<sub>2</sub>/O<sub>2</sub> system. In the figure, the species reactivity is defined as the rate of change of a given species quantity per unit time i.e.  $dN_s/dt$  (1/ns), where  $N_s$  is the number of particles of a given species. The initial H radical concentration was varied from 1% to 6% to represent the different probabilities of hydrogen dissociation at the bubble surface. Moreover, the initial system pressure was set to 30 atm with the box size being kept fixed at 50 nm. As can be seen, the reactivity of the system was found to increase with an increase in the H radical concentration. This was expected, since, the greater the amount of H radicals added, the greater would be the number of HO<sub>2</sub> radicals

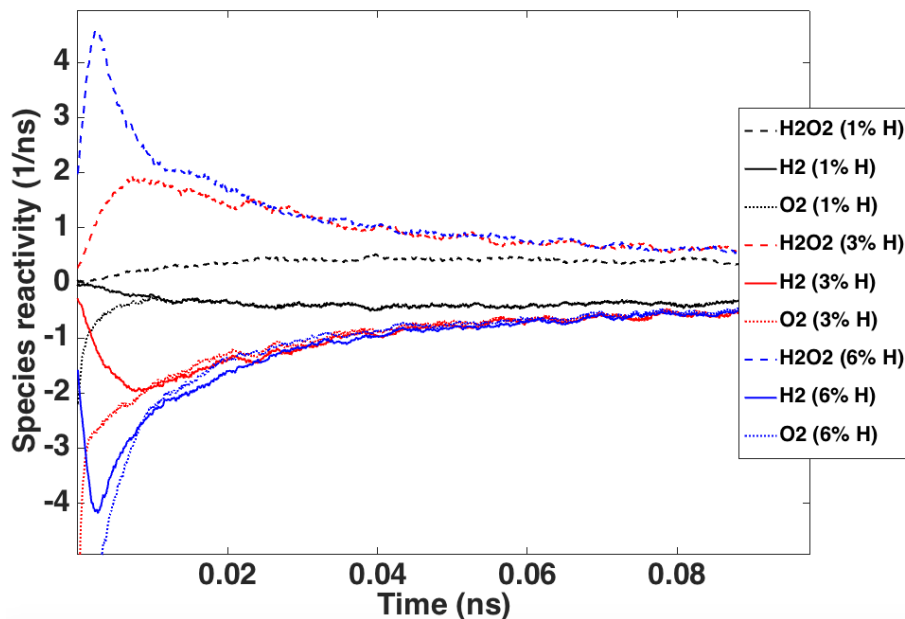


Figure 4.28.: Effect of initial H radical concentration on the reactivity of the  $\text{H}_2/\text{O}_2$  system. The initial system pressure was set to 30 atm with the box size fixed at 50 nm.

produced through reaction R1. For 3% and 6% initial H radical concentrations, a significant amount of initial boost in the  $\text{H}_2\text{O}_2$  reaction rate was observed but then due to the heat loss, a decay was obtained thereafter. However, for 1% H radical concentration, no significant initial boost in the  $\text{H}_2\text{O}_2$  reaction rate was observed but instead the reaction rate increased only slightly before falling down to the steady state value. Thus, for the case of 30 atm initial pressure, at least 3% H radical concentration was required to observe any significant  $\text{H}_2\text{O}_2$  formation. Moreover, as can be seen from Fig. 4.29, the relative amount of  $\text{H}_2\text{O}_2$  to  $\text{H}_2\text{O}$  was found to decrease with an increase in the initial H radical concentration. This could be attributed to the competition of H radicals towards the formation of  $\text{H}_2\text{O}_2$  and  $\text{H}_2\text{O}$ . With an increase in the H radical concentration, the number of  $\text{HO}_2$  and OH radicals produced in the system also increases, which in turn increases both the  $\text{H}_2\text{O}_2$  and  $\text{H}_2\text{O}$  production. But since, reactions R18 and R20 have much larger rate constant values as compared to reactions R13-15 [181], the amount of increase observed in the  $\text{H}_2\text{O}$  production was

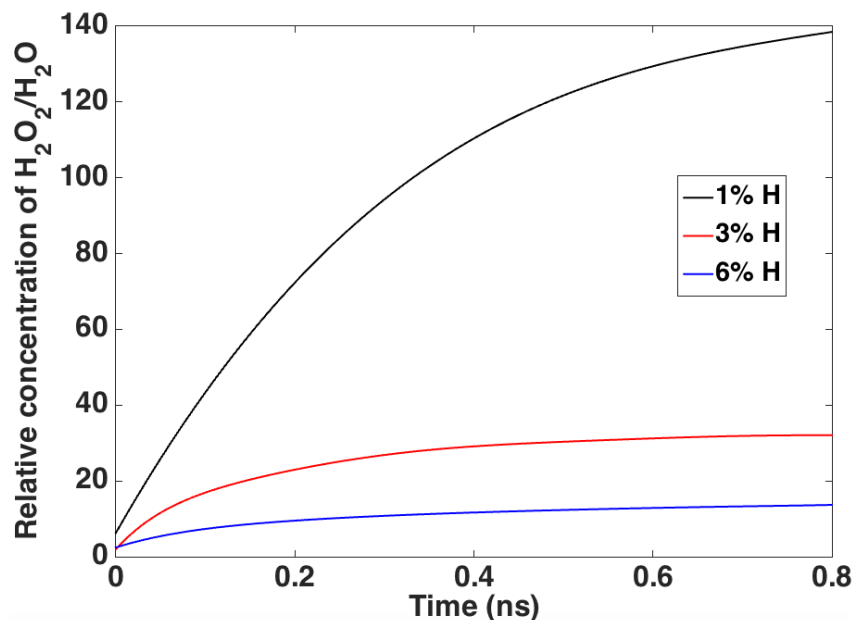


Figure 4.29.: Relative concentration of  $\text{H}_2\text{O}_2$  to  $\text{H}_2\text{O}$  as a function of time for various H radical concentrations. The initial system pressure was set to 30 atm with the box size fixed at 50 nm.

much more as compared to the amount of increase observed in the  $\text{H}_2\text{O}_2$  production.

### Effect of initial system pressure

Fig. 4.30 shows the how the initial system pressure (or the box size) effects the reactivity of the  $\text{H}_2/\text{O}_2$  system. The initial H radical concentration was kept fixed at 3% and no O radicals were added initially. As expected, the reactivity of the system increases with an increase in the system pressure (or a decrease in the box size). This could be attributed to the chain initiation reaction R1. With an increase in the system pressure, the concentration of the third body M also increases, which in turn increases the rate of formation of  $\text{HO}_2$  radicals. This increase in the  $\text{HO}_2$  concentration then translates to greater  $\text{H}_2\text{O}_2$  and  $\text{H}_2\text{O}$  production, as can be seen from the reaction mechanism. For the 30 atm and 80 atm initial pressure cases, a significant amount of initial boost in the  $\text{H}_2\text{O}_2$  production was observed but for the 12 atm initial pressure case, no initial boost was obtained but instead the  $\text{H}_2\text{O}_2$  reac-

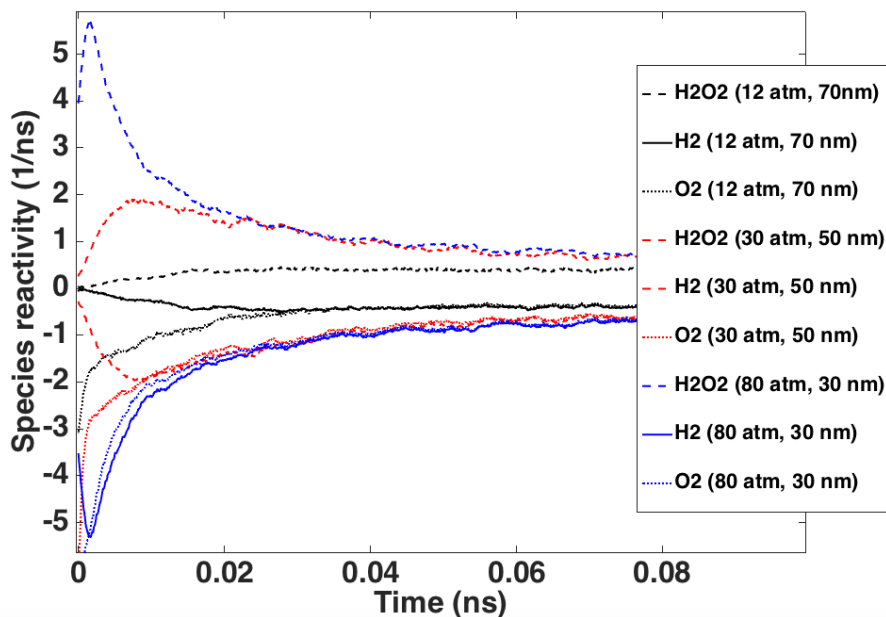


Figure 4.30.: Effect of initial system pressure on the reactivity of the  $\text{H}_2/\text{O}_2$  system. The initial H radical concentration was kept fixed at 3%.

tion rate was increased only slightly, thus, for the 3% initial H radical concentration, the initial system pressure must be greater than 12 atm to observe combustion. In the nanobubble experimental study, faradaic currents up to 0.28 mA were observed for  $20 \times 20 \mu\text{m}^2$  electrodes. Then using the diffusion length and faradaic current equation, for a frequency of 30 kHz (frequency above which substantial temperature rise was obtained), a supersaturation value of 175 was obtained along with a diffusion length of 270 nm, which using non-reactive MD simulations roughly corresponds to a pressure value of 10 atm. Thus, the nanobubble experimental study and the present reactive MD simulations predicted similar threshold pressure values for the combustion to occur.

Fig. 4.31 shows how the relative amount of  $\text{H}_2\text{O}_2$  to  $\text{H}_2\text{O}$  produced is affected by changing the initial system pressure. As can be seen, a decrease in the relative concentration was obtained with a decrease in the system pressure. This can again be attributed to reaction R1. With a decrease in the system pressure, the third body

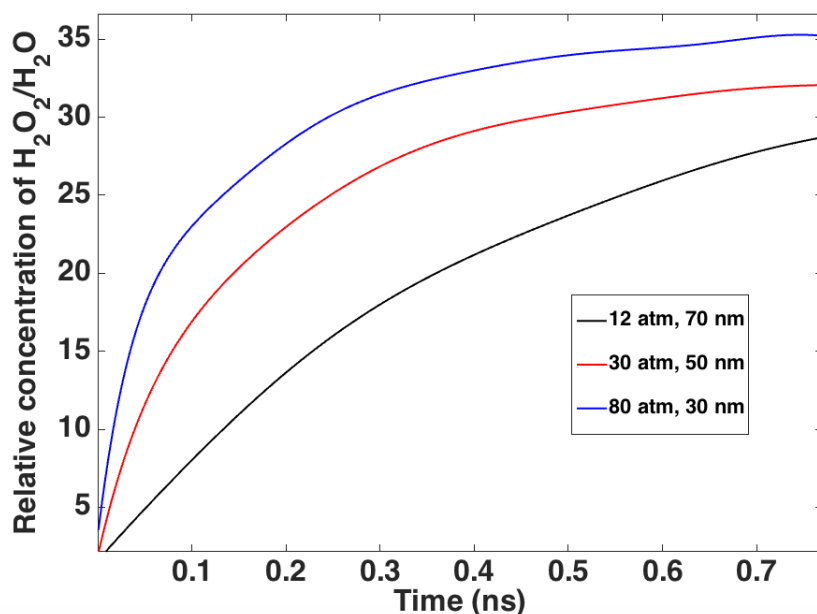


Figure 4.31.: Relative concentration of  $\text{H}_2\text{O}_2$  to  $\text{H}_2\text{O}$  as a function of time for various initial system pressure. The initial H radical concentration was kept fixed at 3%.

concentration,  $M$ , also decreases, which in turn causes a decrease in  $\text{HO}_2$  formation. Since, reactions R14-15 are directly dependent on the  $\text{HO}_2$  concentration, in contrast to reactions R18 and R20, the decrease observed in  $\text{H}_2\text{O}_2$  production was much more as compared to the decrease observed in the  $\text{H}_2\text{O}$  production, resulting in the relative amount of  $\text{H}_2\text{O}_2$  to  $\text{H}_2\text{O}$  to be lowered with a decrease in the system pressure.

### Effect of O radical addition

Fig. 4.32 shows how the reactivity of the system is affected when, instead of H radicals, only O radicals were added. The initial concentration of the respective radicals added was kept fixed at 3%. Moreover, the initial system pressure was set to 30 atm with the box size being kept fixed at 50 nm. As can be seen, for the case of O radical addition, a slight increase in the system reactivity was obtained. However, for both the cases,  $\text{H}_2\text{O}_2$  was dominant stable species formed. The reaction mechanism observed in the case of O radical addition was slightly different from the H radical addition reaction mechanism. For the chain initiation step, reaction R3 now dominates,

since initially, significant amount of O radicals was added, which in turn produced the required H and OH radicals. H radicals were then consumed via reaction R1 producing the main intermediate species, the HO<sub>2</sub> radical. This mechanism could be further confirmed by looking at the rate of consumption of H<sub>2</sub> and O<sub>2</sub> species in Fig. 4.32. For the case of O radical addition, significantly more H<sub>2</sub> molecules were being consumed as compared to the O<sub>2</sub> molecules, which was in contrast to the case of H radical addition, where an opposite trend was obtained. Thus, for the O radical addition, the main initiation was provided by reaction R3, whereas for the H radical addition, the main initiation was provided by reaction R1.

Fig. 4.33 shows how the relative amount of H<sub>2</sub>O<sub>2</sub> to H<sub>2</sub>O produced is affected when instead of H radicals, only O radicals were added. As can be seen, the relative concentration of H<sub>2</sub>O<sub>2</sub> to H<sub>2</sub>O decreases for the case of O radical addition, which is mostly due to an increase in the H<sub>2</sub>O production. The rise obtained in the H<sub>2</sub>O production could be attributed to reaction R3, via which significant amount of H

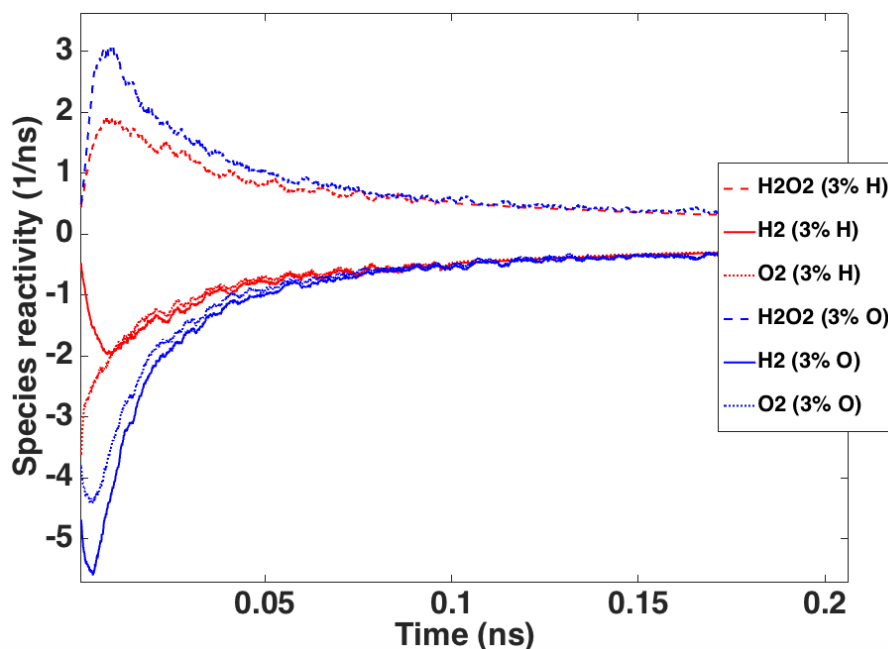


Figure 4.32.: Species reactivity for H radical addition vs. O radical addition. The initial system pressure was set to 30 atm with the box size fixed at 50 nm.

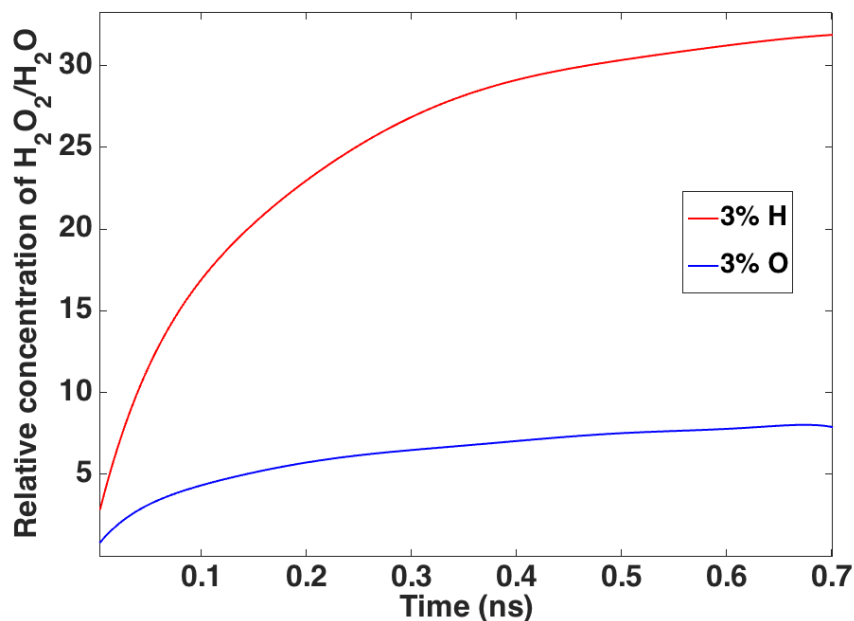


Figure 4.33.: Relative concentration of  $\text{H}_2\text{O}_2$  to  $\text{H}_2\text{O}$  produced for H radical addition vs. O radical addition. The initial system pressure was set to 30 atm with the box size fixed at 50 nm.

and OH radicals were produced. Since, the amount of  $\text{H}_2\text{O}$  molecules produced is strongly dependent on the H and OH radical concentrations, as can be seen from reactions R16-21, a significant rise in the  $\text{H}_2\text{O}$  production was observed. In contrast, for the  $\text{H}_2\text{O}_2$  production, only a slight increase was observed. This was because  $\text{HO}_2$  radicals, instead of H and OH radicals, controlled most of the  $\text{H}_2\text{O}_2$  molecules being produced, as can be seen from reactions R13-15. Moreover, since, the rate constants for reactions R18 and R20 were much larger as compared to the rate constants for reactions R13-15, the increased H and OH radical concentrations effect was even much more enhanced, and thus, a decrease in the relative concentration of  $\text{H}_2\text{O}_2$  to  $\text{H}_2\text{O}$  was observed for the O radical addition as compared to the H radical addition.

## Effect of the H radical concentration and system pressure on the system temperature

Fig. 4.34 shows how the core system temperature changes as a function of the simulation time. The effects of both the initial H radical concentration and system pressure (or box size) were considered. The core of the system represents the interior of the simulation box in which the NVE ensemble was used to simulate the combustion process and thus, allowing for the system temperature to increase. As can be seen, for all the cases, initially a slight rise in the core temperature was obtained but then because of the significant amount of heat being lost to the atoms near the isothermal boundary, a quick drop in the temperature was observed. The amount of temperature rise obtained was found to increase with an increase in the initial H radical concentration or a decrease in the box size. This could be attributed to reaction R1, which was the main initiation reaction producing radicals into the system. Among all the cases simulated, the maximum temperature rise obtained was only 68 K (method I).

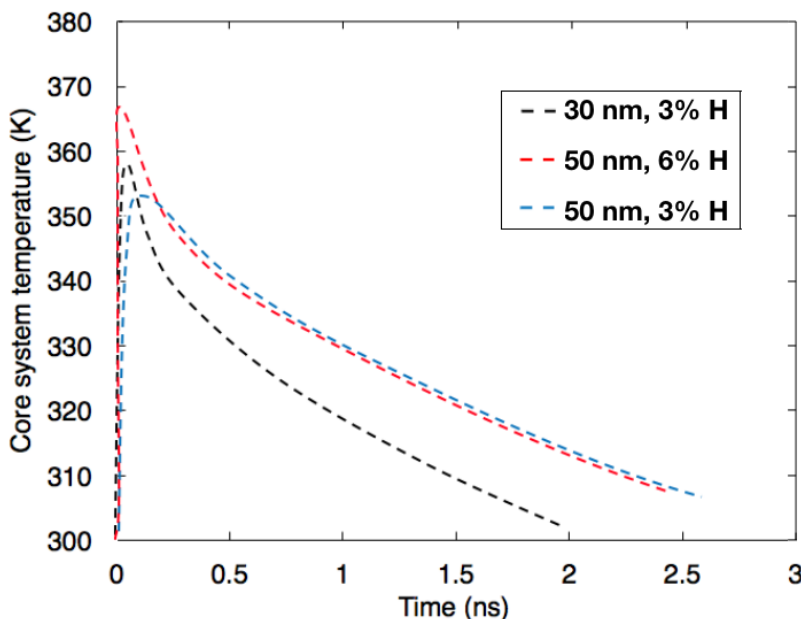


Figure 4.34.: Core system temperature as a function of time for various H radical concentrations and box sizes.

Thus, the first major conclusion that can be made is that the heat losses dominate i.e. the rate at which the heat is lost is much greater than the rate at which the heat is released from the chemical reactions. Second, the heat loss rate was found to be a much stronger function of the simulation box size as compared to the initial H radical concentration. As can be seen, for the 50 nm box, similar asymptotic temperature profiles were obtained for both the 3% and 6% H radical addition. However, for the 30 nm box, a much steeper asymptotic slope was obtained. Similar conclusions were made by Prokaznikov et al. [181], in which a simple heat diffusion equation was used to predict the thermalization time, which was then found to be on the order of 0.1 ns, much faster than the chemical reaction rates. Moreover, the thermal diffusion time was also found to be directly proportional to the box size, again being consistent with the results given in Fig. 4.34.

### Effect of adding H radicals continuously during the combustion process

In contrast to the previous method I, where the H radicals were added only at the beginning of the simulation, in this method II, the H radicals were added continuously at regular intervals of 0.01 ns, according to the reaction rate constant given by Prokaznikov et al. [181], to duplicate a H<sub>2</sub> surface dissociation reaction:

$$K = \frac{\epsilon v S}{4V} \quad (4.10)$$

In the above equation,  $\epsilon$  represents the probability of H<sub>2</sub> dissociation,  $v$  is the thermal velocity and  $S$  and  $V$  are the surface area and volume of the simulation box, respectively. Using a dissociation probability ( $\epsilon$ ) of  $10^{-2}$ , 210 H radicals were added every 0.01 ns.

Fig. 4.35 compares the rate of formation of H<sub>2</sub>O<sub>2</sub> and H<sub>2</sub>O obtained using the two methods (for the method I - 6% H). The simulation box size was kept fixed at 50 nm. As can be seen, for both the methods, H<sub>2</sub>O<sub>2</sub> was the dominant final product

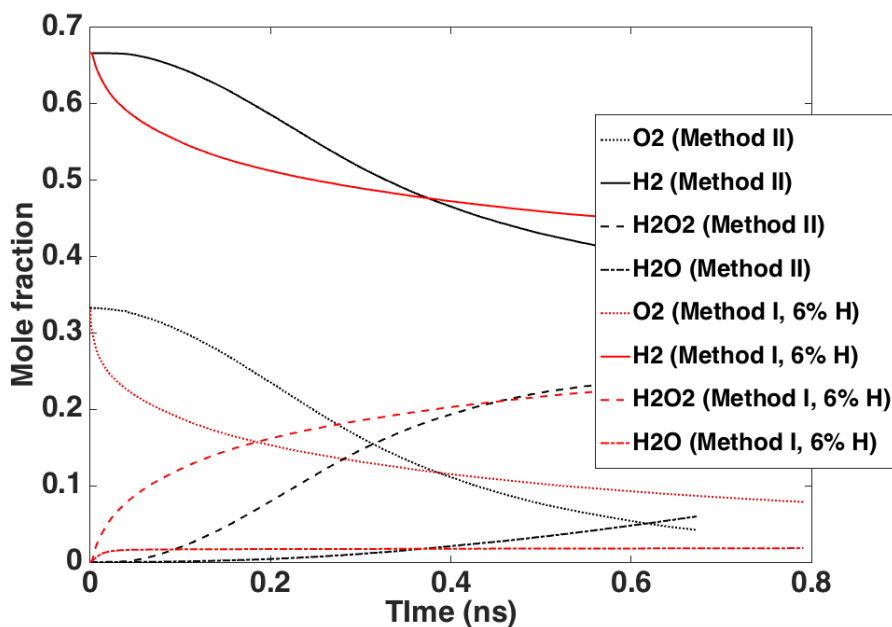


Figure 4.35.: Mole fraction of  $\text{H}_2$ ,  $\text{O}_2$ ,  $\text{H}_2\text{O}_2$  and  $\text{H}_2\text{O}$  as a function of time. The initial system pressure was set to 30 atm with the box size fixed at 50 nm.

formed. For the method I, initially, due to the large amount of H radicals added, a huge spike in both the  $\text{H}_2\text{O}$  and  $\text{H}_2\text{O}_2$  formation was observed but after that the molecules were produced at a much slower rate. This is in contrast to the method II, where both the  $\text{H}_2\text{O}$  and  $\text{H}_2\text{O}_2$  species were formed at a much steadier rate. At 0.47 ns (corresponding to 11,000 H radicals added in both the methods), more  $\text{H}_2\text{O}_2$  and  $\text{H}_2\text{O}$  molecules were produced using the method II. The  $\text{H}_2\text{O}_2$  production was increased slightly but a much greater rise was observed in the  $\text{H}_2\text{O}$  production. After 0.47 ns, however, one to one comparison between the two methods is not possible as the total number of H radicals added in the method II would be much greater than the total number of H radicals added initially in the method I.

The greater  $\text{H}_2\text{O}$  production observed using the method II could be attributed to the greater core system temperature observed, as shown in Fig. 4.36 (395 K for the method II vs 340 K for the method I at 0.47 ns) and to the fact that every time the 210 H radicals were added, not all were consumed via the initiation reactions R1 and R2. Some of these H radicals also combined with other radicals that were

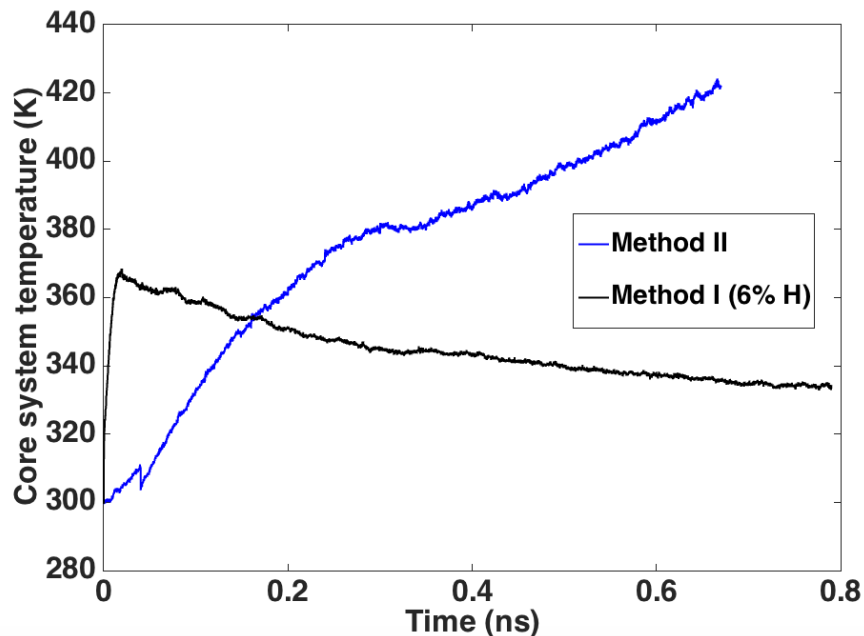


Figure 4.36.: Core system temperature as a function of time. The initial system pressure was set to 30 atm with the box size fixed at 50 nm.

already present in the system via the chain propagating and terminating reactions producing more OH and H<sub>2</sub>O. For the method I, however, since all the H radicals were added instantly at the beginning, reactions R1 and R2 dominated as there were not any other radicals present in the system for the H radicals to react with. Moreover, since the chain terminating and propagating reactions produce more heat in general as compared to the chain initiation reactions, a greater rise in the temperature was observed at the end of 0.47 ns using the method II.

Fig. 4.37 shows the different intermediate species formed using the two methods. As can be seen for the method I, as expected, initially a huge rise in the HO<sub>2</sub> and OH concentrations were observed. However, for the method II, since the H radicals were added periodically, the concentrations of both OH and HO<sub>2</sub> radicals were observed to increase much more steadily. In the HO<sub>2</sub> concentration, however, after 0.2 ns, a decrease was obtained, which could be attributed to reaction R4. Because of the increased core temperature (Fig. 4.36, at 0.2 ns, method II), the rate of reaction

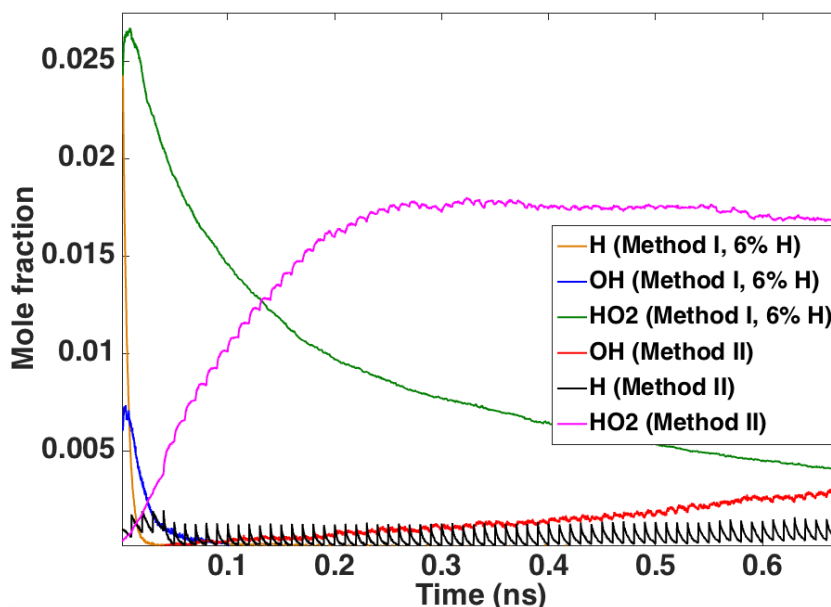


Figure 4.37.: Mole fraction of  $\text{HO}_2$ , H, O and OH as a function of time. The initial system pressure was set to 30 atm with the box size fixed at 50 nm.

R4 was also enhanced and as a result, more  $\text{HO}_2$  radicals were being converted to OH radicals. Moreover, for the method II at 0.47 ns, much more OH and  $\text{HO}_2$  radicals were produced as compared to the method I. The greater  $\text{HO}_2$  production in the method II could again be attributed to the higher core temperature observed, whereas the greater OH production could be attributed to reaction R4 as explained earlier and to the fact that every time the 210 H radicals were added, some of the H radicals reacted with the other intermediates already present in the system, which in turn generated more OH radicals. Another interesting observation that could be made from Fig. 4.37 is that for both the methods, H radicals were being consumed as soon as they were added/produced. A similar behavior in O radicals was observed and thus, a rise in the O radical concentration was never detected during the two methods.

## 4.5 Conclusions

(1) A micro-thermal sensor based on resistance thermometry was first fabricated to measure the temperature changes occurring during the combustion of  $\text{H}_2/\text{O}_2$  gases contained inside the nanobubbles. The bubble production as a function of the voltage, polarity, frequency and duty cycle of the applied square pulses was investigated. Significant amount of bubbles were produced up to 30 kHz but after that the bubble production decreased drastically, although the faradaic current remained unchanged, signifying the combustion of  $\text{H}_2/\text{O}_2$  gases inside the nanobubbles. Moreover, the amount of heat released and the temperature changes measured were also found to increase above this threshold frequency of 30 kHz and temperature changes up to 0.85 K were obtained (for a frequency of 500 kHz). In addition, for each frequency  $> 30$  kHz, the temperature change observed was maximized at a duty cycle of 0.5 (stoichiometric  $\text{H}_2/\text{O}_2$  production). The effect of Joule heating on the temperature changes observed was also considered and was obtained to be negligible as compared to the amount of heat released from the  $\text{H}_2/\text{O}_2$  combustion. Moreover, since joule heating does not depend on the frequency of the applied voltages, the nature of the temperature changes observed further confirms combustion inside the nanobubbles.

(2) Next, non-reactive MD simulations were conducted to determine how does the surface tension of water surrounding the electrodes is affected by the presence of dissolved external gases, which would in turn help to predict the pressures inside nanobubbles. The surface tension of water was found to decrease with an increase in the supersaturation ratio (or an increase in the external gas concentration), thus, the internal pressure inside a nanobubble is much smaller than what would have been predicted using the planar-interface surface tension value of water. For example, for  $S = 200$ , the surface tension of water was lowered by 30%. Nevertheless, the pressures were still very high, which could provide a suitable environment for the spontaneous ignition and combustion to occur.

(3) Finally, using reactive MD simulations, the possibilities of spontaneous ignition of  $\text{H}_2/\text{O}_2$  gases under low temperature and high pressure conditions were explored. The results obtained qualitatively explained as why spontaneous combustion has taken place inside nanobubbles for frequencies greater than 30 kHz. The effects of surface-assisted dissociation of  $\text{H}_2$  and  $\text{O}_2$  gases and initial system pressure on the ignition and reaction kinetics of the  $\text{H}_2/\text{O}_2$  system were determined. In addition, the temperature of the system was not held constant at 300 K but was allowed to be varied according to the amount of heat lost/gained during the combustion process. In macroscale combustion, whenever an ignition is provided, a huge rise in the temperature is observed with  $\text{H}_2\text{O}$  as the final product being formed. However, in the present nanoscale combustion process, due to the large surface to volume ratio, most of the energy released from the exothermic chemical reactions was lost from the walls of the combustion chamber and thus, only a slight rise in the temperature was observed ( $\sim 68$  K, using method I). Moreover, instead of  $\text{H}_2\text{O}$ ,  $\text{H}_2\text{O}_2$  was the final product formed (6-140 times  $\text{H}_2\text{O}$ ). This was attributed to the low temperature and high pressure conditions under which the chemical reactions were taking place. The system reactivity (or the rate of  $\text{H}_2\text{O}_2$  formation) was found to increase with an increase in either the initial H radical concentration or the system pressure. Moreover, the effect of O radical addition was also studied and similar to the H radical addition,  $\text{H}_2\text{O}_2$  was the dominant final product formed. The system reactivity, however, was slightly increased but the overall species evolution of the intermediates remained unchanged. In addition, since the exact mechanism through which the H radicals are produced at the bubble surface is not known, the effect of continuous addition of H radicals (method II) vs. adding H radicals only at the beginning of the simulation (method I) was also studied. And again, similar to all the previous cases simulated,  $\text{H}_2\text{O}_2$  was the final product formed. However, using the method II, slightly higher temperatures and  $\text{H}_2\text{O}$  production was observed.

## Future Work

Building on the knowledge gained from the nanobubble preliminary work, the following experiments are proposed that will help bring the nanobubble one step closer to be used as a practical device:

- 1) Fabricate a device with less amount of heat loss in order to make it more efficient and useful. In the present work, a mm-sized drop of liquid was placed above the electrodes to conduct electrolysis, which absorbed some of the heat produced from the nanobubble combustion. Thus, it would be more useful to fabricate a device by etching micro-channels and reducing the amount of liquid surrounding the electrodes. This will enable a greater rise in the temperature change to be observed.
- 2) Fabricate a device with the back-side of the Si wafer etched out. This, similar to the above recommendation, will help to increase the amount of temperature changes that could be obtained. By etching the Si wafer, the thermal mass of the device will be reduced which will in turn, decrease the amount of heat lost.
- 3) Conduct electrolysis with circular-shaped electrodes. In the present work, only square-shaped electrodes were used, which due to their sharp edges produced a few micro-sized bubbles even for the cases where combustion was observed in the interior of the electrodes (i.e. for frequencies  $> 30$  kHz). Thus, the use of circular-shaped electrodes, due to the absence of any sharp edges, will increase the combustion efficiency by reducing the micro-sized bubble production.
- 4) Analyze the water after combustion for any  $\text{H}_2\text{O}_2$  production to confirm the predictions obtained from reactive MD simulations. A number of methods can be used for identifying  $\text{H}_2\text{O}_2$  in water such as titration, spectrophotometry, fluorescence and chemiluminescence [208].

## 5. CONCLUSIONS

In this work, the burn rate enhancement of solid propellants when coupled to highly conductive graphene-based micro-structures was demonstrated using both experiments and molecular dynamic (MD) simulations. Three different types of graphene-structures were considered i.e. graphite sheet (GS), graphene nano-pellets (GNPs) and graphene foam (GF), with nitrocellulose (NC) as the solid propellant. In most of the traditional burn rate enhancement studies, the chemical effect of a metal/metal-oxides is used to improve the thermal decomposition characteristics of a propellant, which in turn enhances the burn rate. But in this study, the physical effect of enhanced thermal transport was used to improve the burn rates. Only a few studies in the literature have demonstrated this concept, thus, the knowledge gained from this work will be beneficial for the future application of this concept in practical combustion and propulsion systems.

### NC-GS System

(1) Propellant layers (NC) ranging from 25  $\mu\text{m}$  to 170  $\mu\text{m}$  were deposited on the top of a 20  $\mu\text{m}$  thick graphite sheet. Burn rates were measured as a function of the ratio of fuel to graphite layer thickness and an optimum fuel thickness of around 125  $\mu\text{m}$  was obtained with average burn rates up to 2.3 cm/s (3.3 times the bulk NC burn rate). The optimum fuel thickness behavior observed was attributed to the competition between the amount of energy released from the exothermic reactions and the amount of heat lost to the graphite sheet.

(2) The burn rates obtained were not steady but had an oscillatory profile associated with it. The exact period and amplitude of the combustion wave oscillations were

again found to be dependent on the thickness of the fuel layer deposited. For example, for the fuel thickness of  $25\ \mu\text{m}$ , oscillation periods as high as  $0.1\ \text{s}$  were obtained. However, as the fuel thickness was increased to  $70\ \mu\text{m}$  and  $125\ \mu\text{m}$ , oscillation periods on the order of  $0.05\ \text{s}$  and  $0.03\ \text{s}$  were obtained, respectively.

(3) Next, the coupled NC-GS system was analyzed in detail using 1-D energy conservation equations along with simple one-step chemistry. Three important non-dimensional parameters were identified that governed the burn rate enhancement and the oscillatory nature of the combustion waves:  $R$  - ratio of fuel to graphite thickness,  $\alpha_0$  - ratio of graphite to fuel thermal diffusivity and  $\beta$  - inverse adiabatic temperature rise. The average burn rates, and oscillation periods and amplitudes predicted using the 1-D modeling agreed well with the experimental observations.

### **GNP-doped NC System**

(1) For the GNP-doped NC films, propellant layers,  $500 \pm 30\ \mu\text{m}$  thick, were deposited on the top of a thermally insulating glass slide with the doping concentrations of GNPs being varied from 1-5% by mass. An optimum doping concentration of 3% was obtained for which the burn rate enhancement was 2.7 times.

(2) The effective thermal conductivity of GNP-doped NC films were also measured experimentally using a steady state, controlled, heat flux method using the Fourier's law of heat conduction and a linear increase in the thermal conductivity value as a function of the doping concentration was obtained, with a 70% enhancement for the GNP-NC sample having 5% wt. of GNPs.

(3) Finally, the GNPs were found to remain unburned after the combustion process. To confirm, a TG analysis of GNPs was conducted in air and negligible weight loss was obtained up to  $870\ \text{K}$ . Since, the maximum NC surface temperature measured was only  $613\ \text{K}$ , the thermal stability of the GNPs obtained was expected.

## NC-GF System

(1) The effects of both the fuel loading ratio (%) and GF density on the burn rates obtained were studied. An optimum fuel loading of 55% was obtained, however, as a function of the GF density a monotonic decreasing trend was observed. Overall, burn rates up to 5.5 cm/s (7.6 times the bulk NC burn rate) were obtained, which were 2.4 and 2.9 times greater than the burn rates obtained using GS and GNPs, respectively. Such a huge amount of enhancement was attributed to the GF's unique thermal properties resulting from its 3D interconnected network, high thermal conductivity, low thermal boundary resistance and low thermal mass.

(2) The thermal conductivity of the GF strut walls was also measured, using the method similar to that of the GNPs. Two GF structures of densities: 22 mg/cm<sup>3</sup> and 11.3 mg/cm<sup>3</sup> were considered for which the strut walls thermal conductivity values came out to be 102 W/m-K and 271 W/m-k, respectively. The trend observed in the thermal conductivity values was consistent with the burn rate enhancement behavior, thus, confirming that the lower density GF structures grown were indeed of much better quality.

(3) Similar to the GNPs, the GF structure remained unburned after the combustion process with its 3D interconnected network preserved. In addition, the reusability of the GF structure was also tested by re-depositing fuel on the GF surface after combustion. The particular case tested was with the GF of density 18 mg/cm<sup>3</sup> and fuel loading of 75%. Similar burn rates were obtained using the fresh (2.1 cm/s) and re-used (1.7 cm/s) GF structures, implying that the thermal properties of the GF structure was only slightly changed after the combustion process.

### NC-GF-MnO<sub>2</sub> System

(1) To further enhance the burn rates, the GF structures were coated with a transition metal oxide layer (MnO<sub>2</sub>). Burn rates of NC as a function of MnO<sub>2</sub>-NC and NC-GF loadings were studied and an optimum MnO<sub>2</sub>-NC loading corresponding to the maximum burn rate was obtained for each NC-GF loading, which shifted to the right as the NC-GF loading was decreased. With the use of the GF-supported MnO<sub>2</sub> structures, burn rate enhancement up to 9 times was obtained, which was attributed to the coupled physical and chemical effects. The physical effect comes from the use of the GF structure because of its superior thermal transport properties, whereas the chemical effect comes from the addition of the MnO<sub>2</sub> oxide layer, which increases the chemical reactivity (thermal decomposition) of the propellant. The GF supported MnO<sub>2</sub> particles provided a more efficient contact between the propellant NC and MnO<sub>2</sub> in terms of the uniformity and surface area of the catalyst exposed. This is in contrast to the traditional composite propellant mixtures in which a continuous contact between the propellant and the catalyst is not achieved because of the random addition of catalyst particles into the propellant solution.

(2) In addition, the TG and DSC analysis were also conducted to determine the activation energy (E) and peak thermal decomposition (PTD) temperatures of NC for various values of NC-GF and MnO<sub>2</sub>-NC loadings. Similar to the burn rate results (for each NC-GF loading tested), as the MnO<sub>2</sub>-NC loading was increased, an initial decrease in both E and PTD temperatures was obtained but above a certain MnO<sub>2</sub> concentration, a slight rise was observed.

### PETN-MWCNT System (MD Simulations)

(1) Reactive molecular dynamics simulations were conducted first to study the burn rate enhancement of a solid monopropellant, Pentaerythritol Tetranitrate (PETN), when coupled to highly conductive multi-walled carbon nanotubes (MWCNTs). The

thickness of the PETN layer and the diameter of the MWCNTs were varied to determine the effect of PETN-MWCNT loading on the burn rates obtained. Burn rate enhancement up to 3 times was observed and an optimal PETN-MWCNT loading of 45% was obtained. Moreover, the temporal distribution of the species was also studied, which confirmed that the MWCNTs remained unburned during the PETN combustion. Thus, these graphene-structures do not take part in the chemical reactions but act only as thermal conduits, transferring heat from the burned to the unburned portions of the fuel.

(2) In addition to the reactive MD simulations, two additional non-reactive MD simulations were also conducted to better understand the mechanisms contributing to the thermal conductivity enhancement of the composite and in turn, the burn rate enhancement. The increased thermal transport observed among the PETN molecules was attributed to the combined effect of high axial thermal conductivity of the MWCNTs and enhanced ordering of the PETN molecules around the CNTs.

## 6. FUTURE WORK

In this work, the physical effect of high thermal transport, due to the addition of graphene-based materials, was used to enhance the burn rates of a solid monopropellant, nitrocellulose (NC). Three different types of graphene-based micro-structures were tested i.e. graphite sheet (GS), graphene nano-pellets (GNPs) and graphene foam (GF). Of all the three graphene materials, GF provided the maximum amount of burn rate enhancement, around 8 times the bulk NC burn rate. Thus, to further test the potential of GF structures, a thin metal oxide layer ( $\text{MnO}_2$ ) was thermally-coated onto the GF structures using which, even greater burn rate enhancements were observed (up to 9 times). This dissertation is the very first work that has investigated the use of GF structures for the burn rate enhancement of solid propellants and thus, the full potential of the GF structures has yet to be explored. The following are a few experimental and numerical works proposed:

- 1) The amount of burn rate enhancement that could be obtained is a strong function of the chemical and thermal properties of the propellant being used, as was shown by using simple 1-D modeling (section 2.4), thus, as a next step, experiments should be conducted to test the usefulness of GF structures towards enhancing the burn rates of different types of propellants (solids or liquids). Moreover, a few experiments should also be conducted with propellants having high surface burning temperatures ( $> 1100$  K). In the present work, the maximum NC surface temperature obtained was only 613 K, thus, by using propellants with much higher surface temperatures, the GF structures will also get consumed and as a result, increase the energy density of the propellant system.

- 2) Explore the high pressure effect on the burn rate enhancement behavior. Since, most of the solid rockets operate at pressures  $> 100$  psi, it would be beneficial to see how does the effectiveness of GF structures changes with an increase in pressure. For solid propellants, the burn rate can be expressed as a function of pressure using the empirical relationship:  $b$  (burn rate) =  $aP^n$  [209]. Thus, the main objective of this part of the study should be able to determine how does the temperature coefficient ( $a$ ) and the pressure exponent ( $n$ ) of a solid propellant changes when coupled to GF structures.
- 3) Study the burn rate enhancement using GF structures functionalized with different types of transition metal oxides such as  $\text{Co}_3\text{O}_4$ ,  $\text{CuO}$ ,  $\text{CeO}_2$  and  $\text{NiO}$ , all of which have been shown to facilitate the conversion of  $\text{NO}_2$  to  $\text{NO}$  [117, 119]. However, if propellants other than NC (or in which the thermal decomposition mechanism is different) are being considered, than the type of oxides used will be different from the ones mentioned above.
- 4) Perform a numerical study to determine the effects of various parameters such as GF porosity, pore size and sheet thickness; catalyst material and concentration; propellant type and loading on the burn rate enhancement behavior. This will help to support the experimental studies proposed above. Moreover, with the use of numerical modeling, the GF structure, propellant and catalyst can all be tailored to get an idea on the possible combinations possible, to get the desired performance for a particular application.

## REFERENCES

## REFERENCES

- [1] Andrew D. Ketsdever and Michael M. Micci. *Micropropulsion Options for the TechSat21 Space-Based Radar Flight*. Progress in Astronautics and Aeronautics. American Institute of Aeronautics and Astronautics, January 2000.
- [2] C Rossi, S Orieux, B Laranogot, T Do Conto, and D Estève. Design, fabrication and modeling of solid propellant microrocket-application to micropropulsion. *Sensors and Actuators A: Physical*, 99(1):125 – 133, 2002. Special issue from the papers presented in Symposium J in E-MRS 2001 conference.
- [3] K. L. Zhang, S. K. Chou, S. S. Ang, and X. S. Tang. A mems-based solid propellant microthruster with au/ti igniter. *Sensors and Actuators A: Physical*, 122(1):113 – 123, 2005. SSSAMW 04.
- [4] K. L. Zhang, S. K. Chou, and S. S. Ang. Mems-based solid propellant microthruster design, simulation, fabrication, and testing. *Journal of Microelectromechanical Systems*, 13(2):165–175, April 2004.
- [5] D. MORASH and L. STRAND. Miniature propulsion components for the pluto fast flyby spacecraft. Joint Propulsion Conferences. American Institute of Aeronautics and Astronautics, June 1994.
- [6] Johan Kohler, Johan Bejhed, Henrik Kratz, Fredrik Bruhn, Ulf Lindberg, Klas Hjort, and Lars Stenmark. A hybrid cold gas microthruster system for spacecraft. *Sensors and Actuators A: Physical*, 97-98:587 – 598, 2002. Selected papers from Eurosenors XV.
- [7] A.P. London, A.A. Ayon, A.H. Epstein, S.M. Spearing, T. Harrison, Y. Peles, and J.L. Kerrebrock. Microfabrication of a high pressure bipropellant rocket engine. *Sensors and Actuators A: Physical*, 92(1):351 – 357, 2001. Selected Papers for Eurosenors XIV.
- [8] Juergen Mueller. *Thruster options for microspacecraft - A review and evaluation of existing hardware and emerging technologies*. American Institute of Aeronautics and Astronautics, 2018/01/12 1997.
- [9] Jijun Xiong, Zhaoying Zhou, Xiongying Ye, Xiaohao Wang, Yanyin Feng, and Yonghong Li. A colloid micro-thruster system. *Microelectronic Engineering*, 61-62:1031 – 1037, 2002. Micro- and Nano-Engineering 2001.
- [10] R. J. Cassady, W. A. Hoskins, M. Campbell, and C. Rayburn. A micro pulsed plasma thruster (ppt) for the "dawgstar" spacecraft. In *2000 IEEE Aerospace Conference. Proceedings (Cat. No.00TH8484)*, volume 4, pages 7–14 vol.4, 2000.

- [11] L Garrigues, A Heron, J C Adam, and J P Boeuf. Hybrid and particle-in-cell models of a stationary plasma thruster. *Plasma Sources Science and Technology*, 9(2):219, 2000.
- [12] Ron Corey, Nicolas Gascon, Jorge Delgado, Geraldine Gaeta, Saghir Munir, and Jeffery Lin. *Performance and Evolution of Stationary Plasma Thruster Electric Propulsion for Large Communications Satellites*. American Institute of Aeronautics and Astronautics, 2018/01/12 2010.
- [13] L. Garrigues, I. D. Boyd, and J. P. Boeuf. Computation of hall thruster performance. *Journal of Propulsion and Power*, 17(4):772–779, 2018/01/12 2001.
- [14] Claude Phipps and James Luke. Diode laser-driven microthrusters: A new departure for micropropulsion. *AIAA Journal*, 40(2):310–318, 2018/01/12 2002.
- [15] Salvo Marcuccio, Angelo Genovese, and Mariano Andrenucci. Experimental performance of field emission microthrusters. *Journal of Propulsion and Power*, 14(5):774–781, 2018/01/12 1998.
- [16] M. Fehringner, F. Ruedenauer, W. Steiger, M. Fehringner, F. Ruedenauer, and W. Steiger. *Space-proven indium liquid metal field ion emitters for ion microthruster applications*. American Institute of Aeronautics and Astronautics, 2018/01/12 1997.
- [17] Johannes Mitterauer. *Micropropulsion for Small Spacecraft: A New Challenge for FEED and MILMIS*. American Institute of Aeronautics and Astronautics, 2018/01/12 2002.
- [18] Wonjoon Choi, Seunghyun Hong, Joel T. Abrahamson, Jae-Hee Han, Changsik Song, Nitish Nair, Seunghyun Baik, and Michael S. Strano. Chemically driven carbon-nanotube-guided thermopower waves. *Nature Materials*, 9:423 EP –, 03 2010.
- [19] Sumeet Walia, Rodney Weber, Kay Latham, Phred Petersen, Joel T. Abrahamson, Michael S. Strano, and Kouros Kalantar-zadeh. Oscillatory thermopower waves based on bi2te3 films. *Advanced Functional Materials*, 21(11):2072–2079, 2011.
- [20] Sumeet Walia, Rodney Weber, Sharath Sriram, Madhu Bhaskaran, Kay Latham, Serge Zhuiykov, and Kouros Kalantar-zadeh. Sb2te3 and bi2te3 based thermopower wave sources. *Energy Environ. Sci.*, 4:3558–3564, 2011.
- [21] Sumeet Walia, Rodney Weber, Sivacarendran Balendhran, David Yao, Joel T. Abrahamson, Serge Zhuiykov, Madhu Bhaskaran, Sharath Sriram, Michael S. Strano, and Kouros Kalantar-zadeh. Zno based thermopower wave sources. *Chem. Commun.*, 48:7462–7464, 2012.
- [22] Sumeet Walia, Sivacarendran Balendhran, Pyshar Yi, David Yao, Serge Zhuiykov, Muthu Pannirselvam, Rodney Weber, Michael S. Strano, Madhu Bhaskaran, Sharath Sriram, and Kouros Kalantar-zadeh. Mno2-based thermopower wave sources with exceptionally large output voltages. *The Journal of Physical Chemistry C*, 117(18):9137–9142, 2013.

- [23] Yanping Wang, Xiaoyun Xia, Junwu Zhu, Yi Li, Xin Wang, and Xudong Hu. Catalytic activity of nanometer-sized  $\text{CuO}/\text{Fe}_2\text{O}_3$  on thermal decomposition of AP and combustion of AP-based propellant. *Combustion Science and Technology*, 183(2):154–162, 2010.
- [24] Wei Li and Hua Cheng. Cu/c/o nanocomposites: Synthesis and characterization as catalysts for solid state propellants. *Solid State Sciences*, 9(8):750–755, 2007.
- [25] Amy Gerards, Jamie Neidert, and Larry Pledger. *High-Performance Propellant Development and Demonstration*. Joint Propulsion Conferences. American Institute of Aeronautics and Astronautics, 2005.
- [26] Peter Gilbert, Chris Zaseck, Roberto Nazario, and Steven Son. *An Investigation of Novel Metal Complexes as Composite Propellant Burn Rate Modifiers*. Joint Propulsion Conferences. American Institute of Aeronautics and Astronautics, 2008.
- [27] Inder.Pal.Singh Kapoor, Pratibha Srivastava, and Gurdip Singh. Nanocrystalline transition metal oxides as catalysts in the thermal decomposition of ammonium perchlorate. *Propellants, Explosives, Pyrotechnics*, 34(4):351–356, 2009.
- [28] C. W. Fong and R. F. Smith. The effect of binder, particle size and catalyst on the burning rates of PETN and RDX composite propellants. *Combustion Science and Technology*, 57(1-3):1–15, 1988.
- [29] Satyanarayanan R. Chakravarthy, Edward W. Price, and Robert K. Sigman. Mechanism of burning rate enhancement of composite solid propellants by ferric oxide. *Journal of Propulsion and Power*, 13(4):471–480, 1997.
- [30] Matthew L. Gross. *Two-Dimensional Modeling of AP/HTPB Utilizing a Vorticity Formulation and One-Dimensional Modeling of AP and ADN*. Dissertation, Ira A. Fulton College of Engineering and Technology, Chemical Engineering, Brigham Young University, 2007.
- [31] Shalom Abraham, Aped Hadassah, Kivity Moshe, and Horowitz David. *The Effect of Nanosized Aluminum on Composite Propellant Properties*. Joint Propulsion Conferences. American Institute of Aeronautics and Astronautics, 2005.
- [32] Xin Zhang, Walid M. Hikal, Yue Zhang, Sanjoy K. Bhattacharia, Li Li, Sidharth Panditrao, Shiren Wang, and Brandon L. Weeks. Direct laser initiation and improved thermal stability of nitrocellulose/graphene oxide nanocomposites. *Applied Physics Letters*, 102(14):141905, 2013.
- [33] Lisa M. Viculis, Julia J. Mack, Oren M. Mayer, H. Thomas Hahn, and Richard B. Kaner. Intercalation and exfoliation routes to graphite nanoplatelets. *Journal of Materials Chemistry*, 15(9):974–978, 2005.
- [34] R Saito, G Dresselhaus, and M S Dresselhaus. *Physical Properties of Carbon Nanotubes*. PUBLISHED BY IMPERIAL COLLEGE PRESS AND DISTRIBUTED BY WORLD SCIENTIFIC PUBLISHING CO., 2011.
- [35] Zongping Chen, Wencai Ren, Libo Gao, Bilu Liu, Songfeng Pei, and Hui-Ming Cheng. Three-dimensional flexible and conductive interconnected graphene networks grown by chemical vapour deposition. *Nat Mater*, 10(6):424–428, 2011.

- [36] Weiwei Cai, Arden L. Moore, Yanwu Zhu, Xuesong Li, Shanshan Chen, Li Shi, and Rodney S. Ruoff. Thermal transport in suspended and supported monolayer graphene grown by chemical vapor deposition. *Nano Letters*, 10(5):1645–1651, 2010.
- [37] Shanshan Chen, Arden L. Moore, Weiwei Cai, Ji Won Suk, Jinho An, Columbia Mishra, Charles Amos, Carl W. Magnuson, Junyong Kang, Li Shi, and Rodney S. Ruoff. Raman measurements of thermal transport in suspended monolayer graphene of variable sizes in vacuum and gaseous environments. *ACS Nano*, 5(1):321–328, 2011.
- [38] Suchismita Ghosh, Wenzhong Bao, Denis L. Nika, Samia Subrina, Evghenii P. Pokatilov, Chun Ning Lau, and Alexander A. Balandin. Dimensional crossover of thermal transport in few-layer graphene. *Nat Mater*, 9(7):555–558, 2010.
- [39] Savas Berber, Young-Kyun Kwon, and David Tomanek. Unusually high thermal conductivity of carbon nanotubes. *Physical Review Letters*, 84(20):4613–4616, 2000.
- [40] M. K. Samani, N. Khosravian, G. C. K. Chen, M. Shakerzadeh, D. Baillargeat, and B. K. Tay. Thermal conductivity of individual multiwalled carbon nanotubes. *International Journal of Thermal Sciences*, 62:40–43, 2012.
- [41] Ke Sun, Michael A. Stroschio, and Mitra Dutta. Thermal conductivity of carbon nanotubes. *Journal of Applied Physics*, 105(7):074316, 2009.
- [42] Inhwa Jung, Dmitriy A. Dikin, Richard D. Piner, and Rodney S. Ruoff. Tunable electrical conductivity of individual graphene oxide sheets reduced at low temperatures. *Nano Letters*, 8(12):4283–4287, 2008.
- [43] Xiaolin Li, Guangyu Zhang, Xuedong Bai, Xiaoming Sun, Xinran Wang, Enge Wang, and Hongjie Dai. Highly conducting graphene sheets and langmuir-blodgett films. *Nat Nano*, 3(9):538–542, 2008.
- [44] Aiping Yu, Palanisamy Ramesh, Mikhail E. Itkis, Elena Bekyarova, and Robert C. Haddon. Graphite nanoplatelet/epoxy composite thermal interface materials. *The Journal of Physical Chemistry C*, 111(21):7565–7569, 2007.
- [45] Vivek Goyal and Alexander A. Balandin. Thermal properties of the hybrid graphene-metal nano-micro-composites: Applications in thermal interface materials. *Applied Physics Letters*, 100(7):073113, 2012.
- [46] Khan M. F. Shahil and Alexander A. Balandin. Graphene multilayer graphene nanocomposites as highly efficient thermal interface materials. *Nano Letters*, 12(2):861–867, 2012.
- [47] M. J. Biercuk, M. C. Llaguno, M. Radosavljevic, J. K. Hyun, A. T. Johnson, and J. E. Fischer. Carbon nanotube composites for thermal management. *Applied Physics Letters*, 80(15):2767–2769, 2002.
- [48] H. Huang, C. H. Liu, Y. Wu, and S. Fan. Aligned carbon nanotube composite films for thermal management. *Advanced Materials*, 17(13):1652–1656, 2005.
- [49] Su Yong Kwon, Il Min Kwon, Yong-Gyoo Kim, Sanghyun Lee, and Y. oung-Soo Seo. A large increase in the thermal conductivity of carbon nanotube/polymer composites produced by percolation phenomena. *Carbon*, 55:285–290, 2013.

- [50] P. Bonnet, D. Sireude, B. Garnier, and O. Chauvet. Thermal properties and percolation in carbon nanotube-polymer composites. *Applied Physics Letters*, 91(20):201910, 2007.
- [51] Quanwen Liao, Zhichun Liu, Wei Liu, Chengcheng Deng, and Nuo Yang. Extremely high thermal conductivity of aligned carbon nanotube-polyethylene composites. *Scientific Reports*, 5:16543, 2015.
- [52] Jonathan W. Lee, Jr Andrew J. Meade, Enrique V. Barrera, and Jeremy A. Templeton. Thermal transport mechanisms in carbon nanotube-nanofluids identified from molecular dynamics simulations. *Journal of Heat Transfer*, 137(7):072401–072401, 2015.
- [53] A. Moisala, Q. Li, I. A. Kinloch, and A. H. Windle. Thermal and electrical conductivity of single- and multi-walled carbon nanotube-epoxy composites. *Composites Science and Technology*, 66(10).
- [54] Yun-Hong Zhao, Zhen-Kun Wu, and Shu-Lin Bai. Study on thermal properties of graphene foam/graphene sheets filled polymer composites. *Composites Part A: Applied Science and Manufacturing*, 72:200–206, 2015.
- [55] Zhiduo Liu, Dianyuan Shen, Jinhong Yu, Wen Dai, Chaoyang Li, Shiyu Du, Nan Jiang, Hairong Li, and Cheng-Te Lin. Exceptionally high thermal and electrical conductivity of three-dimensional graphene-foam-based polymer composites. *RSC Advances*, 6(27):22364–22369, 2016.
- [56] Xiunan Chen, Yonggen Lu, Xin Zhang, and Fangjia Zhao. The thermal and mechanical properties of graphite foam/epoxy resin composites. *Materials and Design*, 40:497 – 501, 2012.
- [57] Hengxing Ji, Daniel P. Sellan, Michael T. Pettes, Xianghua Kong, Junyi Ji, Li Shi, and Rodney S. Ruoff. Enhanced thermal conductivity of phase change materials with ultrathin-graphite foams for thermal energy storage. *Energy and Environmental Science*, 7(3):1185–1192, 2014.
- [58] Fazel Yavari, Hafez Raeisi Fard, Kamyar Pashayi, Mohammad A. Rafiee, Amir Zamiri, Zhongzhen Yu, Rahmi Ozisik, Theodorian Borca-Tasciuc, and Nikhil Koratkar. Enhanced thermal conductivity in a nanostructured phase change composite due to low concentration graphene additives. *The Journal of Physical Chemistry C*, 115(17):8753–8758, 2011.
- [59] Aiping Yu, Palanisamy Ramesh, Xiaobo Sun, Elena Bekyarova, Mikhail E. Itkis, and Robert C. Haddon. Enhanced thermal conductivity in a hybrid graphite nanoplatelet ? carbon nanotube filler for epoxy composites. *Advanced Materials*, 20(24):4740–4744, 2008.
- [60] M.-T. Hung, O. Choi, Y. S. Ju, and H. T. Hahn. Heat conduction in graphite-nanoplatelet-reinforced polymer nanocomposites. *Applied Physics Letters*, 89(2):023117, 2006.
- [61] M. B. Bryning, D. E. Milkie, M. F. Islam, J. M. Kikkawa, and A. G. Yodh. Thermal conductivity and interfacial resistance in single-wall carbon nanotube epoxy composites. *Applied Physics Letters*, 87.

- [62] Sivasankaran Harish, Daniel Orejon, Yasuyuki Takata, and Masamichi Kohno. Thermal conductivity enhancement of lauric acid phase change nanocomposite with graphene nanoplatelets. *Applied Thermal Engineering*, 80:205–211, 2015.
- [63] Michael Thompson Pettes, Hengxing Ji, Rodney S. Ruoff, and Li Shi. Thermal transport in three-dimensional foam architectures of few-layer graphene and ultrathin graphite. *Nano Letters*, 12(6):2959–2964, 2012.
- [64] Liangjie Chen, Ruqiang Zou, Wei Xia, Zhenpu Liu, Yuanyuan Shang, Jinlong Zhu, Yingxia Wang, Jianhua Lin, Dingguo Xia, and Anyuan Cao. Electro- and photodriven phase change composites based on wax-infiltrated carbon nanotube sponges. *ACS Nano*, 6(12):10884–10892, 2012.
- [65] Jia-Nan Shi, Ming-Der Ger, Yih-Ming Liu, Yang-Cheng Fan, Niann-Tsyr Wen, Chaur-Kie Lin, and Nen-Wen Pu. Improving the thermal conductivity and shape-stabilization of phase change materials using nanographite additives. *Carbon*, 51:365–372, 2013.
- [66] Jun Xu and Timothy S. Fisher. Enhancement of thermal interface materials with carbon nanotube arrays. *International Journal of Heat and Mass Transfer*.
- [67] T. Tong, Y. Zhao, L. Delzeit, A. Kashani, M. Meyyappan, and A. Majumdar. Dense vertically aligned multiwalled carbon nanotube arrays as thermal interface materials. *IEEE Transactions on Components and Packaging Technologies*, 30(1):92–100, 2007.
- [68] M. A. Panzer, G. Zhang, D. Mann, X. Hu, E. Pop, H. Dai, and K. E. Goodson. Thermal properties of metal-coated vertically aligned single-wall nanotube arrays. *Journal of Heat Transfer*, 130(5):052401–052401, 2008.
- [69] K. Zhang, Y. Chai, M. M. F. Yuen, D. G. W. Xiao, and P. C. H. Chan. Carbon nanotube thermal interface material for high-brightness light-emitting-diode cooling. *Nanotechnology*, 19(21):215706, 2008.
- [70] Z. L. Gao, K. Zhang, and M. M. F. Yuen. Fabrication of carbon nanotube thermal interface material on aluminum alloy substrates with low pressure cvd. *Nanotechnology*, 22(26):265611, 2011.
- [71] Hongyuan Chen, Minghai Chen, Jiangtao Di, Geng Xu, Hongbo Li, and Qingwen Li. Architecting three-dimensional networks in carbon nanotube buckypapers for thermal interface materials. *The Journal of Physical Chemistry C*, 116(6):3903–3909, 2012.
- [72] Xinfeng Zhang, Kan Kan Yeung, Zhaoli Gao, Jinkai Li, Hongye Sun, Huansu Xu, Kai Zhang, Min Zhang, Zhibo Chen, Matthew M. F. Yuen, and Shihe Yang. Exceptional thermal interface properties of a three-dimensional graphene foam. *Carbon*, 66:201–209, 2014.
- [73] Wonjun Park, Yufen Guo, Xiangyu Li, Jiuning Hu, Liwei Liu, Xiulin Ruan, and Yong P. Chen. High-performance thermal interface material based on few-layer graphene composite. *The Journal of Physical Chemistry C*, 119(47):26753–26759, 2015.

- [74] Mohsin Ali Raza, Aidan Westwood, and Chris Stirling. Comparison of carbon nanofiller-based polymer composite adhesives and pastes for thermal interface applications. *Materials and Design*, 85:67–75, 2015.
- [75] Xi Shen, Zhenyu Wang, Ying Wu, Xu Liu, Yan-Bing He, and Jang-Kyo Kim. Multilayer graphene enables higher efficiency in improving thermal conductivities of graphene/epoxy composites. *Nano Letters*, 2016.
- [76] Kamal H. Baloch, Norvik Voskanian, Merijntje Bronsgeest, and John Cumings. Remote joule heating by a carbon nanotube. *Nat Nano*, 7(5):316–319, 2012.
- [77] Zhong Yan, Guanxiong Liu, Javed M. Khan, and Alexander A. Balandin. Graphene quilts for thermal management of high-power gan transistors. *Nat Commun*, 3:827, 2012.
- [78] Tzahi Cohen-Karni, Quan Qing, Qiang Li, Ying Fang, and Charles M. Lieber. Graphene and nanowire transistors for cellular interfaces and electrical recording. *Nano Letters*, 10(3):1098–1102, 2010.
- [79] Xiaolin Li, Guangyu Zhang, Xuedong Bai, Xiaoming Sun, Xinran Wang, Enge Wang, and Hongjie Dai. Highly conducting graphene sheets and langmuir-blodgett films. *Nat Nano*, 3(9):538–542, 2008.
- [80] Xiguang Li, Juliusz Warzywoda, and Gregory B. McKenna. Mechanical responses of a polymer graphene-sheet nano-sandwich. *Polymer*, 55(19):4976–4982, 2014.
- [81] Yuxin Liu, Xiaochen Dong, and Peng Chen. Biological and chemical sensors based on graphene materials. *Chemical Society Reviews*, 41(6):2283–2307, 2012.
- [82] Gwangseok Yang, Chongmin Lee, Jihyun Kim, Fan Ren, and Stephen J. Pearton. Flexible graphene-based chemical sensors on paper substrates. *Physical Chemistry Chemical Physics*, 15(6):1798–1801, 2013.
- [83] Hailiang Wang, Yuan Yang, Yongye Liang, Joshua Tucker Robinson, Yanguang Li, Ariel Jackson, Yi Cui, and Hongjie Dai. Graphene-wrapped sulfur particles as a rechargeable lithium/sulfur battery cathode material with high capacity and cycling stability. *Nano Letters*, 11(7):2644–2647, 2011.
- [84] Stefania Nardecchia, Daniel Carriazo, M. Luisa Ferrer, Maria C. Gutierrez, and Francisco del Monte. Three dimensional macroporous architectures and aerogels built of carbon nanotubes and/or graphene: synthesis and applications. *Chemical Society Reviews*, 42(2):794–830, 2013.
- [85] Zhong-Shuai Wu, Yi Sun, Yuan-Zhi Tan, Shubin Yang, Xinliang Feng, and Klaus Mullen. Three-dimensional graphene-based macro- and mesoporous frameworks for high-performance electrochemical capacitive energy storage. *Journal of the American Chemical Society*, 134(48):19532–19535, 2012.
- [86] P. L. Kapitza. *J. Phys. (Moscow)*, 4, 1941.
- [87] N. Shenogina, S. Shenogin, L. Xue, and P. Keblinski. On the lack of thermal percolation in carbon nanotube composites. *Applied Physics Letters*, 87(13):133106, 2005.

- [88] Ce-Wen Nan, Gang Liu, Yuanhua Lin, and Ming Li. Interface effect on thermal conductivity of carbon nanotube composites. *Applied Physics Letters*, 85(16):3549–3551, 2004.
- [89] Ravi S. Prasher, X. J. Hu, Y. Chalopin, Natalio Mingo, K. Lofgreen, S. Volz, F. Cleri, and Pawel Keblinski. Turning carbon nanotubes from exceptional heat conductors into insulators. *Physical Review Letters*, 102(10):105901, 2009.
- [90] Lin Hu, Tapan Desai, and Pawel Keblinski. Thermal transport in graphene-based nanocomposite. *Journal of Applied Physics*, 110(3):033517, 2011.
- [91] Scott T. Huxtable, David G. Cahill, Sergei Shenogin, Liping Xue, Rahmi Ozisik, Paul Barone, Monica Usrey, Michael S. Strano, Giles Siddons, Moonsub Shim, and Pawel Keblinski. Interfacial heat flow in carbon nanotube suspensions. *Nat Mater*, 2(11):731–734, 2003.
- [92] Jungkyu Park. *Thermal transport in novel three dimensional carbon nanostructure*. Dissertation, Case Western Reserve University, Department of Mechanical and Aerospace Engineering, 2016.
- [93] John Hone. *Dekker Encyclopedia of Nanoscience and Nanotechnology*, chapter Carbon nanotubes: thermal properties, pages 603–610. Marcel Dekker, 2004.
- [94] Ravi Prasher, Tao Tong, and Arun Majumdar. An acoustic and dimensional mismatch model for thermal boundary conductance between a vertical mesoscopic nanowire/nanotube and a bulk substrate. *Journal of Applied Physics*, 102(10):104312, 2007.
- [95] S. U. S. Choi, Z. G. Zhang, W. Yu, F. E. Lockwood, and E. A. Grulke. Anomalous thermal conductivity enhancement in nanotube suspensions. *Applied Physics Letters*, 79(14):2252–2254, 2001.
- [96] Jian Wang and Jian-Sheng Wang. Carbon nanotube thermal transport: Ballistic to diffusive. *Applied Physics Letters*, 88(11):111909, 2006.
- [97] Mohammad Alaghemandi, Florian Muller-Plathe, and Michael C. Bohm. Thermal conductivity of carbon nanotube/polyamide-6,6 nanocomposites: Reverse non-equilibrium molecular dynamics simulations. *The Journal of Chemical Physics*, 135(18):184905, 2011.
- [98] Mohammad Reza Gharib-Zahedi, Mohsen Tafazzoli, Michael C. Bohm, and Mohammad Alaghemandi. Interfacial thermal transport and structural preferences in carbon nanotube-polyamide-6,6 nanocomposites: how important are chemical functionalization effects? *Physical Chemistry Chemical Physics*, 17(22):14502–14512, 2015.
- [99] Justin L. Sabourin, Daniel M. Dabbs, Richard A. Yetter, Frederick L. Dryer, and Ilhan A. Aksay. Functionalized graphene sheet colloids for enhanced fuel/propellant combustion. *ACS Nano*, 3(12):3945–3954, 2009.
- [100] Li-Min Liu, Roberto Car, Annabella Selloni, Daniel M. Dabbs, Ilhan A. Aksay, and Richard A. Yetter. Enhanced thermal decomposition of nitromethane on functionalized graphene sheets: Ab initio molecular dynamics simulations. *Journal of the American Chemical Society*, 134(46):19011–19016, 2012.

- [101] Na Li, Minhua Cao, Qingyin Wu, and Changwen Hu. A facile one-step method to produce ni/graphene nanocomposites and their application to the thermal decomposition of ammonium perchlorate. *CrystEngComm*, 14(2):428–434, 2012.
- [102] Na Li, Zhenfeng Geng, Minhua Cao, Ling Ren, Xinyu Zhao, Bing Liu, Yuan Tian, and Changwen Hu. Well-dispersed ultrafine  $\text{mn}_3\text{o}_4$  nanoparticles on graphene as a promising catalyst for the thermal decomposition of ammonium perchlorate. *Carbon*, 54:124–132, 2013.
- [103] XiaoJuan Zhang, Wei Jiang, Dan Song, JianXun Liu, and FengSheng Li. Preparation and catalytic activity of ni/cnts nanocomposites using microwave irradiation heating method. *Materials Letters*, 62(15):2343–2346, 2008.
- [104] J. X. Liu Y. Wang G.-P. Liu Y. Liu, W. Jiang and F. S. Li. Study of catalyzing thermal decomposition and combustion of ap/htpb propellant with nano cu/cnts. *Acta Armamentarii*, 29(9):1029–1033, 2008.
- [105] Wang Renpeng, Li Zhaoqian, Ma Yongjun, Zhao Fengqi, and Pei Chonghua. Preparation of high filling ratio  $\text{fe}_2\text{o}_3/\text{mwcnts}$  composite particles and catalytic performance on thermal decomposition of ammonium perchlorate. *Micro and Nano Letters*, 9:787–791(4), November 2014.
- [106] W. L. Hong, Y. F. Xue, and F.Q. Zhao. Preparation of  $\text{cuo}/\text{cnts}$  and its combustion catalytic activity on double-base propellant. *Chinese Journal of Explosives and Propellants*, 336(336):83–86, 2010.
- [107] W. L. Hong, Y. F. Xue, and F.Q. Zhao. Preparation of  $\text{bi}_2\text{o}_3/\text{cnts}$  composite and its combustion catalytic effect on double-base propellant. *Chinese Journal of Explosives and Propellants*, 6(6):7–11, 2012.
- [108] Q. L. Tan, W. L. Hong, and X. B. Xiao. Preparation of  $\text{bi}_2\text{o}_3/\text{go}$  and its combustion catalytic activity on double-base propellant. *Journal of Nanoscience and Nanotechnology*, 106(106):22–27, 2013.
- [109] Feng qi Zhao, Jian hua Yi, Wei liang Hong, Ting An, and Yan jing Yang. *Chapter Ten - Preparation, Characterization, and Catalytic Activity of Carbon Nanotubes-Supported Metal or Metal Oxide*, pages 231 – 284. Elsevier, Amsterdam, 2016.
- [110] Hui Ren, Yang-yang Liu, Qing-jie Jiao, Xiao-fen Fu, and Ting-ting Yang. Preparation of nanocomposite  $\text{pbo}/\text{cuo}/\text{cnts}$  via microemulsion process and its catalysis on thermal decomposition of rdx. *Journal of Physics and Chemistry of Solids*, 71(2):149–152, 2010.
- [111] Ting An, Hui-Qun Cao, Feng-Qi Zhao, Xiao-Ning Ren, De-Yu Tian, Si-Yu Xu, Hong-Xu Gao, Yi Tan, and Li-Bai Xiao. Preparation and characterization of  $\text{ag}/\text{cnts}$  nanocomposite and its effect on thermal decomposition of cyclotrimethylene trinitramine. *Acta Physico-Chimica Sinica*, 28(9):2202–2208, 2012.
- [112] J. F. Baytos. Specific heat and thermal conductivity of explosives, mixtures, and plastic-bonded explosives determined experimentally. Los Alamos National Laboratory Informal Report LA-8034-MS, Los Alamos National Laboratory, Los Alamos, New Mexico, 1979.

- [113] M.R. Null, W.W. Lozier, and A.W. Moore. Thermal diffusivity and thermal conductivity of pyrolytic graphite from 300 to 2700 K. *Carbon*, 11(2):81 – 87, 1973.
- [114] M. Shimokawabe, A. Ohi, and N. Takezawa. Catalytic decomposition of nitrogen dioxide over various metal oxides. *Applied Catalysis A: General*, 85(2):129–133, 1992.
- [115] L. L. Wikstrom and Ken Nobe. Catalytic dissociation of nitrogen dioxide. *Industrial and Engineering Chemistry Process Design and Development*, 4(2):191–195, 1965.
- [116] Ashok K. Vijn. Sabatier-balandin interpretation of the catalytic decomposition of nitrous oxide on metal-oxide semiconductors. *Journal of Catalysis*, 31(1):51–54, 1973.
- [117] O. V. Sergeev and A. V. Yanilkin. Molecular dynamics simulation of combustion front propagation in a petn single crystal. *Combustion, Explosion, and Shock Waves*, 50(3):323–332, 2014.
- [118] K. K. Andreev. *Thermal Decomposition and Combustion of Explosives*, volume 2nd. ed. revised and supplemented. FOREIGN TECHNOLOGY DIV WRIGHT-PATTERSON AFB OH, Nauka, Moscow, 1966.
- [119] M. F. Foltz. Pressure dependence on the reaction propagation rate of petn at high pressure. In *10th International Detonation Symposium*. Lawrence Livermore National Laboratory (UCRL-JC-111316).
- [120] R. J. Moffat. Using uncertainty analysis in the planning of an experiment. *Journal of Fluids Engineering*, 107(2):173–178, 06 1985.
- [121] G. N. Mercer and R. O. Weber. Combustion waves in two dimensions and their one-dimensional approximation. *Combustion Theory and Modelling*, 1(2):157–165, 1997.
- [122] G. N. Mercer, R. O. Weber, and H. S. Sidhu. An oscillatory route to extinction for solid fuel combustion waves due to heat losses. *Proceedings of the Royal Society of London A: Mathematical, Physical and Engineering Sciences*, 454(1975):2015–2022, 1998.
- [123] M.R. Weismiller, J.Y. Malchi, R.A. Yetter, and T.J. Foley. Dependence of flame propagation on pressure and pressurizing gas for an al/cuo nanoscale thermite. *Proceedings of the Combustion Institute*, 32(2):1895 – 1903, 2009.
- [124] Hyun Su Kim, Hyun Sung Bae, Jaesang Yu, and Seong Yun Kim. Thermal conductivity of polymer composites with the geometrical characteristics of graphene nanoplatelets. *Scientific Reports*, 6:26825 EP –, 05 2016.
- [125] Seong Yun Kim, Ye Ji Noh, and Jaesang Yu. Thermal conductivity of graphene nanoplatelets filled composites fabricated by solvent-free processing for the excellent filler dispersion and a theoretical approach for the composites containing the geometrized fillers. *Composites Part A: Applied Science and Manufacturing*, 69:219 – 225, 2015.

- [126] J.I. Jang. *New Developments in Photon and Materials Research*. Materials science and technologies. Nova Science Publishers, Incorporated, 2013.
- [127] R. Saito, M. Hofmann, G. Dresselhaus, A. Jorio, and M. S. Dresselhaus. Raman spectroscopy of graphene and carbon nanotubes. *Advances in Physics*, 60(3):413–550, 2011.
- [128] Gang Chen. In *Nanoscale Energy Transport and Conversion: A Parallel Treatment of Electrons, Molecules, Phonons, and Photons*, New York, 2005. Oxford University Press.
- [129] W. J. Parker, R. J. Jenkins, C. P. Butler, and G. L. Abbott. Flash method of determining thermal diffusivity, heat capacity, and thermal conductivity. *Journal of Applied Physics*, 32(9):1679–1684, 1961.
- [130] M.R. Null, W.W. Lozier, and A.W. Moore. Thermal diffusivity and thermal conductivity of pyrolytic graphite from 300 to 2700 k. *Carbon*, 11(2):81 – 87, 1973.
- [131] James Taylor and C. R. L. Hall. Determination of the heat of combustion of nitroglycerin and the thermochemical constants of nitrocellulose. *The Journal of Physical and Colloid Chemistry*, 51(2):593–611, 1947.
- [132] J. Richard Ward. Determination of the heat capacities of gun propellants by differential scanning calorimetry. In Roger S. Porter and Julian F. Johnson, editors, *Analytical Calorimetry*, volume 4, pages 143–153, New York, 1977. Plenum Press.
- [133] Martin S. Miller. Thermophysical properties of six solid gun propellants. Technical Report ADA322890, ARMY RESEARCH LAB ABERDEEN PROVING GROUND MD, March 1997.
- [134] Joel T. Abrahamson. *Energy storage and generation from thermopower waves*. Phd thesis, Massachusetts Institute of Technology. Dept. of Chemical Engineering, 2012.
- [135] K. G. Shkadinskii, B. I. Khaikin, and A. G. Merzhanov. Propagation of a pulsating exothermic reaction front in the condensed phase. *Combustion, Explosion and Shock Waves*, 7(1):15–22, Jan 1971.
- [136] Steve Plimpton. Fast parallel algorithms for short-range molecular dynamics. *Journal of Computational Physics*, 117(1):1 – 19, 1995.
- [137] Adri C. T. van Duin, Siddharth Dasgupta, Francois Lorant, and William A. Goddard. Reaxff: a reactive force field for hydrocarbons. *The Journal of Physical Chemistry A*, 105(41):9396–9409, 2001.
- [138] Joanne Budzien, Aidan P. Thompson, and Sergey V. Zybin. Reactive molecular dynamics simulations of shock through a single crystal of pentaerythritol tetranitrate. *The Journal of Physical Chemistry B*, 113(40):13142–13151, 2009. PMID: 19791817.
- [139] H.M. Aktulga, J.C. Fogarty, S.A. Pandit, and A.Y. Grama. Parallel reactive molecular dynamics: Numerical methods and algorithmic techniques. *Parallel Computing*, 38(4):245 – 259, 2012.

- [140] Aidan P. Thompson, Steven J. Plimpton, and William Mattson. General formulation of pressure and stress tensor for arbitrary many-body interaction potentials under periodic boundary conditions. *The Journal of Chemical Physics*, 131(15):154107, 2009.
- [141] Elizabeth A. Zhurova, Adam I. Stash, Vladimir G. Tsirelson, Vladimir V. Zhurov, Ekaterina V. Bartashevich, Vladimir A. Potemkin, and A. Alan Pinkerton. Atoms-in-molecules study of intra- and intermolecular bonding in the pentaerythritol tetranitrate crystal. *Journal of the American Chemical Society*, 128(45):14728–14734, 11 2006.
- [142] J. J. Dick. Effect of crystal orientation on shock initiation sensitivity of pentaerythritol tetranitrate explosive. *Applied Physics Letters*, 44(9):859–861, 1984.
- [143] Tzu-Ray Shan and Aidan P Thompson. Shock-induced hotspot formation and chemical reaction initiation in petn containing a spherical void. *Journal of Physics: Conference Series*, 500(17):172009, 2014.
- [144] Taejin Kim, Mohamed A. Osman, Cecilia D. Richards, David F. Bahr, and Robert F. Richard. Molecular dynamic simulation of heat pulse propagation in multiwall carbon nanotubes. *Phys. Rev. B*, 76:155424, Oct 2007.
- [145] William G. Hoover. Canonical dynamics: Equilibrium phase-space distributions. *Phys. Rev. A*, 31:1695–1697, Mar 1985.
- [146] Shuichi Nose. A unified formulation of the constant temperature molecular dynamics methods. *The Journal of Chemical Physics*, 81(1):511–519, 1984.
- [147] Simone Melchionna, Giovanni Ciccotti, and Brad Lee Holian. Hoover npt dynamics for systems varying in shape and size. *Molecular Physics*, 78(3):533–544, 1993.
- [148] A. C. Landerville, I. I. Oleynik, and C. T. White. Reactive molecular dynamics of hypervelocity collisions of petn molecules. *The Journal of Physical Chemistry A*, 113(44):12094–12104, 2009. PMID: 19817467.
- [149] Florian Muller-Plathe. A simple nonequilibrium molecular dynamics method for calculating the thermal conductivity. *The Journal of Chemical Physics*, 106(14):6082–6085, 1997.
- [150] J. Hone, M. Whitney, and A. Zettl. Thermal conductivity of single-walled carbon nanotubes. *Synthetic Metals*, 103(1):2498 – 2499, 1999. International Conference on Science and Technology of Synthetic Metals.
- [151] H.-S. Philip Wong and Deji Akinwande. *Carbon nanotube interconnects*, page 157–190. Cambridge University Press, 2010.
- [152] Xiaochen Dong, Xuewan Wang, Jing Wang, Hao Song, Xingao Li, Lianhui Wang, Mary B. Chan-Park, Chang Ming Li, and Peng Chen. Synthesis of a mno<sub>2</sub> graphene foam hybrid with controlled mno<sub>2</sub> particle shape and its use as a supercapacitor electrode. *Carbon*, 50(13):4865–4870, 2012.
- [153] Hui Xia, Yu Wang, Jianyi Lin, and Li Lu. Hydrothermal synthesis of mno<sub>2</sub>/cnt nanocomposite with a cnt core/porous mno<sub>2</sub> sheath hierarchy architecture for supercapacitors. *Nanoscale Research Letters*, 7(1):33, Jan 2012.

- [154] H. E. Kissinger. Reaction kinetics in differential thermal analysis. *Analytical Chemistry*, 29(11):1702–1706, 1957.
- [155] Sergey Vyazovkin, Alan K. Burnham, Josa M. Criado, Luis A. Perez-Maqueda, Crisan Popescu, and Nicolas Sbirrazzuoli. Ictac kinetics committee recommendations for performing kinetic computations on thermal analysis data. *Thermochimica Acta*, 520(1):1 – 19, 2011.
- [156] Dun Chen, Xiang Gao, and David Dollimore. A generalized form of the kissinger equation. *Thermochimica Acta*, 215:109 – 117, 1993.
- [157] J.M. Criado and A. Ortega. Non-isothermal transformation kinetics: Remarks on the kissinger method. *Journal of Non-Crystalline Solids*, 87(3):302 – 311, 1986.
- [158] J.M. Criado and A. Ortega. Non-isothermal crystallization kinetics of metal glasses: simultaneous determination of both the activation energy and the exponent  $n$  of the jma kinetic law. *Acta Metallurgica*, 35(7):1715 – 1721, 1987.
- [159] P. Budrugaec and E. Segal. Applicability of the kissinger equation in thermal analysis. *Journal of Thermal Analysis and Calorimetry*, 88(3):703–707, Jun 2007.
- [160] S. M. Pourmortazavi, S. G. Hosseini, M. Rahimi-Nasrabadi, S. S. Hajimirsadeghi, and H. Momenian. Effect of nitrate content on thermal decomposition of nitrocellulose. *Journal of Hazardous Materials*, 162(2):1141–1144, 2009.
- [161] M.R. Sovizi, S.S. Hajimirsadeghi, and B. Naderizadeh. Effect of particle size on thermal decomposition of nitrocellulose. *Journal of Hazardous Materials*, 168(2):1134 – 1139, 2009.
- [162] P. S. Makashir, R. R. Mahajan, and J. P. Agrawal. Studies on kinetics and mechanism of initial thermal decomposition of nitrocellulose. *Journal of thermal analysis*, 45(3):501–509, 1995.
- [163] Robert W. Phillips, Charles A. Orlick, and Rudolph Steinberger. The kinetics of the thermal decomposition of nitrocellulose. *The Journal of Physical Chemistry*, 59(10):1034–1039, 1955.
- [164] Liu Huwei and Fu Ruonong. Studies on thermal decomposition of nitrocellulose by pyrolysis-gas chromatography. *Journal of Analytical and Applied Pyrolysis*, 14(2):163 – 169, 1988.
- [165] G. Lengelle, J. Duterque, and J. F. Trubert. *Physico-Chemical Mechanisms of Solid Propellant Combustion*, pages 287–334. Progress in Astronautics and Aeronautics. American Institute of Aeronautics and Astronautics, 2000.
- [166] Ting Zhang, Ningning Zhao, Jiachen Li, Hujun Gong, Ting An, Fengqi Zhao, and Haixia Ma. Thermal behavior of nitrocellulose-based superthermites: effects of nano- $\text{Fe}_2\text{O}_3$  with three morphologies. *RSC Adv.*, 7:23583–23590, 2017.
- [167] Quanbing Luo, Ting Ren, Hao Shen, Jian Zhang, and Dong Liang. The thermal properties of nitrocellulose: From thermal decomposition to thermal explosion. *Combustion Science and Technology*, 0(0):1–12, 2017.

- [168] F. Shadman-Yazdi and E. E. Petersen. The effect of catalysts on the deflagration limits of ammonium perchlorate. *Combustion Science and Technology*, 5(1):61–67, 1972.
- [169] K. Kishore, V. R. P. Verneker, and M. R. Sunitha. Effect of catalyst concentration on burning rate of composite solid propellants. *AIAA Journal*, 15(11):1649–1651, 1977.
- [170] Satyawati S. Joshi, Prajakta R. Patil, and V. N. Krishnamurthy. Thermal decomposition of ammonium perchlorate in the presence of nanosized ferric oxide. *2008*, 58(6):7, 2008.
- [171] N. N. Bakhman, V. S. Nikiforov, V. I. Avdyunin, A. E. Fogelzang, and Yu S. Kichin. Catalytic effect of ferrous oxide on burning rate of condensed mixtures. *Combustion and Flame*, 22(1):77–87, 1974.
- [172] Tomoki Naya and Makoto Kohga. Burning characteristics of ammonium nitrate-based composite propellants supplemented with mno<sub>2</sub>. *Propellants, Explosives, Pyrotechnics*, 38(1):87–94, 2013.
- [173] Yoshio Oyumi, Toshiyuki Anan, Hakobu Bazaki, and Tadamas Harada. Plateau burning characteristics of ap based azide composite propellants. *Propellants, Explosives, Pyrotechnics*, 20(3):150–155, 1995.
- [174] Kaoru Maruta. Micro and mesoscale combustion. *Proceedings of the Combustion Institute*, 33(1):125 – 150, 2011.
- [175] D. G. Norton and D. G. Vlachos. Combustion characteristics and flame stability at the microscale: a cfd study of premixed methane/air mixtures. *Chemical Engineering Science*, 58(21):4871–4882, 2003.
- [176] Lars Sitzki, Kevin Borer, Steffen Wussow, Ewald Maruta, and Paul Ronney. *Combustion in microscale heat-recirculating burners*. Aerospace Sciences Meetings. American Institute of Aeronautics and Astronautics, 2001.
- [177] Vitaly B. Svetovoy, Remko G. P. Sanders, Theo S. J. Lammerink, and Miko C. Elwenspoek. Combustion of hydrogen-oxygen mixture in electrochemically generated nanobubbles. *Physical Review E*, 84(3):035302, 2011.
- [178] Vitaly B. Svetovoy, Remko G. P. Sanders, and Miko C. Elwenspoek. Transient nanobubbles in short-time electrolysis. *Journal of Physics: Condensed Matter*, 25(18):184002, 2013.
- [179] Vitaly B. Svetovoy, Remco G. P. Sanders, Kechun Ma, and Miko C. Elwenspoek. New type of microengine using internal combustion of hydrogen and oxygen. *Scientific Reports*, 4:4296, 2014.
- [180] A. V. Postnikov, I. V. Uvarov, A. V. Prokaznikov, and V. B. Svetovoy. Observation of spontaneous combustion of hydrogen and oxygen in microbubbles. *Applied Physics Letters*, 108(12):121604, 2016.
- [181] Alexander Prokaznikov, Niels Tas, and Vitaly Svetovoy. Surface assisted combustion of hydrogen-oxygen mixture in nanobubbles produced by electrolysis. *Energies*, 10(2), 2017.

- [182] Chin Li and P. Somasundaran. Reversal of bubble charge in multivalent inorganic salt solutions?effect of magnesium. *Journal of Colloid and Interface Science*, 146(1):215–218, 1991.
- [183] Patrice Creux, Jean Lachaise, Alain Graciaa, and James K. Beattie. Specific cation effects at the hydroxide charged air/water interface. *The Journal of Physical Chemistry C*, 111(9):3753–3755, 2007.
- [184] A. Graciaa, G. Morel, P. Saulner, J. Lachaise, and R. S. Schechter. The zeta-potential of gas bubbles. *Journal of Colloid and Interface Science*, 172(1):131–136, 1995.
- [185] Masayoshi Takahashi. Zeta potential of microbubbles in aqueous solutions: Electrical properties of the gas/water interface. *The Journal of Physical Chemistry B*, 109(46):21858–21864, 2005.
- [186] James K. Beattie, Alex M. Djerdjev, and Gregory G. Warr. The surface of neat water is basic. *Faraday Discussions*, 141(0):31–39, 2009.
- [187] Robert Vacha, Ondrej Marsalek, Adam P. Willard, Douwe Jan Bonthuis, Roland R. Netz, and Pavel Jungwirth. Charge transfer between water molecules as the possible origin of the observed charging at the surface of pure water. *The Journal of Physical Chemistry Letters*, 3(1):107–111, 2012.
- [188] Phil Attard. The stability of nanobubbles. *The European Physical Journal Special Topics*, Apr 2013.
- [189] Michael P. Moody and Phil Attard. Monte carlo simulation methodology of the ghost interface theory for the planar surface tension. *The Journal of Chemical Physics*, 120(4):1892–1904, 2004.
- [190] Songnian He and Phil Attard. Surface tension of a lennard-jones liquid under supersaturation. *Phys. Chem. Chem. Phys.*, 7:2928–2935, 2005.
- [191] B C Joshi, G Eranna, D P Runthala, B B Dixit, O P Wadhawan, and P D Vyas. Lpcvd and pecvd silicon nitride for microelectronics technology. *Indian Journal of Engineering and Materials Sciences (IJEMS)*, 7:303–309, 2000.
- [192] Haiyang Zou, Jun Chen, Yunnan Fang, Jilai Ding, Wenbo Peng, and Ruiyuan Liu. A dual-electrolyte based air-breathing regenerative microfluidic fuel cell with 1.76v open-circuit-voltage and 0.74v water-splitting voltage. *Nano Energy*, 27:619 – 626, 2016.
- [193] Stephen R Turns. An introduction to combustion, 2000. *MacGraw Hill, Boston, Massachusetts, US*, 2000.
- [194] Ralph T. Ferrell and David M. Himmelblau. Diffusion coefficients of nitrogen and oxygen in water. *Journal of Chemical and Engineering Data*, 12(1):111–115, 1967.
- [195] Frederick C. Strong. Faraday’s laws in one equation. *Journal of Chemical Education*, 38(2):98, 1961.
- [196] David L. Russell. *Introduction*, pages 1–36. John Wiley and Sons, Inc., 2006.

- [197] H. J. C. Berendsen, J. R. Grigera, and T. P. Straatsma. The missing term in effective pair potentials. *The Journal of Physical Chemistry*, 91(24):6269–6271, 1987.
- [198] H.J.C. Berendsen, J .P.M. Postma, W.F. van Gunsteren, and J. Hermans. *Intermolecular forces*, chapter Interaction models for water in relation to protein synthesis, pages 331–342. Proceeding of the 14th Jerusalem Symposia on Quantum Chemistry and Biochemistry. D. Reidel, Jerusalem, Israel, 1981.
- [199] Jean-Paul Ryckaert, Giovanni Ciccotti, and Herman J.C Berendsen. Numerical integration of the cartesian equations of motion of a system with constraints: molecular dynamics of n-alkanes. *Journal of Computational Physics*, 23(3):327 – 341, 1977.
- [200] Jörg Behler, Karsten Reuter, and Matthias Scheffler. Nonadiabatic effects in the dissociation of oxygen molecules at the al(111) surface. *Phys. Rev. B*, 77:115421, Mar 2008.
- [201] Jeffrey J. Potoff and J. Ilja Siepmann. Vapor liquid equilibria of mixtures containing alkanes, carbon dioxide, and nitrogen. *AIChE Journal*, 47(7):1676–1682, 2001.
- [202] J.-P. Bouanich. Site-site lennard-jones potential parameters for n<sub>2</sub>, o<sub>2</sub>, h<sub>2</sub>, co and co<sub>2</sub>. *Journal of Quantitative Spectroscopy and Radiative Transfer*, 47(4):243 – 250, 1992.
- [203] J. V. L. Beckers, C. P. Lowe, and S. W. De Leeuw. An iterative pppm method for simulating coulombic systems on distributed memory parallel computers. *Molecular Simulation*, 20(6):369–383, 1998.
- [204] Loup Verlet. Computer ”experiments” on classical fluids. i. thermodynamical properties of lennard-jones molecules. *Phys. Rev.*, 159:98–103, Jul 1967.
- [205] John G. Kirkwood and Frank P. Buff. The statistical mechanical theory of surface tension. *The Journal of Chemical Physics*, 17(3):338–343, 1949.
- [206] C. Vega and E. de Miguel. Surface tension of the most popular models of water by using the test-area simulation method. *The Journal of Chemical Physics*, 126(15):154707, 2007.
- [207] Satyam Agrawalla and Adri C. T. van Duin. Development and application of a reaxff reactive force field for hydrogen combustion. *The Journal of Physical Chemistry A*, 115(6):960–972, 2011. PMID: 21261320.
- [208] Philip J. Brandhuber and Gregory Korshin. *Methods for the Detection ofResidual Concentrations ofHydrogen Peroxide inAdvanced OxidationProcesses*. WasteReuse Foundation, 2009.
- [209] George P. Sutton and Oscar Biblarz. *Rocket Propulsion Elements*. JOHN WILEY and SONS, INC., 7 edition, 2001.

VITA

# CV

## EDUCATION

- Dec. 2018      Ph.D., Aeronautics and Astronautics Engineering, Purdue University  
Dissertation: *Burning Behaviors of Solid Propellants using Graphene-based Micro-structures*
- Aug. 2013      M.S., Aeronautics and Astronautics Engineering, Purdue University  
Thesis: *Study of Thermo-physical of Nanofluid Fuels*
- May 2012      B.S., Aeronautics and Astronautics Engineering, Purdue University

## PROFESSIONAL EXPERIENCE

- Aug. 2012-Present    Graduate Research Assistant  
School of Aeronautics and Astronautics, Purdue University

## SKILLS

- *Micro-fabrication and Nanotechnology*: Mask Design, Lithography, Wet and Dry etching, CVD, PVD, Thin-film Surface Characterizations, Electric Circuit Design, Wire-bonding, Electrical Characterizations, SEM, TEM, Instrumentation and Packaging .
- *Thermal and Chemical Analysis*: Thermal Conductivity Measurements, TG (Thermogravimetric) and DSC (Differential Scanning Calorimetry) Analysis, EDX (Energy-Dispersive X-Ray Spectroscopy), Raman Spectroscopy.
- *Combustion Diagnostics*: High-speed and Infrared (IR) imaging.
- *Modeling and Design*: COMSOL (for conducting heat transfer analysis), ICEM CFD, ANSYS MESH, ANSYS CFX, ANSYS FLUENT (for conducting large-scale flow analysis in compressors and turbines).
- *MD (molecular dynamics) Simulations*: LAMMPS and GROMACS for performing reactive and non-reactive molecular dynamics simulations using both equilibrium and non-equilibrium techniques
- *CAD Softwares*: CATIA, Solidworks, AutoCAD
- *Application and Programing Softwares*: CEA, MATLAB, CHEMKIN, C, C++, Lab View

## AWARDS AND HONORS

- 2017              Koerner Scholarship, Purdue University  
Given to 6 graduate students in Aerospace Engineering based on research achievements
- 2017              Bilsland Dissertation Fellowship, Purdue University  
Given to 2-3 Ph.D. candidates in College of Engineering
- 2017              Stanisic Award, Purdue University  
Given to a graduate student in Aerospace Engineering based on academic performance
- 2016              Combustion Art Competition Honorable Mention, "Mesmerizing Micro-world of a Monopropellant Matrix," The Combustion Institute

- 2011 Warren G. Koerner Scholarship, Purdue University  
Given to an undergraduate student in the Aerospace Engineering based on academic performance
- 2008-2012 Purdue University Trustees Scholarship  
Given to undergraduate students (3 %) based on SAT scores and high school academic performance

## RESEARCH EXPERIENCE

- 2015-Present *Burning Behaviors of Solid Propellants using Carbon-based Micro-structures*  
(PI: Dr. Li Qiao, Maurice J. Zucrow Labs, Purdue University)
- Designed and performed experiments to study flame speed enhancement in solid propellants using highly conductive graphene micro-structures (graphite sheets, graphene nano-pellets, graphene foam)
  - Manufactured functionalized graphene foam structures with transition metal oxides (TMOs) to further test the flame speed enhancement in solid propellants - coupling the chemical effect of TMOs (enhanced thermal decomposition) with the physical effect of graphene-structures (enhanced thermal transport)
  - Modeled partial differential heat equations coupled with first-order reaction kinetics to identify important non-dimensional parameters that govern the flame speed enhancement and the oscillatory nature of the combustion waves
  - Performed reactive molecular dynamic simulations (REAXFF) to investigate the thermal transport and the reactivity of these coupled solid-propellant/graphene structures
- 2014-2018 *Combustion on a Microchip*  
(PI: Dr. Li Qiao, Birck Nanotechnology Center, Purdue University)
- Designed and fabricated a micro-scale thermal sensor based on resistance thermometry for sensitive temperature and heat power measurements during the spontaneous combustion of H<sub>2</sub>/O<sub>2</sub> gases inside nanobubbles (created from high frequency, short-time electrolysis of water)
  - Performed non-reactive molecular dynamic simulations to determine how the surface tension of water is affected by the presence of dissolved external gases, which in turn was used to predict pressures inside nanobubbles
  - Performed reactive molecular dynamics simulations (REAXFF) to model the heat diffusion and chemical reaction rates of H<sub>2</sub>/ O<sub>2</sub> gases at nano-scales.
- Fall 2014 *Flash Point Investigation of an Ionic Liquid, [Emim][EtSO<sub>4</sub>]*  
(PI: Dr. Dr. Timothée Pourpoint, Maurice J. Zucrow Labs, Purdue University)
- Designed a flash point apparatus based on the ASTM methods to measure the flash points of low vapor pressure ionic liquids
  - Identified the mechanisms responsible for the ionic liquid's flammability through the use of TG and DSC analysis.

- Fall 2013      *CFD Flow Analysis of a High Efficiency Advanced Turbo-pump Engine*  
 (PI: Dr. Stephen D. Heister, Maurice J. Zucrow Labs, Purdue University)
- Performed flow cavitation and pressure distribution analysis on a high pressure radial compressor rotating at speeds of around 70,000 rpm by creating a combined 3-D rotating (for the impeller) and stationary (for the volute) unstructured meshes
- 2012-2013      *Study of Thermo-physical of Nanofluid Fuels*  
 (PI: Dr. Li Qiao, Maurice J. Zucrow Labs, Purdue University)
- Performed MD simulations to explore the effects of energetic and catalytic nanoparticles on the surface tension and enthalpy of vaporization of water and ethanol based nanofluid type fuels
  - Conducted experiments to investigate the collision dynamics of micro-sized droplets containing nanofluid type fuels with emphasis on the transition between different collision regimes like bouncing, coalescence, disruption and fragmentation as a function of the collision Weber number and impact parameter

## TEACHING/MENTORING EXPERIENCE

- 2015-present      Graduate Student Mentor  
 Combustion Lab (Dr. Li Qiao), Purdue University
- Ensured the safety protocols were being met
  - Conducted preliminary safety tests for the experiments being run and the equipments present in the lab
  - Trained and guided new students with various experimental and computational techniques
  - Held regular research meetings to provide students constructive feedback and to track their progress
  - *Student Mentees: Omar Yehia, Jacob Hines, Lok Han Josiah Lo, Erica Chadwell and Robert Jezior*
- 2015-2017      Graduate Teaching Assistant  
 School of Aeronautics and Astronautics, Purdue University
- Gave occasional lectures and held weekly office hours to help students with the course materials
  - Helped the instructor with grading, proctoring and providing homework solutions
  - *Related courses:*
    1. Advance Rocket Propulsion (AAE 539, graduate level) - *Spring 2015*
    2. Aerospace propulsion (AAE 339, undergraduate level) - *Fall 2016 and Spring 2017*

## PUBLICATIONS

### Book Chapters

1. L. Qiao, **S Jain**, G. Mo, "Molecular Simulations for Researching Supercritical Fuel Properties in High Pressure Propulsion Systems," in *High Pressure Flows for Propulsion Applications, AIAA Progress in Astronautics and Aeronautics Series*, accepted, 2018.

## Patents

1. **S Jain**, L. Qiao, "Compositions with solid fuel loaded on graphene foams", US Provisional Patent Application # 62478637, March 30 2017

## Peer-reviewed Conference Proceedings

1. **S Jain**, A. Mahmood, L. Qiao, "Quantifying heat produced during spontaneous combustion of H<sub>2</sub>/O<sub>2</sub> nanobubbles", 2016 IEEE Sensor proceedings, Orlando, FL, Oct 30 - Nov 3, 2016

## Journal Publications

1. **S Jain**, L. Qiao, "MnO<sub>2</sub> coated graphene foam micro-structures for the flame speed enhancement of a solid-propellant", Proceedings of the Combustion Institute, (2018)
2. **S Jain**, L. Qiao, "Understanding combustion of H<sub>2</sub>/O<sub>2</sub> gases inside nanobubbles generated by water electrolysis using reactive molecular dynamic simulations", Journal of Physical Chemistry A, 122, 24, (2018)
3. **S Jain**, L. Qiao, "MD simulations of the surface tension of oxygen-supersaturated water", AIP Advances 7, 045001 (2017)
4. **S Jain**, G. Mo, L. Qiao, "Molecular dynamics simulations of flame propagation along a monopropellant PETN coupled with multi-walled carbon nanotubes, Journal of Applied Physics, 121, 054902 (2017)
5. **S Jain**, W. Park, Y. P. Chen, L. Qiao, "Flame speed enhancement of a nitrocellulose monopropellant using graphene microstructures", Journal of Applied Physics, 120, 174902 (2016)
6. **S Jain**, O. Yehia, L. Qiao, "Flame speed enhancement of solid nitrocellulose monopropellant coupled with graphite at microscales", Journal of Applied Physics, 119, 094904 (2016)
7. **S Jain**, S. Tanvir, L. Qiao, "Latent heat of vaporization of nanofluids: measurements and molecular dynamic simulations", Journal of Applied Physics, 118, 014902 (2015)
8. J. Xu, **S Jain**, L. Qiao, "Experimental and modeling study of radiation-induced droplet breakup behavior of nanofluid fuel suspensions", Journal of Applied Physics (**in review**)
9. G. Mo, S. Chakraborty, **S Jain**, L. Qiao, "Transition from subcritical to supercritical of n-Alkane mixture fuels by molecular dynamics investigation", Combustion and Flame (**in preparation**)

## Conference Proceedings and Presentations

1. S Jain, L. Qiao, "Spontaneous combustion of H<sub>2</sub>/O<sub>2</sub> gases inside nanobubbles generated by water electrolysis", 37th International Symposium on Combustion, Dublin, Ireland, July 29 - 3 Aug, 2018
2. S Jain, L. Qiao, "Burn rate enhancement of a solid nitrocellulose monopropellant using functionalized graphene foam microstructure", 6th International Energetic Materials and their Applications, Sendai, Nov 6 - 10, 2017.
3. S Jain, L. Qiao, "Enhancing burn rate of solid propellants using functionalized-graphene foam microstructures", 10th U.S. National Combustion Meeting, University of Maryland, College Park, MD, April 23 - 26, 2017

4. S Jain, L. Qiao, "Exploring the mechanisms of spontaneous combustion of H<sub>2</sub>/O<sub>2</sub> in nanobubbles generated by water electrolysis", 10th U.S. National Combustion Meeting, University of Maryland, College Park, MD, April 23 - 26, 2017
5. S Jain, L. Qiao, "Flame speed enhancement of a nitrocellulose monopropellant using carbon-based microstructures", 2016 Spring Technical Meeting, Central States Section of the Combustion Institute, Knoxville, TN, May 15 - 17, 2016
6. G. Mo, S Jain, L. Qiao, "MD simulations of flame propagation of monopropellant PETN embedded with CNTs," 25th International Colloquium on the Dynamics of Explosions and Reactive Systems, University of Leeds, UK, Aug 2 - 7, 2015

## **PROFESSIONAL AFFILIATIONS**

- Private Pilot
- Member, American Institute of Aeronautics and Astronautics (AIAA)  
*(Served as a judge to the AIAA Region III Student Conference 2018)*
- Reviewer for these journals:
  1. Journal of Thermal Analysis and Calorimetry
  2. Journal of Combustion
- Member, The Combustion Institute